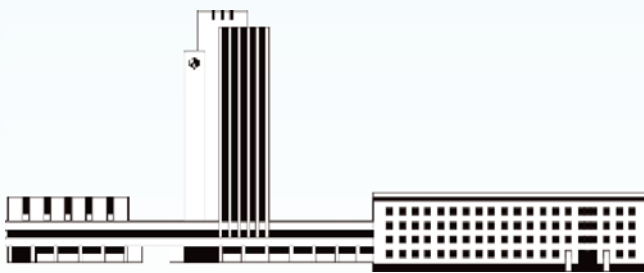


НАНОСИСТЕМИ, НАНОМАТЕРІАЛИ, НАНОТЕХНОЛОГІЇ

**Nanosistemi,
Nanomateriali,
Nanotehnologii**

ЗБІРНИК НАУКОВИХ ПРАЦЬ

ТОМ 22, ВИПУСК 3, 2024



НАЦІОНАЛЬНА АКАДЕМІЯ НАУК УКРАЇНИ



НАНОСИСТЕМИ
НАНОМАТЕРІАЛИ
НАНОТЕХНОЛОГІЇ

NANOSYSTEMS
NANOMATERIALS
NANOTECHNOLOGIES

РЕДАКЦІЙНА КОЛЕГІЯ

| | |
|--------------------------|--|
| В. А. Татаренко | головний редактор, чл.-кор. НАН України, д.ф.-м.н., проф., Ін-т металофізики ім. Г. В. Курдюмова НАН України |
| Б. М. Мордюк | заступник головного редактора, д.ф.-м.н., с.н.с., Ін-т металофізики ім. Г. В. Курдюмова НАН України |
| В. В. Лізунов | відповідальний секретар редколегії, д.ф.-м.н., проф., Ін-т металофізики ім. Г. В. Курдюмова НАН України |
| С. А. Беспалов | д.т.н., с.н.с., СФТМН НОВ Президії НАН України |
| М. Я. Валах | чл.-кор. НАН України, д.ф.-м.н., проф., Ін-т фізики напівпровідників ім. В. С. Лашкарьова НАН України |
| Р. В. Вовк | акад. НАН України, д.ф.-м.н., проф., Харківський національний ун-т імені В. Н. Каразіна МОН України |
| П. П. Горбик | чл.-кор. НАН України, д.ф.-м.н., проф., Ін-т хімії поверхні ім. О. О. Чуйка НАН України |
| В. О. Зажигалов | чл.-кор. НАН України, д.х.н., проф., Ін-т сорбції та проблем ендоекології НАН України |
| Б. Зайді | кандидат фізичних наук, факультет наук про матерію, Ун-т Батни 1 Хадж Лакдар, Батна, Алжир |
| В. Л. Карбівський | д.ф.-м.н., проф., Ін-т металофізики ім. Г. В. Курдюмова НАН України |
| О. А. Кордюк | акад. НАН України, д.ф.-м.н., проф., Київський академічний ун-т |
| С. О. Котречко | чл.-кор. НАН України, д.ф.-м.н., проф., Ін-т металофізики ім. Г. В. Курдюмова НАН України |
| М. П. Куліш | чл.-кор. НАН України, д.ф.-м.н., проф., Київський національний ун-т імені Тараса Шевченка МОН України |
| Б. І. Лев | акад. НАН України, д.ф.-м.н., проф., Ін-т теоретичної фізики ім. М. М. Боголюбова НАН України |
| Є. Г. Лен | д.ф.-м.н., проф., Ін-т металофізики ім. Г. В. Курдюмова НАН України |
| Ю. А. Малетін | чл.-кор. НАН України, д.х.н., с.н.с., Ін-т сорбції та проблем ендоекології НАН України |
| С. І. Оковитий | чл.-кор. НАН України, д.х.н., проф., Дніпровський національний університет імені Олеся Гончара МОН України |
| В. С. Панарін | д.т.н., с.н.с., Ін-т металофізики ім. Г. В. Курдюмова НАН України |
| Р. Р. Панчук | д.б.н., Ін-т біології клітини НАН України |
| О. Д. Погребняк | д.ф.-м.н., проф., Сумський державний ун-т МОН України |
| Ю. І. Прилуцький | д.ф.-м.н., проф., ННЦ «Ін-т біології та медицини» Київського національного ун-ту імені Тараса Шевченка МОН України |
| В. А. Прокопенко | д.т.н., с.н.с., Ін-т біологічної хімії ім. Ф. Д. Овчаренка НАН України |
| О. А. Пуд | д.х.н., проф., Ін-т біоорганічної хімії та нафтохімії ім. В. П. Кухаря НАН України |
| Т. М. Радченко | д.ф.-м.н., с.н.с., Ін-т металофізики ім. Г. В. Курдюмова НАН України |
| П. С. Стрижак | акад. НАН України, д.х.н., проф., Ін-т фізичної хімії ім. Л. В. Писаржевського НАН України |
| В. Й. Суґаков | чл.-кор. НАН України, д.ф.-м.н., проф., Ін-т ядерних досліджень НАН України |
| Л. Ф. Суходуб | чл.-кор. НАН України, д.ф.-м.н., проф., Сумський державний ун-т МОН України |
| В. М. Уваров | чл.-кор. НАН України, д.ф.-м.н., проф., Ін-т металофізики ім. Г. В. Курдюмова НАН України |
| О. М. Файнлейб | чл.-кор. НАН України, д.х.н., проф., Ін-т хімії високомолекулярних сполук НАН України |
| Д. О. Харченко | д.ф.-м.н., проф., Ін-т прикладної фізики НАН України |
| О. В. Хоменко | д.ф.-м.н., проф., Сумський державний ун-т МОН України |

EDITORIAL BOARD

| | |
|--------------------------|--|
| V. A. Tatarenko | Editor-in-Chief , Cor. Mem. of the N.A.S. of Ukraine, Dr. Sci. (Phys.-Math.), Prof., G. V. Kurdyumov Inst. for Metal Physics of the N.A.S. of Ukraine |
| B. M. Mordyuk | Associate Editor , Dr. Sci. (Phys.-Math.), Sr. Researcher, G. V. Kurdyumov Inst. for Metal Physics of the N.A.S. of Ukraine |
| V. V. Lizunov | Executive Managing Editor , Dr. Sci. (Phys.-Math.), Prof., G. V. Kurdyumov Inst. for Metal Physics of the N.A.S. of Ukraine |
| S. A. Bespalov | Dr. Sci. (Tech.), Sr. Researcher, SPHTMS of Sci.-Org. Dept. of Presidium of the N.A.S. of Ukraine |
| M. Ya. Valakh | Cor. Mem. of the N.A.S. of Ukraine, Dr. Sci. (Phys.-Math.), Prof., V. Ye. Lashkaryov Inst. of Semiconductor Physics of the N.A.S. of Ukraine |
| R. V. Vovk | Mem. of the N.A.S. of Ukraine, Dr. Sci. (Phys.- Math.), Prof., V. N. Karazin Kharkiv Natl. Univ. of the Ministry of Education and Science of Ukraine |
| P. P. Gorbyk | Cor. Mem. of the N.A.S. of Ukraine, Dr. Sci. (Phys.-Math.), Prof., O. O. Chuiiko Inst. of Surface Chemistry of the N.A.S. of Ukraine |
| V. O. Zazhigalov | Cor. Mem. of the N.A.S. of Ukraine, Dr. Sci. (Chem.), Prof., Inst. of Sorption and Problems of the Endoecology of the N.A.S. of Ukraine |
| Beddiaf Zaidi | Docteur en Physique, Faculté des sciences de la matière, Université Batna 1 Hadj Lakhdar, Batna, Algérie |
| V. L. Karbivskyy | Dr. Sci. (Phys.-Math.), Prof., G. V. Kurdyumov Inst. for Metal Physics of the N.A.S. of Ukraine |
| O. A. Kordyuk | Mem. of the N.A.S. of Ukraine, Dr. Sci. (Phys.- Math.), Prof., Kyiv Academic Univ. |
| S. O. Kotrechko | Cor. Mem. of the N.A.S. of Ukraine, Dr. Sci. (Phys.- Math.), Prof., G. V. Kurdyumov Inst. for Metal Physics of the N.A.S. of Ukraine |
| M. P. Kulish | Cor. Mem. of the N.A.S. of Ukraine, Dr. Sci. (Phys.- Math.), Prof., Taras Shevchenko Natl. Univ. of Kyiv of the Ministry of Education and Science of Ukraine |
| B. I. Lev | Mem. of the N.A.S. of Ukraine, Dr. Sci. (Phys.- Math.), Prof., M. M. Bogolyubov Inst. for Theoretical Physics of the N.A.S. of Ukraine |
| E. G. Len | Dr. Sci. (Phys.-Math.), Prof., G. V. Kurdyumov Inst. for Metal Physics of the N.A.S. of Ukraine |
| Yu. A. Maletin | Cor. Mem. of the N.A.S. of Ukraine, Dr. Sci. (Chem.), Sr. Researcher, Inst. of Sorption and Problems of Endoecology of the N.A.S. of Ukraine |
| S. I. Okovityy | Cor. Mem. of the N.A.S. of Ukraine, Dr. Sci. (Chem.), Prof., Oles Honchar Dnipro Natl. Univ. of the Ministry of Education and Science of Ukraine |
| V. Ye. Panarin | Dr. Sci. (Tech.), Sr. Researcher, G. V. Kurdyumov Inst. for Metal Physics of the N.A.S. of Ukraine |
| R. R. Panchuk | Dr. Sci. (Biol.), Inst. of Cell Biology of the N.A.S. of Ukraine |
| O. D. Pogrebnyak | Dr. Sci. (Phys.-Math.), Prof., Sumy State Univ. of the Ministry of Education and Science of Ukraine |
| Yu. I. Prylutskyy | Dr. Sci. (Phys.-Math.), Prof., NSC 'Inst. of Biology and Medicine' of the Taras Shevchenko Natl. Univ. of Kyiv of the Ministry of Education and Science of Ukraine |
| V. A. Prokopenko | Dr. Sci. (Tech.), Sr. Researcher, F. D. Ovcharenko Inst. of Biocolloidal Chemistry of the N.A.S. of Ukraine |
| O. A. Pud | Dr. Sci. (Chem.), Prof., V. P. Kukhar Inst. of Bioorganic Chemistry and Petrochemistry of the N.A.S. of Ukraine |
| T. M. Radchenko | Dr. Sci. (Phys.-Math.), Sr. Researcher, G. V. Kurdyumov Inst. for Metal Physics of the N.A.S. of Ukraine |
| P. Ye. Strizhak | Mem. of the N.A.S. of Ukraine, Dr. Sci. (Chem.), Prof., L. V. Pisarzhevsky Inst. of Physical Chemistry of the N.A.S. of Ukraine |
| V. J. Sugakov | Cor. Mem. of the N.A.S. of Ukraine, Dr. Sci. (Phys.-Math.), Prof., Inst. of Nuclear Research of the N.A.S. of Ukraine |
| L. F. Sukhodub | Cor. Mem. of the N.A.S. of Ukraine, Dr. Sci. (Phys.-Math.), Prof., Sumy State Univ. of the Ministry of Education and Science of Ukraine |
| V. M. Uvarov | Cor. Mem. of the N.A.S. of Ukraine, Dr. Sci. (Phys.- Math.), Prof., G. V. Kurdyumov Inst. for Metal Physics of the N.A.S. of Ukraine |
| O. M. Fainleib | Cor. Mem. of the N.A.S. of Ukraine, Dr. Sci. (Chem.), Prof., Inst. of Chemistry of Macromolecular Compounds of the N.A.S. of Ukraine |
| D. O. Kharchenko | Dr. Sci. (Phys.-Math.), Prof., Inst. of Applied Physics of the N.A.S. of Ukraine |
| O. V. Khomenko | Dr. Sci. (Phys.-Math.), Prof., Sumy State Univ. of the Ministry of Education and Science of Ukraine |

НАЦІОНАЛЬНА АКАДЕМІЯ НАУК УКРАЇНИ
Інститут металофізики ім. Г. В. Курдюмова

НАНОСИСТЕМИ, НАНОМАТЕРІАЛИ, НАНОТЕХНОЛОГІЇ

ЗБІРНИК НАУКОВИХ ПРАЦЬ
ТОМ 22, ВИПУСК 3



РВВ ІМФ
КИЇВ — 2024

У збірнику наведено оригінальні та оглядові статті за результатами робіт, виконаних у рамках досліджень за напрямом «Перспективні фундаментальні дослідження та інноваційні розробки наноматеріалів і нанотехнологій для потреб промисловості, охорони здоров'я та сільського господарства». Основну увагу приділено розгляду проблемних питань нанофізики, наноелектроніки, особливостей будови наноструктурованих матеріалів, з'ясуванню їхніх електричних, термічних, механічних, реологічних і хемічних властивостей, поверхневих явищ і самоорганізації. Представлено результати фабрикації, оброблення, тестування й аналізування нанорозмірних частинок, наномасштабних структур і багатофункціональних наноматеріалів технічного та біомедичного призначення в умовах впливу зовнішніх чинників. Розглянуто особливості технологій одержання, діагностики та характеристики наносистем.

Статті друкуються мовами оригіналів.

Збірник розраховано на наукових працівників, інженерів, викладачів ЗВО, аспірантів і студентів відповідних спеціальностей.

РЕДАКЦІЙНА КОЛЕГІЯ:

*С. А. Беспалов, М. Я. Валах, Р. В. Вовк, П. П. Горбик, В. О. Зажигалов,
Б. Зайді, В. Л. Карбівський, О. А. Кордюк, С. О. Котречко, М. П. Куліш,
Б. І. Лев, Є. Г. Лень, В. В. Лізунов (відповідальний секретар),
Ю. А. Малетін, Б. М. Мордюк (заступник головного редактора),
С. І. Оковитий, В. Є. Панарін, Р. Р. Панчук, О. Д. Погребняк,
Ю. І. Прилуцький, В. А. Прокопенко, О. А. Пуд, Т. М. Радченко,
П. Є. Стрижак, В. Й. Сугаков, Л. Ф. Суходуб,
В. А. Татаренко (головний редактор), В. М. Уваров,
О. М. Файнлейб, Д. О. Харченко, О. В. Хоменко*

НАНОСИСТЕМИ, НАНОМАТЕРІАЛИ, НАНОТЕХНОЛОГІЇ

ЗБІРНИК НАУКОВИХ ПРАЦЬ
ЗАСНОВАНИЙ У ЖОВТНІ 2003 р.

Том 22, вип. 3; 2024 р.

ЗМІСТ

| | | |
|----------------------------|--|-----|
| Редакційні повідомлення | Інформація для передплатників | IX |
| | Інформація для авторів | XI |
| | Видавнича етика | XV |
| | C_{60} -фуллерен сприяє відновленню точного позиціонування <i>muscle soleus</i> після спричиненої ахіллозомією атрофії <i>Д. М. НОЗДРЕНКО, О. П. МОТУЗЮК, О. В. ДОЛГОПОЛОВ, І. В. ПАМПУХА, К. І. БОГУЦЬКА</i> | 527 |
| | Enhanced Efficiency of Samarium-Doped TiO_2 Nanoparticles for Targeted Imaging: Characterization and <i>in vivo</i> Evaluation <i>W. M. ABD EL-KADER, R. ABO-GABAL, A. M. ABDELGHANY, and A. H. ORABY</i> | 535 |
| | Synthesis of Silver Nanoparticles <i>via</i> Pulsed-Laser Ablation in Deionized Water: Characterization and Antibacterial Applications <i>Khalaf AJAJ, Mushtaq Abed AL-JUBBORI, and Abdullah M. ALI</i> | 557 |
| | Fabrication of SiC–SrTiO ₃ -Nanoparticles-Doped PMMA/PEO Blend for Antibacterial and Radiation Shielding Fields <i>Hiba Kamil JAAFAR, Ahmed HASHIM, and Bahaa H. RABEE</i> | 569 |
| | Accident Prevention Using IoT-Based Smart Helmet <i>P. VIVEKANANDAN, P. RADHIKA, A. SIVAMANI, P. PRADEESH, and D. RAKESH</i> | 577 |
| | Raman Effect during Formation of the Ordered $L1_0$ - FePd Phase <i>R. A. SHKARBAN, D. S. LEONOV, M. Yu. NATALENKO, T. I. VERBYTSKA, M. Yu. BARABASH, and Iu. M. MAKOGON</i> | 591 |
| | Exploring the Dielectric Properties of Fe_2O_3 – In_2O_3 Nanocomposites for Electrical and Electronics | |

| | |
|---|-----|
| Applications | |
| <i>Ahmed HASHIM and Farhan Lafta RASHID</i> | 603 |
| Optical Properties of PVA–Cr ₂ O ₃ –Sb ₂ O ₃ Nanocomposites for Optoelectronics Fields | |
| <i>Ahmed HASHIM and Farhan Lafta RASHID</i> | 613 |
| Study of the Effect of Li Doping on ZnO Films Using RF-Magnetron Sputtering Method at Low Temperature | |
| <i>Israa Akram ABBAS, Ameera J. KADHM, and Raheem Lafta ALI</i> | 623 |
| Electrophysical Properties and Thermal Conductivity of Composite Based on Zinc Oxide and Reduced Graphene Oxide (1 vol.%) | |
| <i>B. TURKO, V. VASIL'EV, B. SADOVYI, R. BIHUN, I. PYLYPIV, V. KAPUSTIANYK, and D. LEONOV</i> | 637 |
| Design, Optimization, Structural and Electronic Properties of PVA/ZnO/SnO ₂ Nanostructures for Nanoelectronics Fields | |
| <i>Ali S. HASAN and Ahmed HASHIM</i> | 643 |
| Fabrication and Enhanced Dielectric Properties of PVA–Cr ₂ O ₃ –Sb ₂ O ₃ Nanocomposites for Electrical and Electronics Applications | |
| <i>Ahmed HASHIM and M. H. ABBAS</i> | 655 |
| Exploring the Optical Properties of PVA–ZrO ₂ –Sb ₂ O ₃ Nanostructures for Low-Cost Nanoelectronics Fields | |
| <i>Ahmed HASHIM and Aseel HADI</i> | 665 |
| Structural and A.C. Electrical Properties of Polyvinyl Alcohol/Iron Oxide Nanocomposites for Electronic and Electrical Applications | |
| <i>Zainab Sabri JABER and Majeed Ali HABEEB</i> | 675 |
| Exploring the Optical Properties of BaTiO ₃ /CuO-Nanoparticles-Doped PVA Polymer for Optoelectronic Applications | |
| <i>Majeed Ali HABEEB and Araa Hassan HADI</i> | 687 |
| Exploring the Structure, Optical and Electronic Properties of New PVA–PEO–Ba–Si ₃ N ₄ Structures for Electronics Applications | |
| <i>Hind AHMED and Ahmed HASHIM</i> | 699 |
| Design and Exploring the Structure and Electronic Characteristics of PS/MnO ₂ /NiO Nanosystem for Optics and Electronics Nanodevices | |
| <i>Ali S. HASAN, Ahmed HASHIM, and Zinah S. HASAN</i> | 713 |
| Effect of ZrO ₂ –CuO Nanofiller on the Optical Constants and Optical Conductivity of Biopolymer | |
| <i>Majeed Ali HABEEB, Idrees OREIBI, and Rehab Shather ABDUL HAMZA</i> | 727 |
| Low-Cost TiO ₂ /MWCNT/Ag Dye-Sensitized Solar Cell Based on Polypyrrole/SDS Counter Electrode | |
| <i>Nuhad SAAD and Oraas ADNAN</i> | 739 |

Науковий редактор випуску — *В. А. Татаренко*

Відповідальний секретар редакційної колегії — *В. В. Лізунов*

Редактори-коректори: *І. О. Головашич, Д. С. Леонов, Н. А. Леонова*

Технічні редактори — *Д. С. Леонов, І. М. Заболотний*

Оригінал-макет для прямого репродукування виготовлено комп'ютеризованою групою РВВ Інституту металофізики ім. Г. В. Курдюмова НАН України

Друкується за постановою редакційної колегії збірника англійською або українською мовами

Затверджено до друку вченою радою ІМФ ім. Г. В. Курдюмова НАН України

Свідоцтво суб'єкта видавничої справи серії ДК № 5875 від 13.12.2017 р.

Рішення Національної ради України з питань телебачення і радіомовлення № 907 від 21.03.2024 р. про суб'єкт у сфері друкованих медіа (ідентифікатор медіа R30-03169)

Підп. до друку 19.09.2024 р. Формат 70×100/16. Гарн. SchoolBookC. Папір офсет. № 1. Друк різнограф.

Адреса редакції «ННН»: Інститут металофізики ім. Г. В. Курдюмова НАН України,

бульв. Акад. Вернадського, 36, каб. 210; 03142 Київ, Україна

Тел.: +380 44 4241221, +380 44 4249042; факс: +380 44 4242561

Ел. пошта: tatar@imp.kiev.ua, dsleonov@gmail.com

Надруковано в РВВ ІМФ ім. Г. В. Курдюмова НАН України.

бульв. Акад. Вернадського, 36; 03142 Київ, Україна. Тел.: +380 44 4240236

Зав. поліграфічно-розмножувальної групи — *Л. І. Малініна*

NANOSISTEMI, NANOMATERIALI, NANOTEHNOLOGII

FOUNDED IN OCTOBER, 2003

Volume 22, Issue 3 (2024)

CONTENTS

| | | |
|------------------------------------|--|------|
| Editorial Announcements | Information for Subscribers | X |
| | Information for Contributors | XIII |
| | Publication Ethics | XVI |
| | C_{60} Fullerene Contributes to the Restoration of Precise Positioning of the <i>muscle soleus</i> After Achillotomy-Induced Atrophy <i>D. N. NOZDRENKO, O. P. MOTUZUK, O. V. DOLHOPOLOV, I. V. PAMPUHA, and K. I. BOGUTSKA</i> | 527 |
| | Enhanced Efficiency of Samarium-Doped TiO_2 Nanoparticles for Targeted Imaging: Characterization and <i>in vivo</i> Evaluation <i>W. M. Abd EL-KADER, R. ABO-GABAL, A. M. ABDELGHANY, and A. H. ORABY</i> | 535 |
| | Synthesis of Silver Nanoparticles <i>via</i> Pulsed-Laser Ablation in Deionized Water: Characterization and Antibacterial Applications <i>Khalaf AJAJ, Mushtaq Abed AL-JUBBORI, and Abdullah M. ALI</i> | 557 |
| | Fabrication of SiC-SrTiO ₃ -Nanoparticles-Doped PMMA/PEO Blend for Antibacterial and Radiation Shielding Fields <i>Hiba Kamil JAAFAR, Ahmed HASHIM, and Bahaa H. RABEE</i> | 569 |
| | Accident Prevention Using IoT-Based Smart Helmet <i>P. VIVEKANANDAN, P. RADHIKA, A. SIVAMANI, P. PRADEESH, and D. RAKESH</i> | 577 |
| | Raman Effect during Formation of the Ordered $L1_0$ -FePd Phase <i>R. A. SHKARBAN, D. S. LEONOV, M. Yu. NATALENKO, T. I. VERBYTSKA, M. Yu. BARABASH, and Iu. M. MAKOGON</i> | 591 |
| | Exploring the Dielectric Properties of Fe_2O_3 - In_2O_3 | |

| | |
|---|-----|
| Nanocomposites for Electrical and Electronics Applications | |
| <i>Ahmed HASHIM and Farhan Lafta RASHID</i> | 603 |
| Optical Properties of PVA–Cr ₂ O ₃ –Sb ₂ O ₃ Nanocomposites for Optoelectronics Fields | |
| <i>Ahmed HASHIM and Farhan Lafta RASHID</i> | 613 |
| Study of the Effect of Li Doping on ZnO Films Using RF-Magnetron Sputtering Method at Low Temperature | |
| <i>Israa Akram ABBAS, Ameera J. KADHM, and Raheem Lafta ALI</i> | 623 |
| Electrophysical Properties and Thermal Conductivity of Composite Based on Zinc Oxide and Reduced Graphene Oxide (1 vol.%) | |
| <i>B. TURKO, V. VASIL'EV, B. SADOVYI, R. BIHUN, I. PYLYPIV, V. KAPUSTIANYK, and D. LEONOV</i> | 637 |
| Design, Optimization, Structural and Electronic Properties of PVA/ZnO/SnO ₂ Nanostructures for Nanoelectronics Fields | |
| <i>Ali S. HASAN and Ahmed HASHIM</i> | 643 |
| Fabrication and Enhanced Dielectric Properties of PVA–Cr ₂ O ₃ –Sb ₂ O ₃ Nanocomposites for Electrical and Electronics Applications | |
| <i>Ahmed HASHIM and M. H. ABBAS</i> | 655 |
| Exploring the Optical Properties of PVA–ZrO ₂ –Sb ₂ O ₃ Nanostructures for Low-Cost Nanoelectronics Fields | |
| <i>Ahmed HASHIM and Aseel HADI</i> | 665 |
| Structural and A.C. Electrical Properties of Polyvinyl Alcohol/Iron Oxide Nanocomposites for Electronic and Electrical Applications | |
| <i>Zainab Sabri JABER and Majeed Ali HABEEB</i> | 675 |
| Exploring the Optical Properties of BaTiO ₃ /CuO-Nanoparticles-Doped PVA Polymer for Optoelectronic Applications | |
| <i>Majeed Ali HABEEB and Araa Hassan HADI</i> | 687 |
| Exploring the Structure, Optical and Electronic Properties of New PVA–PEO–Ba–Si ₃ N ₄ Structures for Electronics Applications | |
| <i>Hind AHMED and Ahmed HASHIM</i> | 699 |
| Design and Exploring the Structure and Electronic Characteristics of PS/MnO ₂ /NiO Nanosystem for Optics and Electronics Nanodevices | |
| <i>Ali S. HASAN, Ahmed HASHIM, and Zinah S. HASAN</i> | 713 |
| Effect of ZrO ₂ –CuO Nanofiller on the Optical Constants and Optical Conductivity of Biopolymer | |
| <i>Majeed Ali HABEEB, Idrees OREIBI, and Rehab Shather ABDUL HAMZA</i> | 727 |
| Low-Cost TiO ₂ /MWCNT/Ag Dye-Sensitized Solar Cell Based on Polypyrrole/SDS Counter Electrode | |
| <i>Nuhad SAAD and Oraas ADNAN</i> | 739 |

Scientific Editor of the Issue—*V. A. Tatarenko*

Executive Managing Editor—*V. V. Lizunov*

Technical Editors—*D. S. Leonov, I. M. Zabolotnyy*

Editorial-Publishing Department, G. V. Kurdyumov Institute for Metal Physics, N.A.S. of Ukraine

State Registration Certificate of the Printed Mass Medium: Media Identifier R30-03169

Editorial Office: 36 Academician Vernadsky Boulevard, UA-03142 Kyiv, Ukraine

Telephone: +380 44 4241221, +380 44 4249042. Fax: +380 44 4242561

E-mail: tatar@imp.kiev.ua, dsleonov@gmail.com

ІНФОРМАЦІЯ ДЛЯ ПЕРЕДПЛАТНИКІВ

Редакція щоквартального збірника наукових праць
«НАНОСИСТЕМИ, НАНОМАТЕРІАЛИ, НАНОТЕХНОЛОГІЇ»
 (CODEN: NNNAAT; ISSN (Print): 1816-5230, ISSN (Online): 2617-3794;
 у «Каталозі медіа України «Преса поштою»» передплатний індекс: **94919**)
 повідомляє про передплату (починаючи з поточного кварталу випуску).
 Рекомендуємо оформити передплату безпосередньо перерахуванням оплати

у гривнях:

«ОТРИМУВАЧУ»: Інститут металофізики ім. Г. В. Курдюмова НАН України
 на розрахунковий рахунок № UA058201720313291001201001901 в банку ГУДКСУ в м. Києві
 код банку 820172
 код ЗКПО: 05417331

для «ПОСТАЧАЛЬНИКА» — Інституту металофізики ім. Г. В. Курдюмова НАН України
 Свідоцтво платника податку № 36283185
 ПІН 054173326066

Код призначення платежу: 25010100

Призначення платежу: за збірник «Наносистеми, наноматеріали, нанотехнології» для РВВ
 ІМФ НАНУ

Підстава: передоплата 100%

в іноземній валюті (доларах США, євро) через відповідні банки-кореспонденти АТ «Державний експортно-імпорتنний банк України»:

«ОТРИМУВАЧУ»: Філія АТ «Державний експортно-імпорتنний банк України» в м. Києві (Україна,
 04053 Київ, вул. Бульварно-Кудрявська, 11^б)
 на розрахунковий рахунок № UA603223130000025308000000067
 МФО 322313

для «ПОСТАЧАЛЬНИКА» — Інституту металофізики ім. Г. В. Курдюмова НАН України

Призначення платежу: за збірник «Наносистеми, наноматеріали, нанотехнології» для РВВ
 ІМФ НАНУ

Підстава: передоплата 100%

За цього способу передплати необхідно сповістити редакцію збірника за поштовою адресою:

РВВ (№ 83) ІМФ НАНУ,

бульв. Акад. Вернадського, 36,

03142 Київ, Україна

e-mail: tatar@imp.kiev.ua; факс: +380 44 4242561; телефон: +380 44 4241221, +380 44 4249042

дату сплати, назву установи або найменування передплатника, адресу для поштової доставки, а за потреби — свої реквізити для податкової накладної.

Періодичність — том з 4 випусків у рік.

Із врахуванням поштової пересилки

для передплатників в Україні передплатна ціна: одного примірника випуску — 390 грн., тому — 1560 грн.;

для іноземних передплатників передплатна ціна: одного примірника випуску — 40 US\$ (37 EUR), тому — 160 US\$ (148 EUR).

✂

Зразок для оплати річної передплати

Рахунок-фактура

«ПОСТАЧАЛЬНИК»: Інститут металофізики ім. Г. В. Курдюмова НАН України
 «ОТРИМУВАЧУ»: Філія АТ «Державний експортно-імпорتنний банк України» в м. Києві
 (Україна, 04053 Київ, вул. Бульварно-Кудрявська, 11^б)

на розрахунковий рахунок № UA603223130000025308000000067, МФО 322313

Призначення платежу: за збірник «Наносистеми, наноматеріали, нанотехнології» для ІМФ НАНУ

«ПЛАТНИК»:

Підстава: передоплата 100%

| № | Назва | Од. вим. | Кількість | Ціна | Сума |
|----------------|---|----------|-----------|---------|----------|
| 1 | збірник «Наносистеми, наноматеріали, нанотехнології» (включаючи доставку поштою) | прим. | 4 | 40 US\$ | 160 US\$ |
| Сума до сплати | | | | | 160 US\$ |

INFORMATION FOR SUBSCRIBERS

**Editorial Board of Quarterly Collected Scientific Transactions
'NANOSISTEMI, NANOMATERIALI, NANOTEHNOLOGII'**

(i.e. 'NANOSYSTEMS, NANOMATERIALS, NANOTECHNOLOGIES')

(CODEN: NNNAAT; ISSN (Print): 1816-5230, ISSN (Online): 2617-3794)

advertises the subscription on an annual basis for this year. Orders should be placed through one of the methods described below.

Besides the subscription *via* the centralized service by JSC 'Ukrposhta' (22 Khreshchatyk Str., UA-01001 Kyiv, Ukraine; phone: 0 800 300 545; e-mail: ukrposhta@ukrposhta.ua) or *via* Internet:

<https://peredplata.ukrposhta.ua/index.php?route=product/search&search=94919&type=main>

the Editorial Board will take orders sent directly to the Editorial Board. To obtain our edition, the persons and institutions, interested in this title, should made the definite payment sent, according to the order, to the account of the Publisher—Institute for Metal Physics of the N.A.S. of Ukraine.

This edition frequency is 4 issues per year. The annual subscription rate for 'Nanosistemi, Nanomateriali, Nanotehnologii' is of 160 US\$ (or 148 EUR), including airmail postage, packing and handling charges. All other currency payments should be made using the current conversion rate set by the Publisher (subscribers should contact the Editorial Board).

Subscription is valid after obtaining by the Editorial Board of banker's order. Banker's order should be sent to the address:

G. V. Kurdyumov Institute for Metal Physics, N.A.S. of Ukraine,
currency account No. UA60322313000002530800000067, MFO 322313
in the Kyiv's Branch of JSC 'The State Export-Import Bank of Ukraine'
(Joint Stock Company 'Ukreximbank')
(11^b Bulvarno-Kudriavska Str., UA-04053 Kyiv, Ukraine)

simultaneously with written notice providing the Editorial Board with a copy of banker's order for subscription and detailed address for mailing.

Address of the Editorial Board Office:

G. V. Kurdyumov Institute for Metal Physics, N.A.S. of Ukraine,
36 Academician Vernadsky Blvd.,
UA-03142 Kyiv, Ukraine.

E-mail: tatar@imp.kiev.ua (with subject beginning by word 'nano').

Fax: +380 44 4242561.

After receiving of banker's order, the Editorial Board will send the guarantee letter to the subscriber's address for mailing the collected scientific transactions for a corresponding term.

Editorial Board of this edition hopes for effective co-operation with its present and future readers and asks to promote the maximum information about its contents to persons, institutions and organizations concerned.

ІНФОРМАЦІЯ ДЛЯ АВТОРІВ

Сборник научных трудов «Наносистеми, наноматеріали, нанотехнології» (ННН) публікує ще неопубліковані та не знаходячися на розгляді для опублікування в інших виданнях наукові огляди та оригінальні статті, що містять та характеризують результати експериментальних та теоретичних досліджень в області фізики, хімії, біології, техніки, методів синтезу, обробки та діагностики нанорозмірних систем та наномасштабних матеріалів: кластерів, наночастиць, нанотрубок, нанокристалів та наноструктур (апатитоподібних та др. біосистем, аморфних та колоїдних нанорозмірних систем, наноструктурних плівок та покриттів, нанопорошків та т.д.).

Сборник ННН не публікує: статті полемическі, класифікаційні та узкоспеціальні, що містять рішення стандартних завдань; статті описальні та методическі (если метод не являється принципіально новим); статті, в яких викладаються окремі етапи дослідження або матеріал, розділений на декілька послідователіх публікацій; статті о рядових дослідженнях, не представляючих загального інтересу та не містять значимих висновків.

Статті публікуються на одному з двох мов: **англійськом** або **українськом**.

Статті, в оформленні яких не дотримано наступні правила для публікації в ННН, повертаються авторам без розгляду по суті. (Датою подання вважається день повторного подання статті після дотримання вказаних нижче правил.)

1. Стаття повинна бути підписана всіма авторами (з вказанням їх адресів електронної пошти); слід вказати прізвище, ім'я та по батькові автора, з яким редакція буде вести переписку, його поштовий адрес, номер телефону (факса), адрес електронної пошти.

2. Виклад повинен бути ясним, структурованим (розділами «1. Вступ», «2. Експериментальна/Теоретична методика», «3. Результати та їх обговорення», «4. Висновки», «Цитування літератури»), стислим, без довгих вступів, відступів та повторів, дублювання в тексті даних таблиць, рисунків та підписів до них. Анотація та розділ «Висновки» повинні не дублювати друг друга. Числові дані слід вказувати в загальноприйнятих одиницях.

3. Обсяг статті повинен бути не більше 5000 слів (з урахуванням основного тексту, таблиць, підписів до рисунків, списку літератури) та 10 рисунків. Питання, пов'язані з публікацією наукових оглядів (не більше 22000 слів та 60 рисунків), вирішуються редколлегією ННН на основі попереднього надання авторами розширеної анотації роботи.

4. В редакцію обов'язково надається по e-mail (або на компакт-дискі) файл рукопису статті (з ілюстративним матеріалом), набраний в текстовому редакторі Microsoft Word 2003, 2007 або 2010 з назвою, що містить прізвище першого автора (латиницею), наприклад, Smirnov.doc.

5. Електронна версія рукопису повинна містити анотацію (200–250 слів) статті (разом з 5–6 ключовими словами) та 5–7 індексів PACS (в останній редакції 'Physics and Astronomy Classification Scheme 2010'—<http://publishing.aip.org/publishing/pacs/pacs-2010-regular-edition>). Тексти україномовних статей повинні також містити заголовок статті (разом з переліком авторів та адресами відповідальних установ), розширену анотацію (300–350 слів), ключові слова, заголовки таблиць та підписи до рисунків на англійськом мові. Крім того, зміст анотацій на українськом та англійськом мові повинні бути ідентичними по змісту.

7. Різунки (кольорові, чорно-білі або напівтоніві) повинні бути представлені в вигляді окремих файлів (предпочтительно в графіческих форматах TIFF, EPS або JPEG) з назвами, що містять прізвище першого автора (латиницею) та номеру рисунка, наприклад, Smirnov_fig2a.tiff. Якість ілюстрацій (в тому числі напівтонівіх) повинна забезпечувати їх відтворення з дозволом 300–600 точок на дюйм. Додатково різунки надаються в форматі програми, в якій вони створювались.

8. Підписи на рисунках (особенно напівтонівіх) повинні бути заміннені буквенними позначеннями (набраними на контрастном фоні), а криві позначити цифрами або різного типу лініями/маркерами, роз'яснюваними в підписах до рисунків або в тексті. На графіках всі лінії/маркери повинні бути чорного кольору та достаточної товщини/розміру для якісного відтворення в зменшеному в 2–3 рази вигляді (рекомендована ширина рисунка — 12,7 см). Знімки повинні бути чіткими та контрастними, а підписи та позначення повинні не закривати суттєві деталі (для чого можна використовувати стрілки). Замість вказання в підтекстовці збільшення при зйомці бажано поставити масштаб (на контрастном фоні) на одному з ідентичних знімків. На графіках підписи до осей, виконані на мові статті, повинні містити позначення (або найменування) відкладаємих величин та через комаху їх одиниці вимірювання.

9. Формули в текст необхідно вставляти з допомогою редактора формул MathType, повністю сумісного з MS Office 2003, 2007, 2010.

10. Різунки, а також таблиці та підстрочні примічання (сноски) повинні мати загальну нумерацію по всій статті.

11. Посилання на літературні джерела слід давати в вигляді порядкового номера, надрукованого в рядку в квадратних дужках. Список літератури складається в порядку першого згаданого джерела. Приклади оформлення посилань наведено нижче; просимо звернути увагу на порядок вказування ініціалів та прізвищ авторів, бібліографіческих відомостей та на розділові знаки, а також на необхідність вказування всіх співавторів цитованої роботи та (в кінці

каждой ссылке) её **цифрового идентификатора DOI**, если таковой имеется у соответствующей публикации (и указан на её интернет-странице издательства):

1. T. M. Radchenko and V. A. Tatarenko, *Usp. Fiz. Met.*, **9**, No. 1: 1 (2008) (in Ukrainian); <https://doi.org/10.15407/ufm.09.01.001>
2. T. M. Radchenko, A. A. Shylau, and I. V. Zozoulenko, *Phys. Rev. B*, **86**: 035418 (2012); <https://doi.org/10.1103/PhysRevB.86.035418>
3. A. Meisel, G. Leonhardt, and R. Szargan, *Röntgenspektren und Chemische Bindung* [X-Ray Spectra and Chemical Bond] (Leipzig: Akademische Verlagsgesellschaft Geest & Portig K.-G.: 1977) (in German).
4. J. M. Ziman, *Printsipy Teorii Tvorydoga Tela* [Principles of the Theory of Solids] (Moskva: Mir: 1974) (Russian translation).
5. M. A. Stucke, D. M. Dimiduk, and D. M. Hazzledine, *High Temperature Ordered Intermetallic Alloys. V* (Eds. I. Baker and R. Darolia) (Pittsburgh, PA, USA: MRS: 1993), p. 471.
6. *Handbook of Mathematical Functions with Formulas, Graphs and Mathematical Tables* (Eds. M. Abramowitz and I. A. Stegun), Nat'l Bureau of Standards. Appl. Math. Ser. Vol. 55 (Washington, D.C.: U.S. Govt. Printing Office: 1964).
7. B. B. Karpovych and O. B. Borovkoff, *Proc. of Symp. 'Micromaterials Engineering' (Dec. 25–31, 1999)* (Kyiv: RVV IMF: 2000), vol. 2, p. 113 (in Ukrainian).
8. T. M. Radchenko, *Vplyv Uporiadkuvannya Defektnoyi Struktury na Transportni Vlastyivosti Zmishanykh Krystaliv* [Influence of Ordering of the Defect Structure on Transport Properties of the Mixed Crystals] (Thesis of Dissert. for Dr. Phys.-Math. Sci.) (Kyiv: G. V. Kurdyumov Institute for Metal Physics, N.A.S.U.: 2015) (in Ukrainian).
9. E. M. Gololobov, V. B. Shipilo, N. I. Sedrenok, and A. I. Dudyak, *Sposob Polucheniya Karbonitridov Metallov* [Production Method of Metal Carbonitrides], Authors' Certificate 722341 SSSR (Published November 21, 1979) (in Russian).
10. V. G. Trubachev, K. V. Chuistov, V. N. Gorshkov, and A. E. Perekos, *Sposob Polucheniya Metallicheskikh Poroshkov* [The Technology of Metallic Powder Production]: Patent 1639892 SU. MKI, B22 F9/02, 9/14 (Otkrytiya i Izobreteniya, **34**, No. 13: 11) (1991) (in Russian).
11. Yu. M. Koval' and V. V. Nemoshkalenko, *O Prirode Martensitnykh Prevrashchenij* [On the Nature of Martensitic Transformations] (Kyiv: 1998) (Prepr./N.A.S. of Ukraine. Inst. for Metal Physics. No. 1, 1998) (in Russian).

Следует применять общепринятые сокращения названий журналов и сборников трудов:

<http://www.cas.org/content/references/corejournals>; <http://rmp.aps.org/files/rmpguapb.pdf>;
http://images.webofknowledge.com/WOK46P9/help/WOS/A_abrvjt.html;
<http://www.ams.org/msnhtml/serials.pdf>.

Обязательным требованием является предоставление дополнительного списка цитированной литературы (**References**) в латинской транслитерации (система **BGN/PCGN**; рекомендуемые транслитераторы: <http://www.slovnuk.ua/services/translit.php>; <http://ru.translit.net/?account=bgn>). После транслитерированных названий книг, диссертаций, патентов и пр. надо приводить в квадратных скобках их англоязычный перевод. При транслитерации статей из ННН надо использовать написание Ф.И.О. авторов, приведенное только в англоязычном оглавлении соответствующего выпуска, и официальное транслитерированное название сборника (см. также сайт).

12. Корректур авторам может быть выслана электронной почтой в виде pdf-файла. На проверку корректуры авторам отводятся 5 рабочих дней, начиная со дня, следующего за датой отправки корректуры. По истечении указанного срока статья автоматически направляется в печать. Исправления следует отметить и прокомментировать в самом pdf-файле либо оформить в виде перечня исправлений и переслать (от имени уполномоченного представителя коллектива авторов) по электронной почте в адрес редакции.

Рукописи можно направлять непосредственно в редакцию ННН по почтовому адресу: **бульвар Акад. Вернадского, 36, каб. 210; 03142 Киев, Украина** либо члену редакционной коллегии (состав редколлегии указан на 2-й странице обложки). Электронный вариант статьи направляется по e-mail: tatar@imp.kiev.ua (с темой, начинающейся словом 'nano').

В соответствии с договорённостью между редакцией ННН и учредителями сборника, редакция считает, что авторы, посылая ей рукопись статьи, передают учредителям и редколлегии право опубликовать эту рукопись на **английском (украинском) языке**, и просит авторов сразу прикладывать к рукописи подписанное авторами «Соглашение о передаче авторского права»:

Угода про передачу авторського права

Ми, що нижче підписалися, автори рукопису «.....», передаємо засновникам і редколегії збірника наукових праць «*Наносистеми, наноматеріали, нанотехнології*» право опублікувати цей рукопис англійською (чи то українською) мовою. Ми підтверджуємо, що ця публікація не порушує авторського права інших осіб, установ або організацій. Підписи авторів: (ПРИЗВИЩЕ Ім'я, дата, адреса, № телефону, e-mail)

При этом за авторами сохраняются все остальные права как собственников этой рукописи. Авторы могут получить опубликованный выпуск со своей статьёй в редакции сборника по вышеуказанному адресу (тел. №№: +380 44 4241221, +380 44 4249042), а также загрузить pdf-файл статьи с сайта сборника: <http://www.imp.kiev.ua/nanosys/ru/articles/index.html>.

INFORMATION FOR CONTRIBUTORS

Submission of Manuscripts: Papers should be sent to the Executive Managing Editor, Editorial Office, Institute for Metal Physics, N.A.S.U., 36 Academician Vernadsky Boulevard, UA-03142 Kyiv, Ukraine. Manuscripts may also be submitted to a member of the Editorial Advisory Board or to the appropriate Editorial Board Member who is familiar with the research presented.

Submission of a paper to '*Nanosistemi, Nanomateriali, Nanotehnologii*' (i.e., 'Nanosystems, Nanomaterials, Nanotechnologies') will be taken to imply that it represents original work not previously published, it is not being considered for publication elsewhere, and if accepted for publication, it will not be published in the same language without the consent of the Editors and Publisher. It is a condition of acceptance by the Editor of a typescript for publication that the Publishers acquire automatically the copyright in the typescript throughout the world.

Scope of the Collected Scientific Transactions: '*Nanosistemi, Nanomateriali, Nanotehnologii*' (i.e., 'Nanosystems, Nanomaterials, Nanotechnologies'—NNN) is the quarterly multidisciplinary peer-reviewed collected scientific transactions, which publish high-quality work on all aspects of nanoscience and nanotechnology. Currently, transactions stand alone in serving the 'nano' community in providing up-to-date information on all developments and progresses being made in nanoscience and nanotechnology and the future predictions for this extraordinary technology. The topics covered by the transactions relate to all 'nano' related areas of the latest research and recent development works including nanomaterials, characterization tools, fabrication methods, numerical simulation, and theory as well as discussions in the field of nanoscience and technology ranging from basic aspects of the science of nanoscale systems and materials to practical applications of such systems and materials ranging from civil engineering to advanced molecular electronics so promising to transform our everyday technology as well as basic economics. The subjects covered include the following: 1. physical sciences; 2. chemical sciences; 3. life sciences; 4. theoretical and computational science and engineering.

The Transactions does not publish: articles, which are polemical and classifying, have a restricted meaning, or contain the solutions of standard problems; descriptive and methodical articles (if the method is not basically new); articles presenting separate stages of studies or the material divided into several parts for subsequent publications; articles with trivial results, which are not of general interest and do not contain significant conclusions.

Language: The language of publication may be English or Ukrainian.

Abstract: Each paper requires an English abstract of 200–250 words summarizing the significant coverage and findings.

Keywords and PACS numbers: Up to six keywords and PACS numbers reflecting the content of the contribution should be supplied (see 'Physics and Astronomy Classification Scheme 2010' at <http://publishing.aip.org/publishing/pacs/pacs-2010-regular-edition>).

Manuscript Preparation: Papers should be typed (in duplicate) with double spacing and wide margins on good quality paper (A4 size). The length of original contributions should not in general exceed 5000 words and 10 figures, and subject review articles should not exceed 22000 words and 60 figures, including tables and diagrams. Authors are urged to arrange the subject matter clearly under headings such as 1. Introduction, 2. Experimental/Theoretical Details, 3. Results, 4. Discussion, 5. Conclusion, References. Subsections should be identified with section and subsection numbers (such as 6.1. Second-Value Subheading).

References and Notes: Notes are indicated in the text by consecutive superior Arabic numbers (without parentheses). References should be numbered consecutively (in square brackets) throughout the text. The full list should be collected and typed at the end of the paper in numerical order. Listed references should be completed in all details including **DOI** (if available) but excluding article titles in journals. All authors' initials should precede their surnames. Examples of references preparation:

1. T. M. Radchenko and V. A. Tatarenko, *Usp. Fiz. Met.*, **9**, No. 1: 1 (2008) (in Ukrainian);

<https://doi.org/10.15407/ufm.09.01.001>

2. T. M. Radchenko, A. A. Shylau, and I. V. Zozoulenko, *Phys. Rev. B*, **86**: 035418 (2012);

<https://doi.org/10.1103/PhysRevB.86.035418>

3. A. Meisel, G. Leonhardt, und R. Szargan, *Röntgenspektren und Chemische Bindung* [X-Ray Spectra and Chemical Bond] (Leipzig: Akademische Verlagsgesellschaft Geest & Portig K.-G.: 1977) (in German).

4. J. M. Ziman, *Printsipy Teorii Tvyordogo Tela* [Principles of the Theory of Solids] (Moscow: Mir: 1974) (Russian translation).

5. M. A. Stucke, D. M. Dimiduk, and D. M. Hazzledine, *High Temperature Ordered Intermetallic Alloys. V* (Eds. I. Baker and R. Darolia) (Pittsburgh, PA, USA: MRS: 1993), p. 471.

6. *Handbook of Mathematical Functions with Formulas, Graphs and Mathematical Tables* (Eds. M. Abramowitz and I. A. Stegun), Nat'l Bureau of Standards. Appl. Math. Ser. Vol. 55 (Washington, D.C.: U.S. Govt. Printing Office: 1964).

7. B. B. Karpovych and O. B. Borovkoff, *Proc. of Symp. 'Micromaterials Engineering' (Dec. 25–31, 1999)* (Kyiv: RVV IMF: 2000), vol. 2, p. 113 (in Ukrainian).

8. T. M. Radchenko, *Vplyv Uporyadkuvannya Defektnoyi Struktury na Transportni Vlastyvoli Zmishanykh Krystaliv* [Influence of Ordering of the Defect Structure on Transport Properties of the Mixed

ІНФОРМАЦІЯ ДЛЯ ПЕРЕДПЛАТНИКІВ І АВТОРІВ

Crystals] (Thesis of Dissert. for Dr. Phys.-Math. Sci.) (Kyiv: G. V. Kurdyumov Institute for Metal Physics, N.A.S.U.: 2015) (in Ukrainian).

9. E. M. Gololobov, V. B. Shipilo, N. I. Sedrenok, and A. I. Dudyak, *Sposob Polucheniya Karbonitridov Metallov* [Production Method of Metal Carbonitrides], Authors' Certificate 722341 SSSR (Published November 21, 1979) (in Russian).

10. V. G. Trubachev, K. V. Chuistov, V. N. Gorshkov, and A. E. Perekos, *Sposob Polucheniya Metallicheskikh Poroshkov* [The Technology of Metallic Powder Production]: Patent 1639892 SU. MKI, B22 F9/02, 9/14 (Otkrytiya i Izobreneniya, 34, No. 13: 11) (1991) (in Russian).

11. Yu. M. Koval' and V. V. Nemoshkalenko, *O Prirode Martensitnykh Prevrashchenij* [On the Nature of Martensitic Transformations] (Kyiv: 1998) (Prepr./N.A.S. of Ukraine. Inst. for Metal Physics. No. 1, 1998) (in Russian).

Journal title abbreviations should conform to generally accepted styles:

<http://www.cas.org/content/references/corejournals>; <http://rmp.aps.org/files/rmpguapb.pdf>;

http://images.webofknowledge.com/WOK46P9/help/WOS/A_abrvjt.html;

<http://www.ams.org/msnhtml/serials.pdf>.

Equations and Formulae: Formulas in the text should be inserted by MathType, which is fully compatible with MS Office 2003, 2007, 2010.

Tables: Number tables consecutively with Arabic numerals and give a clear descriptive caption at the top.

Figures: All figures should be numbered with consecutive Arabic numerals, have descriptive captions and be mentioned in the text. Keep figures separate at the end of the text and clearly label each figure with author's name and figure number. The labels at axis should contain the designation (or notation) of quantities and their units.

Preparation: Figures submitted (**black-and-white or greyscale** recommended) must be of a high enough standard for reproduction with 300–600 dpi resolution (including half-tone illustrations). Redrawing or retouching of unusable figures will be charged to the authors.

Colour Plates: Whenever the use of colour is an integral part of the research, or where the work is generated in colour, the Transactions will insert the colour illustrations into the PDF version of the article published on the Editorial Office site. Reprints in colour will carry a surcharge. Please write to the Publisher for details.

Submission of Electronic Text with Figures: Authors should submit papers (with figures) by e-mail (tatar@imp.kiev.ua) or on a CD. The file should be saved in the native formats of the Microsoft Word 2003, 2007 or 2010 with a name consisting of the name of the first author, for example, Smirnov.doc. The electronic form of figures (graphics files in **TIFF, EPS or JPEG** formats preferably and with name consisting of the name of the first author also, for example, Smirnov_fig2a.tiff) should be planned so that they reduce to 12.7 cm column width (or less), and keep them separate from the text file. It is necessary to submit additionally all the figures within the format of the program, in which they were created.

Proofs: In a special emergency, contributors may receive page proofs for correction by e-mail as a PDF document. In that case, these must be returned to Kyiv office (tatar@imp.kiev.ua) with subject beginning by word 'nano' within 120 hours of receipt.

Page Charges: There are no page charges to individuals or institutions.

Reprints: Hard-copy reprints provided to the first-named author of each paper may be ordered by completing the appropriate form sent with proofs. Authors can de-archive a PDF version of their published article from the Editorial Office site: <http://www.imp.kiev.ua/nanosys/ru/articles/index.html>.

Further Information: All questions arising after the acceptance of manuscripts, especially those relating to reprints, should be directed to Executive Managing Editor, Editorial Office, G. V. Kurdyumov Institute for Metal Physics, N.A.S.U., 36 Academician Vernadsky Blvd., UA-03142 Kyiv, Ukraine.

Fax: +380 44 4242561, e-mail: tatar@imp.kiev.ua (with subject beginning by word 'nano').

We ask the authors to apply with their manuscript

Copyright Transfer Agreement

We, the undersigned authors of the manuscript '_____', transfer to the founders and the Editorial Board of the Collected Scientific Transactions 'Nanosistemi, Nanomateriali, Nanotehnologii' the right to publish this manuscript in English language (or in the Ukrainian translation). We confirm that publication of this manuscript will not infringe a copyright of other persons, institutions or organizations.

Author(s): _____

(Last Name, First Name, Affiliation)

Correspondence Address: _____

Phone and e-mail: _____

(Signature)

(Date)

ВИДАВНИЧА ЕТИКА

ТА ЗАПОБІГАННЯ НЕСУМЛІННІЙ ПРАКТИЦІ ПУБЛІКАЦІЙ

Редакційна колегія збірника наукових праць «Наносистеми, наноматеріали, нанотехнології» дотримується етичних норм, прийнятих міжнародним науковим співтовариством, і робить усе для запобігання будь-яким порушенням їх. У своїй діяльності редакція спирається на рекомендації Комітету з етики наукових публікацій (<http://publicationethics.org>).

Обов'язки редакції

- Всі представлені статті рецензуються експертами в даній області.
- Під час розгляду статті враховуються її відповідність предметній області, обґрунтованість, значимість, оригінальність, читабельність і мова (правопис).
- За результатами рецензування стаття може бути прийнята до опублікування без доробки, прийнята з доробкою або відхилена.
- Відхилені статті повторно не рецензуються.
- Статті можуть бути відхилені без рецензії, якщо вони очевидним чином не підходять для публікації.
- Редакція ухвалює рішення щодо публікації, керуючись політикою збірника, з урахуванням діючого законодавства в області авторського права.
- Не допускається до публікації інформація, якщо є достатньо підстав уважати, що вона є плагіатом.

За наявності яких-небудь конфліктів інтересів (фінансових, академічних, особистих) всі учасники процесу рецензування повинні сповістити про це редколегії. Всі спірні питання розглядаються на засіданні редколегії.

Прийняті до опублікування статті розміщуються у відкритому доступі на сайті збірника; авторські права зберігаються за авторами.

Етичні принципи в діяльності рецензентів

- Рецензенти оцінюють статті за їхнім вмістом, безвідносно до національності, статі, сексуальної орієнтації, релігійних переконань, етнічної приналежності або політичних переконань авторів.
- Співробітники редакції не повинні повідомляти яку-небудь інформацію про статті, що надійшли, особам, які не є рецензентами, авторами, співробітниками редакції та видавництва.
- Рецензування повинне бути проведено об'єктивно. Персональна критика автора неприпустима. Рецензенти зобов'язані обґрунтовувати свою точку зору чітко й об'єктивно.
- Рецензування допомагає видавцеві приймати рішення та за допомогою співробітництва з рецензентами й авторами поліпшити статтю.
- Матеріали, отримані для рецензії, є конфіденційними документами та рецензуються анонімно.
- Рецензент також зобов'язаний звертати увагу редактора на істотну або часткову подібність представленої статті з якою-небудь іншою роботою, з якою рецензент безпосередньо знайомий.

Принципи, якими повинні керуватися автори наукових публікацій

- Автори статей повинні надавати точний звіт про виконану роботу й об'єктивне обговорення її значимості.
- Автори статті повинні надавати достовірні результати проведеного огляду й аналізу досліджень. Свідомо помилкові або сфальсифіковані твердження неприйнятні.
- Стаття повинна містити достатню кількість інформації для перевірки та повторення експериментів або розрахунків іншими дослідниками. Шахрайські або свідомо неправдиві заяви порівнюються до неетичного поводження і є неприйнятними.
- Автори можуть надавати оригінальні регулярні й оглядові роботи. За використання текстової або графічної інформації, отриманої з робіт інших осіб, обов'язково необхідні посилання на відповідні публікації або письмовий дозвіл їхніх авторів.
- Подача статті більш ніж в один журнал розцінюється як неетичне поводження і є неприйнятною.
- Авторство повинне бути обмежене тими, хто зробив значний внесок у концепцію, розробку, виконання або інтерпретацію заявленого дослідження.
- Джерела фінансової підтримки дослідження, що публікується, можуть бути зазначені.

PUBLICATION ETHICS

AND MALPRACTICE STATEMENT

The Editorial Board of the Collected Scientific Transactions '*Nanosistemi, Nanomateriali, Nanotehnologii*' (i.e., 'Nanosystems, Nanomaterials, Nanotechnologies') follows ethics norms accepted by international scientific community and makes every endeavour to prevent any infringements of the norms. The Editorial Board follows the guidelines of the Committee on Publication Ethics (<http://publicationethics.org>).

Duties of Editors

- All submitted papers are subject to strict peer-review process by reviewers that are experts in the area of the particular paper.
- The factors, which are taken into account in reviewing process, are relevance, soundness, significance, originality, readability, and quality of language.
- The possible decisions include acceptance, acceptance with revisions, or rejection.
- If authors are encouraged to revise and resubmit a submission, there is no guarantee that the revised submission will be accepted.
- Rejected articles will not be re-reviewed.
- Articles may be rejected without review, if they are obviously not suitable for publication.
- The paper acceptance is constrained by such legal requirements as shall then be in force regarding libel, copyright infringement, and plagiarism.

When a conflict of interests arising, all the participants of reviewing process should inform the Editorial Board. All the contentions questions are considered in the Board meeting.

The accepted papers are allocated in open access on the journal site; copyrights reserved.

Duties of Reviewers

- The reviewers evaluate manuscripts for their intellectual content without regard to race, gender, sexual orientation, religious belief, ethnic origin, citizenship, or political philosophy of the authors.
- The staff must not disclose any information about a submitted manuscript to anyone other than the corresponding author, reviewers, other editorial advisers, and the Publisher, as appropriate.
- Reviews should be conducted objectively. Personal criticism of the author is inappropriate. Referees should express their views clearly with supporting arguments.
- Peer review assists the Publisher in making editorial decisions and through the editorial communications with the experts from the scientific board and the author may assist the author in improving the paper.
- Manuscripts received for review are treated as confidential documents and are reviewed by anonymous staff.
- A reviewer should also call to the Publisher's attention any substantial similarity or overlap between the manuscript under consideration and any other published paper of which they have personal knowledge.

Duties of Authors

- Authors of contributions and studies research should present an accurate account of the work performed as well as an objective discussion of its significance.
- A paper should contain sufficient details and references to permit others to replicate the work. Fraudulent or knowingly inaccurate statements constitute unethical behaviour and are unacceptable.
- The authors should ensure that they have written original regular or entirely review works, if the authors have used the work and/or words of others that this has been obligatory and appropriately cited or quoted.
- Submitting the same manuscript to more than one publication concurrently constitutes unethical publishing behaviour and is unacceptable.
- Authorship should be limited to those who have made a significant contribution to the conception, design, execution, or interpretation of the reported study.
- Sources of financial support for the reported results can be specified.

PACSnumbers: 81.16.Fg, 87.16.dp, 87.16.dr, 87.19.Ff, 87.19.lt, 87.19.R-, 87.19.xn, 87.85.G-

C₆₀-фуллерен сприяє відновленню точного позиціонування *muscle soleus* після спричиненої ахіллозомією атрофії

Д. М. Ноздренко¹, О. П. Мотузюк^{1,2}, О. В. Долгополов³,
І. В. Пампуха¹, К. І. Богуцька¹

¹Київський національний університет імені Тараса Шевченка,
вул. Володимирська, 64/13,
01601 Київ, Україна

²Волинський національний університет імені Лесі Українки,
просп. Волі, 13,
43025 Луцьк, Україна

³ДУ «Інститут травматології та ортопедії НАМН України»,
вул. Бульварно-Кудрявська, 27,
01054 Київ, Україна

Досліджено вплив водного розчину C₆₀-фуллеренів (щоденна пероральна доза — 1 мг/кг) на відновлення гістерезисних ефектів м'язового скорочення, відповідальних за корекцію точного позиціонування суглобів за розвитку атрофічних змін, пов'язаних із довготривалим знерухомленням. Для розвитку атрофії м'язів використовували клінічний модель розриву Ахіллового сухожилля. Фіксація параметрів скорочення м'яза робилася на 15-ту, 30-ту й 45-ту добу після ініціації атрофії. Одержані результати підтверджують ефективність дії C₆₀-фуллеренів на функції антиоксидантної системи організму за розвитку патологічних процесів.

The effect of C₆₀-fullerene aqueous solution (with daily oral dose of 1 mg/kg) on the restoration of hysteresis effects of muscle contraction responsible for the correction of the precise positioning of joints in the development of atrophic changes associated with long-term immobilisation is investigated. A clinical model of Achilles-tendon rupture is used to study the development of muscle atrophy. Muscle-contraction parameters are recorded on the 15th, 30th, and 45th day after the initiation of atrophy. The obtained results confirm the effectiveness of C₆₀-fullerenes' influence on the functions of the antioxidant system in the development of pathological processes.

Ключові слова: *muscle soleus*, атрофія, C₆₀-фуллерен, біомеханічні параметри.

Key words: *muscle soleus*, atrophy, C₆₀ fullerene, biomechanical parameters.

(Отримано 29 січня 2024 р.)

1. ВСТУП

М'язова атрофія — це втрата м'язової маси та сили, що виникає під час багатьох захворювань, зокрема, таких як рак, СНІД, серцева та ниркова недостатність, тяжкі опіки тощо [1]. Тривале знерухомлення є однією з основних причин атрофії м'язів [2], що істотно погіршує якість життя хворих [3]. Під час аналізу розвитку атрофії недостатньо уваги приділяється нелінійним (гістерезним) ефектам скорочення м'язів, адже порушення їхнього функціонування може призводити до втрати точного позиціонування суглобів [4]. Такі порушення виникають під час отруєнь [5], розвитку м'язової втоми [6], травмах опорно-рухового апарату [7].

Для розуміння нелінійних особливостей м'язової динаміки важливим є питання модифікування скорочувальних механізмів під впливом змін механічного стану м'яза внаслідок руху [8]. Крім того, ще одна важлива нелінійна властивість скорочувального апарату проявляється у формі співвідношення між вже виробленою та майбутньою (що ще розвивається) силою, яке істотно змінюється за наявності навіть незначних патологічних процесів, які впливають на систему «нейрон–м'яз» [9]. Вважають, що у випадку циклічного поступального руху відбувається поглинання механічної енергії [8], завдяки чому активні м'язи функціонують в автоколивному режимі. Водночас виникають високочастотні ритмічні рухи, що істотно адаптує м'язову систему до реалізації наступних складних модуляційних сигналів. Цей так званий ефект передісторії руху відіграє важливу роль у відтворенні точності рухів. Тому навіть незначні м'язові та нервові патології, насамперед, впливають на систему контролю м'язових реакцій [9, 10].

Нині відсутні методи ефективного лікування м'язової атрофії. У літературі повідомляється про наявність потенційних препаратів, які можуть регулювати втрату м'язової маси. Механізм їхньої дії базується на пониженні активності міостатину, циклооксигенази-2, прозапальних цитокінів, опосередкованих катаболічним виснаженням, або підвищенні активності циклічного АМФ-рецептора, що активує проліфератор пероксисом [11]. Водночас більшість з цих препаратів проявляють небажані побічні (токсичні) ефекти. Особливу увагу наразі приділяють сполукам, які мають антиоксидантні властивості [12]. Показано, що флавоноїдна олія солодки, що містить глабридин, який виявляє сильні антиоксидантні властивості, збільшує масу м'язів мишей за їхньої атрофії [13]. З іншого боку, під час вивчення впливу антиоксиданту вітаміну С на загоєння Ахіллового сухожилля у щурів не ви-

явили переваг перорального приймання досліджуваної добавки в синтезі колагену або поліпшенні біомеханічних властивостей атрофованих м'язів [14]. Молекула C₆₀ здатна ефективно захоплювати й інактивувати вільні радикали у системах *in vitro* та *in vivo* [15, 16]. У наших попередніх роботах було показано, що введення водорозчинних C₆₀-фуллеренів після ініціації м'язової травми й отруєння організму пестицидами приводить до значних терапевтичних ефектів [17, 18]. Відтак, метою цієї роботи було оцінити здатність C₆₀-фуллеренів як потужних антиоксидантів понижувати патологічний вплив м'язової атрофії, викликаної довготривалим знерухомленням, на гістерезні ефекти скорочення *muscle soleus* щурів.

2. МЕТОДИКА ЕКСПЕРИМЕНТУ

Для одержання водного розчину C₆₀-фуллеренів було застосовано методу, яка ґрунтується на переведенні молекул C₆₀ з толуолу у воду з подальшим обробленням ультразвуком [19]. Одержаний водний розчин цієї сполуки за максимальної концентрації у 0,15 мг/мл є типовим наноколоїдом [20] і залишається стабільним упродовж 12–18 місяців за температури у +4–25°C.

Експерименти проводили на щурах-самцях лінії Wistar віком у 1–3 місяці та вагою у 200±6 г. Протокол дослідження був затверджений комісією з питань біоетики ННЦ «Інститут біології та медицини» Київського національного університету імені Тараса Шевченка згідно з правилами «Європейської конвенції про захист хребетних тварин, що використовуються в експериментальних та інших наукових цілях» і норм біомедичної етики згідно із Законом України № 3447–IV від 21.02.2006 р. (м. Київ) «Про захист тварин від жорстокого поводження» під час проведення медико-біологічних досліджень.

Анестезію тварин здійснювали внутрішньоочеревинним введенням нембуталу (40 мг/кг). Перед початком дослідження щури піддавалися ахіллотомії — перерізу Ахіллесового сухожилля [21]. Досліджували 4 групи тварин: контроль і після 15, 30 та 45 діб після ахіллотомії. Введення водного розчину C₆₀-фуллеренів здійснювали перорально, щоденно дозою в 1 мг/кг упродовж експерименту.

Muscle soleus звільняли від навколишніх тканин; у дистальній частині його сухожилля частину приєднували до датчиків вимірювання сили. Дослідження динамічних властивостей м'язового скорочення проводили в умовах активації м'яза з використанням методи модульованої стимуляції еферентів [22]. Стимуляцію еферентів здійснювали електричними імпульсами тривалістю у 2 мс, сформованими за допомогою генератора імпульсів. Використову-

вали 3 пули безрелаксаційних стимуляцій частотою у 50 Гц і тривалістю у 3 с кожний. Силу скорочення м'яза реєстрували за допомогою тензодатчиків.

Статистичну обробку результатів міряння проводили методами варіаційної статистики за допомогою програмного забезпечення Origin 9.4. Кожна із силових кривих, наведених у цій роботі, є результатом усереднення 10 аналогічних експериментів.

3. РЕЗУЛЬТАТИ Й ОБГОВОРЕННЯ

Один із достатньо ефективних і широко застосовуваних способів ідентифікації рівня патологій динамічних систем полягає у визначенні їхніх реакцій на різні швидкісні діапозони стимулювальних подразнень. За застосованої стимуляції нерва спостерігали зменшення сили м'язової відповіді та швидкості її приросту внаслідок наявності залишкових патологічних змін, спричинених атрофією. За реалізації 1-го пулу модульованого стимуляційного сигналу (рис. 1) силова відповідь м'яза змінювалася дуже швидко, майже стрибкоподібно, як реакція слабо демпфованого послідовного пружного компонента. Однак за реалізації 2-го і особливо 3-го пулу такої ж модульованої стимуляції виникало повільне наростання сили скорочення до нового, нижчого за рівнем рівноважного стану (його рівень напряму корелював з рівнем розвитку патології) (рис. 1).

З рисунку 2 видно, що за реалізації 2-го і 3-го пулу стимуляції у контролі часова затримка зменшується незначно. У цьому випадку гістерезна властивість м'яза, — так звана передісторія руху, — допомагає м'язовій системі більш коректно та з меншими енергетичними затратами здійснювати послідовні балістичні рухи [23]. Після 15-ї доби знерухомлення ці ефекти зникають, а час досягнення силою максимальних значень зростає на кожному пулі стимуляції: на 15-ту добу він склав 501 ± 12 , 552 ± 9 і 650 ± 10 мс за реалізації 1-го, 2-го і 3-го пулу стимуляції відповідно; у контролі: 123 ± 6 , 110 ± 3 і 96 ± 2 мс відповідно. Отже, відмінність між контрольними значеннями склала понад 300%. Використання водного розчину C_{60} -фуллерену зменшило часові затримки на 66%, 79% і 84% відповідно. На 30-ту добу відмінність часових затримок в атрофованих м'язах порівняно з контролем склала 203%, 250% і 280% відповідно, а C_{60} -фуллеренова терапія поліпшила ці показники на 51%, 56% і 62% за реалізації 1-го, 2-го і 3-го пулу стимуляції відповідно. На 45-ту добу експерименту затримки м'язового скорочення в атрофованих м'язах склали 22%, 29% і 31%, але ефект передісторії руху (зменшення затримки на 2-му і 3-му пулі порівняно із першим) так і не спостерігався. Використання водного розчину C_{60} -фуллерену наблизило ці

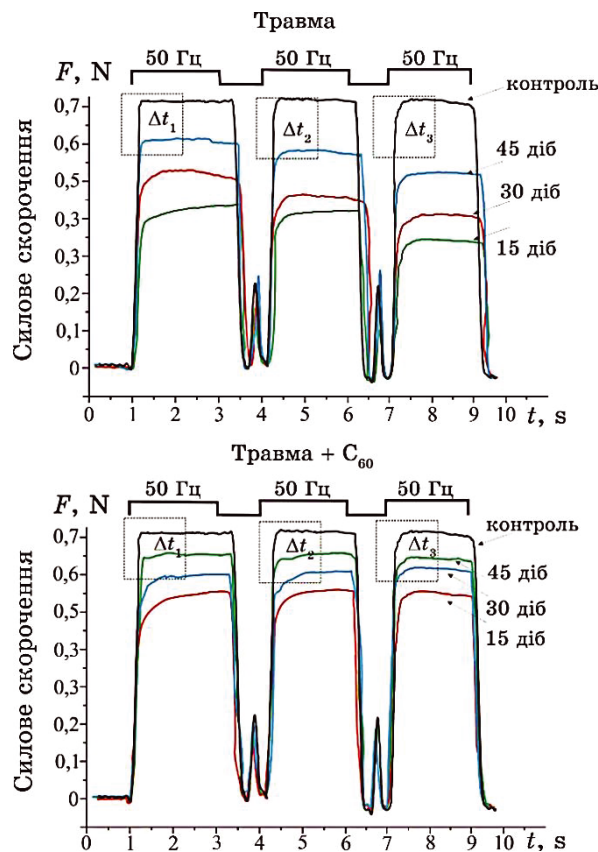


Рис. 1. Силова відповідь *muscle soleus* щура після атрофії, спричиненої ахіллотомією, на 15-ту, 30-ту і 45-ту добу за використання трикомпонентного модульованого сигналу: травма та травма + C₆₀ — сила скорочення атрофованого *muscle soleus* без введення C₆₀-фуллерену та на тлі його введення; Δt_1 , Δt_2 та Δt_3 — час досягнення силою свого максимального рівня на 1-му, 2-му та 3-му пулі стимуляційного сигналу; 15-й, 30-й і 45-й день — доба після ініціації атрофії; $n = 7$ у кожній групі.¹

показники майже до контрольних значень (відмінність не перевищувала 12%). Таким чином, використання C₆₀-фуллеренової терапії відновило гістерезний ефект передісторії руху після 45-ї доби експерименту.

4. ВИСНОВКИ

Таким чином, дослідження механокінетики скорочення *muscle soleus* щура за використання трикомпонентного стимуляційного пулу уможливили оцінити її зміни, що виникали за розвитку

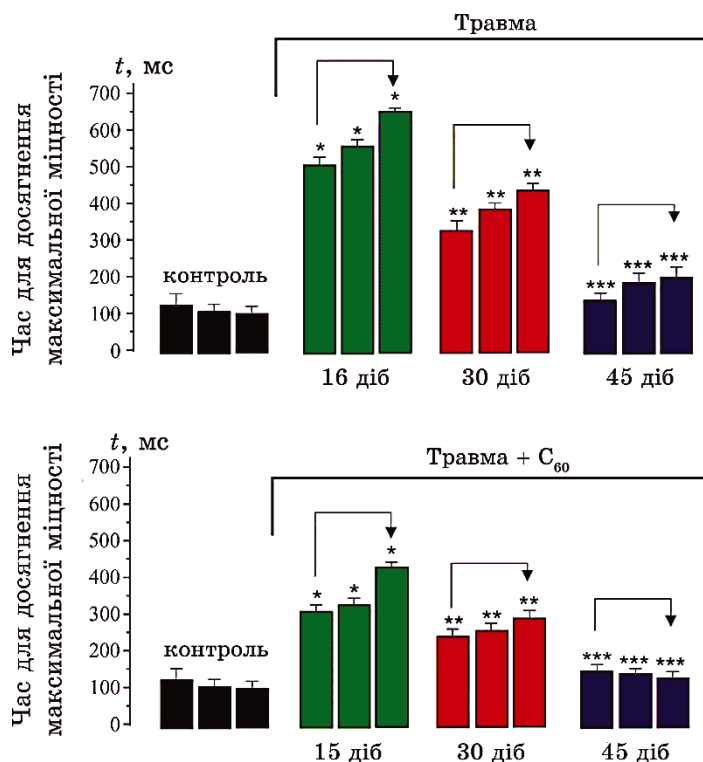


Рис. 2. Час досягнення *muscle soleus* щура свого максимального рівня скорочення після атрофії, спричиненої ахілотомією, на 15-ту, 30-ту та 45-ту добу за використання трикомпонентного модульованого сигналу: травма та травма + C₆₀ — сила скорочення атрофованого *muscle soleus* без введення C₆₀-фуллерену та на тлі його введення; 15, 30 і 45 днів — доба після ініціації атрофії; $n = 7$ у кожній групі; * $p < 0,05$ порівняно з контролем; ** $p < 0,05$ порівняно з даними на 15-ту добу експерименту; *** $p < 0,05$ порівняно з даними на 30-ту добу експерименту.²

м'язової атрофії, пов'язаної з довготривалим знерухомленням. Це, зокрема, стосується виявлених змін у динаміці складних рухів, пов'язаних з точним позиціонуванням суглобів, та нормалізації їх за використання водного розчину C₆₀-фуллеренів. Це слугує підтвердженням одержаних нами раніше даних про позитивний терапевтичний вплив водорозчинних C₆₀-фуллеренів на функції антиоксидантної системи організму за розвитку запальних і патологічних процесів [17, 18, 21].

ПОДЯКА

Роботу виконано за підтримки МОН України в рамках проекту

№ 24БП018-02).

ЦИТОВАНА ЛІТЕРАТУРА—REFERENCES

1. R. Y. Cao, J. Li, Q. Dai, Q. Li, and J. Yang, *Adv. Exp. Med. Biol.*, **1088**: 605 (2018); https://doi.org/10.1007/978-981-13-1435-3_29
2. Y. Ohira, T. Yoshinaga, T. Nomura, F. Kawano, A. Ishihara, I. Nonaka, R. R. Roy, and V. R. Edgerton, *Adv. Space Res.*, **30**, No. 4: 777 (2002); [https://doi.org/10.1016/s0273-1177\(02\)00395-2](https://doi.org/10.1016/s0273-1177(02)00395-2)
3. J. A. Hodgson, R. R. Roy, N. Higuchi, R. J. Monti, H. Zhong, E. Grossman, and V. R. Edgerton, *J. Exp. Biol.*, **208**, Pt. 19: 3761 (2005); <https://doi.org/10.1242/jeb.01825>
4. D. N. Nozdrenko and K. I. Bogutska, *Biopolym. Cell*, **21**, No. 3: 285 (2005) (in Russian); <http://dx.doi.org/10.7124/bc.0006F3>
5. K. I. Bohuts'ka, Iu. I. Pryluts'kyi, and D. M. Nozdrenko, *Fiziol. Zh.*, **60**, No. 1: 91 (2014) (in Ukrainian).
6. A. I. Kostyukov, L. A. Bugaychenko, I. Kalezic, A. I. Pilyavskii, U. Windhorst, and M. Djupsjöbacka, *Exp. Brain Res.*, **163**, No. 3: 284 (2005); <https://doi.org/10.1007/s00221-004-2188-3>
7. D. M. Cordero, T. A. Miclau, A. V. Paul, S. Morshed, T. Miclau, C. Martin, and D. W. Shearer, *OTA Int.*, **3**, No. 2: e062 (2020); <https://doi.org/10.1097/OI9.000000000000062>
8. A. I. Kostyukov, *Neuroscience*, **83**, No. 1: 303 (1998); [https://doi.org/10.1016/s0306-4522\(97\)00379-5](https://doi.org/10.1016/s0306-4522(97)00379-5)
9. D. N. Nozdrenko, A. N. Shut, and Yu. I. Prylutskyi, *Biopolym. Cell*, **21**, No. 1: 80 (2005) (in Russian); <http://dx.doi.org/10.7124/bc.0006E0>
10. D. N. Nozdrenko, O. M. Abramchuk, V. M. Soroca, and N. S. Miroshnichenko, *Ukr. Biochem. J.*, **87**, No. 5: 38 (2015); <https://doi.org/10.15407/ubj87.05.038>
11. V. Dutt, S. Gupta, R. Dabur, E. Injeti, and A. Mittal, *Pharmacol. Res.*, **99**: 86 (2015); <https://doi.org/10.1016/j.phrs.2015.05.010>
12. M. A. Ruegg and D. J. Glass, *Annu. Rev. Pharmacol. Toxicol.*, **51**: 373 (2011); <https://doi.org/10.1146/annurev-pharmtox-010510-100537>
13. Y. Yoshioka, Y. Kubota, Y. Samukawa, Y. Yamashita, and H. Ashida, *Arch. Biochem. Biophys.*, **664**: 157 (2019); <https://doi.org/10.1016/j.abb.2019.02.006>
14. H. C. Gemalmaz, K. Sariyilmaz, O. Ozkunt, S. G. Gurgen, and S. Silay, *Acta Orthop. Traumatol. Turc.*, **52**, No. 6: 452 (2018); <https://doi.org/10.1016/j.aott.2018.06.012>
15. S. V. Prylutska, I. I. Grynyuk, K. O. Palyvoda, and O. P. Matyshevska, *Exp. Oncol.*, **32**, No. 1: 29 (2010).
16. S. Goodarzi, T. Da Ros, J. Conde, F. Sefat, and M. Mozafari, *Materials Today*, **20**: 460 (2017); <https://doi.org/10.1016/j.mattod.2017.03.017>
17. D. N. Nozdrenko, T. Yu. Matvienko, O. V. Vygovska, V. M. Soroca, K. I. Bogutska, N. E. Nuryshechenko, Yu. I. Prylutskyi, and A. V. Zholos, *Nanosistemi, Nanomateriali, Nanotehnologii*, **18**, Iss. 1: 205 (2020) (in Russian); <https://doi.org/10.15407/nnn.18.01.205>
18. D. Nozdrenko, O. Abramchuk, S. Prylutska, O. Vygovska, V. Soroca,

- K. Bogutska, S. Khrapatyi, Yu. Prylutsky, P. Scharff, and U. Ritter, *Int. J. Mol. Sci.*, **22**, No. 9: 4977 (2021); <https://doi.org/10.3390/ijms22094977>
19. S. Prylutska, S. Politenkova, K. Afanasieva, V. Korolovych, K. Bogutska, A. Sivolob, L. Skivka, M. Evstigneev, V. Kostjukov, Yu. I. Prylutsky, and U. Ritter, *Beilstein J. Nanotechnol.*, **8**: 1494 (2017); <https://doi.org/10.3762/bjnano.8.149>
20. Yu. I. Prilutski, S. S. Durov, V. N. Yashchuk, T. Yu. Ogul'chansky, V. E. Pogorelov, Yu. A. Astashkin, E. V. Buzaneva, Yu. D. Kirghizov, G. V. Andrievsky, and P. Scharff, *Europ. Phys. J. D*, **9**, Nos. 1–4: 341 (1999).
21. D. Nozdrenko, S. Prylutska, K. Bogutska, N. Nurishchenko, O. Abramchuk, O. Motuziuk, Yu. Prylutsky, P. Scharff, and U. Ritter, *Life (Basel)*, **12**, No. 3: 332 (2022); <https://doi.org/10.3390/life12030332>
22. D. M. Nozdrenko, L. V. Korchinska, and V. M. Soroca, *Ukr. Biochem. J.*, **87**, No. 4: 63 (2015); <https://doi.org/10.15407/ubj87.04.063>
23. S. Sasajima, A. Yasuda, T. Kosaka, and K. Kubo, *J. Musculoskelet. Neuronal. Interact.*, **23**, No. 1: 84 (2023).

¹Taras Shevchenko National University of Kyiv,
64, Volodymyrska Str.,
UA-01601 Kyiv, Ukraine

²Lesya Ukrainka Volyn National University,
13 Volya Ave.,
UA-43025 Lutsk, Ukraine

³SI 'Institute of Traumatology and Orthopaedics of the N.A.M.S. of Ukraine',
27, Bulvarno-Kudriavska Str.,
UA-01054 Kyiv, Ukraine

¹ Fig. 1. Strength response of the rat *muscle soleus* after atrophy caused by achillotomy on 15th, 30th, and 45th day using a three-component modulated signal: injury and injury + C₆₀—the strength of contraction of the atrophied *muscle soleus* without C₆₀-fullerene administration and against its administration; Δt_1 , Δt_2 and Δt_3 —the time when the force reaches its maximum level on the 1st, 2nd, and 3rd pool of the stimulation signal; 15th, 30th, and 45th day—day after initiation of atrophy; $n = 7$ in each group.

² Fig. 2. The time for the rat *muscle soleus* to reach its maximum level of contraction after atrophy caused by achillotomy on 15th, 30th, and 45th day using a three-component modulated signal: injury and injury + C₆₀—the force of contraction of the atrophied *muscle soleus* without the introduction of C₆₀ fullerene and against the background of its introduction; 15th, 30th, and 45th day—day after initiation of atrophy; $n = 7$ in each group; * $p < 0.05$ compared to the control; ** $p < 0.05$ compared to data on the 15th day of the experiment; *** $p < 0.05$ compared to data on the 30th day of the experiment.

PACS numbers: 68.37.Lp, 78.55.-m, 87.63.Lr, 87.64.Cc, 87.64.km, 87.64.mh, 87.85.jj

Enhanced Efficiency of Samarium-Doped TiO₂ Nanoparticles for Targeted Imaging: Characterization and *in vivo* Evaluation

W. M. Abd El-Kader¹, R. Abo-Gabal², A. M. Abdelghany³, and A. H. Oraby¹

¹*Faculty of Science, Physics Department,
Mansoura University,
Mansoura, Egypt*

²*Mansoura Urology and Nephrology Centre,
Mansoura University,
35516 Mansoura, Egypt*

³*Physics Division, Spectroscopy Department,
National Research Centre,
33 ElBehouth Str.,
12311 Dokki, Cairo, Egypt*

In this study, we synthesize samarium-doped TiO₂ nanoparticles (Ti(Sm)O₂ NPs) using solvothermal synthesis and enhance their stability and biocompatibility by coating them with polymeric materials. Extensive characterization studies confirm the desired morphology, crystal structure, optical properties, surface charge, and biocompatibility of the Ti(Sm)O₂ NPs. Additionally, *in vivo* imaging evaluations reveal their excellent imaging capabilities, particularly, in distinguishing lung pathologies, making them highly promising for targeted imaging applications. Importantly, *in vivo* toxicity studies demonstrate the biocompatibility and safety of the nanoparticles. These findings contribute to the development of advanced contrast agents for improved diagnostic imaging in biomedical applications, offering potential as effective tools for targeted imaging and enhancing the diagnosis and monitoring of various lung pathologies.

У цьому дослідженні ми синтезуємо леговані Самарієм наночастинки TiO₂ (Ti(Sm)O₂ НЧ) за допомогою сольвотермічної синтези та підвищуємо їхню стабільність і біосумісність шляхом покриття їх полімерними матеріалами. Різноманітні характеристичні дослідження підтверджують бажану морфологію, кристалічну структуру, оптичні властивості, заряд поверхні та біосумісність Ti(Sm)O₂ НЧ. Крім того, оцінки візуалізації *in vivo* показали їхні чудові можливості візуалізації, зокрема у розрізненні патологій легенів, що робить їх дуже перспективними для цільових візуалізаційних застосувань. Важливо, що дослідження токсичності *in vivo* демонструють біосумісність і безпечність наночастинок. Ці висновки сприяють розробці

передових контрастних речовин для поліпшеної діагностичної візуалізації в біомедичних застосуваннях, пропонуючи потенційні ефективні інструменти для цілеспрямованої візуалізації та поліпшення діагностики та моніторингу різних патологій легенів.

Key words: nanoparticles, contrast agents, K-edge, titanium oxide, biocompatibility.

Ключові слова: наночастинки, контрастні речовини, K-край, оксид Титану, біосумісність.

(Received 26 June, 2023; in revised form, 28 June, 2023)

1. INTRODUCTION

The versatility of nanomaterials in performing multiple functions has greatly facilitated their widespread use in the field of cancer imaging, diagnosis, and treatment [1]. Accurate diagnosis of diseases often requires comprehensive information that cannot be obtained through a single imaging modality alone. As a result, multimodal imaging systems have emerged as a promising approach for highly efficient cancer theranostics. In recent years, x-ray computed tomography (CT) has witnessed significant advancements in its core technology and innovative therapeutic applications. However, the development of clinical x-ray contrast agents has seen limited progress in the past few decades. There is a need to overcome challenges such as achieving high concentration in the bloodstream, maintaining stable concentration over time, and enhancing aggregation at specific regions of interest. Addressing these challenges is crucial for improving the performance and efficacy of CT imaging, ultimately advancing the diagnosis and treatment of cancer [2].

The limitations of conventional iodine-based x-ray contrast agents used in CT imaging, such as rapid blood clearance, have prompted the exploration of alternative solutions. In recent years, there has been growing interest in the development of nanoparticle-based contrast agents to address these limitations [3]. Nanoparticulate probes offer several advantages over single molecule-based agents, including the ability to integrate different contrast-generating materials, longer circulation time in the bloodstream, and higher payload capacity. This review highlights the significance of nanoparticle-based contrast agents in medical imaging, particularly in the context of CT imaging, and their potential to enhance imaging performance and capabilities [4]. By leveraging the unique properties of nanoparticles (NPs), researchers aim to overcome the challenges associated with conventional contrast agents and improve the accuracy and quality of CT imaging for various medical applications.

Gold nanoparticles (AuNPs) show promise as iodine-free x-ray contrast agents in medical applications [5]. Gold unique properties, including its higher nuclear number, *K*-edge, and mass x-ray absorption coefficient compared to iodine, make it an attractive alternative. AuNPs provide 2.7 times greater x-ray contrast per unit weight than iodine and exhibit optimal x-ray absorption in the 80–100 keV range, enabling improved visualization of blood vessels [6]. Moreover, AuNPs have demonstrated excellent biocompatibility and low toxicity, rendering them suitable for a range of biological applications [7].

Bismuth (Bi), a metal with a high nuclear number ($Z_{\text{Bi}} = 83$), has gained interest as a potential alternative to iodine-based x-ray contrast agents due to its low toxicity and diverse applications in medicine, cosmetics, and surgery. Bismuth salts were among the earliest contrast agents used in x-ray imaging of patients [8]. Coated bismuth NPs were introduced as injectable contrast agents for CT imaging in mice, demonstrating prolonged circulation compared to iodine-based agents [9]. Bismuth-enhanced nanocolloids have also been utilized as contrast agents for spectral CT molecular imaging to visualize thrombus [10]. However, due to their high cost and adverse effects, high doses of bismuth compounds were eventually replaced by more cost-effective alternatives. This review highlights the potential of bismuth as an x-ray contrast agent, its early applications, and the challenges in its widespread use.

In the early 1970s, tantalum NPs were investigated as a contrast agent for bronchography. However, compared to iodine, tantalum had a limited contrast impact, especially at high x-ray voltages [11]. *In vivo* studies in mice demonstrated the absence of immediate or harmful effects, and the NPs were eliminated through renal clearance without adverse effects. More recently, Hyeon *et al.* developed a microemulsion strategy to synthesize uniform-sized TaO_x particles in large quantities, opening up new possibilities for their application as contrast agents. This review highlights the historical usage of tantalum NPs in bronchography, their contrast properties, and the latest advancements in their synthesis for potential medical imaging applications [12].

Lanthanide elements, such as gadolinium and ytterbium, have shown significant potential for use in x-ray scanning techniques. These elements possess higher nuclear numbers than iodine, resulting in increased x-ray attenuation and enhanced contrast in polyspectrum imaging. Gadolinium, in particular, exhibits a higher *K*-edge (52 keV) compared to iodine, leading to more pronounced x-ray attenuation and superior contrast. Ytterbium, among the lanthanide elements, stands out as a promising candidate for diagnostic and molecular imaging applications due to its excellent biocompatibility and high mass x-ray absorption coefficient [8]. Among the lanthanide elements, ytterbium is the most promising contender for diagnostic and molecular imaging

applications due to its excellent biocompatibility and high mass x-ray absorption coefficient ($3.88 \text{ cm}^2 \cdot \text{g}^{-1}$ at 100 keV) [13].

Titanium dioxide (TiO_2) NPs have gained significant attention as a semiconductor material due to their high photochemical stability and cost-effectiveness [14]. To optimize their radiosensitizing effects, doping TiO_2 NPs with high Z -elements while preserving their fundamental physical properties was explored [15]. In this regard, the incorporation of samarium (Sm) into TiO_2 NPs has been investigated, resulting in enhanced efficiency. These $\text{Ti}(\text{Sm})\text{O}_2$ NPs immobilized with polyethylene glycol (PEG) and fluorescent dye offer a multifunctional platform for x-ray computed tomography (CT) and fluorescence imaging. Notably, $\text{Ti}(\text{Sm})\text{O}_2$ NPs exhibit desirable characteristics such as biocompatibility, antimicrobial properties, high chemical stability, specific surface area, and catalytic activity. This review highlights the potential of $\text{Ti}(\text{Sm})\text{O}_2$ NPs and their unique properties for various biomedical applications, including imaging and therapeutic interventions [2].

The surface characteristics of NPs play a crucial role in their biomedical applications, influencing their interactions within the human body. Coatings on NPs can provide protection against mononuclear phagocyte and protein adsorption *in vivo*, thereby, maintaining their stability. However, creating a surface coating material that offers colloidal stability and biocompatibility under physiological conditions is a significant challenge [16]. The choice of coating agent and its interaction with the biological environment determine the stability and biocompatibility of NPs [17]. Different classes of coating substances, such as synthetic and natural hydrophilic polymers like poly(ethylene glycol) (PEG), poly(vinyl alcohol) (PVA), and poly(*L*-lysine) (PLL), have been investigated for their potential in biomedical applications [18, 19]. These coatings have shown benefits such as enhanced colloidal stability, reduced cytotoxicity, and improved biocompatibility of various NPs, including iron oxide and titanium dioxide NPs [20]. One common class of compounds are synthetic and natural hydrophilic polymers such as poly(ethylene glycol) (PEG) which modified USPIOs synthesized [20], and poly(vinyl alcohol) (PVA), which shows superparamagnetic, hydrophilic properties and may serve as a potential candidate for biomedical applications [21], poly(*L*-lysine) (PLL) which provide good colloidal stability for iron oxide and modified NPs less than 10 nm in diameter were tested for cell labelling [22].

Mano *et al.* found that modifying TiO_2 NPs with PEG reduces their cytotoxicity and the induction of stress-related genes [23]. This study aims to enhance the imaging capabilities of titanium dioxide (TiO_2) NPs by incorporating lanthanides and improving their physical and biological properties. By coating these NPs with polymers, they can be used as safe and biocompatible x-ray computed tomography (CT) contrast agents *in vivo*. The findings of this study demonstrate the poten-

tial applications of lanthanide-doped TiO₂ NPs and other multifunctional NPs in cancer diagnostics and therapy. These results underscore the importance of harnessing the unique properties of lanthanide-doped TiO₂ NPs for advanced imaging techniques and their potential significance in cancer research and treatment.

2. MATERIALS AND METHODS

2.1. Materials

Titanium dioxide (TiO₂ = 79.89 g, min. assay (*ex Ti*) 99%, max. limits of impurities, loss on drying 5%, iron (Fe) 05%). Sodium hydroxide (sodium hydroxide pellets AR assay 99.5%, MW.40.00, SO. 55592, Egypt). Carboxymethyl (CMC), carmellose sodium, assay: 99.5% pure Na-CMC, maximum 5 salts, PH: 6.5:8.5, density: 1.59 g/cm³, soluble in water, loss on drying max. 10%. Polyvinyl pyrrolidone (PVP), (K-30), pure, M.W. = 40000, Mumbai, India. Polyethylene glycol 6000 (PEG 6000), molecular mass: 40.3 g/cm³, soluble in water, density: 3.58 g/cm³. Samarium (III) nitrate hexahydrate, 99.9% (REO), hygroscopic, store under nitrogen, 10 g, LOT: D12X008, FW: 444.45, Germany. All the aqueous solutions are prepared using triple distilled deionized water (DW).

2.2. Synthesis of TiO₂ NPs

TiO₂ NPs were synthesized using the hydrothermal method. Initially, a solvent mixture was prepared by combining 5 g of TiO₂ and 4.8 g of NaOH in 60 ml of deionized water at room temperature. The mixture was stirred for 3 hours at 60°C, resulting in a clear solution. To achieve a pH of 7, filtration using filter papers was performed. The solution was then dried at 60°C.

The dried solution was magnetically stirred and transferred to a 100 ml teflon-lined stainless steel autoclave, which was heated to 150°C for 3 hours. After cooling to room temperature, the obtained product was washed five times with pure ethyl alcohol and distilled water. The resulting white precipitate was dried overnight at 60°C and subsequently calcined at 500°C for 2 hours.

2.3. Synthesis of 1% Sm-Doped TiO₂ NPs (Ti(Sm)O₂ NPs)

To synthesize the Ti(Sm)O₂ NPs, samarium (III) nitrate hexahydrate was added to the mixture. Following the hydrothermal method mentioned earlier, the preparation involved the use of ethanol, HCl, and deionized water. Specifically, a solution was created by mixing 30 ml

of ethanol, 0.5 ml of HCl, 2 ml of deionized water, and 1% samarium. Under stirring, 5 ml of titanium oxides were added drop by drop to the solution and vigorously stirred for 15 minutes, following the same procedure as described previously.

2.4. Synthesis of Polymer Encapsulated TiO₂ and Sm-Doped TiO₂ NPs

To enhance the stability of the CT contrast agents, we implemented three surface modifications on the NPs. The NPs were designed with a core-shell structure, where the NP core comprised multiple CT-dense nanocrystals (NCs), and the shell was formed using FDA-approved polymers: polyethylene glycol (PEG), polyvinylpyrrolidone (PVP), and carboxymethyl cellulose (CMC). To carry out the surface modification, a solution containing 0.1 g of TiO₂ NPs and 0.1 g of each polymer (PEG, PVP, and CMC) was mixed in 100 ml of deionized water. The mixture was then stirred at 60°C for 3 hours. Subsequently, the solutions were separated through centrifugation at 60 rpm for 2 minutes, and the resulting NPs were dried at 60°C.

2.5. Characterization Techniques

The optical properties of the synthesized NPs were characterized using a UV–Vis spectrometer (Pg instruments, T₈₀⁺, UV/Vis spectrometer, China). Absorbance spectra measurements were performed in the wavelength range of 200–900 nm to investigate the optical properties of the NPs. This range encompasses the UV, visible, and near-infrared regions of the electromagnetic spectrum, where electronic transitions occur. Molecules with bonding and non-bonding electrons (*n*-electrons) can absorb energy from ultraviolet or visible light, causing them to be excited to higher antibonding molecular orbitals. The UV–Vis spectroscopy provides valuable insights into the electronic transitions and optical behaviour of the NPs [24].

The functional groups present in the synthesized TiO₂ NPs were identified using Fourier transform infrared (FTIR) spectroscopy. The FTIR spectra were collected using an FTIR spectrophotometer (PerkinElmer-99075, Germany) employing the standard KBr pellet technique. The spectral range analysed was 4000–450 cm⁻¹, with a resolution accuracy of 4 cm⁻¹. FTIR spectroscopy is a powerful technique that enables the characterization and identification of various functional groups present in the NPs, providing valuable information about the chemical composition and structure of the synthesized TiO₂ NPs.

Transmission electron microscopy (TEM) imaging was performed using a JEOL JEM-2100 instrument from Japan, equipped with a CCD camera. To prepare the samples for TEM measurements, a wax plate

was covered with a copper grid, and a diluted nanosuspension was sprayed onto the surface of the grid [25]. This ensured that the nanostructures formed in the colloids were visualized under the TEM. The obtained TEM images provided high-resolution details of the NPs and their morphology.

Additionally, the size distribution of the NPs was analysed using ImageJ 64-bit software (version ij 153-win-java 8), and a size distribution histogram was generated to estimate the particle size range and distribution.

The zeta potential of the NPs was determined using a zeta potential analyser and particle sizing devices at a temperature of 25 degrees Celsius. The specific instrument used for this analysis was the Malvern Zetasize Nano-zs 90 from the U.S.A. The zeta potential measurement provides information about the surface charge of the NPs. When particles have a high negative or positive zeta potential, they tend to repel each other, leading to a stable colloidal suspension with no flocculation. Conversely, particles with low zeta potential values lack the repulsive force necessary to prevent their collision and flocculation. According to the principle of electrophoresis, NPs with zeta potentials exceeding +30 mV or falling below -30 mV are considered to be colloidal and exhibit stability (Franks, 2002). The zeta potential analysis helps assess the stability of the NPs and their potential for aggregation or dispersion in solution [26].

Luminescence qualities were assessed using a spectrofluorometer (Jasco FP-6500, Japan) and two-photon laser confocal microscopy (690–1040 nm) (Xenon arc Lamp 150 watt). The excitation and emission spectra were used to analyse the nanocomposites' luminescence capabilities. Before measurement, the nanocomposite is purified by dialysis against distilled water for one week, and the purified samples are distributed in distilled water [19].

2.6. Cytotoxicity and Cell Viability Assay

In the cytotoxicity and cell viability assay, peripheral mononuclear cells (PBMC) were isolated from whole blood using density centrifugation with Ficoll–Paque. The procedure involved centrifuging Hanks balanced salt solution (HBSS) with heparinized human blood, collecting the upper fraction containing PBMCs, and resuspending the cells in PBS buffer. Cell counting was performed using a haemocytometer and the trypan blue exclusion method. The isolated PBMCs were then seeded in a 96-well plate with a culture medium and incubated at 37°C with 5% CO₂.

For cell characterization, PBMCs at passage three were analysed by flow cytometry using anti-CD45 PE antibody [27]. The cells were stained, and data analysis was performed using a flow cytometer. To

assess cell viability and cytotoxicity of the NPs, cells were seeded in a 96-well plate and incubated with the NPs for a specific duration. After incubation, trypan blue was added to each well, and the plates were further incubated and placed on a shaker to facilitate cell–NP interaction. Cell morphology was assessed by capturing photographs of living cells' interaction with different NPs. These experimental procedures, as described by Gabal *et al.* (2022), allowed for the evaluation of cytotoxicity and cell viability using peripheral mononuclear cells. The isolation and characterization of PBMCs provided a standardized cell population for the assessment, and the incubation with NPs allowed for the observation of any potential effects on cell viability and morphology [28].

2.7. Assessment of the Toxicity and Safety Profile

The study was conducted on 51 male mice weighing 29–40 g. They were obtained from the animal house of MERC, the faculty of medicine, Mansoura University, and after approval by our local ethical committee. Considering that accumulation of NPs *in vivo* might stimulate toxicity or adverse side effects after long-term treatment, we next evaluated the potential long-term toxicity of NPs *in vivo*.

Animal Model. The mice were randomly allocated into two groups (24 rats each) and three control. The control group was injected with saline only; after intravenous injection (IV) of NPs, mice were sacrificed after 3 hrs and 7 days, major organs (liver, heart, lung, spleen, pancreas, and kidneys) were collected for H&E staining. Samples were then fixed in 10% formalin, followed by routine dehydration, immersion, and paraffin embedding. They were sectioned into 4- μ m-thick slices for haematoxylin and eosin staining and examined by light microscopy.

Degenerative changes were observed and graded into: absent, defined as no obvious pathological changes; mild, defined as focal pathological changes; or marked, defined as diffuse pathological changes, as modified from a previous report. Blood biochemistry analyses were performed, and blood samples were also collected to investigate nephrotoxicity and hepatotoxicity. Aspartate aminotransferase, alanine aminotransferase, and creatinine levels were determined after 1 hr and 6 days of treatment in serum samples collected. Levels of ALT and AST refer to liver damage. A measurement of the serum creatinine level is often used to evaluate kidney function.

2.8. *In vitro* Phantom Imaging

For *in vitro* phantom measurements, solutions of TiO₂ and samarium-doped TiO₂ were prepared at various concentrations 6.25, 12.5, 25.0,

50.0, and 100.0 mM diluted in DW in 1.0 ml microtubes. Phantom CT images were acquired on a Toshiba Alexion CT scanner operating at 80, 100, 120 keV, and 22, 30, 37 μ A, respectively, with a slice thickness of 0.5 mm and gantry rotation time of 0.6 s. Images were analysed using J-image 64-bit (ij 153-win-java 8). Create a circular region of interest (ROI) over each tube, and the attenuation and standard deviation were recorded for each ROI analysed [29]. From these values, the Contrast rates were calculated for different image sets *via* the equation

$$\text{Contrast} = (I_{\max} + I_{\min}) / (I_{\max} - I_{\min}).$$

3. RESULTS AND DISCUSSION

3.1. UV/Visible Optical Absorption Spectral Data

The study involved recording ultraviolet–visible (UV/Vis) absorbance spectra to evaluate the electronic structure and optical band gap of the NPs. The UV/Vis spectra of pure titanium dioxide (TiO₂) NPs and samarium-doped TiO₂ NPs were obtained and analysed.

In Figure 1, *a*, the absorbance peak at 364.23 nm corresponds to the presence of TiO₂ in the sample. In Figure 1, *b*, two absorption peaks are observed for samarium-doped TiO₂ at 366.65 nm and 409.2 nm, with the latter attributed to the presence of samarium. The specific absorption characteristics may vary with different polymeric precursors used in the synthesis process. The absorption edge in the UV region represents electronic transitions from the occupied valence band to the empty conduction band. Absorption occurs when the energy of the incident

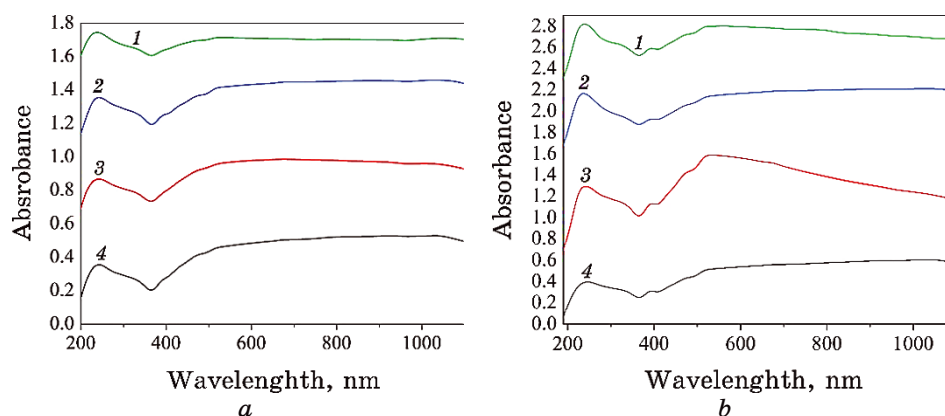


Fig. 1. (a) UV spectra of: 1—TiO₂, 2—PVP@TiO₂, 3—PEG@TiO₂, and 4—CMC@TiO₂ NPs; (b) UV spectra of: 1—Ti(Sm)O₂, 2—PVP@Ti(Sm)O₂, 3—PEG@Ti(Sm)O₂, and 4—CMC@Ti(Sm)O₂ NPs.

photon matches or exceeds the band gap energy of the material.

3.2. FTIR Analysis

Infrared spectroscopy (FTIR) was employed to analyse the functional groups present in the synthesized compounds. Figure 2 illustrates a series of FTIR spectra for TiO_2 and samarium-doped TiO_2 NPs, coated with PVA, PEG, and CMC. In the spectra, a prominent and strong band in the range of $580\text{--}660\text{ cm}^{-1}$ corresponds to the characteristic modes of TiO_2 . This band provides evidence of the presence of TiO_2 in the samples. Additionally, an absorption range around 3427 cm^{-1} indicates the stretching vibrations of hydroxyl groups, which may be influenced by in-situ spectra recording and water reabsorption from the ambient atmosphere. Another absorption range around 1553 cm^{-1} is attributed to the bending vibrations of hydroxyl groups in molecular water. The bands in the range of $1000\text{--}400\text{ cm}^{-1}$ are associated with the Ti–O modes, further confirming the presence of TiO_2 .

Furthermore, the FTIR spectrum of the coated TiO_2 NPs is presented in Fig. 2 too. The absorbance observed in the range of $1066\text{--}1700\text{ cm}^{-1}$ corresponds to the vibrations of organic polymers. The appearance of new bands in this region is attributed to the existence of the organic polymer coating. For example, bands around 2881 , 1352 , and 1066 cm^{-1} represent the stretching vibrations of C–H bonds, the bending vibrations of C–H bonds, and the stretching vibrations of C–O bonds, respectively. The presence of these bands indicates the hydrogen-bonding nature and confirms the interaction between the organic polymer and the surface of TiO_2 and samarium-doped TiO_2 NPs. This interaction between the polymers and the NPs further supports the

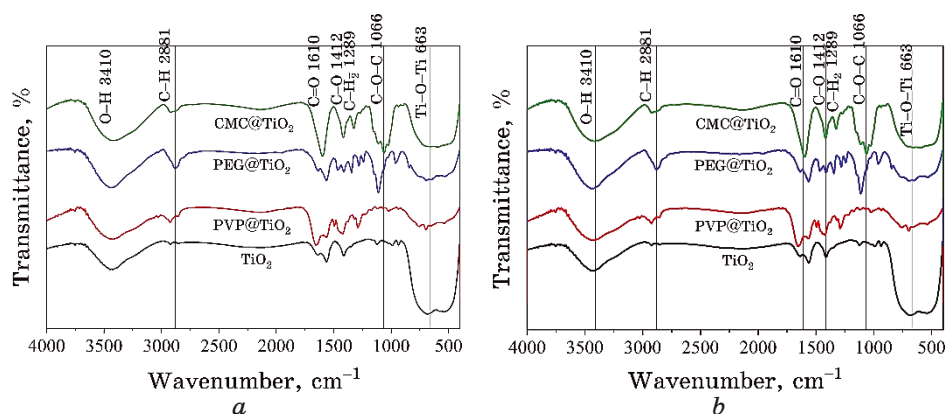


Fig. 2. FTIR spectra of: (a) PVP@ TiO_2 , PEG@ TiO_2 , CMC@ TiO_2 NPs; (b) $\text{Ti}(\text{Sm})\text{O}_2$, PVP $\text{Ti}(\text{Sm})\text{O}_2$, PEG @ $\text{Ti}(\text{Sm})\text{O}_2$, CMC @ $\text{Ti}(\text{Sm})\text{O}_2$ NPs.

successful coating process and provides valuable information about the surface chemistry of the synthesized NPs.

3.3. Zeta Potential

The ζ -potential values of prepared NPs sintered are shown in Fig. 3. ζ -potential has been utilized to be aware of the nature of prepared nano-

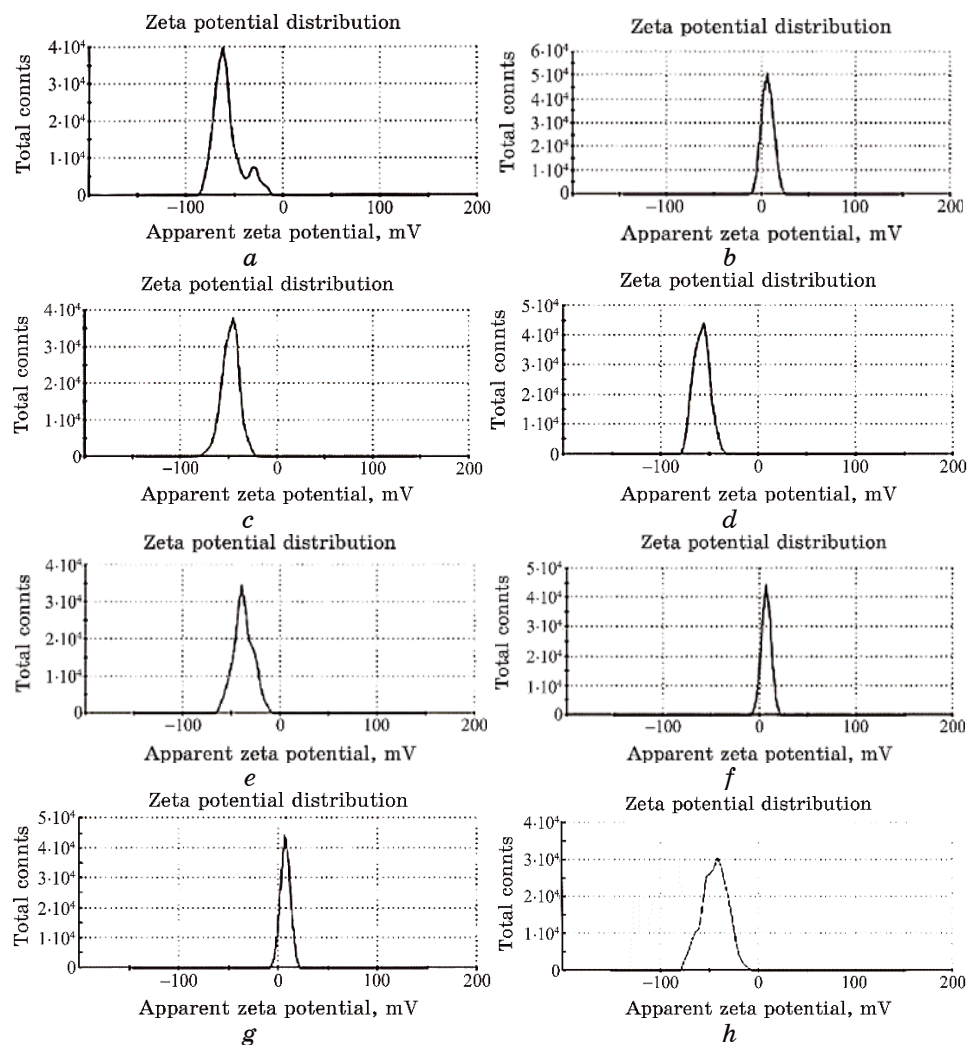


Fig. 3. Zeta potential for NPs: (a) TiO₂; (b) PVP@ TiO₂; (c) PEG@ TiO₂; (d) CMC@TiO₂; (e) Ti(Sm)O₂; (f) PVP@Ti(Sm)O₂; (g) PEG@Ti(Sm)O₂; (h) CMC@Ti(Sm)O₂.

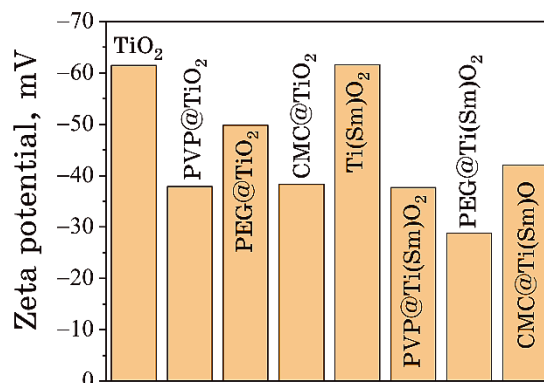


Fig. 4. Zeta potential distribution of TiO₂, PVP@TiO₂, PEG@TiO₂, CMC@TiO₂, Ti(Sm)O₂, PVP@Ti(Sm)O₂, PEG@Ti(Sm)O₂, and CMC@Ti(Sm)O₂ NPs.

particle charges in DW. ζ -potential with a negative value ranging from -37.7 mV to -61.5 mV was obtained for the nanoparticle diluted in DW, corresponding to a stable colloidal without particle settlement. ζ -potential lowered as the NPs was coated with polymers, as in Fig. 4. Moreover, the prepared suspension endorsed with general ζ -potential value of 30 mV with a positive or negative sign for better stability. Lower values of ζ -potential suggest aggregation of NPs due to van der Waals forces. Zhang *et al.* confirmed the measurement of the ζ -potential of the material to understand the nature of cellular interaction, cellular diagnostics, and therapeutics of normal and cancer cell effects.

3.4. Transmission Electron Microscopy (TEM) and Photoluminescence

TEM of TiO₂, Ti(SmO₂) NPs declared a spherical morphology and a comparably narrow size dispersion characteristic of the hydrothermal method.

The particle-size distribution histogram was outlined regarded the counted ten NPs as shown in Fig. 5. The mean particle size is of 80 nm with a 23.59 nm standard deviation. The particle-size distribution histogram was outlined regarded to the counted ten NPs. The mean particle size of Ti(SmO₂) is 83 nm with a 22.30 nm standard deviation.

As an indirect band gap semiconductor, TiO₂ shows no band gap photoluminescence. Photoluminescence (PL) arises from recombining oppositely charged trapped and free carriers. Photoluminescence from Ti(Sm)O₂ suspension contains a band at 600 nm and a band at around 515 nm. The band at 600 nm exhibits a strong correlation with defects, and the 515 nm band shows a close relationship with the oxygen vacancies.

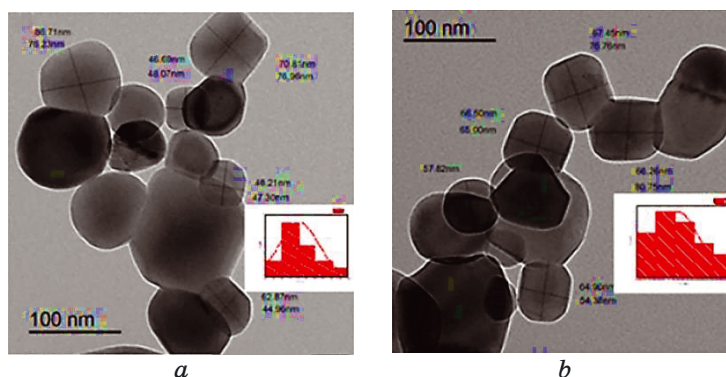


Fig. 5. (a) TEM of TiO₂ NPs and the corresponding particle size distribution histogram; (b) TEM of Ti(Sm)O₂ and the corresponding particle-size distribution histogram.

A series of Ti(Sm)O₂ PL studies in different coated samples in Fig. 6. The normal emission of NPs is dominated by PL arising from the recombination of trapped electrons with valence band holes, leading to a broad spectrum with a peak in 600 nm. In addition, it is presented a higher energy emission from recombining mobile electrons with trapped holes. Because both types of recombination depend on the spatial coincidence of trapped and roaming charges, comparing the energy

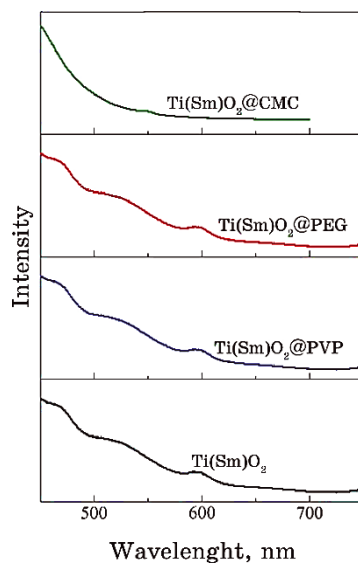


Fig. 6. Photoluminescence of Ti(Sm)O₂, PVP@Ti(Sm)O₂, PEG@Ti(Sm)O₂, and CMC@Ti(Sm)O₂ NPs.

TABLE 1. Characterization of TiO₂ NPs.

| Sample | Zeta potential, mv | Conductivity, ms/cm | Energy gap, eV | Particle size, nm |
|--------------------------|--------------------|---------------------|----------------|-------------------|
| TiO ₂ | -61.5 | 3.16 | 3.4 | 70.5 |
| PVP@TiO ₂ | -37.9 | 0.99 | 2.95 | |
| PEG@TiO ₂ | -49.8 | 2.2 | 2.99 | |
| CMC@TiO ₂ | -38.27 | 2.2 | 2.88 | |
| Ti(Sm)O ₂ | -61.6 | 2.5 | 2.97 | 83.03 |
| PVP@Ti(Sm)O ₂ | -37.7 | 3.02 | 2.9 | |
| PEG@Ti(Sm)O ₂ | -28.8 | 1.56 | 2.7 | |
| CMC@Ti(Sm)O ₂ | -42.6 | 4.08 | 2.8 | |

gaps and conductivity values (Table 1) with PL (Fig. 6) obtained from prepared samples, we can conclude that the PL intensity is greater when transport is hindered and lower when the charges are more mobile. As shown in Table 1, the PL peaks diminishes in CMC@Ti(Sm)O₂ with more conductivity value and less energy gap.

3.5. Phenotypic Characterization of PBMCs

In passage three, PBMCs were characterized using flow cytometric analysis. The results showed that PBMC cells positively express hematopoietic markers CD45 (70.9% ; Fig. 7).

3.6. Human Mononuclear Cell Culture and Treatment Protocol

The morphological microstructure ($\times 100$) is observed using an Olympus IX51 inverted fluorescence microscope.

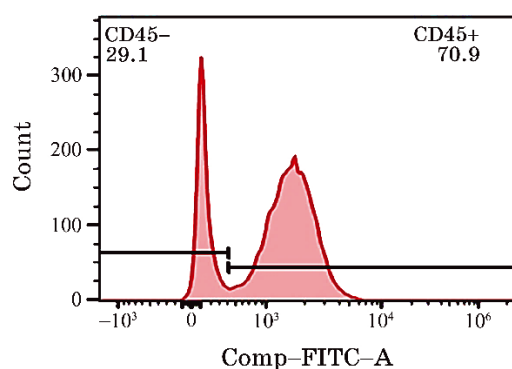


Fig. 7. CD 45 FITC mouse antihuman (561865, BD).

Recording the viability for each plate after 90 min, as shown in Fig. 8, shows the viability for the mononuclear cells after incubation with NPs in the dilatation (1NPs:1cells), (1NPs:3cells), (1NP_s:5cells). Cell viability results ensure TiO₂, PVP@TiO₂, PEG@TiO₂, CMC@TiO₂, Ti(Sm)O₂, PVP@Ti(Sm)O₂, PEG@Ti(Sm)O₂, and CMC@Ti(Sm)O₂ NPs is blood biocompatibility; so, it will be completely safe within few hours before any interaction with blood cells occurs. The blood biocom-

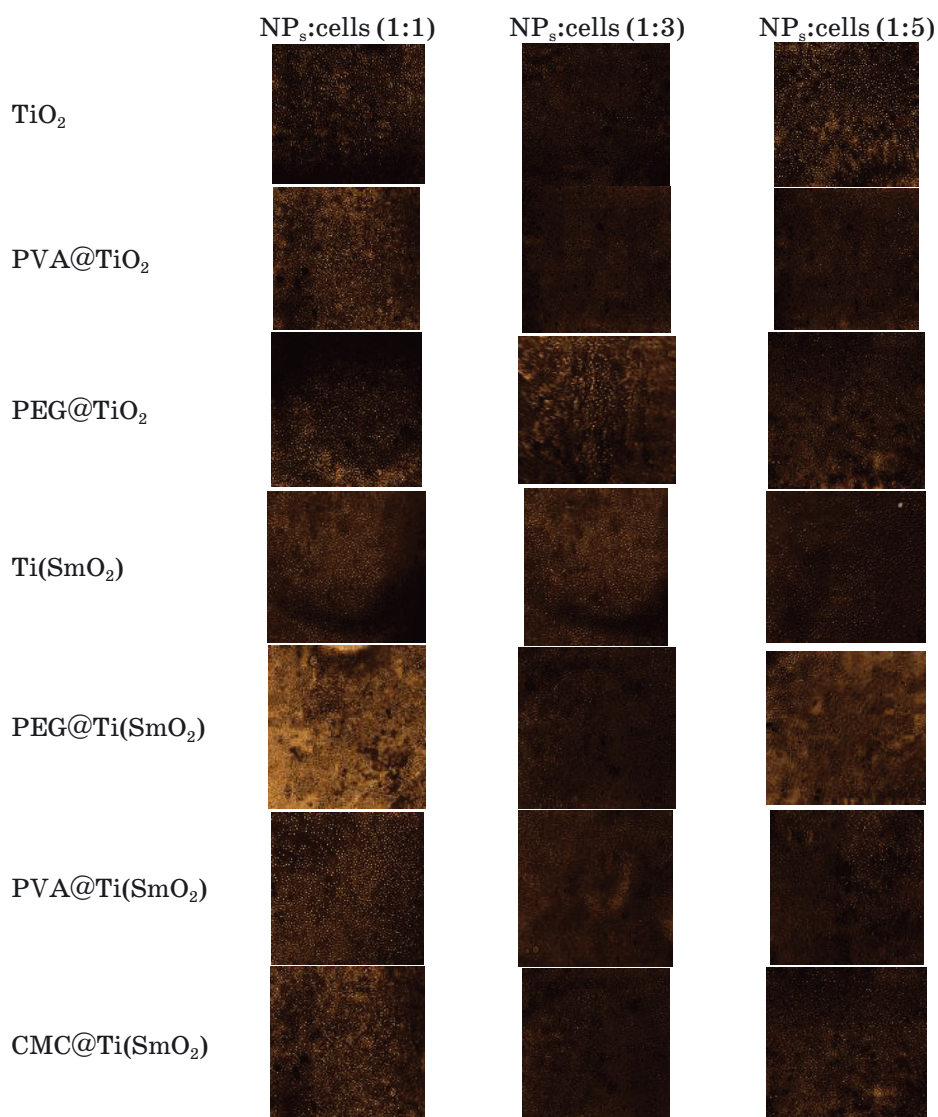


Fig. 8. The mononuclear cells after incubation with NPs after 90 min.

patibility of our synthesized NPs may relate to its surface nature.

After injecting a dose of NPs (0.1 ml), rats were dissected and subjected to haematoxylin and eosin (H&E) examination at 1 hour and 6 days post-injection. The H&E examination results at 1 hour showed that most of the NPs accumulated in the lung. However, no adverse effects of the NPs were observed in the pancreas, heart, lung, or kidney. Nonetheless, variable levels of injuries were observed in the lung, liver, and heart, depending on the nature of the injected NPs. In the lung samples taken after 1 hour, diffuse alveolar damage (DAD) was observed.

DAD is characterized by congested lung vessels, interstitial haemorrhage and fibrosis, interstitial neutrophils, bloody exudates in the alveoli, pulmonary congestion, bronchiolar epithelial damage, and hemosiderin-laden macrophages. In the liver, mild portal inflammation and little bile duct proliferation were observed in samples injected with NPs, except for TiO₂ coated with PVA, which showed minimal portal inflammation and no bile duct proliferation. Hepatocyte degeneration (pyknotic) was observed in zone 1, 2, and 3 of the liver for TiO₂. TiO₂@CMC and Ti(SmO)₂@PVA exhibited hepatocyte degeneration and injury in zone 2 and 3. TiO₂@PVA and Ti(SmO)₂ showed hepatocyte degeneration and injury in zone 3. TiO₂ coated with PEG showed scattered spotty necrosis in hepatocytes in zone 3. However, no hepatocyte injury was found in Ti(SmO)₂@PEG and Ti(SmO)₂@CMC.

To assess the long-term toxicity of the NPs, histological examination was conducted on several organs, including the heart, liver, lung, pancreas, kidney, and spleen after seven days (see Fig. 9). H&E examination revealed no adverse effects of the NPs on the heart, pancreas, kidney, and spleen. Fortunately, the lung showed complete resolution for TiO₂, PEG@TiO₂, CMC@TiO₂, Ti(Sm)O₂, PVP@Ti(Sm)O₂ NPs.

Serum levels of alanine aminotransferase (ALT), aspartate aminotransferase (AST), and creatinine (Cr) were measured after 1 hour and seven days to evaluate liver and kidney function (Table 2). After 1 hour, ALT levels indicated minimal liver toxicity, while creatinine levels indicated normal kidney function. However, AST levels were higher. After seven days, ALT and AST levels indicated minimal liver toxicity, and creatinine levels indicated normal kidney function.

Based on the biodistribution of TiO₂ NPs, they can potentially be developed as target-specific agents for lung-related pathologies, allowing for the selective distinction of lung diseases.

X-ray CT phantom images were captured using various concentrations of TiO₂ and Ti(Sm)O₂ coated with various polymers diluted with distilled water (Fig. 10).

The CT number increased as the concentration of NPs increased (Fig. 11); the variation, in contrast, is slightly varied. However, the high contrast was gained at 80 keV.

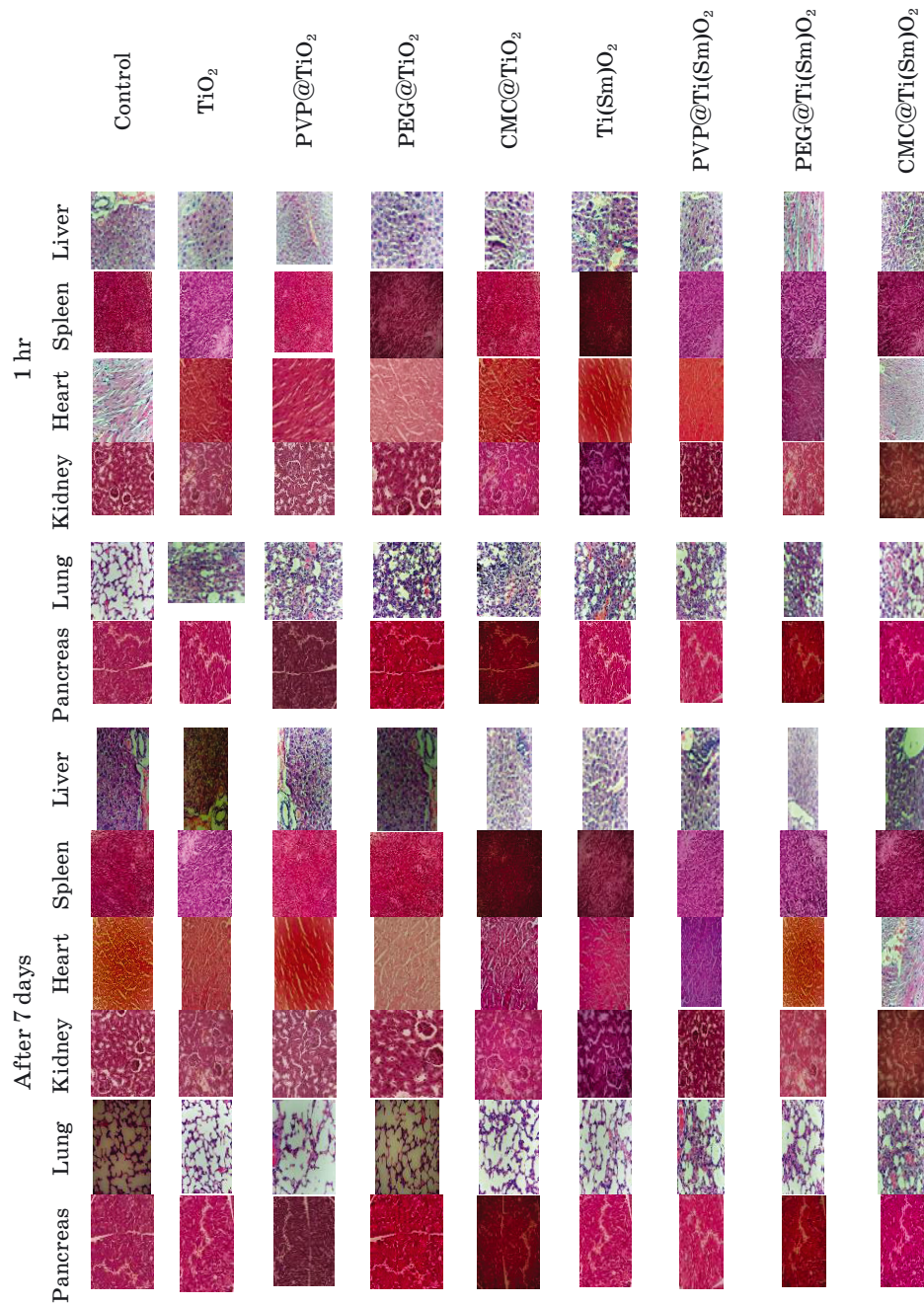
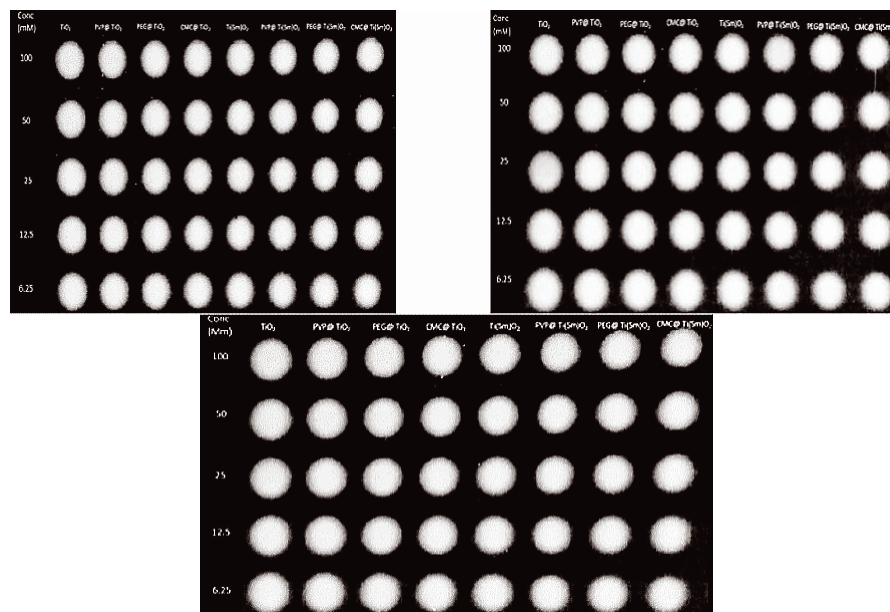


Fig. 9. Histological examination of heart, liver, lung, pancreas, kidney, and spleen injected by 0.1 ml saline and NPs followed by dissection after 1 hr and 7 days, sections were stained with H&E and observed under the light microscope at 400× magnification.

TABLE 2. Toxicological effect on serum levels of ALT, AST, and creatinine.

| After 1 h | Creatinine, U/L | ALT, U/L | AST, U/L |
|--------------------------|-----------------|----------|----------|
| Control | 0.15 | 22 | 110 |
| TiO ₂ | 0.27 | 47 | 516 |
| PVP@TiO ₂ | 0.29 | 57 | 671 |
| PEG@TiO ₂ | 0.26 | 39 | 310 |
| CMC@TiO ₂ | 0.25 | 45 | 305 |
| Ti(Sm)O ₂ | 0.25 | 40 | 480 |
| PVP@Ti(Sm)O ₂ | 0.24 | 56 | 620 |
| PEG@Ti(Sm)O ₂ | 0.23 | 63 | 588 |
| CMC@Ti(Sm)O ₂ | 0.24 | 50 | 638 |
| After 7 days | | | |
| TiO ₂ | 0.25 | 30 | 220 |
| PVP@TiO ₂ | 0.28 | 26 | 229 |
| PEG@TiO ₂ | 0.24 | 24 | 145 |
| CMC@TiO ₂ | 0.23 | 24 | 130 |
| Ti(Sm)O ₂ | 0.24 | 28 | 163 |
| PVP@Ti(Sm)O ₂ | 0.23 | 30 | 177 |
| PEG@Ti(Sm)O ₂ | 0.24 | 29 | 176 |
| CMC@Ti(Sm)O ₂ | 0.16 | 23 | 260 |

**Fig. 10.** CT phantom images of TiO₂, PVP@TiO₂, PEG@TiO₂, and CMC@TiO₂ NPs by UV spectra of Ti(Sm)O₂, PVP@Ti(Sm)O₂, PEG@Ti(Sm)O₂, and CMC@Ti(Sm)O₂ NPs.

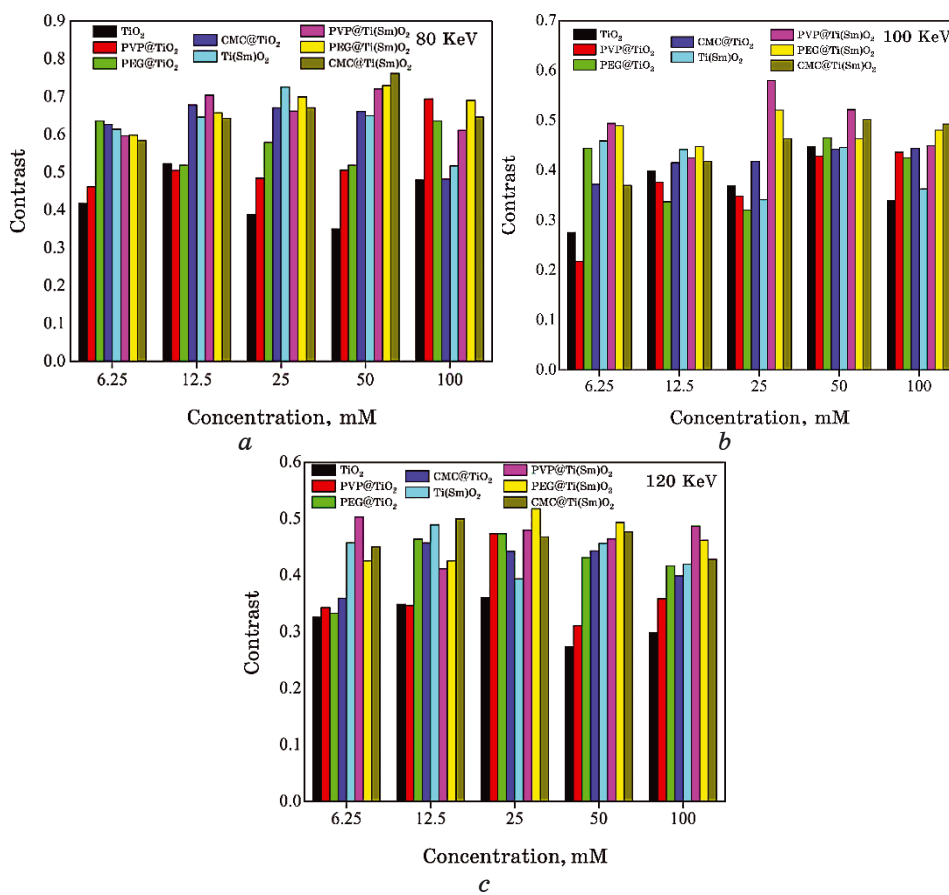


Fig. 11. Contrast of TiO₂, Ti(SmO₂) coated with PEG, CMC, PVP: (a) 80 keV; (b) 100 keV; (c) 120 keV.

4. CONCLUSION

The synthesized TiO₂ and Ti(Sm)O₂ NPs coated with PVA, PEG, and CMC have shown promising characteristics for use as CT scan contrast agents. These NPs exhibit small size, high stability, high contrast, long blood retention time, and low toxicity. Both *in vitro* and *in vivo* toxicity assessments have demonstrated their excellent biocompatibility and low risk of adverse effects. Furthermore, the imaging performance of these NPs in CT scans has been found to be superior. They exhibit higher x-ray absorption coefficients and longer blood circulation time, making them effective contrast agents for CT imaging. The incorporation of samarium doping in TiO₂ NPs has further enhanced their performance in fluorescent imaging, making them suitable for

dual imaging applications. Based on these findings, the synthesized TiO₂ and Ti(Sm)O₂ NPs coated with PVA, PEG, and CMC hold significant potential for clinical applications in dual imaging. Their unique properties and biocompatibility make them promising candidates for improving the accuracy and effectiveness of CT imaging in medical diagnostics.

ETHICS APPROVAL AND CONSENT TO PARTICIPATE

Animal studies were performed in MERC accredited facility under the approval of Faculty of Medicine, Mansoura University.

REFERENCES

1. K. H. Bae, H. J. Chung, and T. G. Park, *Mol. Cells*, **31**, Iss. 4: 295 (2011); doi:10.1007/s10059-011-0051-5
2. F. Hallouard, N. Anton, P. Choquet, A. Constantinesco, and T. Vandamme, *Biomaterials*, **31**, Iss. 24: 6249 (2010); doi:10.1016/j.biomaterials.2010.04.066
3. Y. Liu, K. Ai, and L. Lu, *Accounts of Chemical Research*, **45**, Iss. 10: 1817 (2012); doi:10.1021/ar300150c
4. D. P. Cormode, P. C. Naha, and Z. A. Fayad, *Contrast Media Mol. Imaging*, **9**, No. 1: 37 (2014); doi:10.1002/cmml.1551
5. J. F. Hainfeld, D. N. Slatkin, T. M. Focella, and H. M. Smilowitz, *Br. J. Radiol.*, **79**, No. 939: 248 (2006); doi:10.1259/bjr/13169882
6. P. A. Jackson, W. N. Rahman, C. J. Wong, T. Ackerly, and M. Geso, *European Journal of Radiology*, **75**, No. 1: 104 (2010); doi:10.1016/j.ejrad.2009.03.057
7. E. E. Connor, J. Mwamuka, A. Gole, C. J. Murphy, and M. D. Wyatt, *NANO·MICRO Small*, **1**, Iss. 3: 325 (2005); doi:10.1002/sml.200400093
8. A. Jakhmola, N. Anton, and T. F. Vandamme, *Advanced Healthcare Materials*, **1**, Iss. 4: 413 (2012); doi:10.1002/adhm.201200032
9. O. Rabin, J. Manuel Perez, J. Grimm, G. Wojtkiewicz, and R. Weissleder, *Nature Mater.*, **5**, No. 2: 118 (2006); doi:10.1038/nmat1571
10. D. Pan, E. Roessl, J. P. Schlomka, S. D. Caruthers, A. Senpan, M. J. Scott, J. S. Allen, H. Zhang, G. Hu, and P. J. Gaffney, *Angewandte Chemie [International Ed. in English]*, **49**, No. 50: 9635 (2010); doi:10.1002/anie.201005657
11. J. A. Nadel, W. G. Wolfe, P. D. Graf, J. E. Youker, N. Zamel, J. H. Austin, W. A. Hinchcliffe, R. H. Greenspan, and R. R. Wright, *New Engl. J. Med.*, **283**: No. 6: 281 (1970); doi:10.1056/nejm197008062830603
12. S. Chakravarty, J. M. L. Hix, K. A. Wiewiora, M. C. Volk, E. Kenyon, D. D. Shuboni-Mulligan, B. Blanco-Fernandez, M. Kiupel, J. Thomas, L. F. Sempere, and E. M. Shapiro, *Nanoscale*, **12**, No. 14: 7720 (2020); doi:10.1039/d0nr01234c
13. H. Xing, W. Bu, Q. Ren, X. Zheng, M. Li, S. Zhang, H. Qu, Z. Wang, Y. Hua, K. Zhao, L. Zhou, W. Peng, and J. Shi, *Biomaterials*, **33**, Iss. 21: 5384 (2012); doi:10.1016/j.biomaterials.2012.04.002
14. S. Jafari, B. Mahyad, H. Hashemzadeh, S. Janfaza, T. Gholikhani, and L.

- Tayebi, *Int. J. Nanomedicine*, **15**, 3447 (2020); doi:10.2147/ijn.s249441
15. H. E. Townley, E. Rapa, G. Wakefield, and P. J. Dobson, *Nanomedicine: Nanotechnology, Biology and Medicine*, **8**, Iss. 4: 526 (2012); doi:10.1016/j.nano.2011.08.003
 16. X. Michalet, F. F. Pinaud, L. A. Bentolila, J. M. Tsay, S. Doose, J. J. Li, G. Sundaresan, A. M. Wu, S. S. Gambhir, and S. Weiss, *Science*, **307**, No. 5709: 538 (2005); doi:10.1126/science.1104274
 17. A. Koudrina and M.C. DeRosa, *ACS Omega*, **5**, Iss. 36: 22691 (2020); doi:10.1021/acsomega.0c02650
 18. H. M. Fahmy, A. M. Mosleh, A. A. Elghany, E. Shams-Eldin, E. S. Abu Serea, S. A. Ali, and A. E. Shalan, *RSC Advances*, **9**, 35: 20118 (2019); doi:10.1039/c9ra02907a
 19. R. Abo Gabal, S. Osama, N. Hanafy, and A. Oraby, *Appl. Phys. A*, **129**, No. 3: 201-1 (2023); doi:10.1007/s00339-023-06482-8
 20. J. Y. Park, P. Daksha, G. H. Lee, S. Woo, and Y. Chang, *Nanotechnology*, **19**, No. 36: 365603 (2008); doi:10.1088/0957-4484/19/36/365603
 21. T. S. Gaaz, A. B. Sulong, M. N. Akhtar, A. A. Kadhun, A. B. Mohamad, and A. A. Al-Amiery, *Molecules*, **20**, No. 12: 22833 (2015); doi:10.3390/molecules201219884
 22. M. Babic, D. Horák, M. Trchová, P. Jendelová, K. Glogarová, P. Lesný, V. Herynek, M. Hájek, and E. Syková, *Bioconjug. Chem.*, **19**, Iss. 3: 740 (2008); doi:10.1021/bc700410z
 23. S. S. Mano, K. Kanehira, S. Sonezaki, and A. Taniguchi, *Int. J. Mol. Sci.*, **13**, No. 3: 3703 (2012); doi:10.3390/ijms13033703
 24. M. F. Vitha, *Spectroscopy. Principles and Instrumentation* (John Wiley & Sons: 2018).
 25. M. Kannan, *Transmission Electron Microscope: Principle, Components and Applications Illumination System (Electron Gun and Condenser Lenses) Electron Gun*. In: *A Textbook on Fundamentals and Applications of Nanotechnology* (New Delhi: Daya Publishing House® A Division of Astral International Pvt. Ltd.: 2018), pp. 93–101.
 26. G. V. Franks, *Journal of Colloid and Interface Science*, **249**, Iss. 1: 44 (2002); doi:10.1006/jcis.2002.8250
 27. I. De Dios, L. Ramudo, J. R. Alonso, J. S. Recio, A. C. Garcia-Montero, and M. A. Manso, *FEBS Lett.*, **579**, Iss. 28: 6355 (2005); doi:10.1016/j.febslet.2005.10.017
 28. R. A. Gabal, D. Shokeir, and A. Orabi, *Trends in Sciences*, **19**, No. 3: 2062 (2022); doi:10.48048/tis.2022.2062
 29. E. M. Pogson, J. McNamara, P. Metcalfe, and R. A. Lewis, *Quantitative Imaging in Medicine and Surgery*, **3**, No. 1: 18 (2013); doi:10.3978/j.issn.2223-4292.2013.02.05

PACS numbers: 68.37.Hk, 68.37.Lp, 68.37.Vj, 78.67.Bf, 81.16.Mk, 87.19.xb, 87.64.Cc

Synthesis of Silver Nanoparticles *via* Pulsed-Laser Ablation in Deionized Water: Characterization and Antibacterial Applications

Khalaf Ajaj¹, Mushtaq Abed Al-Jubbori², and Abdullah M. Ali¹

¹*College of Education for Pure Sciences,
Department of Physics,
University of Tikrit,
41001 Mosul, Iraq*

²*College of Education for Pure Sciences,
Department of Physics,
University of Mosul,
41001 Mosul, Iraq*

In this present study, the fabrication of silver nanoparticles (NPs) is achieved through Q-switched Nd:YAG-laser ablation. A disc-shaped silver target immersed in deionized water served as the substrate for the ablation process. Varying number of pulses, specifically, 300 and 500 pulses, is used along with two laser fluences of 6.36 J/cm² and 12.73 J/cm². To ascertain the nanoparticles' morphological and optical attributes, UV-Vis spectrophotometry, transmission electron microscopy (TEM) and field-emission scanning electron microscopy (FE-SEM) analyses are employed. The augmentation of absorbance spectra proportional to pulse counts indicates escalated silver-nanoparticles' concentrations. The absorption spectra exhibit surface-plasmon resonance peaks at \cong 400 nm, which are intensified with increasing laser pulses. An observable decrease in the optical band gap is also noted. TEM and FE-SEM analyses corroborate the existence of nearly spherical Ag nanoparticles. The analyses reveal their average diameters of approximately 34 nm and 57 nm for laser fluences of 6.36 J/cm² and 12.73 J/cm², respectively. Intriguingly, the inhibitory effect on *Klebsiella pneumoniae* and *Staphylococcus aureus* is more pronounced with Ag NPs generated at lower laser fluence, despite the equivalent pulse number.

У цьому дослідженні виготовлення наночастинок (НЧ) срібла було досягнуто за допомогою абляції лазером Nd:YAG із модуляцією добротності. Срібна мішень у формі диска, занурена у дейонізовану воду, слугувала підкладкою у процесі абляції. Було застосовано різну кіль-

кість імпульсів, а саме, 300 і 500 імпульсів, разом із двома лазерними флюенсами у 6,36 Дж/см² і 12,73 Дж/см². Щоб визначити морфологічні й оптичні характеристики наночастинок, використовували спектроскопію УФ- і видимого діапазонів, трансмісійну електронну мікроскопію (ТЕМ) і сканувальну електронну мікроскопію за допомогою польової емісії (ПМ-СЕМ). Збільшення спектрів вбирання пропорційно кількості імпульсів вказувало на підвищення концентрації наночастинок срібла. Спектри вбирання показали піки поверхневого плазмонного резонансу в околі \cong 400 нм, які посилювалися зі збільшенням лазерних імпульсів. Також було відзначено помітне зменшення ширини забороненої зони. Аналіза даних ТЕМ і ПЕ-СЕМ підтвердила наявність майже сферичних наночастинок срібла. Аналіза виявила їхні середні діаметри приблизно у 34 нм і 57 нм для потоків лазерного світла у 6,36 Дж/см² і 12,73 Дж/см² відповідно. Цікаво, що інгібувальна дія на *Klebsiella pneumoniae* та *Staphylococcus aureus* була більш вираженою з Ag НЧ, створеними за меншого потоку лазерного світла, незважаючи на еквівалентну кількість імпульсів.

Key words: laser ablation, silver nanoparticles, nanoparticle size, antibacterial activity.

Ключові слова: лазерна абляція, наночастинок срібла, розмір наночастинок, антибактеріальна активність.

(Received 17 August, 2023)

1. INTRODUCTION

In the past ten years or so, there has been a significant increase in the risk of biological and bacterial attacks, particularly, in areas, which are used for human consumption, like food, food packaging and water. Scientists have been inspired by the rising risk to create new, risk-free, and simple-to-use inorganic antibacterial nanoparticle substances. Certain materials, like metal-oxide semi-conductors, could produce entirely new materials with optical and/or electronic properties, when their dimensions are shrunk to the nanoscale. This makes it possible for researchers to examine the advantages of nanomaterials in a variety of fields, including biomedicine, optoelectronics and the environment [1–3].

The use of nanoparticles as new agents to inhibit microbial growth has increased as a result of the development of antibiotic resistance [4]. Optimized synthesis of nanoparticles (NPs) increased the production of ultrapure and perfectly spherical NPs with smaller average sizes [5]. Ultrashort laser-pulse interaction with materials has received much attention from researchers in micro and nanomachining, especially for the generation of nanoparticles in liquid environments, because of the straightforward method and direct

application for organic solvents. In addition, the colloidal nanoparticles produced by laser ablation have very high purity they are free from surfactants and reaction products [6]. Moreover, the pulsed-laser ablation in liquid (PLAL) technique is gaining more importance due to its simplicity, rapid rate of formation of nanoparticles and eco-friendly approach [7]. There are numerous literature papers on laser interaction with hard and soft materials that focus on potential future applications in the fields of biomedicine and nanoenergy production [8]. Typical laser parameters that affect the ablation rate include wavelength, fluence, pulse duration, repetition rate, the target materials' ability to absorb light, transmission, laser pulse energy, and the chemical makeup of the liquid [9–11].

Laser parameters can be used to modify the size, shape, surface properties, aggregation state, solubility, structure, and chemical makeup of nanoparticles. The same processes could be used with various types of materials to create nanostructured materials in a variety of shapes and sizes. Besides, when a solid target is ablated in liquid, hot plasma is created, the surrounding liquid is vaporized, and a cavitation bubble (CB) is created. In this bubble, target atoms and clusters as well as liquid species can react under extreme pressure and temperature conditions. The ablation products quickly cool to room temperature once they are released into the surrounding liquid [12].

Among all metallic nanoparticles, silver NPs have the most intriguing physical characteristics for biosensing, and its antimicrobial properties can be improved by adjusting its size at the nanoscale. Additionally, Ag NPs with nanoscale sizes demonstrated potent bactericidal activity against both gram-positive and gram-negative bacteria. However, this technique is preferred for producing nanoparticles because it does not involve any potentially dangerous materials. In other techniques, the nanoparticles are contaminated with substances that might be harmful to human cells due to the use of surfactants or chemical precursors [13, 14]. A metallic-nanoparticles' surface-plasmon resonance peak (SPRP) is produced, when light excite the electrons within it, resulting in a resonant oscillation in the visible range, the SPRP is related to the size of the particle [15]. Gram-negative rod-shaped bacilli known as *Klebsiella* bacteria can be found in the intestines of people, animals and the environment [16]. A typical species of *Klebsiella pneumoniae* is known to cause a number of infections in people, including pneumonia, intra-abdominal infections, and urinary tract infections. Additionally, it is a pathogen, which is multidrug resistant and frequently causes serious morbidity and mortality in healthcare settings [17]. Besides that, *Staphylococcus aureus* is a gram-positive coccus that can cause a variety of clinical infections, such as abscesses, pneumonia, sepsis

and it is a significant contributor to food poisoning [18, 19]. *S. aureus* has the capacity to develop resistance to antimicrobial agents, making treatment and control of infections challenging [20].

The current study uses the PLAL technique to create silver nanoparticles under controlling the number of pulses and ablated energies. Using UV–Visible spectrophotometer, transmission electron microscopy and field-emission scanning electron microscopy analyses, the optical and morphology characteristics of the prepared samples were examined. Ag NPs were used to test the antibacterial effectiveness against *Klebsiella pneumoniae* and *Staphylococcus aureus*.

2. EXPERIMENTAL METHODS

2.1. Preparation of Silver Nanoparticles

A silver metal plate (high-purity of 99.99%) disc-shaped with dimensions 2 cm in diameter and 2 mm thick, Ag target were cleaned with acetone for 5 min before ablation in order to remove the oxide layer that was formed due to exposure to air and was placed at the bottom of the beaker is filled with 5 ml of deionized water (DIW). The distance between the target and the laser source is of 10 cm. Under mechanical stirring, the target was irradiated with the focused output of fundamental wavelength 1064 nm of nanosecond pulsed Q-switched Nd:YAG laser with the pulse repetition rate and pulse duration of the laser were 7 Hz and 10 ns, respectively, with operated at two different laser fluences of 6.36 J/cm^2 and 12.73 J/cm^2 , and the number of pulses was 300 and 500 pulses for each energy. The experimental setup for laser ablation is illustrated in Fig. 1.

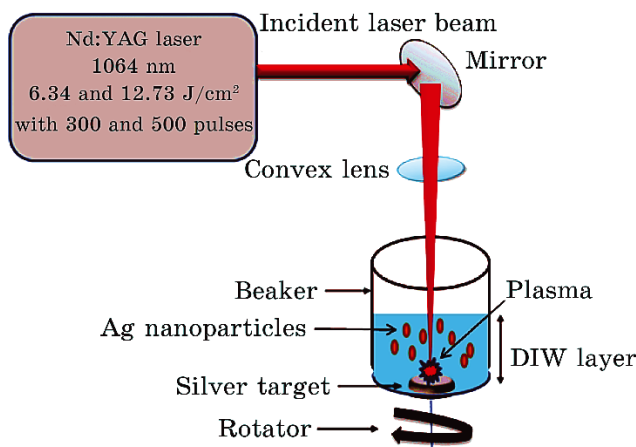


Fig. 1. PLAL system schematic diagram.

2.2. Agar Well Diffusion Method and Antibacterial Activity of Ag NPs

Mueller Hinton agar of 37 g was dissolved in 1 liter of distilled water to form a medium. A sterilization tool known as a syringe (autoclave) was used to sterilize the medium, and the pH was adjusted to 7.2. After that, it is transferred to disposable Petri dishes and put into the refrigerator at 4°C until it is needed. The disposable Petri dishes are placed on a flat surface and poured into them to a depth of about 4 mm. With 500 pulses of samples, the antibacterial activity of laser fluence of 6.36 J/cm² and 12.73 J/cm² of Ag NPs was assessed against two bacterial strains, *Klebsiella pneumoniae* (gram-negative) and *Staphylococcus aureus* (gram-positive). In this method, the bacteria were thoroughly wiped on the media of the plates using sterile cotton swabs. Then, 150 µl of a solution containing silver NPs was added to the spot that had been prepared for each kind of bacteria. The test organism and Ag NPs were then added to the plates, which were then incubated at 37°C for 24 hours. By observing the inhibition zone and the surface transformation into a transparent layer after incubation, which indicated the inhibition of bacterial growth, it was possible to determine the effect of Ag NPs on the growth of bacteria.

3. RESULTS AND DISCUSSION

3.1. The Optical Absorption Analysis

The spectroscopic absorption of a synthesized colloidal solution of Ag NPs in deionized water was examined using a Shimadzu (UV-1800) UV-Vis spectrophotometer. As shown in Fig. 2, the observed

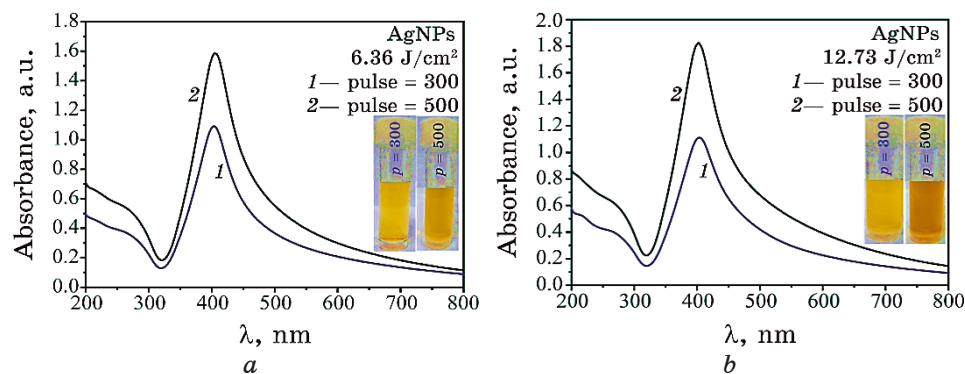


Fig. 2. Absorption spectra of Ag NPs in DIW prepared by PLAL at (a) 6.36 J/cm² and (b) 12.73 J/cm² at various numbers of pulses: 300 and 500.

increase in absorption shows that the absorption spectra of silver NPs exhibit absorbance as a function of wavelength. The increase in absorption, as both the number of pulses and the laser fluence increase, indicates an increase in concentration. The colour change of the solution and the appearance of the surface plasmonic resonance peak are considered evidence for the formation of Ag nanoparticles. The elevation has been found to have higher light absorption at ≈ 400 nm, which returns to the SPRP, indicating the formation of spherical particles. Furthermore, on the higher wavelength side, which includes the visible spectrum and wavelengths up to 500 nm, the NPs have a low absorption value (high transmission). It is also shown in the figure that the spectrum of laser fluence is of 12.73 J/cm^2 , which is more than 6.36 J/cm^2 , that indicates an increase in concentration and possibly size nanoparticles as well.

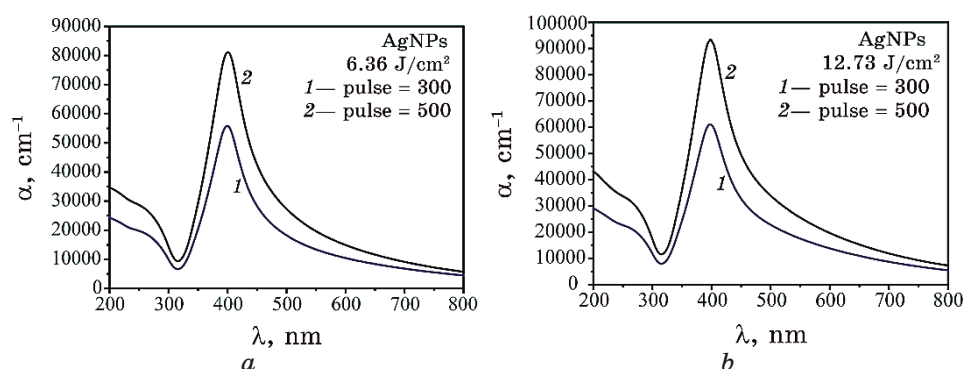


Fig. 3. Absorption coefficient of Ag NPs as a function of wavelength prepared by PLAL at (a) 6.36 J/cm^2 and (b) 12.73 J/cm^2 .

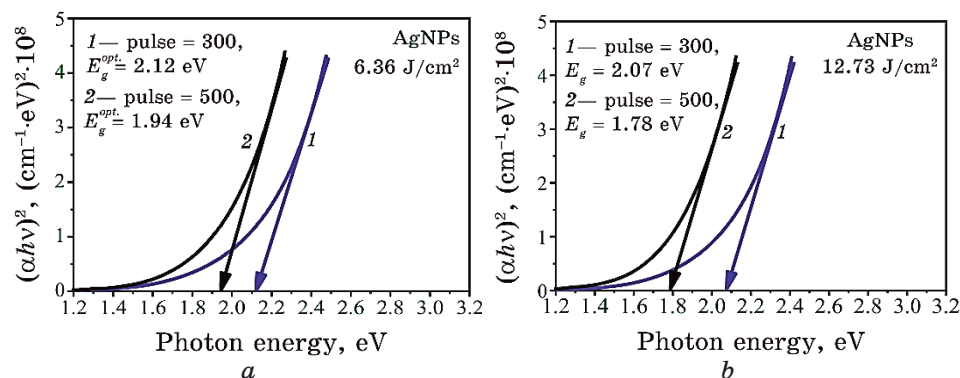


Fig. 4. Optical band gap of the silver NPs prepared at (a) 6.36 J/cm^2 and (b) 12.73 J/cm^2 .

The incident photon energy, as well as the properties of the material itself, has an impact on a materials' absorption coefficient. According to Beer's law, the transmission (T) and reflection (R) spectra are related to the absorption coefficient [21]:

$$\alpha = \frac{1}{d} \log \left[\frac{(1-R)^2}{2T} + \frac{(1-R)^2}{\sqrt{2T^2 + R^2}} \right], \quad (1)$$

where d is the thickness of the sample. The absorption coefficient (α) at the wavelength of maximum absorption increases with the number of pulses and laser fluence, due to the concentration of silver NPs increased as shown in Fig. 3.

An important factor affecting materials' optical and electronic properties is the optical band gap $E_g^{opt.}$. The optical band gap of the silver NPs was determined using the Tauc plot and UV-Vis spectroscopy. The samples' $E_g^{opt.}$ was calculated by fitting the equation to the data [22]:

$$(\alpha h\nu)^{1/2} = k(h\nu - E_g^{opt.}), \quad (2)$$

where k is a constant of effective mass, $h\nu$ is the energy of the incident photons.

Figure 4 shows that as the number of pulses increases, the optical band gap experiences a slight decrease. The quantum confinement effect is responsible for this reduction. Additionally, the high laser fluence can also have this effect. The laser fluence can heat up the target more, removing more NPs and making it larger, and the optical energy gap narrowing as a result.

3.2. Particle Size and Morphology Analysis

3.2.1. Transmission Electron Microscopy Analysis

Transmission electron microscopy (TEM) analysis was used to confirm the average particle size and morphology of silver NPs prepared by the PLAL technique at laser fluences of 6.36 J/cm² and 12.73 J/cm² with 500 pulses.

The TEM image in Fig. 5 shows that NPs have morphology, which is almost spherical. Ag NP diameters are between 37 and 51 nm for 6.36 J/cm² and 12.73 J/cm². On the other hand, because metal nanoparticles tend to agglomerate, the agglomeration of nanoparticles can be attributed to the absence of antiagglomeration agents in the colloidal aqueous solution.

It is shown by TEM image analysis that, with increasing of laser fluence, the concentration and size of silver nanoparticles increase.

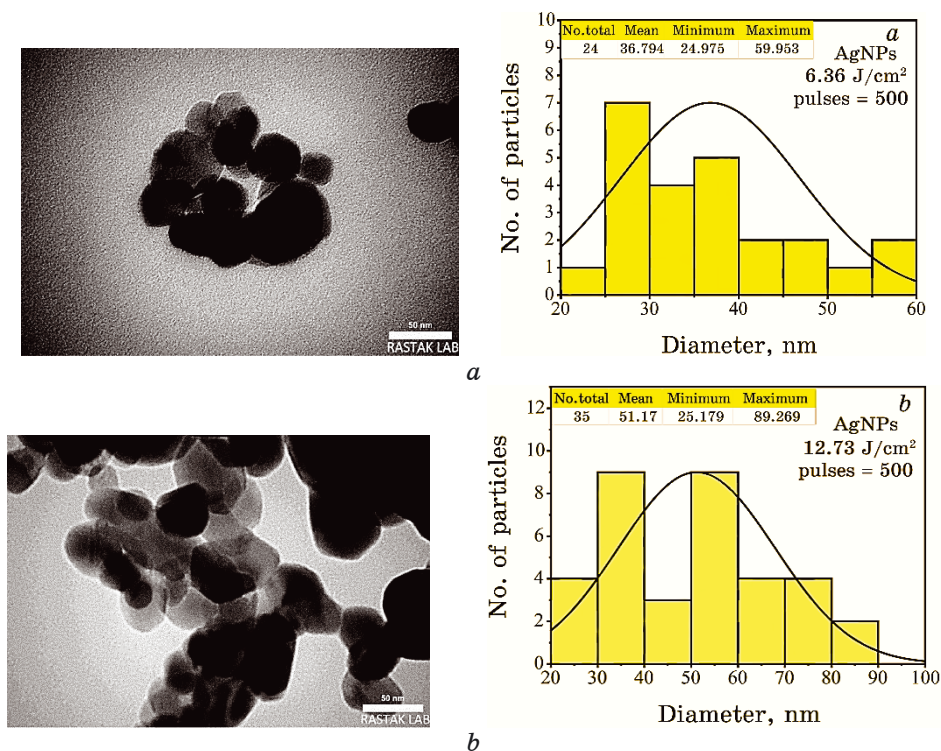


Fig. 5. TEM image of Ag NPs and the particle-size distribution: (a) 6.36 J/cm², (b) 12.73 J/cm² at the same number 500 pulses.

3.2.2. Field-Emission Scanning Electron Microscopy Analysis

Utilizing the field-emission scanning electron microscopy (FE-SEM) analysis at a 200 k \times magnification, it is possible to analyze the morphology and particle-size distribution of Ag NPs at 6.36 J/cm² and 12.73 J/cm² with 500 pulses. In Figure 6, the FE-SEM image and distribution histograms show information for Ag nanoparticles with a size range from 31 nm to 63 nm. The spherical shape and uniform distribution of the nanoparticles are obvious. UV-Vis and TEM measurements support these findings.

3.2.3. Antibacterial Activity of Ag NPs

The inhibitory activity of silver nanoparticles was examined against two bacterial strains: *Klebsiella pneumoniae* and *Staphylococcus aureus*. Using the etch diffusion method on the surface of the agar to determine the effect of the prepared nanoparticles with two laser

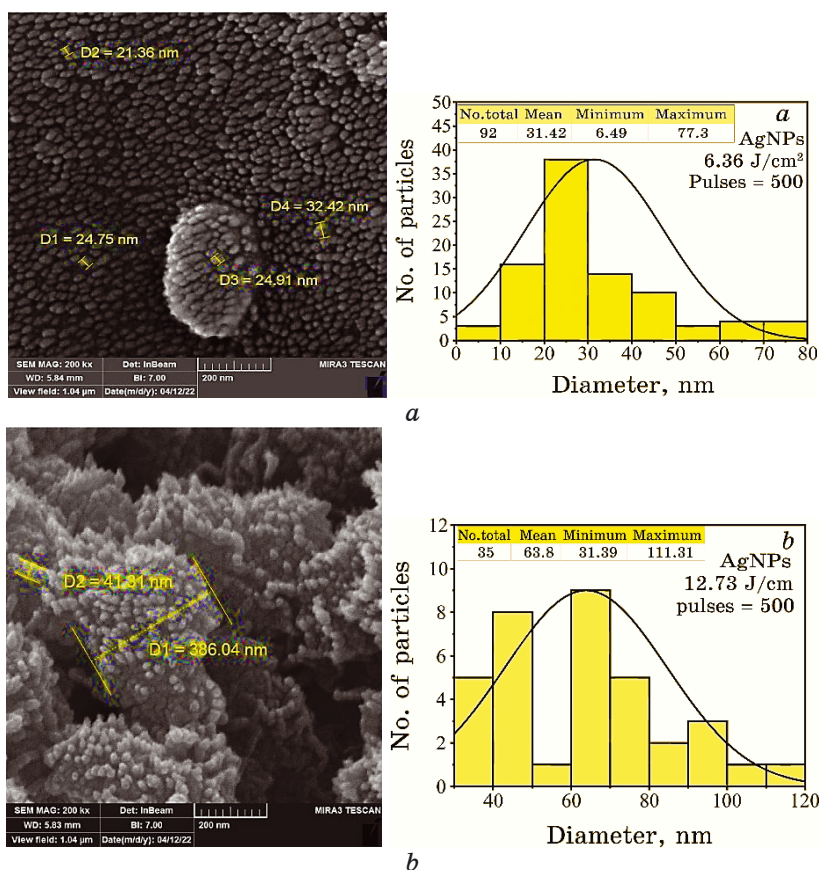


Fig. 6. FE-SEM micrographs of Gaps and the particle size distribution for (a) 6.36 J/cm² (b) 12.73 J/cm² at 500 pulses.

fluences of 6.36 J/cm² and 12.73 J/cm² with 500 pulses. The control medium as a negative control (the solution used in the experiment (DIW)) does not show a growth-inhibiting effect on bacterial strains. Additionally, silver ions released from the nanoparticles can also cause damage to bacterial DNA and interfere with cellular processes. On the other hand, due to particle size, our study reveals that silver NPs exhibit varying degrees of antibacterial activity; it was found through our study that the inhibitory effect of the silver nanoparticles is greater for the particles prepared at 6.36 J/cm², more effective compared to the nanoparticles prepared at 12.73 J/cm² and with the same number of pulses as shown in Fig. 7 and Fig. 8.

The ability of nanoparticles to interact with cell walls or even pass through them and directly change intracellular components de-

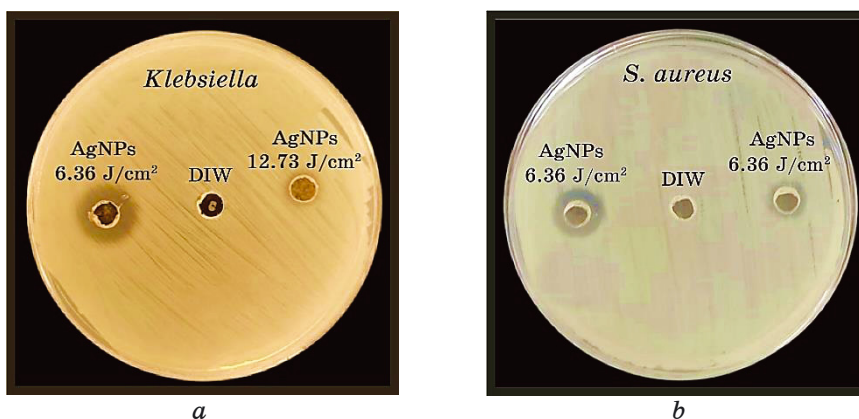


Fig. 7. The antibacterial activity test results for Ag NPs prepared for laser fluences of 6.36 J/cm² and 12.73 J/cm² at a number of 500 pulses for: (a) *Klebsiella G(+v_e)*, (b) *S. aureus G(-v_e)*.

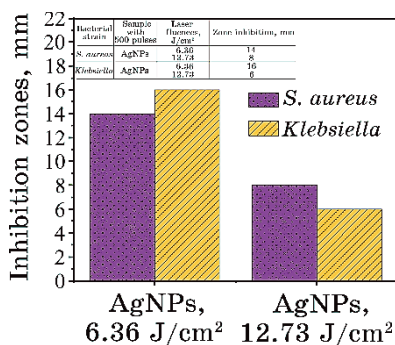


Fig. 8. Histogram for the inhibition zone as a function of the sample prepared for laser fluences of 6.36 J/cm² and 12.73 J/cm².

depends largely on their physical and chemical properties, such as concentration and type of substance. This also allows them to have an inhibitory effect on pathogenic bacteria. Due to the low concentration of nanoparticles prepared using PLAL technique compared to other techniques, it is observed that there is weak diffusion of NPs, which produces a rather weak inhibition zone.

4. CONCLUSION

Pulsed-laser ablation of a silver target immersed in deionized water is used to synthesize noble metal nanoparticles. The result shows that the ablation rate increased as the number of pulses increased and the

laser fluence increased. The absorption spectra show a sharp and single peak at around 400 nm, which produces a stronger plasmon resonance. TEM and FE-SEM images indicate a change in the size of Ag nanoparticles with increasing laser fluence, and the surface morphology is predominantly spherical. Furthermore, the findings of our study indicate that Ag nanoparticles have an antibacterial effect against both *Klebsiella pneumoniae* and *Staphylococcus aureus*, especially at low laser fluences.

ACKNOWLEDGEMENTS

The authors would like to express their warmest thanks to University of Mosul, College of Education for Pure Science and Department of Physics for supporting this work.

REFERENCES

1. J. S. Golightly and A. W. Castleman, *The Journal of Physical Chemistry B*, **110**, Iss. 40: 19979 (2006); <https://doi.org/10.1021/jp062123x>
2. K. S. Khashan and M. H. Mohsin, *Surface Review and Letters*, **22**, Iss. 4: 1550055 (2015); <https://doi.org/10.1142/S0218625X15500559>
3. A. Hamad, K. S. Khashan, and A. Hadi, *Journal of Inorganic and Organometallic Polymers and Materials*, **30**, Iss. 12: 4811 (2020); <https://doi.org/10.1007/s10904-020-01744-x>
4. R. P. Allaker, *Journal of Dental Research*, **89**, Iss. 11: 1175 (2010); <https://doi.org/10.1177/0022034510377794>
5. H. Naser, M. A. Alghoul, M. K. Hossain, N. Asim, M. F. Abdullah, M. S. Ali, F. G. Alzubi, and N. Amin, *Journal of Nanoparticle Research*, **21**, Iss. 249: 1 (2019); <https://doi.org/10.1007/s11051-019-4690-3>
6. S. Stroj, W. Plank, and M. Muendlein, *Applied Physics A*, **127**, Iss. 1: 7 (2021); <https://doi.org/10.1007/s00339-020-04192-z>
7. S. Z. Mat Isa, R. Zainon, and M. Tamal, *Materials*, **15**, Iss. 3: 875 (2022); <https://doi.org/10.3390/ma15030875>
8. E. Fazio, A. Scala, S. Grimato, A. Ridolfo, G. Grassi, and F. Neri, *Journal of Materials Chemistry B*, **3**, Iss. 46: 9023 (2015); <https://doi.org/10.1039/C5TB01076D>
9. D. Riabinina, M. Chaker, and J. Margot, *Nanotechnology*, **23**, Iss. 13: 135603 (2012); <https://doi.org/10.1088/0957-4484/23/13/135603>
10. M. Mahdieha and B. Fattahi, *Applied Surface Science*, **329**, Iss. 1: 47 (2015); <https://doi.org/10.1016/j.apsusc.2014.12.069>
11. G. Guillén, V. Ibarra, I. Palma, B. Krishnan, D. Avellaneda, and S. Shaji, *Chem. Phys. Chem.*, **18**, Iss. 9: 1035 (2017); <https://doi.org/10.1002/cphc.201601056>
12. J. Long, M. H. Eliceiri, L. Wang, Z. Vangelatos, Y. Ouyang, X. Xie, Y. Zhang, and C. P. Grigoropoulos, *Optics & Laser Technology*, **134**: 106647 (2021); <https://doi.org/10.1016/j.optlastec.2020.106647>
13. J. S. Kim, E. Kuk, K. N. Yu, J. H. Kim, S. J. Park, H. J. Lee, S. H. Kim,

- Y. K. Park, Y. H. Park, C. Y. Hwang, and Y. K. Kim, *Biology and Medicine*, **3**, Iss. 1: 95 (2007); <https://doi.org/10.1016/j.nano.2006.12.001>
14. J. R. Morones, J. L. Elechiguerra, A. Camacho, K. Holt, J. B. Kouri, J. T. Ramirez, and M. J. Yacaman, *Nanotechnology*, **16**, Iss. 10: 2346 (2005); <https://doi.org/10.1088/0957-4484/16/10/059>
 15. S. Nie and S. R. Emory, *Science*, **275**, Iss. 5303: 1102 (1997); <https://doi.org/10.1126/science.275.5303.1102>
 16. Y. Yibin, C. Yuhua, L. Yongtao, S. Yi, and A. Xiaohui, *Transboundary and Emerging Diseases*, **68**, Iss. 4: 2051 (2021); <https://doi.org/10.1111/tbed.13852>
 17. K. Sathyavathy and B. K. Madhusudhan, *Journal of Pharmaceutical Research International*, **32**, Iss. 21: 12 (2020); <https://doi.org/10.9734/jpri/2020/v32i2130745>
 18. A. Tigabu and A. Getaneh, *Clinical Laboratory*, **67**, Iss. 7: 1539 (2021); <https://doi.org/10.7754/Clin.Lab.2020.200930>
 19. G. A. Nai, D. A. L. Medina, C. A. T. Martelli, M. S. C. de Oliveira, I. D. Caldeira, B. C., Henriques, M. J. S. Portelinha, M. de Carvalho Almeida, L. K. W. Eller, F. V. de Oliveira Neto, and M. E. A. Marques, *Research, Society and Development*, **10**, Iss. 5: e15310514701 (2021); <http://dx.doi.org/10.33448/rsd-v10i5.14701>
 20. M. Mikłasińska-Majdanik, *Antibiotics*, **10**, Iss. 11: 1406 (2021); <https://doi.org/10.3390/antibiotics10111406>
 21. I. Saini, J. Rozra, N. Chandak, S. Aggarwal, K. Sharma, and A. Sharma, *Materials Chemistry and Physics*, **139**, Iss. 2–3: 802 (2013); <http://dx.doi.org/10.1016/j.matchemphys.2013.02.035>
 22. J. Tauc, R. Grigorvici, and A. Vancu, *physica status solidi (b)*, **15**, Iss. 2: 627 (1966); <https://doi.org/10.1002/pssb.19660150224>

PACS numbers: 78.67.-n, 81.07.Pr, 82.35.Np, 83.60.Np, 87.19.xb, 87.64.M-, 87.85.Rs

Fabrication of SiC–SrTiO₃-Nanoparticles-Doped PMMA/PEO Blend for Antibacterial and Radiation Shielding Fields

Hiba Kamil Jaafar, Ahmed Hashim, and Bahaa H. Rabee

*College of Education for Pure Sciences,
Department of Physics,
University of Babylon,
Hillah, Iraq*

This paper focuses on fabrication of new PMMA–PEO/SiC–SrTiO₃ nanostructures for the antibacterial and gamma-shielding actions with lightweight, flexibility and moderate price. The results of gamma-radiation shielding for PMMA–PEO/SiC–SrTiO₃ nanostructures show that the attenuation coefficient is enhanced by increasing the SiC–SrTiO₃-nanoparticles' content. The PMMA–PEO/SiC–SrTiO₃ nanostructures are tested for antibacterial application. The results demonstrate that the PMMA–PEO/SiC–SrTiO₃ nanostructures have good activity for antibacterial action. Therefore, new PMMA–PEO/SiC–SrTiO₃ nanostructures may be useful for the antibacterial and gamma-shielding applications.

Ця стаття стосується виготовлення нових наноструктур поліметилметакрилат–поліоксietiлен (ПММА–ПОЕ)/SiC–SrTiO₃ для протимікробної дії та захисту від гамма-випромінення з легкою вагою, гнучкістю та доступною ціною. Результати екранування гамма-випромінення для наноструктур ПММА–ПОЕ/SiC–SrTiO₃ показали, що коефіцієнт ослаблення підвищується за рахунок збільшення вмісту наночастинок SiC–SrTiO₃. Наноструктури ПММА–ПОЕ/SiC–SrTiO₃ було протестовано на протимікробне застосування. Результати показали, що наноструктури ПММА–ПОЕ/SiC–SrTiO₃ мають хорошу протимікробну дію. Таким чином, нові наноструктури ПММА–ПОЕ/SiC–SrTiO₃ можуть бути корисними для протимікробних і гамма-екранувальних застосувань.

Key words: SiC, SrTiO₃, PMMA–PEO, attenuation coefficient, antibacterial application.

Ключові слова: SiC, SrTiO₃, поліметилметакрилат–поліоксietiлен, коефіцієнт ослаблення, протимікробне застосування.

(Received 15 July, 2023)

1. INTRODUCTION

Radiant energy particles, such as alpha, beta, neutron particles, and electromagnetic wave emissions, are produced in a multitude of sectors as by-products including nuclear power plants, the medical devices, and space exploration [1–3]. Ionising radiation, including x-rays and γ -rays, is one of the most dangerous factors that could harm people's health. This behaviour is a result of ionising radiation's strong ability to penetrate human tissues and disrupt biological molecules that make up the human genome, such DNA [4]. From this point of view, the quality of the shielding material is viewed as the key to safeguarding against these dangerous radiations [5]. The idea behind shielding materials is based on how ionising radiation interacts with the electron density of the materials [6].

There are several different ways that gamma radiation interacts with shielding materials, including the photoelectric effect, Compton scattering, and pair creation. Each of these interactions depends on both the incident photon energy and the atomic number of the shielding materials [7]. Multiple factors, such as γ -rays' photon energy, density, and atomic weight of the shielding material, determine how shielding material attenuates γ -rays [8]. Generally, materials own both huge atomic number and density with a great stopping power providing high attenuation efficiency [9, 10]. Lead-free shielding materials offer a suitable, affordable, and eco-friendly replacement for traditional lead shielding and lead composite materials [11, 12]. Poly(methyl methacrylate) (PMMA), also referred to as 'acrylic', has superior optical clarity, strong abrasion resistance, hardness, and stiffness. Though it has lower mechanical strength and gamma ray shielding capacity than other metal shielding materials, it can be used with high- Z elements to enhance the mechanical and shielding capacity [13]. Additionally, PMMA is inexpensive, simple to work with it, and biocompatible, which accounts for its widespread use in dentistry [14]. Polyethylene oxide (PEO) is a semi-crystalline and linear polymer. Because polyethylene oxide is a linear polymer, a high degree of crystallinity is permitted by the regularity of the structural device. The cations of the metal salts can interact and form bonds with the polar group O in the chemical structure of PEO [15].

Due to its excellent mechanical, electrical, and thermal properties, such as fracture strength, large elastic modulus, stiffness and toughness, chemical stability, relatively low density and perfect thermal conductivity, as well as low thermal-expansion coefficient and high resistivity, silicon carbide (SiC) is one of the attractive filter ceramics for elevated temperature structural components [16].

There many studies on silicon and silicon carbide doped polymers to employ in various fields like optical, electronics, photonics and dielectric applications [17–23]. This work focuses on synthesis of new PMMA–PEO/SiC–SrTiO₃ nanostructures for antibacterial and gamma-shielding applications.

2. MATERIALS AND METHODS

The PMMA/PEO/SiC/SrTiO₃ nanostructures films were prepared using casting technique. The PMMA (75%) and PEO (25%) were dissolved 40 ml of chloroform with a magnetic stirrer for 1 hour to get a more uniform solution. The SiC/SrTiO₃ nanoparticles (NPs) with various weight percentages of 1.6, 3.2, 4.8, and 6.4 added to the PMMA/PEO solution. The distribution of SiC/SrTiO₃ NPs inside the PMMA/PEO blend was explored by optical microscope (OM) Nanostructured PMMA/PEO/SiC/SrTiO₃ are examined as antibacterial for gram-positive (*Staphylococcus aureus*) and gram-negative (*E. coli*) bacteria by using a disc diffusion method. The gamma-ray attenuation properties for various percentages of SiC/SrTiO₃ NPs have been examined. The samples were putted in front of a collimated beam hail from gamma-ray sources (Cs-137).

3. RESULTS AND DISCUSSION

Figure 1 displays the distribution of SiC–SrTiO₃ NPs *via* the PMMA/PEO matrix with various contents of SiC–SrTiO₃ NPs. At low concentration, the SiC–SrTiO₃ NPs are diffusing as a cluster. When the SiC–SrTiO₃ NPs percentages raise, the nanoparticles form paths connect inside the polymeric matrix [24–31].

Figures 2 and 3 show the antibacterial activity of the PMMA–PEO/SiC–SrTiO₃ nanostructures' films, which are tested against gram-negative (*Escherichia coli*) and gram-positive (*Staphylococcus*) bacteria. From these figures, the inhibition enhances with the increasing ratio of SiC–SrTiO₃ NPs. Reactive oxygen species (ROS), which are produced at various ratio of SiC–SrTiO₃ NPs, may be the cause of the antibacterial activity of PMMA–PEO/SiC–SrTiO₃ nanostructures.

At low ratio of nanoparticles, the interactions of particles with the cell wall of bacteria diminish, whereas the accumulation probability of particles rises at high percentage of particles. As a result, the effective surface to volume ratio of particles increases, and the resulting interaction between particles and the cell wall of bacteria reduces. It is notably from the result that the antibacterial activity of the samples was stronger against gram-negative bacteria (*Esche-*

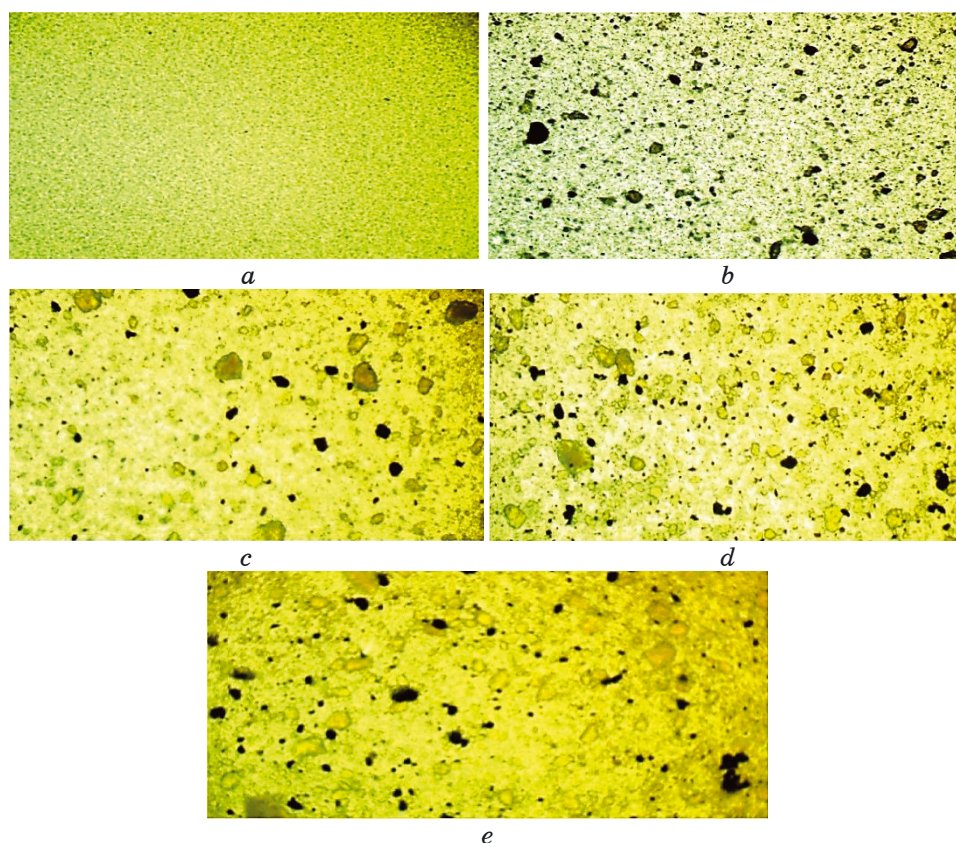


Fig. 1. Optical microscope images ($\times 10$) for PMMA-PEO-SiC-SrTiO₃ nanostructures: (a) pure; (b) 1.6 wt.% SiC-SrTiO₃ NPs; (c) 3.2 wt.% SiC-SrTiO₃ NPs; (d) 4.8 wt.% SiC-SrTiO₃ NPs; (e) 6.4 wt.% SiC-SrTiO₃ NPs.

richia coli) than gram-positive bacteria (*Staphylococcus*) on nanoparticles. This is because the gram-positive bacteria possess a thick cell wall contains several peptidoglycan layers. On the other hand, gram-negative bacteria own a comparatively thin cell wall formed up some layers of peptidoglycan [32–41].

Figure 4 depicts the change of ratio (N/N_0) for PMMA/PEO with varied concentrations of SiC-SrTiO₃ NPs. The transmission radiation reduced with a rise in the SiC-SrTiO₃-nanoparticles' loading. This takes place as a result of a rise in attenuation radiation.

Figure 5 shows the behaviour of attenuation coefficient for PMMA-PEO blend with different ratios of SiC-SrTiO₃ NPs. The attenuation coefficients rise as the ratio of nanoparticles rises because nanostructures' shielding materials either absorb or reflect gamma-radiation [42–45].

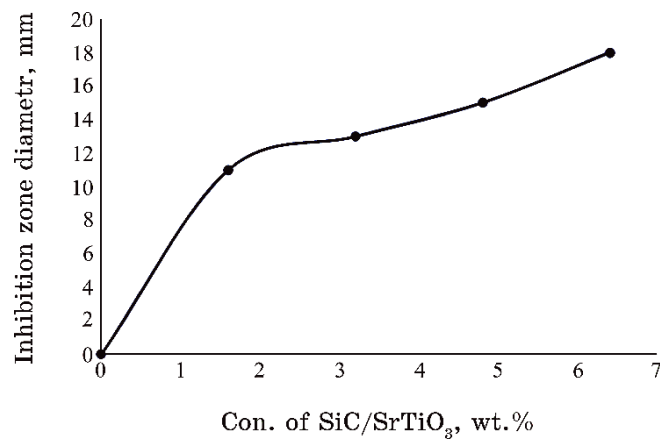


Fig. 2. Inhibition zone diameter of PMMA/PEO/SiC/SrTiO₃ nanostructures against *Escherichia coli*.

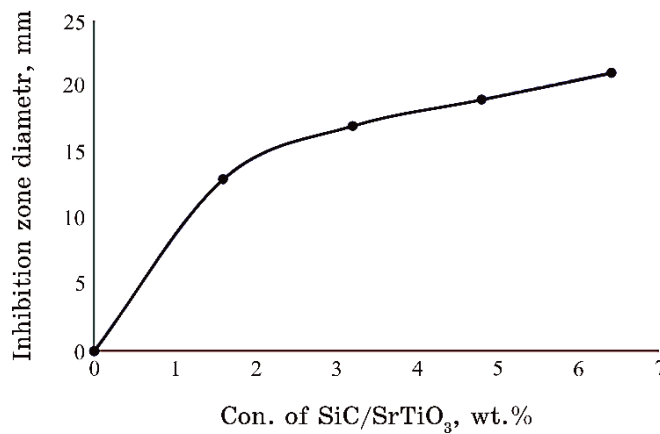


Fig. 3. Inhibition zone diameter of PMMA/PEO/SiC/SrTiO₃ nanostructures against *Staphylococcus* bacterium.

4. CONCLUSION

This article involves fabrication of PMMA–PEO/SiC–SrTiO₃ nanostructures with lightweight and flexible, which have good gamma-ray attenuation coefficients and high antibacterial activity. The results of gamma-radiation shielding for PMMA–PEO/SiC–SrTiO₃ nanostructures showed that the attenuation coefficient is enhanced by increasing the SiC–SrTiO₃-NPs' content. The PMMA–PEO/SiC–SrTiO₃ nanostructures were tested for antibacterial application. The results demonstrated the PMMA–PEO/SiC–SrTiO₃ nanostructures have good antibacterial activity. Therefore, new

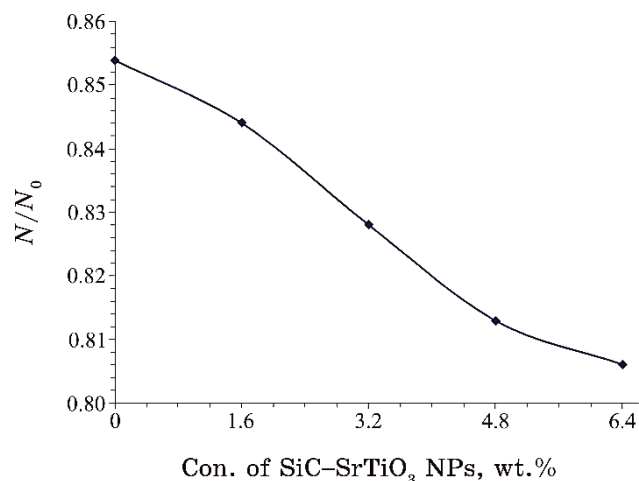


Fig. 4. Variance of (N/N_0) for PMMA/PEO with different concentrations of SiC-SrTiO₃ NPs.

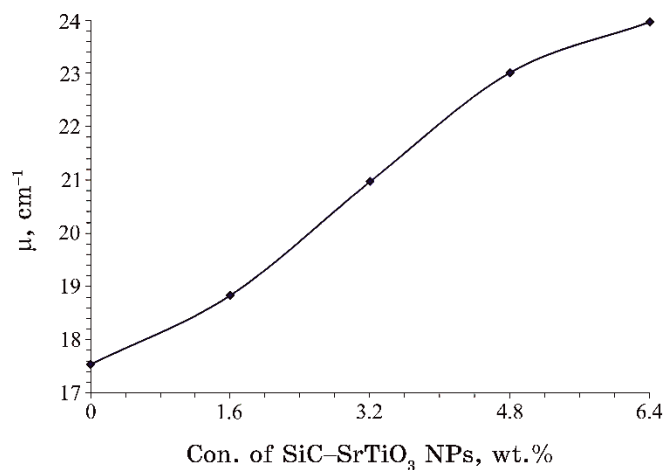


Fig. 5. Variance of attenuation coefficients of gamma-radiation for PMMA/PEO blends with different concentrations of SiC-SrTiO₃ NPs.

PMMA-PEO/SiC-SrTiO₃ nanostructures may be useful in antibacterial and gamma-shielding applications.

REFERENCES

1. N. A. Kawady, M. Elkattan, M. Salah, and A. A. Galhoum, *Journal of Materials Science*, **57**, No. 24: 11046 (2022); doi:10.1007/s10853-022-07213-9
2. P. J. Bora, A. G. Anil, P. C. Ramamurthy, and D. Q. Tan, *Materials Advances*, **1**,

- No. 2: 177 (2020); doi:10.1039/D0MA00005A
3. S. Nambiar and J. T. W. Yeow, *ACS Applied Materials & Interfaces*, **4**, No. 11: 5717 (2012); doi:10.1021/am300783d
 4. M. A. Kiani, S. J. Ahmadi, M. Outokesh, R. Adeli, and H. Kiani, *Applied Radiation and Isotopes*, **143**: 141 (2019);
<https://doi.org/10.1016/j.apradiso.2018.10.006>
 5. O. Baykara, Ş. G. İrim, A. A. Wis, M. A. Keskin, G. Ozkoc, A. Avcı, and M. Doğru, *Polymers for Advanced Technologies*, **31**, No. 11: 2466 (2020);
<https://doi.org/10.1002/pat.4962>
 6. R. Li, Y. Gu, G. Zhang, Z. Yang, M. Li, and Z. Zhang, *Composites Science and Technology*, **143**: 67 (2017);
<https://doi.org/10.1016/j.compscitech.2017.03.002>
 7. Z. Xu, K. Glass, C. Lau, N. Geard, P. Graves, and A. Clements, *Scientific Reports*, **6**: 1 (2016); <https://doi.org/10.1038/srep27721>
 8. I. Akkurt, B. Mavi, A. Akkurt, C. Basyigit, S. Kilincarslan, and H. A. Yalim, *J. of Quant. Spectr. and Radiative Transfer*, **94**, No. 3: 379 (2005);
<https://doi.org/10.1016/j.jqsrt.2004.09.024>
 9. Salah Ud-Din Khan, Shahab Ud-Din Khan, Z. Almutairi, S. Haider, and S. M. Ali, *J. of Radiation Res. and Applied Sciences*, **13**, No. 1: 606 (2020);
<https://doi.org/10.1080/16878507.2020.1812798>
 10. A. Saim, A. Tebboune, H. Berkok, N. Belameiri, and A. H. Belbachir, *Journal of Alloys and Compounds*, **602**: 261 (2014);
<https://doi.org/10.1016/j.jallcom.2014.03.012>
 11. O. F. Er, A. Caglar, B. Ulas, H. Kivrak, and A. Kivrak, *Materials Chemistry and Physics*, **241**: 1 (2020); <https://doi.org/10.1016/j.matchemphys.2019.122422>
 12. R. Mirji and B. Lobo, *Radiation Physics and Chemistry*, **135**: 32 (2017);
<https://doi.org/10.1016/j.radphyschem.2017.03.001>
 13. T. Bel, C. Arslan, and N. Baydogan, *Materials Chemistry and Physics*, **221**: 58 (2019); <https://doi.org/10.1016/j.matchemphys.2018.09.014>
 14. S. M. Pituru, M. Greabu, A. Totan, M. Imre, M. Pantea, T. Spinu, A. M. C. Tancu, N. O. Popoviciu, I.-I. Stanescu, and E. Ionescu, *Materials*, **13**, No. 13: 2894 (2020).
 15. B.-R. Choi, S.-J. Park, and S. Kim, *Journal of Industrial and Engineering Chemistry*, **31**: 352 (2015); <https://doi.org/10.1016/j.jiec.2015.07.009>
 16. Z. Li, W. Zhou, X. Su, F. Luo, D. Zhu, and P. Liu, *Journal of the American Ceramic Society*, **91**, No. 8: 2607 (2008).
 17. N. Al-Huda Al-Aaraji, A. Hashim, A. Hadi, and H. M. Abduljalil, *Silicon*, **14**: 10037 (2022); <https://doi.org/10.1007/s12633-022-01730-7>
 18. H. Ahmed and A. Hashim, *International Journal of Scientific & Technology Research*, **8**, Iss. 11: 1014 (2019).
 19. H. Ahmed and A. Hashim, *Silicon*, **14**: 6637 (2022);
<https://doi.org/10.1007/s12633-021-01449-x>
 20. N. Al-Huda Al-Aaraji, A. Hashim, A. Hadi, and H. M. Abduljalil, *Silicon*, **14**: 4699 (2022); <https://doi.org/10.1007/s12633-021-01265-3>
 21. H. Ahmed and A. Hashim, *Silicon*, **13**: 4331 (2020);
<https://doi.org/10.1007/s12633-020-00723-8>
 22. H. Ahmed and A. Hashim, *Silicon*, **14**: 4907 (2022);
<https://doi.org/10.1007/s12633-021-01258-2>
 23. H. Ahmed and A. Hashim, *Silicon*, **14**: 7025 (2021);
<https://doi.org/10.1007/s12633-021-01465-x>

24. M. H. Meteab, A. Hashim, and B. H. Rabee, *Opt. Quant Electron.*, **55**: 187 (2023); <https://doi.org/10.1007/s11082-022-04447-4>
25. M. H. Meteab, A. Hashim, and B. H. Rabee, *Silicon*, **15**: 1609 (2023); <https://doi.org/10.1007/s12633-022-02114-7>
26. W. O. Obaid and A. Hashim, *Silicon*, **14**: 11199 (2022); <https://doi.org/10.1007/s12633-022-01854-w>
27. O. B. Fadil and A. Hashim, *Silicon*, **14**: 9845 (2022); <https://doi.org/10.1007/s12633-022-01728-1>
28. M. H. Meteab, A. Hashim, and B. H. Rabee, *Silicon*, **15**: 251 (2023); <https://doi.org/10.1007/s12633-022-02020-y>
29. A. Hashim, A. Hadi, and M. H. Abbas, *Opt. Quant. Electron.*, **55**: 642 (2023); <https://doi.org/10.1007/s11082-023-04929-z>
30. A. Hashim, A. Hadi, and M. H. Abbas, *Silicon*, **15**: 6431 (2023); <https://doi.org/10.1007/s12633-023-02529-w>
31. A. F. Kadhim and A. Hashim, *Opt. Quant. Electron.*, **55**: 432 (2023); <https://doi.org/10.1007/s11082-023-04699-8>
32. J. H. Roque-Ruiz, D. Castillo-Ramírez, Á. de Jesús Ruíz-Baltazar, L. F. Espinosa-Cristóbal, and S. Y. Reyes-López, *Journal of Nanomaterials*, **2018**: 7127843 (2018); doi:10.1155/2018/7127843
33. M. A. Awad, W. K. Mekhamer, N. M. Merghani, A. A. Hendi, K. M. O. Ortashi, F. Al-Abbas, and N. E. Eisa, *Journal of Nanomaterials*, **2015**: 943821 (2015); doi:10.1155/2015/943821
34. H. K. Oudah, *Iraqi Journal of Physics*, **16**, No. 39: 124 (2018); <https://doi.org/10.30723/ijp.v16i39.111>
35. W. O. Obaid and A. Hashim, *Nanosistemi, Nanomateriali, Nanotehnologii*, **20**, Iss. 4: 1009 (2022); <https://doi.org/10.15407/nnn.20.04.1009>
36. M. H. Meteab, A. Hashim, and B. H. Rabee, *Nanosistemi, Nanomateriali, Nanotehnologii*, **21**, Iss. 1: 199 (2023); <https://doi.org/10.15407/nnn.21.01.199>
37. M. H. Meteab, A. Hashim, and B. H. Rabee, *Nanosistemi, Nanomateriali, Nanotehnologii*, **21**, Iss. 2: 451 (2023); <https://doi.org/10.15407/nnn.21.02.451>
38. A. Hashim, I. R. Agool, and K. J. Kadhim, *Journal of Bionanoscience*, **12**, No. 5: 608 (2018); doi:10.1166/jbns.2018.1580
39. A. Hazim, A. Hashim, and H. M. Abduljalil, *International Journal of Emerging Trends in Engineering Research*, **7**, No. 8: 68 (2019); <https://doi.org/10.30534/ijeter/2019/01782019>
40. A. Hazim, H. M. Abduljalil, and A. Hashim, *International Journal of Emerging Trends in Engineering Research*, **7**, No. 8: 104 (2019); <https://doi.org/10.30534/ijeter/2019/04782019>
41. O. B. Fadil and A. Hashim, *Nanosistemi, Nanomateriali, Nanotehnologii*, **20**, Iss. 4: 1029 (2022); <https://doi.org/10.15407/nnn.20.04.1029>
42. A. Hashim and Z. S. Hamad, *Journal of Bionanoscience*, **12**, No. 4: 504 (2018); doi:10.1166/jbns.2018.1561
43. B. Abbas and A. Hashim, *International Journal of Emerging Trends in Engineering Research*, **7**, No. 8: 131 (2019); <https://doi.org/10.30534/ijeter/2019/06782019>
44. K. H. H. Al-Attayah, A. Hashim, and S. F. Obaid, *Journal of Bionanoscience*, **12**: 200 (2018); doi:10.1166/jbns.2018.1526
45. A. Hashim and Z. S. Hamad, *Journal of Bionanoscience*, **12**, No. 4: 488 (2018); doi:10.1166/jbns.2018.1551

PACS numbers: 07.07.Df, 07.50.Qx, 85.40.Bh, 85.40.Xx, 85.85.+j, 89.20.Ff, 89.20.Hh

Accident Prevention Using IoT-Based Smart Helmet

P. Vivekanandan, P. Radhika, A. Sivamani, P. Pradeesh, and D. Rakesh

*SNS College of Technology,
Department of Mechatronics Engineering,
Coimbatore, Tamilnadu, India*

Many people die from not wearing helmets. They also die from delayed treatment. Remote accidents are hard for emergency services to detect. Helmets save lives. Early treatment prevents 60% of accident deaths. This scheme will ensure riders wear helmets and call 911, if they crash. Bike accidents are rising as our country's bikers. Many deaths occur due to not wearing helmets and not receiving prompt medical attention. The project protects bikers from traffic accidents. The primary aim of this work is to detect smart helmets and report accidents. The system uses sensors, Wi-Fi processors, and cloud computing. The processor checks accelerometer values from the accident detection system for irregularities. Cloud-based services send emergency contacts accident details. GPS locates vehicles. A smart helmet 'Konnect' guarantees real-time, verified accident information. Thus, a smart helmet for accident detection uses smart city's ubiquitous connectivity.

Багато людей помирає через відсутність шоломів. Вони також гинуть від несвоєчасного лікування. Екстреним службам важко виявити віддалені аварії. Шоломи рятують життя. Своєчасне лікування запобігає 60% смертельних випадків. Ця схема гарантує, що водії одягнуть шоломи та зателефонують у 911 у разі аварії. Велосипедні аварії зростають із кількістю байкерів нашої країни. Багато смертей трапляються через відсутність шоломів і відсутність швидкої медичної допомоги. Проект захищає байкерів від ДТП. Екстреним службам важко виявити віддалені аварії. Основною метою цієї роботи є виявлення розумних шоломів і повідомлення про аварії. Система використовує датчики, процесори Wi-Fi і хмарні обчислення. Процесор перевіряє значення акселерометра від системи виявлення аварій на наявність порушень. Хмарні служби надсилають екстреним контактам деталі нещасного випадку. GPS визначає місцезнаходження транспортних засобів. Розумний шолом «Konnect» гарантує перевірену інформацію про аварії в реальному часі. Таким чином, розумний шолом для виявлення аварій використовує повсюдне підключення розумного міста.

Key words: smart helmet, IR sensor, vibration sensor, MEMS sensor, temperature sensor, GSM, GPS.

Ключові слова: розумний шолом, інфрачервоний давач, давач вібрації, давач мікроелектромеханічної системи, датчик температури, глобальна система мобільного зв'язку з рухомими об'єктами, глобальна система навігації та визначення положення.

(Received 25 August, 2023)

1. INTRODUCTION

Technology dominates education, product manufacturing, transportation, communication, and health. Transportation has always supported the economy and governance. Youth and the world love motorcycles. Motorcycle safety involves equipment, vehicle design, and operator ability. Motorcyclists are unique. They are the most dangerous road users without protection. Even the smallest mistake can kill. Speeding, drunk driving, and traffic offenses kill people. Helmetlessness caused brain damage and death. Helmets save 80% of head injuries and lives. IoT prevents traffic accidents [20], modeling motorcycles with sensors, communicating with riders and the environment, and requiring helmets. Road accidents kill 4 people each hour, 70% without helmets, according to a poll. Global statistics show safety rules and new technology are being created to prevent such incidents and ensure rider safety. We encourage 'Safety on Two Wheels' for safe travel [11].

This method aims to build a helmet that protects bikers and prevents drunk driving. If the rider crashes, it alerts the guardian via SMS. Drunk driving causes most accidents in today's fast-paced world. Uncivilized drivers are breaking helmet laws in most nations. Thus, this project aims to get people to wear helmets and ride bikes. The cyclist must not be intoxicated. Drunken riders cannot ride bikes. Another goal is to reduce accident fatalities by notifying passengers' relatives. Advanced features including alcohol detection, accident recognition, location tracking, and hands-free, solar-powered use accomplish this. Helmets are required for ignition.

The IoT is a network of interconnected computers, mechanical and electronic devices, furniture, living things, and people, all of which have individual IDs and are able to exchange data without the need for human interaction. The IoT makes it possible to integrate the physical world more directly into computer-based systems, improving efficiency, accuracy, and economic value while minimizing human involvement. Additionally, it enables the use of existing network infrastructure for remote sensing and control of objects.

IoT was made possible by wireless technologies, MEMS, micro-services, and the internet [21].

The remote monitoring equipment receives data from the working environment through Wi-Fi. Wi-Fi is the latest data transfer technology and spans a broader region. Things peak application collects, stores, and analyses sent data. Things peak is a new IoT app that analyses wireless sensor network data.

2. LITERATURE REVIEW

A. Jesudoos [1] suggested using mems with IR, vibration, and gas sensors. The helmets' gas sensor checks a person's breathe for alcohol consumption. MEMS controls car bars. PIC microcontrollers connect sensors. The gas sensor displays alcohol consumption on the LED display. Vibration sensors detect accidents and relay GPS data to hospitals. The MEME sensor deducts the rider's bank account balance for reckless driving. IR sensors detect helmet wear. This system automatically books ambulances from ten locations and is precise.

K. M. Mehata [2] proposed a method to protect workers or detect workplace falls. The proposed system is two-part. Sensor-equipped wearable devices are one. Cell phones are another component. GSM module connects them. These gadgets continuously monitor worker health and safety. The register person receives medical attention via this fall detection system.

N. Divyasudha [3] presented a system using an IOT modem to prevent accidents and monitor alcohol intake. IOT modems notify police and specified numbers of accidents. This helmet is cheaper than others are. Manish Uniyal [4] proposed a helmet-two-wheeler system. The TW microcontroller continuously checks helmet position. The TW vehicle also has accelerometers, Hall-effect sensors, and GPS modules. If there is an internet connection, sensors provide data to the microcontroller, which then sends it to the server. This technology lets anyone check the vehicle speed anytime. This system shows vehicle speed. Parents may see if their kids wear helmets.

Shoeb Ahmed Shabbeer [5] designed smart helmets to detect and report incidents. This approach uses microcontroller with accelerometer and GSM module. Cloud infrastructures report accidents. This system identified accidents 94.82% of the time and sent correct coordinates 96.72%. P. Rojaet [6] presented a system with six units: remover sensor, IR sensor, air quality sensor, Arduino UNO microcontroller, GPRS, GSM. If removed, this helmet alerts miners to harmful gases and sends information to the server. IOT transmits this info. C. J. Bheret [7] presented a smart mining helmet that detects dangerous gases, helmet removal, and collisions. They use IR, gas, and accelerometer sensors.

Sreenithy Chandran *et al.* [8] proposed a smart helmet called ‘Konnnect’. They detect and prevent accidents using integrated sensor networks, Wi-Fi-enabled processors, and cloud computing infrastructures. If a speed exceeds the threshold, this system texts the contact. Mohammed *et al.* [9] used Arduino UNO, Bluetooth module, push button, and 9 V battery. The Bluetooth-enabled smart helmet connects to cell phones and has an emergency button. D. Archana *et al.* [10] presented a sensor that detects human EAI to reduce accidents. Agung Rahmat Budiman [12] designed a multifunctional smart helmet. If a rider does not wear a helmet, comes in risky conditions, or does not lock his helmet, he is warned.

Sayan Tapadar [13] proposed an IOT module and sensor prototype that identifies rider alcohol consumption and accidents. Real-time simulation is used to train Support Vector Machines to anticipate whether sensor values indicate an accident. This method works well. ***High accuracy and precision.*** Prashant Ahuja *et al.* presented a GSM/GPRS smart helmet [14]. Since ambulances can arrive late, this prototype alerts the concerned party first, so, they can take action. This system is accurate, cost-effective, and provides accident information in minutes.

Mingi Jeong *et al.* [15] suggested a system including thermal cameras, visible light cameras, drone cameras, oxygen sensors, inertia sensors, smartwatches, HMDs, and command centres to prevent accidents. This framework simplifies IOT service integration, management, and real-time notification. M. Kabilan *et al.* [17] suggested employing vibration sensors. If the rider’s helmet vibrator sensor reaches the threshold, this technology detects and reports accidents, saving lives. Vivekananda Reddy *et al.* [18] designed a helmet-bike system. The helmet has IR, alcohol, and LCD sensors to detect intoxication. Vibration sensors in bikes detect accidents and relay data through GSM and GPS.

3. METHODOLOGY

This module has a transmitter circuitry and various sensors. Three sensors are included in a microcontroller: an alcohol sensor, a vibrate sensor, and a temperature, MEMS, and infrared sensor. Alcohol focus has been recognized using an alcohol sensor. The alcohol sensor will be located within the rider’s helmet, near to his or her mouth. The crash location is determined via a vibration sensor. The pulse sensor and UV sensor are two sensors on another microcontroller. The measurement of pulse rate has been done using a pulse sensor. The pulse rate stimulates LED1, causing it to blink white light. To prevent collisions and manage accidents, UV sensors will detect the front moving vehicle.

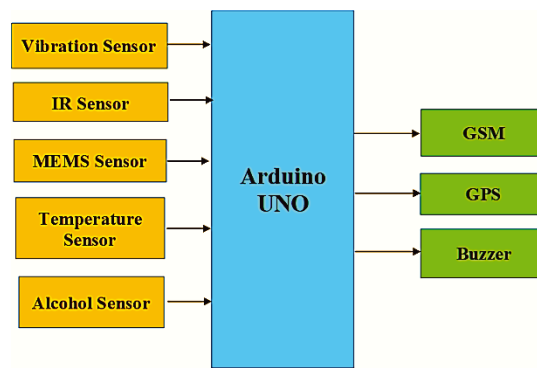


Fig. 1. Block diagram for proposed method.

Utilizing IoT technology to create a smart helmet that will ensure the riders' safety. The car will only start if the rider is wearing a helmet, which the system can detect. The bike engine will not start, if the rider has consumed too much alcohol. When a bike rider has an accident, the bike recognizes it and notifies the contacts that have been registered with a location. We are utilizing the most recent technologies for the bike rider's safety. IoT technology offers cutting-edge methods for warning the rider and ensuring that the rider complies with the law. Helmets are the most fundamental form of protection for two-wheeler riders and are required for all motorbike and bicycle riders. However, it does not guarantee the rider's safety, and the rider will not adhere to the traffic laws. The majority of individuals use regular helmets merely to avoid handing over a ticket to the traffic police; yet, these helmets do not protect the driver. Therefore, we must use the smart helmet to solve these issues. Figure 1 shows the proposed smart helmet.

3.1. Arduino

Microcontroller. A microcontroller is a single-chip computer with a CPU core, memory, and programmable input/output peripherals. A microcontroller has a CPU, memory, and controllable input/output pins—General Purpose Input Output Pins (GPIO). The Arduino Uno board, which is shown in Fig. 2, has a microcontroller and accessories to make building and debugging projects easier—ATmega328P-based microcontroller board Uno [16].

3.2. Temperature Sensor — LM35

The temperature sensors in the LM35 family are accurate integrat-



Fig. 4. MEMS sensor.

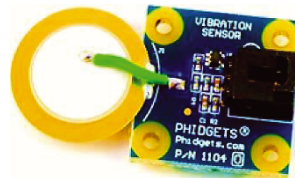


Fig. 5. Vibration sensor.

neath. It is crucial to establish the vibration level that will cause a vibration sensor to activate in the event of a debris flow before installing one. Additionally, it is crucial to consider the possibility of accidentally activating the sensor due to earthquakes, as well as locations where there is construction traffic and other potential vibration sources. Figure 5 illustrates vibration sensor.

3.5. IR Sensor

Radiation-sensitive optoelectronic elements with spectral sensitivities ranging from 780 nm to 50 m are known as infrared sensors (IR sensors). IR sensors are being used more frequently in motion detectors that activate lights or alarm systems in buildings to detect unwanted visitors. IR sensors create and detect radiation. Active IR sensors have an LED and a receiver. The receiver detects infrared light from the LED reflected off an item as it approaches the sensor. Sensors detect humans privately. PIR sensors detect people. This only detects moving people. The Grid-EYE sensor overcomes the PIR sensor limitation by recognizing a stationary human. These sensors detect objects 100 cm to 500 cm (3–15 feet/1–5 meters). Their long range makes them superb sonar sensors. IR sensor is given in Fig. 6.

3.6. GPS Module

The GPS module L10 boosts the MTK positioning engines' industry-



Fig. 6. IR Sensor.

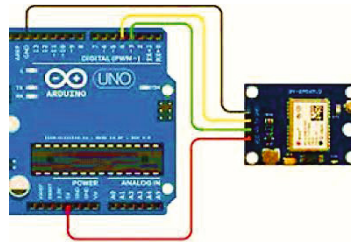


Fig. 7. GPS module.

leading performance. L10 supports 210 PRN channels. It can quickly acquire and track satellites at low indoor signal levels with 66 search channels and 22 concurrent tracking channels. This standalone receiver has several functions and flexible connectivity. Their easy integration speeds up consumer, industrial, and automotive applications. Figure 7 shows GPS module.

GNSS tracks GPS. GPS receivers use microwave signals from numerous satellites to locate, speed, time, and direction. Thus, a GPS tracking system provides historical and real-time navigational data for any journey. Receiver GPS signals. GPS receivers track location, velocity, and time. Four GPS satellites enable three-dimensional positioning. 27 GPS satellites orbit Earth. 24 functioning satellites and 3 backups orbit Earth every 12 hours, transmitting radio signals to the GPS receiver. Positioning System stations are widespread. These stations track GPS signals. Spacecraft send microwave signals. GPS receivers translate satellite signals into location, velocity, and time. Trilateration, a simple mathematical concept, powers the method. 2-D and 3-D trilateration exist. Simple math requires two things for the GPS receiver. It must first realize at least three satellites can pinpoint the spot. It also needs their distances.

GPS-equipped spacecraft. Radio waves travel at light speed. GPS tracking is multifaceted. Businesses track cars via GPS. A modem

in the GPS system unit periodically sends data to a central database or stores it in the GPS tracking system (passive tracking). Passive GPS tracking devices track events. This GPS system can log 12 hours of travel. This GPS tracking technology stores data on a memory card or internal memory for computer processing.

3.7. GSM Modem

Digital cellular communication is standardized by GSM. GSM was founded in 1982 to produce specifications for a pan-European 900 MHz mobile cellular radio system.

GSM standardizes. GSM suggests, not commands. GSM specifications provide functionality and interface, but not hardware. The idea is to limit designers as little as possible while letting operators buy equipment from multiple suppliers.

GSM modems use GSM network, which is given in Fig. 8. Wireless modems work like dial-up modems. Wireless modems use radio waves to deliver and receive data, while dial-up modems use a telephone connection. GSM modems can be external or PC Card/PCMCIA Cards. External GSM modems are connected to computers using serial or USB cables. Laptops can use PC Card or PCMCIA GSM modems. It goes in the laptops' PC Card or PCMCIA Card slot. GSM modems, like GSM phones, need SIM cards from wireless carriers.

3.8. Alcohol Sensor

The MQ3 alcohol sensor detects airborne ethanol. An alcohol sensor monitors the amount of ethanol in an intoxicated person's breath and produces information. Higher alcohol percentages lit more LEDs (500 to 905). Thus, values above 650 indicate alcohol vapour, which degrades the sensor value slowly. MQ3 alcohol sensor is

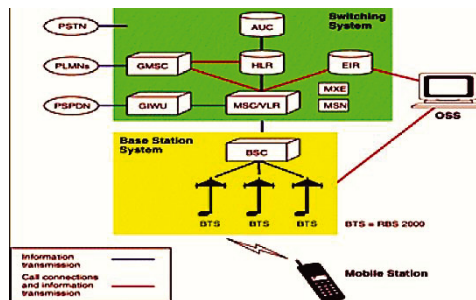


Fig. 8. GSM network elements.



Fig. 9. MQ-3 alcohol sensor.

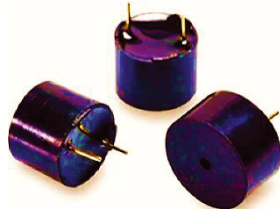


Fig. 10. Buzzer.

shown in Fig. 9.

The alcohol detector project can be installed in many cars to detect intoxication. Breathing analysers can also be used in enterprises to track employee alcohol use. An alcohol sensor infrared cell detects unabsorbed energy on the other side by passing energy through the sample. Like sunglasses, alcohol absorbs infrared light at higher ethanol concentrations.

3.9. Buzzer

Electronic buzzers or beepers are used in autos, microwaves, and game shows in Fig. 10. An electromechanical device resembling an electric bell without the metal gong that produces the ringing sound served as the foundation for the original design. Major industries use piezo buzzers to identify or alert. It can meet the most challenging audio alarm applications.

3.10. Arduino IDE

Arduino IDE is generally used to write and compile code for Arduino Modules. Code compilation is so easy with official Arduino software that even a beginner can learn. Uno, Mega, Leonardo, Micro, and others are Arduino modules. Each has a code-reading mi-

microcontroller on its board.

4. RESULTS AND DISCUSSION

The Internet of Things-based, intelligent helmet-based two-wheeler safety solution is very dependable and secure. The main objective of this system is to prevent injuries when a person wearing this helmet is engaged in an accident. It stops drunk driving from happening. The results are able to pinpoint the accident, and they send a 90% accurate location notification to the registered contacts so they are aware of the person's condition and can offer the necessary medical attention. The findings of a helmet tilt are compared to the threshold value and helmet fall value to determine whether an accident has occurred. The technology detected alcohol in the rider's breath, according to the results; if the rider is too drunk, the bike will not start. The whole operation of this system will be dictated by rider activity.

Figure 11 illustrates the simulation model. Figure 12 shows the proposed smart helmet. Figure 13 depicts the notification message from the smart helmet.

All of the parts have been put together and successfully tested.

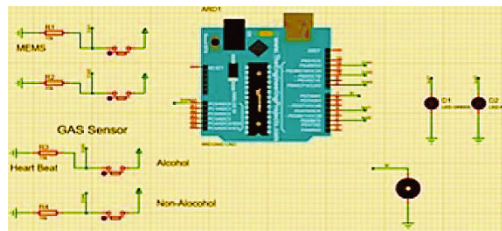


Fig. 11. Modelling and simulation.

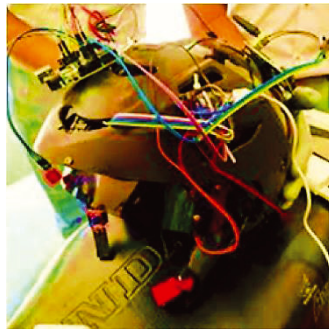


Fig. 12. Proposed smart helmet.

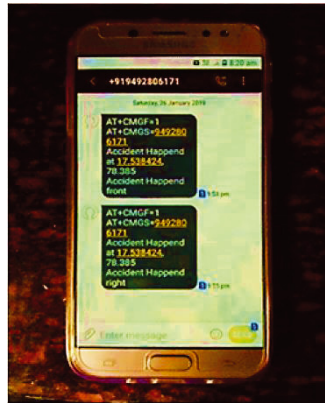


Fig. 13. Notification message.

The course is set up so that the bike will not start unless the rider is wearing a helmet. Additionally, if the rider is intoxicated, the bike will not start, and this helmet buzzes an alarm to warn the rider if he exceeds a set speed limit. The engine will immediately turn off in the event of an accident to prevent further injuries. Prototype Helmet Unit The experimentation stage was so over. This investigation was carried out in a planned manner. Therefore, there is no urgent need for additional real-world experimentation; however, more simulations must be run before full-time deployment. Future systems that use a sensor to alert family members and neighbouring law enforcement to an emergency situation can use GPS and GSM modules. This can be done by programming GSM and GPS modules to communicate the precise GPS locations of the accident to the relevant authorities, alerting them to the serious situation and urging them to take prompt action that might save lives. All the features were properly integrated when the project was successfully finished.

5. CONCLUSION

Smart helmet promotes motorcycle safety and awareness. Road safety is enhanced by the smart helmets' blind spot awareness. The smart helmet improves driver safety. The smart helmet team spent a lot of time studying and building a proximity measurement and subsystem communication system. Money limited the project. Unfortunately, cheaper proximity sensors lacked the wide-angle reading needed to meet specifications. It must develop an accurate proximity measurement algorithm to combine several proximity sensor data into a single measurement. It developed important engineer-

ing, communication, and teamwork skills. Smart Helmet will meet milestones. It can include GPS, a live stream, and brightness dimmer if they can build a working model ahead of deadline.

In future self-driving motorcycles can keep riders' safe to record the motorist with a tiny camera. Wireless transmitters allow vehicles to communicate. The helmets' bioelectric sensors can measure the rider's activity to use voice commands for bike basics. The rider can now park the two-wheeler with the helmet on without extra security to charge phones and electric cars with two-wheeler solar power.

REFERENCES

1. Li Li, Jikuang Yang, Dietmar Otte, Zhou Xuenong, Zhang Chao, Yu Xiaoping, and Li Weiqiang, *2013 Fifth Conference on Measuring Technology and Mechatronics Automation (ICMTMA 2013) (January 16–17, 2013, Hong Kong)* (Institute of Electrical and Electronics Engineers (IEEE): 2013), p. 110; <https://www.proceedings.com/content/017/017826webtoc.pdf>
2. Suwarna Gothane and M. V. Sarode, *2016 IEEE 6th International Conference on Advanced Computing (IACC 2016) (February 27–28, 2016, Bhimavaram, India)* (Institute of Electrical and Electronics Engineers (IEEE): 2016), p. 15; <https://www.proceedings.com/content/030/030992webtoc.pdf>
3. J. Zarif, '16 Deaths Every Hour: Indian Roads Claim the Maximum Number of Lives in 2014' (2020) [Online]; <http://timesofindia.indiatimes.com/india/16-deaths-every-hourIndianroads-claim-the-maximum-number-of-lives-in-2014/articleshow/48128946.cms>
4. Sayan Tapadar, Shinjini Ray, Himadri Nath Saha, Arnab Kumar Saha, and Robin Karlose, *IEEE 8th Annual Computing and Communication Workshop and Conference (CCWC 2018) (January 8–10, 2018, Las Vegas, USA)* (Institute of Electrical and Electronics Engineers (IEEE): 2018), p. 584–590; doi:10.1109/CCWC.2018.8301639
5. N. Divyasudha, P. Arulmozhivarman, and E. R. Rajkumar, *2019 1st International Conference on Innovations in Information and Communication Technology (ICIICT 2019) (April 25–26, 2019, Chennai, India)* (Institute of Electrical and Electronics Engineers (IEEE): 2019), p. 146; <https://www.proceedings.com/content/049/049318webtoc.pdf>
6. Rashida Nazir, Ayesha Tariq, Sadia Murawwat, and Sajjad Rabbani, *Int. J. Communications, Network and System Sciences*, **7**, No. 8: 286 (2014); <http://dx.doi.org/10.4236/ijcns.2014.78031>
7. Dinesh Kumar HSDK, Shreya Gupta, Sumeet Kumar, and Sonali Srivastava, *Journal of Emerging Technologies and Innovative Research (JETIR)*, **2**, No. 5: 1433 (2015); <https://www.jetir.org/download1.php?file=JETIR1505018.pdf>
8. Namrata H. Sane, Damini S. Patil, Snehal D. Thakare, and Aditi V. Rokade, *International Journal on Recent and Innovation Trends in Computing and Communication*, **4**, Iss. 4: 479 (2016); https://ijritcc.org/download/conferences/ICMTEST_2016/ICMTEST_2016_Track/1462861671_10-05-2016.pdf

9. Chander Prabha, R. Sunitha, and R. Anitha, *International Journal of Advanced Research in Electrical, Electronics and Instrumentation Engineering*, **3**, Iss. 7: 2320 (2014); doi:10.15662/ijareeie.2014.0307062
10. N. Manjesh and Sudarshan Raj, *International Journal of Electrical and Electronics Research*, **2**, Iss. 4: 122 (2014);
<https://www.researchpublish.com/upload/book/Smart%20Helmet%20Using%20GSM-799.pdf>
11. Jennifer William, Kaustubh Padwal, Nexon Samuel, Akshay Bawkar, and Smita Rukhande, *International Journal of Scientific and Engineering Research*, **2**, Iss. 3: 591 (2016);
<https://www.ijser.org/researchpaper/Intelligent-Helmet.pdf>
12. Hasan Mehdi Naqvi and Geetam Tiwari, *International Journal of Injury Control and Safety Promotion*, **25**, No. 3: 319 (2018);
<https://doi.org/10.1080/17457300.2018.1431937>
13. Khaled Shaaban and Anurag Pande, *Journal of Traffic and Transportation Engineering*, **5**, No. 1: 66 (2018);
<https://doi.org/10.1016/j.jtte.2017.04.005>
14. Romuere Rodrigues Veloso e Silva, Kelson Rômulo Teixeira Aires, and Rodrigo de Melo Souza Veras, *27th SIBGRAPI Conference on Graphics Patterns and Images (August 26–30, 2014, Rio de Janeiro, Brazil)*, p. 141–148; doi:10.1109/SIBGRAPI.2014.28
15. Sayan Tapadar, Shinjini Ray, Himadri Nath Saha, Arnab Kumar Saha, and Robin Karlose, *2018 IEEE 8th Annual Computing and Communication Workshop and Conference (CCWC) (January 8–10, 2018, Las Vegas, USA)*, p. 584–590; doi:10.1109/CCWC.2018.8301639
16. Sreenithy Chandran, Sneha Chandrasekar, and N. Edna Elizabeth, *2016 IEEE Annual India Conference (INDICON) (December 16–18, 2016, Bangalore, India)*; doi:10.1109/INDICON.2016.7839052
17. Jie Li, Huanming Liu, Tianzheng Wang, Min Jiang, Shuai Wang, Kang Li, and Xiaoguang Zhao, *2017 Ninth International Conference on Advanced Computational Intelligence (ICACI) (February 4–6, 2017, Doha, Qatar)*, p. 201–205; doi:10.1109/ICACI.2017.7974509
18. R. Rathinakumar and D. Manivannan, *Research Journal of Applied Sciences, Engineering and Technology*, **4**, No. 18: 3323 (2012);
<https://maxwellsci.com/print/rjaset/v4-3323-3326.pdf>
19. Mohd Khairul Afiq Mohd Rasli, Nina Korlina Madzhi, and Juliana Johari, *2013 International Conference on Electrical, Electronics and System Engineering (ICEESE) (December 4–5, 2013, Kuala Lumpur, Malaysia)*, p. 21–26; doi:10.1109/ICEESE.2013.6895036
20. N. Manjesh and Sudarshan Raj, *International Journal of Electrical and Electronics Research*, **2**, Iss. 4: 122 (2014);
<https://doi.org/10.17577/IJERTV4IS041398>
21. J. Vijay, B. Saritha, B. Priyadharshini, S. Deepeka, and R. Laxmi, *International Journal of Scientific & Engineering Research*, **2**, Iss. 12: 1 (2011).

PACS numbers: 68.55.Nq, 75.30.Kz, 75.50.Vv, 75.60.Ej, 75.70.Ak, 78.30.Er, 81.30.Hd

Raman Effect During Formation of the Ordered $L1_0$ -FePd Phase

R. A. Shkarban¹, D. S. Leonov², M. Yu. Natalenko¹, T. I. Verbytska¹,
M. Yu. Barabash^{1,2}, and Iu. M. Makogon¹

¹*National Technical University of Ukraine
'Igor Sikorsky Kyiv Polytechnic Institute',
37, Beresteiskyi Prosp.,
UA-03056 Kyiv, Ukraine*

²*Technical Centre, N.A.S. of Ukraine,
13, Pokrovs'ka Str.,
UA-04070 Kyiv, Ukraine*

Effect of the hydrogen heat treatment compared with vacuum annealing in the temperature range of 500–700°C on the formation of the ordered $L1_0$ -FePd phase and variations in Raman spectra of the equiatomic FePd films are studied. The hydrogen atoms introduced into the nanoscale FePd films change the electronic structure and magnetic properties and states of the film. Ordering processes are accelerated under hydrogen treatments compared with vacuum annealing. By changing of parameters of the hydrogen annealing of the FePd film, it is possible to control the phase composition, ferromagnet \leftrightarrow paramagnet-variation in the magnetic states. The Raman spectroscopy allows investigate the dynamics of structural changes in the FePd films during the ordering and the ordered $L1_0$ -FePd-phase formation.

Досліджено вплив водневого термічного оброблення порівняно з відпалом у вакуумі в інтервалі температур 500–700°C на формування впорядкованої фази $L1_0$ -FePd та зміну спектрів комбінаційного розсіяння світла в еквіатомних плівках FePd. Атоми Гідрогену, введені в нанорозмірні плівки FePd, змінили електронну структуру, магнетні властивості та стани плівки. Процеси впорядкування пришвидшуються під час оброблення воднем порівняно з вакуумним відпалом. Змінюючи параметри відпалу плівки FePd у водні, можна керувати фазовим складом, зміною феромагнетик \leftrightarrow парамагнетик магнетних станів. Раманова спектроскопія уможливорює дослідити динаміку структурних змін плівок FePd під час упорядкування й утворення впорядкованої фази $L1_0$ -FePd.

Key words: hydrogen, ordering, coercivity, Raman scattering spectroscopy, paramagnetism, hard-magnetic material, $L1_0$ -FePd, magnetization.

Ключові слова: водень, впорядкування, коерцитивна сила, Раманова спектроскопія комбінаційного розсіяння, парамагнетик, магнетотвердий матеріал, $L1_0$ -FePd, намагнетованість.

(Received 9 April, 2024)

1. INTRODUCTION

The ordered $L1_0$ -FePd films are a promising material for use as magnetic media with ultra-high density, and in spintronics devices [1–3]. Usually, the FePd films deposited at room temperature have a (111) texture and soft-magnetic properties [1, 4, 5]. The annealing environment significantly affects the structure, magnetic and optical properties of the films [4–8].

It was found that hydrogenation increases the coercivity and residual magnetization in films of alloys enriched with Pd [9]. Electron–phonon interactions in the magnetic equiatomic layered $L1_0$ -FePd structure were studied in Ref. [10]. Position of H in the structure has a direct influence on the Curie temperature T_C values and the suppression of magnetism. Annealing-induced cyclic enhancement of the coercivity is related to the competition between thermal activation and H binding [11]. Magnetic films based on Pd can provide the ability to manipulate magnetic states using a current of spin–orbit torques [12]. The authors of Ref. [13] theoretically and experimentally investigated the disappearance of magnetism in Fe–H at a pressure of approximately 28 GPa and revealed the existence of a magnetic transition from a ferromagnetic state to a paramagnetic one, which was caused by pressure. According to the calculations, the H absorption is a favourable process in both the A1-FePd phase and $L1_0$ -FePd one [13]. The authors showed that the location of hydrogen atom in the tetrahedral interstitial site of the A1 phase is more stable than in the octahedral interstitial site in the $L1_0$ -phase lattice. The influence of hydrogen on magnetism is reversible [15–17].

In Ref. [16], a hydrogen-sensitive FePd alloy film was deposited on a Co/[Pt/Co]₄/Pt multilayer substrate with perpendicular magnetic anisotropy. As a result of hydrogenation, a spin reorientation transition from the perpendicular to the planar direction in the 2-nm thick FePd layer was observed. These findings are valuable for applications in spintronics using electronic control of hydrogen atom migration.

For obtaining the desired properties and multifunctionality, it is necessary to understand the interaction between the material structure and functionality.

Surface-enhanced Raman spectroscopy (SERS) is a powerful ana-

lytical method that provides amplification of the Raman signal by an order of 10^6 – 10^{14} [18]. New nanostructured materials are being developed for use as highly sensitive substrates for SERS [18]. An innovative substrate based on a nanoporous FePd alloy, which enhances surface Raman scattering, has ferromagnetic properties and can be used as a quantitative tool.

The aim of this work is to study the effect of hydrogen treatment compare the vacuum annealing on the ordered $L1_0$ -FePd phase formation and application of the Raman scattering for investigation of dynamic of ordering processes.

2. EXPERIMENTAL

Equiatomic nanoscale FePd films by thickness of 5 nm were deposited at room temperature on the $\text{SiO}_2/\text{Si}(001)$ substrates by magnetron co-sputtering from separate Fe and Pd targets. The film was deposited under an Ar working pressure of $3.5 \cdot 10^{-1}$ Pa in a chamber with a starting ultra-high vacuum of $3 \cdot 10^{-6}$ Pa. The deposition rate and layer thicknesses were monitored using a quartz resonator. In addition, the composition of the deposited films was controlled using Rutherford backscattering spectrometry (RBS). After deposition, the samples were annealed in vacuum ($P = 10^{-3}$ Pa) and in hydrogen (pressure $\cong 1$ atm) for 1–2 h in a temperature range of 500–700°C.

The phase composition and structure of the films after deposition and annealing were studied by the x-ray diffraction on ULTIMA IV (Rigaku) diffractometer (CuK_α radiation). Magnetic measurements were performed using a vibrating sample magnetometer (SQUID-VSM). All measurements were performed at room temperature.

Structural changes in the FePd films was investigated by Raman spectroscopy at a Renishaw InVia Raman Microscope spectrometer with the optical excitation wavelength of 785 nm and an analysis of the frequency criterion of radiation scattering [20].

3. RESULTS AND DISCUSSION

3.1. Processes of Ordering in FePd Films during Annealing in Vacuum

Figure 1, *a* shows the XRD patterns of the as-deposited FePd films and annealed in vacuum at 650°C for 0.5–20 h. After deposition, the weak FePd(111) peak and reflection from the substrate are observed (Fig. 1, *a*). The coercivity of the soft-magnetic FePd film is of 177 Oe (Fig. 2, *a*). The intensity of FePd(111) peak increases af-

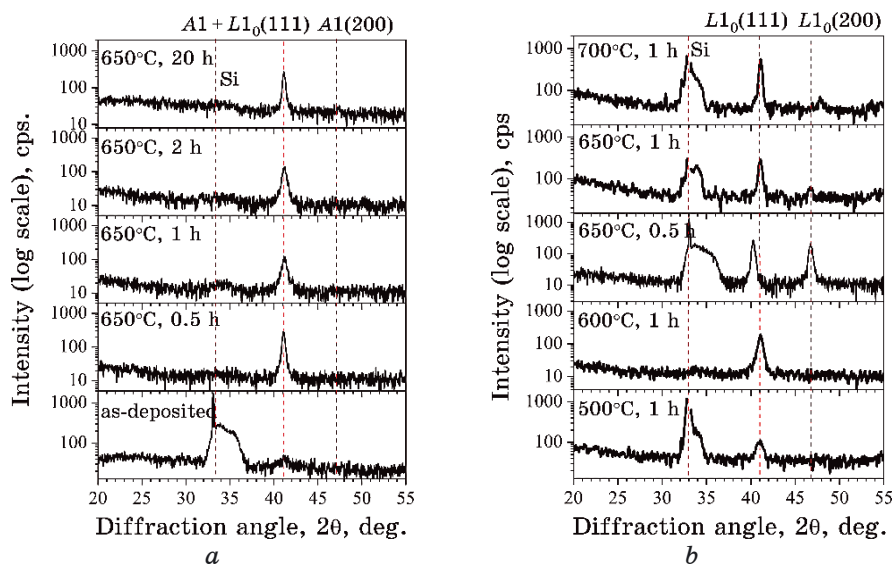


Fig. 1. XRD patterns of the as-deposited FePd (5 nm) films, after annealing in vacuum at 650°C for 0.5–20 h (a) and in hydrogen at 500–700°C for 0.5–1 h (b), CuK_α radiation.

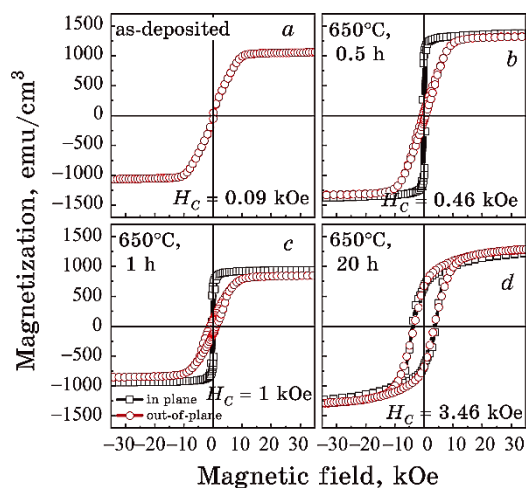


Fig. 2. M - H -hysteresis loops of FePd films after deposition (a) and annealing in vacuum at 650°C for 0.5 h (b), 1 h (c) and 20 h (d).

ter annealing at 650°C for 0.5–20 h that indicates preferential grains growth with (111) texture. After annealing, this reflection can be belonging to either disordered A1- or the ordered L1₀-FePd phases.

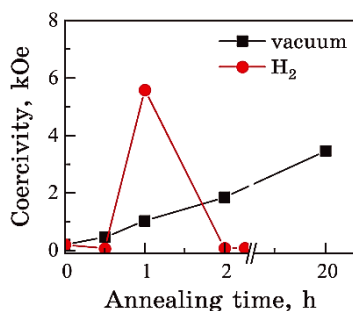


Fig. 3. Changes in coercivity value of the FePd films on annealing time in vacuum and hydrogen at 650°C.

However, regardless of the absence of the superstructural FePd(001) and fundamental FePd(002) peaks, the hard magnetic $L1_0$ -FePd phase is formed according to the measurements of magnetic properties (Fig. 2, *b*, *c*, *d*). The film after annealing in vacuum for 20 h is magnetically isotropic (Fig. 2, *d*).

Figure 3 shows the change in the coercivity of FePd films annealed in vacuum and hydrogen atmospheres in dependence on the time of annealing. The coercivity of the film after annealing in vacuum at 650°C for 1 h is of about 1 kOe that indicates the hard-magnetic $L1_0$ -phase formation (Fig. 2, *c*, Fig. 3). Volume fraction of this phase increases with an increase in the annealing time to 20 h, and the coercivity reaches 3.46 kOe (Fig. 2, *d*, Fig. 3).

3.2. Processes of Ordering in FePd Films during Annealing in Hydrogen

Processes of ordering in FePd films during annealing in hydrogen differ from annealing in vacuum. The intensity of the (111) reflection increased after heat treatment in the temperature range of 500–600°C for 1 h (Fig. 1, *b*). The grains of the $L1_0$ -FePd phase have a (111) texture. After annealing at 600°C, the $L1_0$ phase is formed and the coercivity becomes of 0.9 kOe (Fig. 4, *a*).

The (111) peak shifts toward smaller angles and (200) peak appears after annealing at 650°C for 0.5 h (Fig. 1, *b*). This indicates an increase in the lattice parameters and unit cell volume of the $A1$ -FePd phase. However, the magnetic properties become uncharacteristic for both the $A1$ - and $L1_0$ -FePd phases (Fig. 4, *b*).

A hard-magnetic $L1_0$ -FePd phase formed after annealing at 650°C for 1 h has a coercivity value of 5.5 kOe (Fig. 1, *b*, Fig. 4, *c*). Increasing the annealing time to 2 h resulted in the film becoming x-ray amorphous and losing its hard-magnetic properties (Fig. 4, *d*).

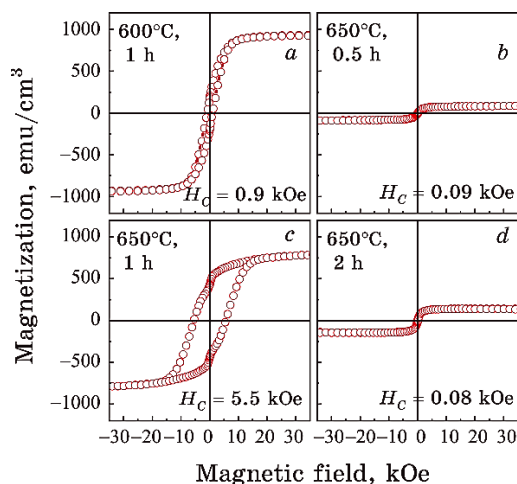


Fig. 4. M - H -hysteresis loops of FePd films annealed in hydrogen at 600°C for 1 h (*a*), at 650°C for 0.5 h (*b*), 1 h (*c*) and 2 h (*d*).

The magnetic state of the FePd film changed from hard-magnetic state to paramagnetic one as a result of incorporation of hydrogen atoms into the film. A further increase in the annealing temperature to 700°C led to rise in the (111) peak intensity.

3.3. Raman Scattering in FePd Films after Annealing in Vacuum and Hydrogen

Figure 5, *a* shows the Raman spectra of as-deposited sample irradiated from two sides, namely, from the substrate and from the film and annealed in vacuum at 650°C. The narrow spectrum at a frequency of 530 cm^{-1} corresponds to silicon. The next two resonance peaks of the spectrum can be attributed to oxides and the last peak to the luminescence of the substrate, which is caused by defects (inhomogeneities) in the silicon structure. The hydrogen atoms introduced into the FePd phase change the electronic structure and magnetic properties of the film [14]. After annealing in vacuum at 650°C, the magnetic properties correspond to a two-phase state in the film (Fig. 2, *b*, *c*). The luminescence peak is structurally sensitive to external influences. Its amplitude is greater than for pure substrate. This effect is caused by the enhancement of luminescence due to the presence of the film. The frequency shift of optical spectra indicates the appearance of stimulated Raman scattering, which enhances the oscillations of atoms or molecules during the ordering process. Figure 5, *b* shows the results of Raman spectroscopy for the FePd films annealed at different temperatures in hydrogen.

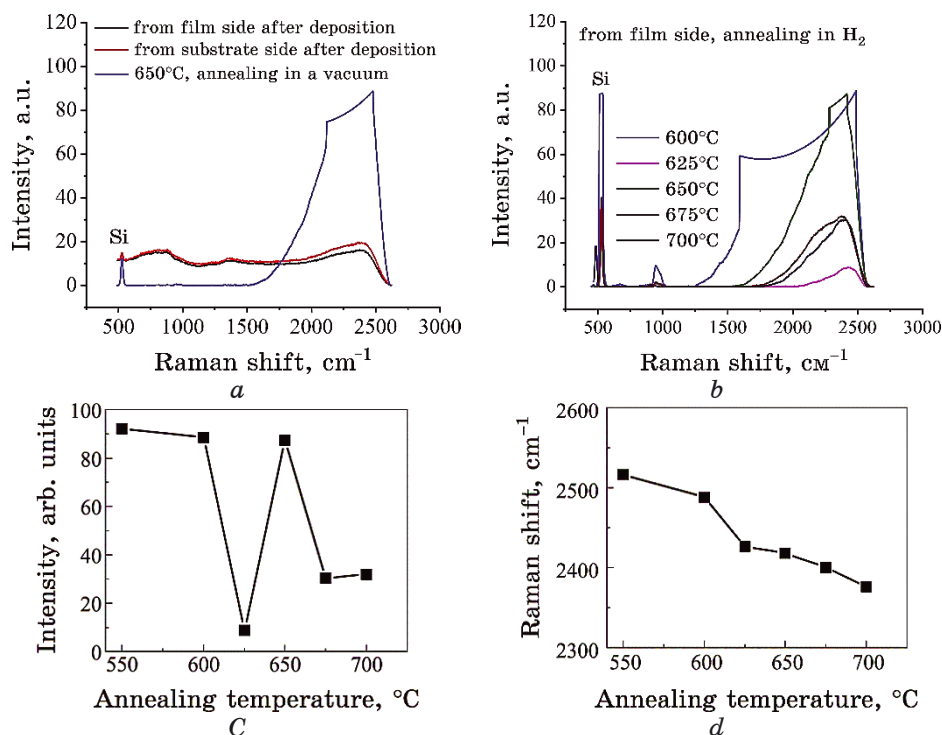


Fig. 5. Raman spectra of magnetic FePd film after deposition and annealing in vacuum at 650°C (*a*), after annealing in hydrogen at 600–700°C for 1 h (*b*); dependences of the intensity (*c*) and position (Raman shift) of the resonance peak (*d*) on annealing temperature [17].

There are maxima at $\cong 2376$ – 2516 cm⁻¹, which indicate the excitation of coupled E modes of Pd and Fe oscillations. There is a broad peak of significant intensity in the range 1594–2488 cm⁻¹ of the spectrum of the FePd film annealed in hydrogen at 600°C (Fig. 5, *b*).

Such a broadening can occur because of the diffusion of hydrogen atoms into the film and the beginning of the ordered $L1_0$ -FePd phase. The resonant frequency peak from the film has an asymmetric shape in the frequency range 1500–2600 cm⁻¹. The asymmetry of the Raman spectrum is related to the two-phase state ($A1 + L1_0$) that is present in the film. Annealing in hydrogen atmosphere led to the disappearance of an oxide peaks that can be explained by the reduction properties of hydrogen (Fig. 5, *b*). The oxidation process was suppressed by annealing in an Ar + H₂ (3 vol.%) atmosphere [11]. With increasing temperature of the ordering process, the number of grains of the ordered phase increases and the width of the resonance Raman peak decreases (Fig. 5, *b*). The width of the

resonance peak and its variations in the temperature range 500–700°C are associated with the ordering process and formation of the hard magnetic $L1_0$ phase from the disordered A1-FePd phase during annealing of the FePd films both in vacuum (Fig. 5, *a*) and in hydrogen (Fig. 5, *b*).

The results show that during annealing in hydrogen atmosphere, the position of the peak at 2376–2516 cm^{-1} corresponds to the formation of the ordered $L1_0$ -FePd phase, and its width decreases with increasing annealing temperature (Fig. 5, *b*). The resonance peak at $\approx 2500 \text{ cm}^{-1}$ corresponds to the ordered $L1_0$ -FePd phase, and the less intense broad part of the peak corresponds to the disordered A1-FePd phase in the zone with a different ordering degree. As the amount of ordered phase increases, this peak shifts to higher frequencies (Fig. 5, *b*). After annealing in hydrogen atmosphere at 625°C, there is a sharp decrease in the intensity of the peaks, which is due to the influence of the hydrogen atoms on the electronic structure of the FePd film (Fig. 5, *b*, *c*). An increase in the intensity of oscillations at $\approx 2418 \text{ cm}^{-1}$ and a decrease in the width of this peak after annealing in hydrogen at 650°C, compared to annealing in vacuum, indicates increased amount of the ordered $L1_0$ phase in the FePd film (Fig. 5, *a-c*). The luminescence peak with higher intensity corresponds to the state of the film with the largest amount of the $L1_0$ phase both after annealing in vacuum and in hydrogen at 650°C for 1 h (Fig. 5, *b*, *c*). In this case, the resonance peak from the film remains slightly asymmetric, which is caused by the residual amount of the A1-FePd phase. After annealing at 675°C and 700°C, there is a broad peak of lower intensity in the range 2376–2400 cm^{-1} , which may correspond to the oscillations of excess iron atoms. The changes in the intensity of the Raman scattering spectra of the FePd film with the annealing temperature correspond to the changes in the magnetic states in the film (Fig. 5, *c*).

However, the intensity of the Raman resonance peak changes nonlinearly with an increase in the temperature of the heat treatment in hydrogen atmosphere (Fig. 5, *c*). The ferromagnetic state in a film with uncompensated spins of Fe atoms leads to an increased intensity of the resonance signal of the Raman spectrum compared to the paramagnetic state in which the polarization is insignificant. The intensity minima in the Raman spectra at 625, 675 and 700°C correspond to paramagnetic states. Figure 5, *d* shows the changes in the resonance peak position on the Raman spectra of the magnetic FePd film after annealing in hydrogen atmosphere on annealing temperature. As the annealing temperature increases, the value of the Raman shift reduces due to an increase in the amount of ordered $L1_0$ -FePd phase. The Raman shift changes almost linearly with the annealing temperature and does not reflect changes in the

magnetic states of the film (Fig. 5, *d*).

The obtained results show that hydrogen atoms incorporated in the FePd film during annealing in the temperature range of 500–700°C have a significant effect not only on the dynamics of ordering processes, structure, but also on the reversibility of the ferromagnetic \leftrightarrow paramagnetic state compared to annealing in vacuum [16]. The ordering process is influenced by two factors, namely, the effect of introduced hydrogen atoms on the electronic structure of the film and the change in the volume of the unit cell during the A1-FePd-to- $L1_0$ -FePd transformation.

In the as-deposited FePd film, a disordered soft-magnetic A1-FePd phase forms. There are five electrons with positive spins and one with negative spin on the 3*d* shell in the outer layer of iron atom; as a result, four spins remain uncompensated. The exchange energy between two neighbouring Fe atoms causes atom polarization and leads to a ferromagnetic state. Annealing in hydrogen atmosphere is accompanied by the incorporation of hydrogen atoms into the film. Hydrogen atoms are located in octahedral and tetrahedral interstitial sites and increase the volume of the A1-FePd phase unit cell. This weakens atomic bonds and accelerates the formation of the $L1_0$ -FePd phase. The soft-magnetic state in the film preserves up to annealing at 600°C for 1 h (Fig. 4, *a*). Hydrogen atom introduced in the film gives its electron to Fe atom. As a result, the film electronic structure changes. When the hydrogen concentration in the film changes with increase in annealing time or temperature and the process of ordering and formation of $L1_0$ grains develops, the magnetic properties and states change: soft-magnetic A1 (as-deposited film) \rightarrow soft-magnetic A1 + hard-magnetic $L1_0$ (600°C, 1 h) \rightarrow paramagnetic (625°C, 1 h–650°C, 0.5 h) \rightarrow hard-magnetic $L1_0$ (650°C, 1 h) \rightarrow paramagnetic (650°C, 2 h). With the gradual filling of the inner *d*-shell of Fe atoms, part of the positive uncompensated spins becomes compensated ones. After annealing at a temperature of 625°C for 1 h or at 650°C for 0.5 h, the magnetic state of the film changes to paramagnetic. As the annealing time at 650°C increases to 1 h, the volume of the lattice cell decreases as the A1 \rightarrow $L1_0$ -ordering process develops, and the second necessary factor a/r (the ratio of the interatomic distance to the radius of the unfilled shell of Fe atoms) for the appearance of ferromagnetism begins to act. A hard magnetic state appears in the film. Further filling of the 3*d* shell of Fe atoms with hydrogen electrons after annealing at 700°C for 1 h is accompanied by the reappearance of the paramagnetic state. During annealing in vacuum, the ordering process (A1 \rightarrow $L1_0$) proceeds more slowly than in hydrogen, and the change from the soft-magnetic state to the hard-magnetic state is affected only by the decrease in the volume of the unit cell during

the formation of the $L1_0$ -FePd phase.

The highest values of the coercivity in the film at $\cong 5.5$ kOe are observed after annealing in hydrogen at 650°C for 1 h, which is 5-times higher in comparison with annealing in vacuum. The ferromagnetic state in the film with uncompensated spins of Fe atoms leads to an increase in the intensity of the resonance spectrum of the Raman signal compared to the paramagnetic state in which the polarization is insignificant. The shift in the frequency of scattered light during the $A1 \rightarrow L1_0$ -FePd solid-state transformation is a manifestation of forced scattering of optical radiation. It is advisable to use the SERS method to study the dynamics of structural changes in magnetic FePd films during the ordering process. By changing the annealing parameters of the equiatomic FePd film in hydrogen, it is possible to control the phase composition, magnetic properties and states. The use of the FePd film as a template enhances surface Raman scattering and increases the sensitivity for organic objects. Reversible ferromagnet \leftrightarrow paramagnet change of the film magnetic state can find practical application in nanoelectronics.

4. CONCLUSION

Annealing atmosphere, temperature and time of annealing affect the ordered $L1_0$ -phase formation, structure, magnetic properties and states of the equiatomic FePd films. As revealed, the annealing in hydrogen at $500\text{--}700^\circ\text{C}$ results in the reversible change of the magnetic state of the FePd films: soft-magnetic \rightarrow soft-magnetic + hard-magnetic \rightarrow paramagnetic \rightarrow hard-magnetic \rightarrow paramagnetic. Obviously, this is caused by changes in electronic structure.

The SERS is promising method for studying of the ordering process and dynamics of the structural and magnetic changes in the FePd films. Use of the FePd films as templates enhances the surface Raman scattering and sensitivity for organic objects.

REFERENCES

1. D. Weller, A. Moser, L. Folks, M. E. Best, Wen Lee, M. F. Toney, M. Schwickert, J.-U. Thiele, and M. F. Doerner, *IEEE Trans. Magn.*, **36**: 10e15 (2000); <https://doi.org/10.1109/20.824418>
2. De-Lin Zhang, Congli Sun, Yang Lv, Karl B. Schliep, Zhengyang Zhao, Jun-Yang Chen, Paul M. Voyles, and Jian-Ping Wang, *Phys. Rev. Appl.*, **9**: 044028 (2018); <https://doi.org/10.1103/PhysRevApplied.9.044028>
3. L. Ma, D. A. Gilbert, V. Neu, R. Schafer, J.-G. Zheng, and X. Q. Yan, *J. Appl. Phys.*, **116**: 033922 (2014); <https://doi.org/10.1063/1.4890936>
4. M. N. Shamis, N. Y. Schmidt, T. I. Verbytska, P. V. Makushko, G. Beddies, M. Albrecht, and Yu. N. Makogon, *Appl. Nanosci.*, **12**: 1227 (2022);

- <https://doi.org/10.1007/s13204-021-01809-4>
5. M. N. Shamis et al., *Metallofiz. Noveishie Tekhnol.*, **43**, No. 4: 505 (2021); <https://mfint.imp.kiev.ua/article/v43/i04/MFiNT.43.0505.pdf>
 6. A. B. Shevchenko and M. Yu. Barabash, *Low Temp. Phys.*, **39**, No. 2: 151 (2013); <https://doi.org/10.1063/1.4792131>
 7. I. A. Vladymyrskyi, M. V. Karpets, F. Ganss, G. L. Katona, D. L. Beke, S. I. Sidorenko, T. Nagata, T. Nabatame, T. Chikyow, G. Beddies, M. Albrecht, and Iu. M. Makogon, *J. Appl. Phys.*, **114**: 164314 (2013); <https://doi.org/10.1063/1.4827202>
 8. P. V. Makushko, M. Yu. Verbytska, M. N. Shamis, T. I. Verbytska, G. Beddies, N. Y. Safonova, M. Albrecht, and Iu. N. Makogon, *Applied Nanoscience*, **10**: 2775 (2020); <https://doi.org/10.1007/s13204-019-01066-6>
 9. W. C. Lin, B.-Y. Wang, H.-Y. Huang, C.-J. Tsai, and V. R. Mudinepalli, *J. Alloys Comp.*, **661**: 20 (2016); <https://doi.org/10.1016/j.jallcom.2015.11.144>
 10. A. Boufelfel, *J. of Hydrogen Energy*, **41**, No. 8: 4719 (2016); <https://doi.org/10.1016/j.ijhydene.2016.01.063>
 11. P.-C. Chang, T.-H. Chuang, D.-H. Wei, and W.-C. Lin, *Appl. Phys. Lett.*, **116**: 102407 (2020); <https://doi.org/10.1063/1.5142625>
 12. B. Y. Wang et al., *J. of Alloys and Comp.*, **748**: 223 (2018); <https://doi.org/10.1016/j.jallcom.2018.03.121>
 13. N. Bouldi, P. Sainctavit, A. Juhin, L. Nataf, and F. Baudalet, *Phys. Rev. B*, **98**: 064430 (2018); <https://doi.org/10.1103/PhysRevB.98.064430>
 14. E. A. Gonzalez, P. V. Jasen, N. J. Castellani, and A. Juan, *J. Phys. Chem. Solids*, **65**, No. 11: 1799 (2004); <https://doi.org/10.1016/j.jpcs.2004.05.008>
 15. W. C. Lin, C.-J. Tsai, H.-Y. Huang, B.-Y. Wang, V. R. Mudinepalli, and H.-C. Chiu, *Appl. Phys. Lett.*, **106**: 12404 (2015); <https://doi.org/10.1063/1.4905463>
 16. P.-C. Chang, L.-J. Liaw, A. Dhanarajagopal, K.-J. Hsueh, M.-T. Lin, and W. C. Lin, *ACS Appl. Nano Mater.*, **6**, No. 4: 2784 (2023); <https://doi.org/10.1021/acsnm.2c05095>
 17. Leonid Levchuk, Ruslan Shkarban, Igor Kotenko, Kateryna Graivoronska, Olena Fesenko, Ivan Lukianenko, Tetiana Verbytska, Iurii Makogon, and Maksym Barabash, *Thin Solid Films*, **789**: 1402000 (2024); <https://doi.org/10.1016/j.tsf.2024.140200>
 18. H. Sharma, E. Carmichael, and D. McCall, *Vibration Spectroscopy*, **83**: 159 (2016); <https://doi.org/10.1016/j.vibspec.2016.01.011>
 19. Matteo Cialone, Federica Celegato, Federico Scaglione, Gabriele Barrera, Deepti Raj, Marco Consson, Paola Tiberto, and Paola Rizzi, *Appl. Surf. Sci.*, **543**: 148759 (2021); <https://doi.org/10.1016/j.apsusc.2020.148759>
 20. M. Yu. Barabash, G. G. Vlaykov, A. A. Kolesnichenko, and L. V. Rybov, *Advances in Thin Films, Nanostructured Materials, and Coatings*, **804**: 169 (2019); https://link.springer.com/chapter/10.1007/978-981-13-6133-3_17

PACS numbers: 72.80.Tm, 77.22.Ch, 77.22.Gm, 78.67.Sc, 81.07.Pr, 81.40.Tv, 82.35.Np

Exploring the Dielectric Properties of $\text{Fe}_2\text{O}_3\text{--In}_2\text{O}_3$ Nanocomposites for Electrical and Electronics Applications

Ahmed Hashim¹ and Farhan Lafta Rashid²

¹*College of Education for Pure Sciences,
Department of Physics,
University of Babylon,
Hillah, Iraq*

²*College of Engineering,
Petroleum Engineering Department,
University of Kerbala,
Kerbala, Iraq*

Nanocomposites' films of pure PVA and PVA doped with $\text{Fe}_2\text{O}_3\text{--In}_2\text{O}_3$ nanoparticles (NPs) are fabricated to utilize in numerous electrical and electronic applications. The dielectric properties at frequency ranged from 100 Hz to 5 MHz are tested for PVA- $\text{Fe}_2\text{O}_3\text{--In}_2\text{O}_3$ nanocomposites. Results show the improving dielectric constant, dielectric loss and electrical conductivity of PVA with adding various ratios of $\text{Fe}_2\text{O}_3\text{--In}_2\text{O}_3$ NPs. The dielectric constant and dielectric loss of fabricated nanocomposites are reduced, while the electrical conductivity is increased, when frequency rises. Finally, the dielectric-properties' results demonstrate that the PVA- $\text{Fe}_2\text{O}_3\text{--In}_2\text{O}_3$ nanocomposites may be applied in various electrical and electronics applications.

Нанокompозитні плівки з чистого полівінілового спирту (ПВС) та полівінілового спирту, допованого наночастинками (НЧ) $\text{Fe}_2\text{O}_3\text{--In}_2\text{O}_3$, було виготовлено для використання в численних електричних та електронних застосуваннях. Для нанокompозитів ПВС- $\text{Fe}_2\text{O}_3\text{--In}_2\text{O}_3$ перевіряли діелектричні властивості в діапазоні частот від 100 Гц до 5 МГц. Результати показали поліпшення діелектричної проникності, діелектричних втрат та електропровідності ПВС із додаванням різних співвідношень НЧ $\text{Fe}_2\text{O}_3\text{--In}_2\text{O}_3$. Діелектрична проникність і діелектричні втрати виготовлених нанокompозитів зменшуються, а електропровідність підвищується, коли частота зростає. Нарешті, результати стосовно діелектричних властивостей показали, що нанокompозити ПВС- $\text{Fe}_2\text{O}_3\text{--In}_2\text{O}_3$ можуть бути застосовні в різних електричних та електронних застосуваннях.

Key words: polyvinyl alcohol (PVA), $\text{Fe}_2\text{O}_3\text{-In}_2\text{O}_3$, nanocomposites, dielectric properties, conductivity.

Ключові слова: полівініловий спирт, $\text{Fe}_2\text{O}_3\text{-In}_2\text{O}_3$, нанокompозити, діелектричні властивості, електропровідність.

(Received 18 August, 2023; in revised form, 26 August, 2023)

1. INTRODUCTION

Nanocomposite materials have been a major area of research interest owing to their distinct electrochemical properties that differ significantly from those of their constituent components. Similarly, devices based on polymer nanocomposites have received an enormous attention owing to their ability to solve both energy and environmental problems [1]. Recently, oxide-based transparent conducting thin films have attracted much attention due to their wide applications in transparent thin-film transistors (TFTs), light-emitting diodes, solar cells, gas sensors, transparent display. In particular, In_2O_3 has several advantages for transparent electronic applications, because it has a high optical transparency, a low electrical resistivity of the order of $10^{-4} \Omega\cdot\text{cm}$ and a wide band gap of 3.7 eV [2].

Fe_2O_3 NPs have special properties like good electron mobility, magnetic ability, and a 2.2 eV optical-energy band gap, which are useful for optoelectronic applications. Fe_2O_3 NPs have potential applications in the fields of medicine, life sciences and computer technology like magnetic resonance imaging (MRI), drug carriers in delivery, gene carriers in gene therapy, nanofertilizers, non-fungicides, nanopesticides, nanofood, food packing, nanocoating, nanosensors, nanoscale memory, nanowires, spintronics etc. They can be used as filters in sunscreens, biosensors [3].

As one of the biodegradable polymers, polyvinyl alcohol (PVA) is a non-toxic, water-soluble, semi-crystalline synthetic biopolymer with excellent film-forming, emulsifying, and adhesive properties. It has a wide range of uses in fields such as pharmacology, food chemistry, biomedicine, biotechnology, paper coatings, and the production of water-soluble flexible packaging films. In recent studies, it has been reported that PVA is a safe material for food packaging because it is made from renewable resources and is environmentally friendly [4]. The properties of polymers may be improved by adding of various materials into polymers that caused to improve the optical properties, electronic properties and electrical properties [5–39].

The present work aims to prepare of nanocomposites films from pure PVA and PVA doped with $\text{Fe}_2\text{O}_3\text{-In}_2\text{O}_3$ nanoparticles to utilize in numerous electrical and electronic applications.

2. MATERIALS AND METHODS

The PVA-Fe₂O₃-In₂O₃ nanocomposites films were prepared from pure PVA and PVA doped with Fe₂O₃-In₂O₃ nanoparticles using casting method. The PVA film was fabricated by dissolving of 0.5 gm PVA in 30 ml of distilled water employing magnetic stirrer for 1 hour to obtain more homogeneous solution. The Fe₂O₃-In₂O₃ NPs were added to polymer solution by a variety of contents are 1%, 2% and 3% with concentration of 1:1. The dielectric properties of PVA-Fe₂O₃-In₂O₃ nanocomposites were tested different frequency ranged between 100 Hz and 5·10⁶ Hz utilizing LCR meter type (HIOKI 3532-50 LCR HI TESTER).

The dielectric constant (ϵ') was found by [40] as follows:

$$\epsilon' = C_p/C_0, \quad (1)$$

where C_p is the material capacitance and C_0 is the vacuum capacitance.

Dielectric loss (ϵ'') was calculated by [41] as follows:

$$\epsilon'' = \epsilon' D, \quad (2)$$

where D is the dispersion factor.

The A.C. electrical conductivity was given by [42] as follows:

$$\sigma_{A.C.} = 2\pi f \epsilon' D \epsilon_0. \quad (3)$$

3. RESULTS AND DISCUSSION

The performance of dielectric constant and dielectric loss for PVA-Fe₂O₃-In₂O₃ nanocomposites with frequency and Fe₂O₃-In₂O₃ NPs content are represented in Figs. 1-4, respectively. The dielectric constant and loss behaviour in the given frequency range as the following, the strong frequencies dispersion of the permittivity is seen at low range of frequency. The values of dielectric constant and loss are reduced with rise of frequency related to the relaxation process and may be attributed to charge accumulation inside the nanocomposites due to influence of interfacial polarization on permittivity. With addition of the filler, the values of both dielectric constant and loss are increased at the range of lower frequency and nearly the same at the range of the higher frequency attributed to the filler cause more localization of charge carriers along with mobile ions causing higher ionic conductivity. The increase of dielectric constant and dielectric loss with increasing filler content related to rise of charges carriers numbers [43-55].

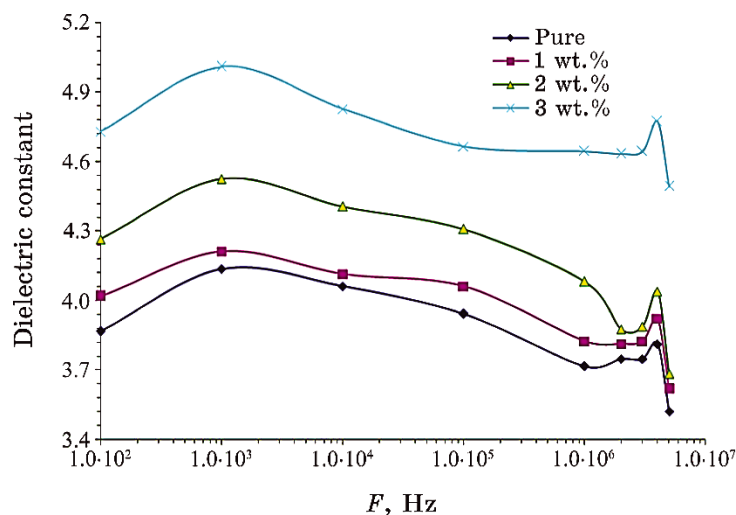


Fig. 1. Variation of dielectric constant for PVA-Fe₂O₃-In₂O₃ nanocomposites with frequency.

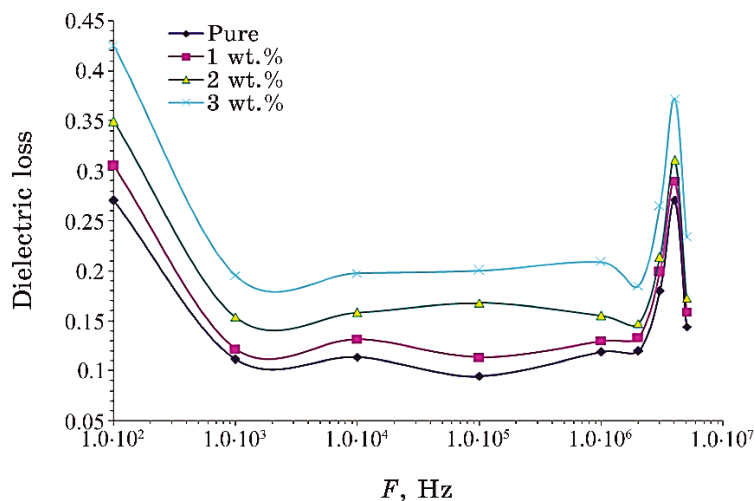


Fig. 2. Performance of dielectric loss for PVA-Fe₂O₃-In₂O₃ nanocomposites with frequency.

Figures 5 and 6 show the variation of A.C. electrical conductivity for PVA-Fe₂O₃-In₂O₃ nanocomposites with frequency and Fe₂O₃-In₂O₃-NPs' concentration, respectively. As shown in these figures, the conductivity increases with increasing of Fe₂O₃-In₂O₃-NPs' concentration. The low frequencies region exhibited dispersion due to spatial charging or inter-polarization.

The reduced conductivity at lower frequency was related to decrease number of mobile ions resulting from charged cumulative at polymer interfaces. The electrical conductivity enhancement with $\text{Fe}_2\text{O}_3\text{-In}_2\text{O}_3$ -NPs' concentration was because of the increasing the number of dopants, where the $\text{Fe}_2\text{O}_3\text{-In}_2\text{O}_3$ -NPs' molecules begin to bridge the gaps between two localized states and lower potential barriers separating them, therefore the transfer of charge carriers is easy between them, according to the percolation theory; there-

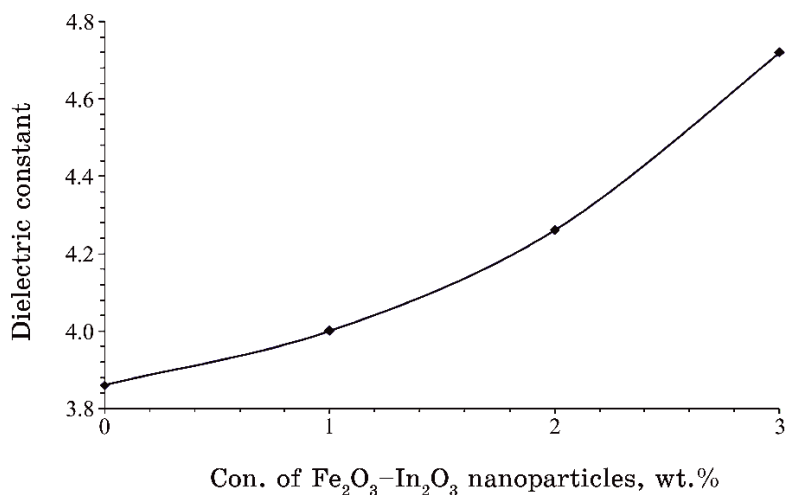


Fig. 3. Effect of $\text{Fe}_2\text{O}_3\text{-In}_2\text{O}_3$ NPs content on dielectric constant for PVA.

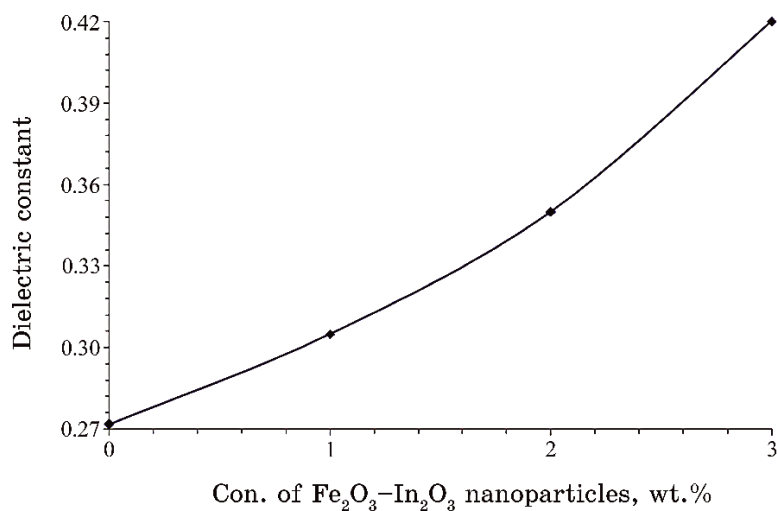


Fig. 4. Effect of $\text{Fe}_2\text{O}_3\text{-In}_2\text{O}_3$ NPs content on dielectric loss for PVA.

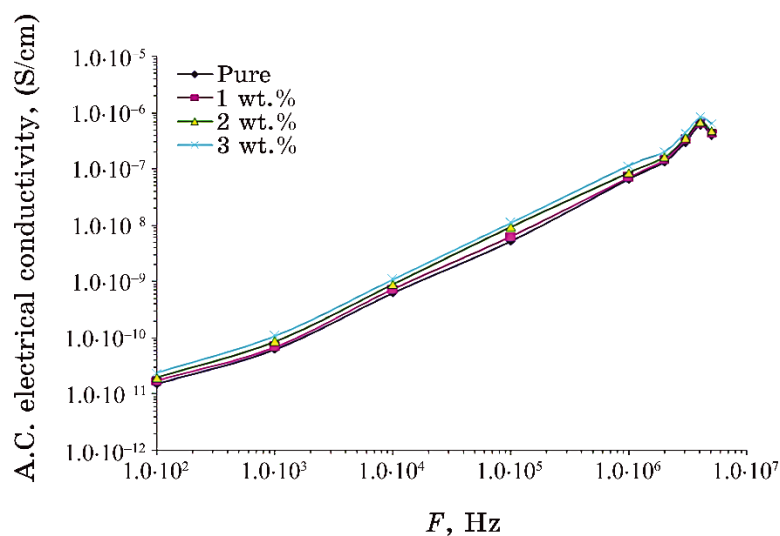


Fig. 5. Variation of A.C. electrical conductivity for PVA- Fe_2O_3 - In_2O_3 nanocomposites with frequency.

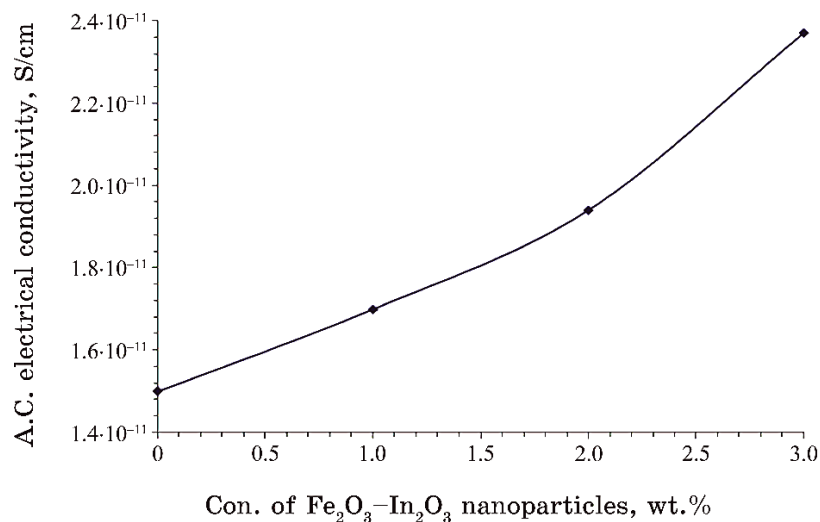


Fig. 6. Behaviour of A.C. electrical conductivity for PVA with Fe_2O_3 - In_2O_3 -NPs' concentration.

fore, the conductivity increases as a results of increase the number of charges carriers. Moreover, this enhancement is assigned to the higher conductivity of the added Fe_2O_3 - In_2O_3 NPs and increased charge mobility, related to the increased amorphous degree inside the doped samples [56–67].

4. CONCLUSIONS

The current work includes fabrication of films from PVA and PVA doped with Fe₂O₃-In₂O₃ NPs to use in different electrical and electronic fields. The dielectric properties for PVA-Fe₂O₃-In₂O₃ nanocomposites were studied. Results showed that the dielectric properties: dielectric constant, dielectric loss and electrical conductivity of PVA are enhanced by adding various ratios of Fe₂O₃-In₂O₃ NPs. The final results of dielectric properties demonstrated that the PVA-Fe₂O₃-In₂O₃ nanocomposites may be useful in many electrical and electronics fields.

REFERENCES

1. A. U. Agobi, A. I. Ikeuba, A. J. Ekpunobi, I. L. Ikhioya, K. I. Udofia, J. Effiom-Edem Ntibi, C. N. Ozoemena, and M. A. Abua, *Revista Mexicana de Fisica*, **69**: 1 (2023); <https://doi.org/10.31349/RevMexFis.69.031001>
2. W. Cui, X. L. Zhao, Y. H. An, G. S. Yao, Z. P. Wu, P. G. Li, L. H. Li, C. Cui, and W. H. Tang, *Journal of Nanoscience and Nanotechnology*, **18**, No. 2: 1220 (2018); <https://doi.org/10.1166/jnn.2018.14111>
3. J. S. Goud and N. Narsimlu, *Indian Journal of Chemical Technology*, **29**: 737 (2022); [doi:10.56042/ijct.v29i6](https://doi.org/10.56042/ijct.v29i6)
4. I. Erol, Ö. Hazman, and M. Aksu, *Journal of Inorganic and Organometallic Polymers and Materials*, **33**: 731 (2023); <https://doi.org/10.1007/s10904-023-02532-z>
5. A. F. Kadhim and A. Hashim, *Opt. Quant Electron.*, **55**: 432 (2023); <https://doi.org/10.1007/s11082-023-04699-8>
6. H. Ahmed and A. Hashim, *Opt. Quant Electron.*, **55**: 280 (2023); <https://doi.org/10.1007/s11082-022-04528-4>
7. G. Ahmed and A. Hashim, *Silicon*, **15**: 3977 (2023); <https://doi.org/10.1007/s12633-023-02322-9>
8. M. H. Meteab, A. Hashim, and B. H. Rabee, *Opt. Quant Electron.*, **55**: 187 (2023); <https://doi.org/10.1007/s11082-022-04447-4>
9. B. Mohammed, H. Ahmed, and A. Hashim, *Nanosistemi, Nanomateriali, Nanotehnologii*, **21**, Iss. 1: 113 (2023); <https://doi.org/10.15407/nnn.21.01.113>
10. A. Hashim, *Nanosistemi, Nanomateriali, Nanotehnologii*, **19**, Iss. 3: 647 (2021); <https://doi.org/10.15407/nnn.19.03.647>
11. Q. M. Jebur, A. Hashim, and M. A. Habeeb, *Transactions on Electrical and Electronic Materials*, **20**: 334 (2019); <https://doi.org/10.1007/s42341-019-00121-x>
12. A. Hazim, A. Hashim, and H. M. Abduljalil, *Nanosistemi, Nanomateriali, Nanotehnologii*, **18**, Iss. 4: 983 (2020); <https://doi.org/10.15407/nnn.18.04.983>
13. A. Hashim and Z. S. Hamad, *Nanosistemi, Nanomateriali, Nanotehnologii*, **18**, Iss. 4: 969 (2020); <https://doi.org/10.15407/nnn.18.04.969>
14. A. Hazim, A. Hashim, and H. M. Abduljalil, *Egypt. J. Chem.*, **64**, No. 1: 359

- (2021); doi:10.21608/EJCHEM.2019.18513.2144
15. H. Ahmed and A. Hashim, *Journal of Molecular Modeling*, **26**: 1 (2020); doi:10.1007/s00894-020-04479-1
 16. H. Ahmed and A. Hashim, *Silicon*, **14**: 4907 (2022); <https://doi.org/10.1007/s12633-021-01258-2>
 17. A. Hashim, *Opt. Quant Electron.*, **53**: 1 (2021); <https://doi.org/10.1007/s11082-021-03100-w>
 18. H. Ahmed and A. Hashim, *Trans. Electr. Electron. Mater.*, **23**: 237 (2022); <https://doi.org/10.1007/s42341-021-00340-1>
 19. H. Ahmed and A. Hashim, *Silicon*, **14**: 7025 (2021); <https://doi.org/10.1007/s12633-021-01465-x>
 20. A. Hazim, A. Hashim, and H. M. Abduljalil, *Trans. Electr. Electron. Mater.*, **21**: 48 (2019); <https://doi.org/10.1007/s42341-019-00148-0>
 21. H. Ahmed and A. Hashim, *International Journal of Scientific & Technology Research*, **8**, Iss. 11: 1014 (2019).
 22. A. Hashim and A. Jassim, *Journal of Bionanoscience*, **12**, No. 2: 170 (2018); doi:10.1166/jbns.2018.1518
 23. A. Hashim and A. Jassim, *Sensor Letters*, **15**, No. 12: 1003 (2017); doi:10.1166/sl.2018.3915
 24. A. Hashim, M. A. Habeeb, and A. Hadi, *Sensor Letters*, **15**, No. 9: 758 (2017); doi:10.1166/sl.2017.3876
 25. A. Hashim, K. H. H. Al-Attiyah, and S. F. Obaid, *Ukr. J. Phys.*, **64**, No. 2: 157 (2019); <https://doi.org/10.15407/ujpe64.2.157>
 26. H. Ahmed and A. Hashim, *Transactions on Electrical and Electronic Materials*, **22**: 335 (2021); <https://doi.org/10.1007/s42341-020-00244-6>
 27. N. A.-H. Al-Aaraji, A. Hashim, A. Hadi, and H. M. Abduljalil, *Silicon*, **14**: 10037 (2022); <https://doi.org/10.1007/s12633-022-01730-7>
 28. H. Ahmed and A. Hashim, *Opt. Quant Electron.*, **55**: 1 (2023); <https://doi.org/10.1007/s11082-022-04273-8>
 29. W. O. Obaid and A. Hashim, *Silicon*, **14**: 11199 (2022); <https://doi.org/10.1007/s12633-022-01854-w>
 30. O. B. Fadil and A. Hashim, *Silicon*, **14**: 9845 (2022); <https://doi.org/10.1007/s12633-022-01728-1>
 31. K. H. H. Al-Attiyah, A. Hashim, and S. F. Obaid, *Journal of Bionanoscience*, **12**: 200 (2018); doi:10.1166/jbns.2018.1526
 32. S. Hadi, A. Hashim, and A. Jewad, *Australian Journal of Basic and Applied Sciences*, **5**, No. 9: 2192 (2011).
 33. F. A. Jasim, A. Hashim, A. G. Hadi, F. Lafta, S. R. Salman, and H. Ahmed, *Research Journal of Applied Sciences*, **8**, Iss. 9: 439 (2013).
 34. F. A. Jasim, F. Lafta, A. Hashim, M. Ali, and A. G. Hadi, *Journal of Engineering and Applied Sciences*, **8**, No. 5: 140 (2013).
 35. A. Hashim, M. A. Habeeb, A. Khalaf, and A. Hadi, *Sensor Letters*, **15**, No. 7: 589 (2017); <https://doi.org/10.1166/sl.2017.3856>
 36. I. R. Agool, F. S. Mohammed, and A. Hashim, *Advances in Environmental Biology*, **9**, No. 11: 1 (2015).
 37. B. H. Rabee and A. Hashim, *European Journal of Scientific Research*, **60**, No. 2: 247 (2011).
 38. A. Hashim and M. A. Habeeb, *Transactions on Electrical and Electronic Materials*, **20**: 107 (2019); doi:10.1007/s42341-018-0081-1

39. M. A. Habeeb, A. Hashim, and A. Hadi, *Sensor Letters*, **15**, No. 9: 785 (2017); doi:10.1166/sl.2017.3877
40. S. Uddin, N. Akhtar, S. Bibi, A. Zaman, A. Ali, K. Althubeiti, H. Alrobei, and M. Mushtaq, *Materials*, **14**: 1 (2021); <https://doi.org/10.3390/ma14185430>
41. E. Elbayoumy, N. A. El-Ghamaz, F. Sh. Mohamed, M. A. Diab, and T. Nakano, *Polymers*, **13**: 1 (2021); <https://doi.org/10.3390/polym13173005>
42. P. Beena and H. S. Jayanna, *Polymers and Polymer Composites*, **27**, No. 9: 619 (2019); doi:10.1177/0967391119856140
43. A. A. Menazea, A. M. Ismail, and I. S. Elashmawi, *J. of Materials Research and Technology*, **9**, Iss. 3: 5689 (2020); <https://doi.org/10.1016/j.jmrt.2020.03.093>
44. Z. S. Hamad and A. Hashim, *Nanosistemi, Nanomateriali, Nanotehnologii*, **20**, Iss. 1: 159 (2022); <https://doi.org/10.15407/nnn.20.01.159>
45. A. Hashim and Z. S. Hamad, *Nanosistemi, Nanomateriali, Nanotehnologii*, **20**, Iss. 1: 165 (2022); <https://doi.org/10.15407/nnn.20.01.165>
46. D. Hassan and A. H. Ah-Yasari, *Bulletin of Electrical Engineering and Informatics*, **8**, Iss. 1: 52 (2019); doi:10.11591/eei.v8i1.1019
47. A. Hashim, M. H. Abbas, N. A.-H. Al-Aaraji, and A. Hadi, *J. Inorg. Organomet Polym.*, **33**: 1 (2023); <https://doi.org/10.1007/s10904-022-02485-9>
48. M. A. Habbeeb, A. Hashim, and Abdul-Raheem K. AbidAli, *European Journal of Scientific Research*, **61**, No. 3: 367 (2011).
49. D. Hassan and A. Hashim, *Bulletin of Electrical Engineering and Informatics*, **7**, Iss. 4: 547 (2018); doi:10.11591/eei.v7i4.969
50. A. Hashim, M. A. Habeeb, A. Hadi, Q. M. Jebur, and W. Hadi, *Sensor Letters*, **15**, No. 12: 998 (2017); doi:10.1166/sl.2018.3935
51. I. R. Agool, F. S. Mohammed, and A. Hashim, *Advances in Environmental Biology*, **9**, No. 11: 1 (2015).
52. B. Mohammed, H. Ahmed, and A. Hashim, *Journal of Physics: Conference Series*, **1879**: 1 (2021); doi:10.1088/1742-6596/1879/3/032110
53. B. H. Rabee and A. Hashim, *European Journal of Scientific Research*, **60**, No. 2: 247 (2011).
54. A. Hashim and A. Jassim, *Nanosistemi, Nanomateriali, Nanotehnologii*, **20**, Iss. 1: 177 (2022); <https://doi.org/10.15407/nnn.20.01.177>
55. A. Hashim and Z. S. Hamad, *Nanosistemi, Nanomateriali, Nanotehnologii*, **20**, Iss. 2: 507 (2022); <https://doi.org/10.15407/nnn.20.02.507>
56. N. Al-Huda Al-Aaraji, A. Hashim, A. Hadi, and H. M. Abduljalil, *Silicon*, **14**: 4699 (2022); <https://doi.org/10.1007/s12633-021-01265-3>
57. M. H. Meteab, A. Hashim, and B. H. Rabee, *Silicon*, **15**: 251 (2023); <https://doi.org/10.1007/s12633-022-02020-y>
58. A. Hashim, M. H. Abbas, N. A.-H. Al-Aaraji, and A. Hadi, *Silicon*, **15**: 1283 (2023); <https://doi.org/10.1007/s12633-022-02104-9>
59. M. H. Meteab, A. Hashim, and B. H. Rabee, *Silicon*, **15**: 1609 (2023); <https://doi.org/10.1007/s12633-022-02114-7>
60. A. Hashim, A. Hadi, and M. H. Abbas, *Opt. Quant Electron.*, **55**: 642 (2023); <https://doi.org/10.1007/s11082-023-04929-z>
61. B. Hussien, A. K. Algidsawi, and A. Hashim, *Australian Journal of Basic and Applied Sciences*, **5**, No. 7: 933 (2011).
62. A. Hashim, A. Hadi, N. A. H. Al-Aaraji, and F. L. Rashid, *Silicon*, **15**: 5725

- (2023); <https://doi.org/10.1007/s12633-023-02471-x>
63. A. F. Kadhim and A. Hashim, *Silicon*, **15**: 4613 (2023); <https://doi.org/10.1007/s12633-023-02381-y>
64. A. Hashim, A. Hadi, and M. H. Abbas, *Silicon*, **15**: 6431 (2023); <https://doi.org/10.1007/s12633-023-02529-w>
65. H. A. J. Hussien, and A. Hashim, *J. Inorg. Organomet. Polym.*, **33**: 2331 (2023); <https://doi.org/10.1007/s10904-023-02688-8>
66. H. A. Jawad and A. Hashim, *Nanosistemi, Nanomateriali, Nanotehnologii*, **21**, Iss. 1: 133 (2023); <https://doi.org/10.15407/nnn.21.01.133>
67. M. A. Sebak, T. F. Qahtan, G. M. Asnag, E. M. Abdallah, *Journal of Inorganic and Organometallic Polymers and Materials*, **32**: 4715 (2022); <https://doi.org/10.1007/s10904-022-02440-8>

PACS numbers: 78.20.Ci, 78.66.Sq, 78.67.Sc, 81.07.Pr, 81.40.Tv, 82.35.Np, 85.60.Bt

Optical Properties of PVA–Cr₂O₃–Sb₂O₃ Nanocomposites for Optoelectronics Fields

Ahmed Hashim¹ and Farhan Lafta Rashid²

¹College of Education for Pure Sciences,
Department of Physics,
University of Babylon,
Hillah, Iraq

²College of Engineering,
Petroleum Engineering Department,
University of Kerbala,
Kerbala, Iraq

This study aims to prepare the PVA–Cr₂O₃–Sb₂O₃ nanocomposites to utilize them in many optoelectronics fields. The optical properties of PVA–Cr₂O₃–Sb₂O₃ nanocomposites are investigated in photon wavelengths from 200 nm to 800 nm. The experimental results illustrate that the absorbance (A) and absorption coefficient (α) of PVA are increased, while the transmittance (T) and energy band gap (E_g) are decreased with increasing of the Cr₂O₃–Sb₂O₃-nanoparticles' content. The obtained results display that the PVA–Cr₂O₃–Sb₂O₃ nanocomposites might be appropriate to use in different optoelectronics applications.

Це дослідження спрямоване на приготування нанокompозитів полівініловий спирт (ПВС)–Cr₂O₃–Sb₂O₃ для використання в багатьох галузях оптоелектроніки. Досліджено оптичні властивості нанокompозитів ПВС–Cr₂O₃–Sb₂O₃ в довжинах хвиль фотонів від 200 нм до 800 нм. Експериментальні результати показали, що поглинання (A) та коефіцієнт поглинання (α) ПВС збільшувалися, тоді як коефіцієнт пропускання (T) і ширина забороненої зони (E_g) зменшувалися зі збільшенням вмісту наночастинок Cr₂O₃–Sb₂O₃. Одержані результати показали, що нанокompозити ПВС–Cr₂O₃–Sb₂O₃ можуть бути доречними для використання в різних оптоелектронних застосуваннях.

Key words: nanocomposites, polyvinyl alcohol, Cr₂O₃–Sb₂O₃, energy gap, absorbance.

Ключові слова: нанокompозити, полівініловий спирт, Cr₂O₃–Sb₂O₃, енергетична щілина, абсорбція.

(Received 3 September, 2023)

1. INTRODUCTION

In the last decade, several flexible and stretchable type organic polymer matrices and inorganic nanomaterials based hybrid polymer nanocomposites (HPNCs) were prepared with state-of-the-art and characterized to confirm their uses as multifunctional promising materials in advances of polymer engineering and technology based lightweight, cost-effective, and miniaturized electronic devices. Most of the HPNCs were characterized for confirmation of their appropriately controllable morphological, nanostructural, thermal, mechanical, dielectric, electrical, and optical properties in order to meet tremendously increased industrial demand [1].

Usually, flexible electronic devices take advantage of the mechanical properties of conventional plastics and the semiconductor properties of conjugated polymers. Many polymers exhibit high flexibility, low density, and transparency. Some of them are biocompatible and biodegradable and, therefore, are the dominant materials in flexible electronics [2]. Recent research has demonstrated the benefits of using inorganic nanofillers in preparing polymeric nanocomposites. For example, integrating semiconductor materials as nanofillers doped onto polymer membranes has attracted critical attention due to their potential applications in optics and electronics. The high miscibility of these materials on polymeric membranes explains the complexity of their interaction, although it is important to note that adding nanofillers to the polymer matrix can alter the properties of the polymer itself [3].

Chromium oxide (Cr_2O_3) attracted a lot of interest as a wide-band-gap material ($E_g \cong 3$ eV). Indeed, Cr_2O_3 is a transition-metal-oxide semiconductor belonging to the rhombohedral crystal system. Otoh, Cr_2O_3 has particular photoresponse properties, ensuring a good detection within the long and large optical range [4]. Sb_2O_3 was acknowledged as playing several critical roles: reorienting the active lubricating component, providing a mechanically hard surface to support and isolate a thin layer of the active lubricant, preventing crack growth, and serving as an oxidation barrier [5]. Polyvinyl alcohol (PVA) is a biocompatible, fully biodegradable and non-toxic water-soluble polymer. It has gained increasing attention for biomedical applications. PVA-based nanocomposites combine the properties of both additives and polymers. Adding specified nanoparticles (NPs) into the PVA matrix could modify its properties to be suitable for a particular application. These nanocomposites have several applications in the medical and engineering technologies be-

cause of their electron transport, mechanical and optical properties [6]. The nanocomposites involved enhanced characteristics to apply in a variety of fields such as radiation shielding and bioenvironmental [7–12], optical fields [13–22], energy storage [23–25], electronics and optoelectronics [26–43], antibacterial [44–50], sensors [51, 52], *etc.*

Here, synthesis of PVA-Cr₂O₃-Sb₂O₃ nanocomposites and the optical properties are studied to use in many optoelectronics fields.

2. MATERIALS AND METHODS

The PVA-Cr₂O₃-Sb₂O₃ nanocomposites films were synthesized using casting method. The pure polymer film was fabricated by dissolving of 0.5 gm PVA in 30 ml of distilled water by using magnetic stirrer to mix the polymer for 1 hour to obtain more homogeneous solution. The Cr₂O₃ and Sb₂O₃ nanoparticles were added to PVA of constant concentration 1:1 with ratios of 2.2%, 4.4% and 6.6%. The optical properties of PVA-Cr₂O₃-Sb₂O₃ nanocomposites films were measured at wavelength ranged from 200 nm to 800 nm using the double beam spectrophotometer (Shimadzu, UV-1800A). The absorption coefficient (α) is found by [53] as follows:

$$\alpha = 2.303A/t, \quad (1)$$

where A is the absorbance and t is the film thickness. The energy gap is given by [54] as follows:

$$ah\nu = C(h\nu - E_g)^m, \quad (2)$$

where C is the constant; $h\nu$ represents the photon energy; E_g indicates to the energy gap, and $m = 2$ and 3 for the allowed and forbidden indirect transitions, respectively.

3. RESULTS AND DISCUSSION

Figures 1 and 2 display the variations of absorbance and transmittance spectra of PVA-Cr₂O₃-Sb₂O₃ nanocomposites with wavelength. The PVA-Cr₂O₃-Sb₂O₃ nanocomposites include high absorbance values and low transmittance values for UV spectra, which related to the electrons excitation at these energies. The absorbance reduces while the transmittance increases with increasing of the photon wavelength. The absorbance values of PVA increases with rising of the Cr₂O₃-Sb₂O₃-NPs' ratio, which can be related to the absorption and scattering of photons by nanoparticles. The absorbance of PVA

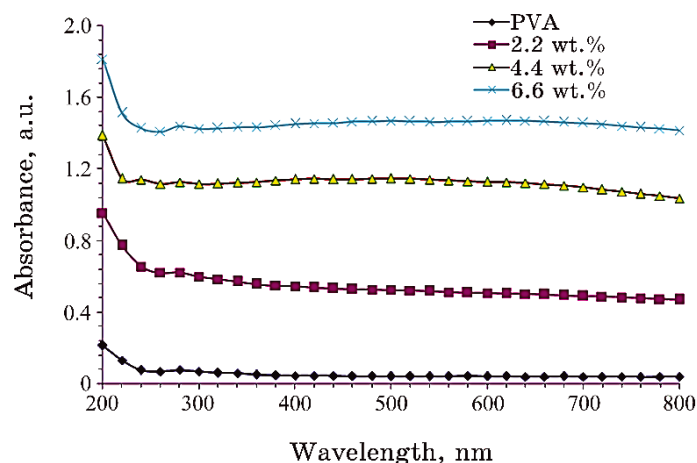


Fig. 1. Variation of absorbance for PVA-Cr₂O₃-Sb₂O₃ nanocomposites with wavelength.

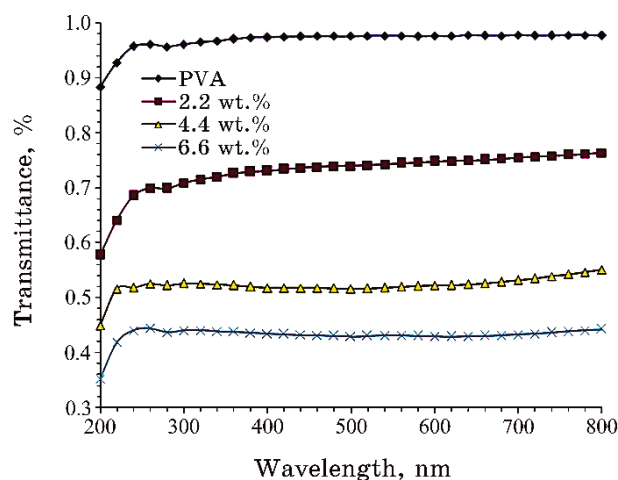


Fig. 2. Transmittance behaviour for PVA-Cr₂O₃-Sb₂O₃ nanocomposites with wavelength.

risers, while the transmittance is reduced with increasing of Cr₂O₃-Sb₂O₃-NPs' ratios, which is due to enhance in the number of charges carriers [55–65].

The behaviour of absorption coefficient for PVA-Cr₂O₃-Sb₂O₃ nanocomposites with energy of photon is shown in Fig. 3. The absorption coefficient for PVA-Cr₂O₃-Sb₂O₃ nanocomposites increases with photon energy and Cr₂O₃-Sb₂O₃-NPs' ratio.

Figures 4 and 5 demonstrate the allowed and forbidden indirect

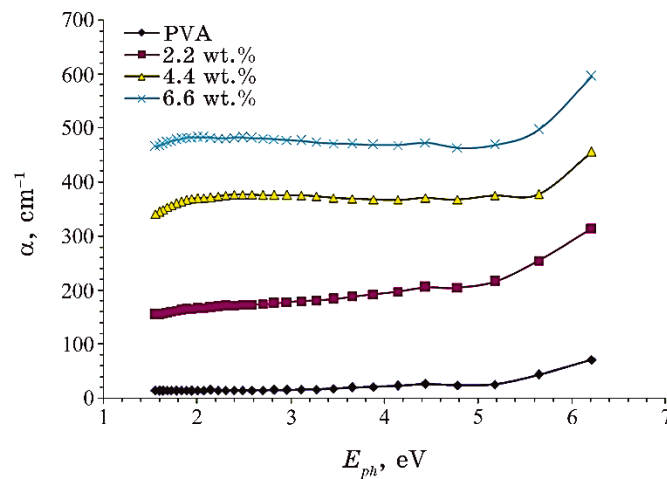


Fig. 3. Absorption coefficient behaviour for PVA-Cr₂O₃-Sb₂O₃ nanocomposites with photon energy.

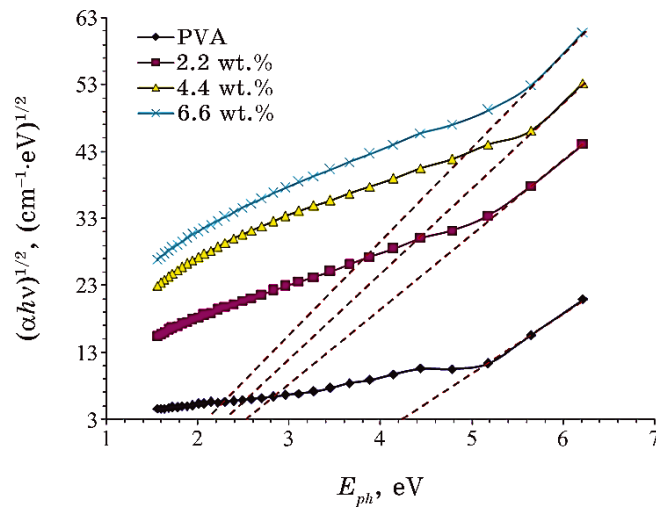


Fig. 4. Allowed indirect energy gap for PVA-Cr₂O₃-Sb₂O₃ nanocomposites.

energy gap for PVA-Cr₂O₃-Sb₂O₃ nanocomposites, respectively. The energy-gap values for PVA are reduced with increasing Cr₂O₃-Sb₂O₃-NPs' ratio that relates to the complex creation of charges' transfer along with the PVA functional groups and Cr₂O₃-Sb₂O₃-NPs' atoms. The embedded Cr₂O₃-Sb₂O₃ NPs create a centre band among the PVA structure causing the decrease of energy gap for nanocomposites.

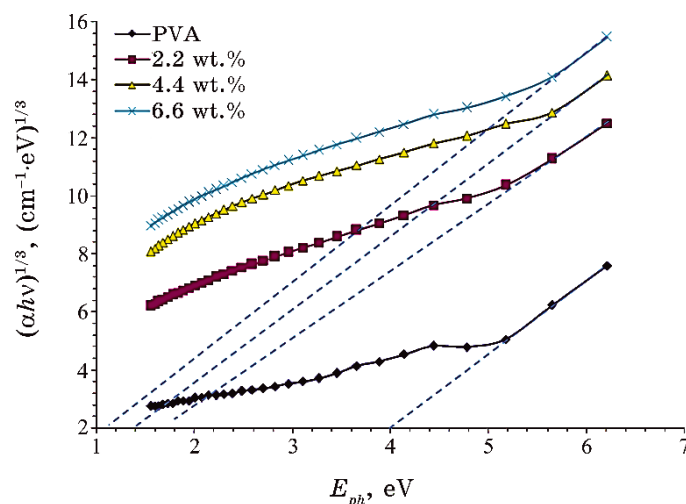


Fig. 5. Forbidden indirect energy gap for PVA–Cr₂O₃–Sb₂O₃ nanocomposites.

The reducing of energy gap is proposed to increase the localized levels in the nanocomposite structures [66–70].

4. CONCLUSIONS

The current study comprised fabrication of PVA–Cr₂O₃–Sb₂O₃ nanocomposites to utilize them in numerous optoelectronics applications. The results showed that the absorbance and absorption coefficient of PVA are increased with increasing of the Cr₂O₃–Sb₂O₃-NPs' content, while the transmittance and energy band gap are decreased with increasing of the Cr₂O₃–Sb₂O₃ content. The final results indicated that the PVA–Cr₂O₃–Sb₂O₃ nanocomposites may be useful for various optoelectronics fields.

REFERENCES

1. P. Dhatarwa, S. Choudhary, and R. J. Sengwa, *Indian Journal of Chemical Technology*, **28**: 693 (2021).
2. N. E. Guimarães, É. R. B. Ximenes, L. A. D. Silva, R. F. D. S. Santos, E. S. Araújo, and K. A. D. S. Aquino, *Materials Research*, **26**: 1 (2023); <https://doi.org/10.1590/1980-5373-MR-2022-0308>
3. S. H. Zyoud, T. H. AlAbdulaal, A. Almoadi, M. S. Alqahtani, F. A. Harraz, M. S. Al-Assiri, I. S. Yahia, H. Y. Zahran, M. I. Mohammed, and M. S. Abdel-wahab, *Crystals*, **13**: 1 (2023); <https://doi.org/10.3390/cryst13040608>

4. M. Rabia, A. B. G. Trabelsi, A. M. Elsayed, and F. H. Alkallas, *Coatings*, **13**: 1 (2023); <https://doi.org/10.3390/coatings13071240>
5. G. J. Dudder, X. Zhao, B. Krick, W. G. Sawyer, and S. S. Perry, *Tribol. Lett.*, **42**: 203 (2011); [doi:10.1007/s11249-011-9764-z](https://doi.org/10.1007/s11249-011-9764-z)
6. A. Abou Elfadl, *Arab J. Nucl. Sci. Appl.*, **52**, No. 4: 145 (2019); [doi:10.21608/ajnsa.2019.8081.1177](https://doi.org/10.21608/ajnsa.2019.8081.1177)
7. A. Hashim and N. Hamid, *Journal of Bionanoscience*, **12**, No. 6: 788 (2018); [doi:10.1166/jbns.2018.1591](https://doi.org/10.1166/jbns.2018.1591)
8. A. Hashim and Z. S. Hamad, *Journal of Bionanoscience*, **12**, No. 4: 488 (2018); [doi:10.1166/jbns.2018.1551](https://doi.org/10.1166/jbns.2018.1551)
9. A. Hashim and Z. S. Hamad, *Journal of Bionanoscience*, **12**, No. 4: 504 (2018); [doi:10.1166/jbns.2018.1561](https://doi.org/10.1166/jbns.2018.1561)
10. B. Abbas and A. Hashim, *International Journal of Emerging Trends in Engineering Research*, **7**, No. 8: 131 (2019); <https://doi.org/10.30534/ijeter/2019/06782019>
11. K. H. H. Al-Attiyah, A. Hashim, and S. F. Obaid, *Journal of Bionanoscience*, **12**: 200 (2018); [doi:10.1166/jbns.2018.1526](https://doi.org/10.1166/jbns.2018.1526)
12. H. A. J. Hussien, A. Hadi, and A. Hashim, *Nanosistemi, Nanomateriali, Nanotehnologii*, **20**, Iss. 4: 1001 (2022); <https://doi.org/10.15407/nnn.20.04.1001>
13. H. Ahmed and A. Hashim, *Silicon*, **14**: 6637 (2022); <https://doi.org/10.1007/s12633-021-01449-x>
14. H. Ahmed and A. Hashim, *Silicon*, **13**: 4331 (2020); <https://doi.org/10.1007/s12633-020-00723-8>
15. H. Ahmed and A. Hashim, *Transactions on Electrical and Electronic Materials*, **22**: 335 (2021); <https://doi.org/10.1007/s42341-020-00244-6>
16. N. A.-H. Al-Aaraji, A. Hashim, A. Hadi, and H. M. Abduljalil, *Silicon*, **14**: 10037 (2022); <https://doi.org/10.1007/s12633-022-01730-7>
17. H. Ahmed and A. Hashim, *Opt. Quant. Electron.*, **55**: 1(2023); <https://doi.org/10.1007/s11082-022-04273-8>
18. W. O. Obaid and A. Hashim, *Silicon*, **14**: 11199 (2022); <https://doi.org/10.1007/s12633-022-01854-w>
19. O. B. Fadil and A. Hashim, *Silicon*, **14**: 9845 (2022); <https://doi.org/10.1007/s12633-022-01728-1>
20. H. Ahmed and A. Hashim, *Silicon*, **15**: 2339 (2023); <https://doi.org/10.1007/s12633-022-02173-w>
21. H. B. Hassan, H. M. Abduljalil, and A. Hashim, *Nanosistemi, Nanomateriali, Nanotehnologii*, **20**, Iss 4: 941 (2022); <https://doi.org/10.15407/nnn.20.04.941>
22. H. A. Jawad and A. Hashim, *Nanosistemi, Nanomateriali, Nanotehnologii*, **20**, Iss. 4: 963 (2022); <https://doi.org/10.15407/nnn.20.04.963>
23. A. S. Shareef, F. Lafta Rashid, A. Hadi, and A. Hashim, *International Journal of Scientific & Technology Research*, **8**, Iss. 11: 1041 (2019).
24. A. Hadi, A. Hashim, and D. Hassan, *Bulletin of Electrical Engineering and Informatics*, **9**, No. 1: 83 (2020); [doi:10.11591/eei.v9i1.1323](https://doi.org/10.11591/eei.v9i1.1323)
25. H. Ahmed and A. Hashim, *Nanosistemi, Nanomateriali, Nanotehnologii*, **20**, Iss. 4: 951 (2022); <https://doi.org/10.15407/nnn.20.04.951>
26. A. Hazim, A. Hashim, and H. M. Abduljalil, *Nanosistemi, Nanomateriali, Nanotehnologii*, **18**, Iss. 4: 983(2020).

27. A. Hashim and Z. S. Hamad, *Nanosistemi, Nanomateriali, Nanotehnologii*, **18**, Iss. 4: 969 (2020).
28. A. Hazim, A. Hashim, and H. M. Abduljalil, *Egypt. J. Chem.*, **64**, No. 1: 359 (2021); doi:10.21608/EJCHEM.2019.18513.2144
29. H. Ahmed and A. Hashim, *Journal of Molecular Modeling*, **26**: 1 (2020); doi:10.1007/s00894-020-04479-1
30. H. Ahmed and A. Hashim, *Silicon*, **14**: 4907 (2022); <https://doi.org/10.1007/s12633-021-01258-2>
31. A. Hashim, *Opt. Quant. Electron.*, **53**: 1 (2021); <https://doi.org/10.1007/s11082-021-03100-w>
32. H. Ahmed and A. Hashim, *Trans. Electr. Electron. Mater.*, **23**: 237 (2022); <https://doi.org/10.1007/s42341-021-00340-1>
33. H. Ahmed and A. Hashim, *Silicon*, **14**: 7025 (2021); <https://doi.org/10.1007/s12633-021-01465-x>
34. A. Hazim, A. Hashim, and H. M. Abduljalil, *Trans. Electr. Electron. Mater.*, **21**: 48 (2019); <https://doi.org/10.1007/s42341-019-00148-0>
35. A. F. Kadhim and A. Hashim, *Opt. Quant. Electron.*, **55**: 432 (2023); <https://doi.org/10.1007/s11082-023-04699-8>
36. H. Ahmed and A. Hashim, *Opt. Quant. Electron.*, **55**: 280 (2023); <https://doi.org/10.1007/s11082-022-04528-4>
37. G. Ahmed and A. Hashim, *Silicon*, **15**: 3977 (2023); <https://doi.org/10.1007/s12633-023-02322-9>
38. M. H. Meteab, A. Hashim, and B. H. Rabee, *Opt. Quant. Electron.*, **55**: 187 (2023); <https://doi.org/10.1007/s11082-022-04447-4>
39. B. Mohammed, H. Ahmed, and A. Hashim, *Nanosistemi, Nanomateriali, Nanotehnologii*, **21**, Iss. 1: 113 (2023); <https://doi.org/10.15407/nnn.21.01.113>
40. A. Hashim, *Nanosistemi, Nanomateriali, Nanotehnologii*, **19**, Iss. 3: 647 (2021); <https://doi.org/10.15407/nnn.19.03.647>
41. A. F. Kadhim and A. Hashim, *Silicon*, **15**: 4613 (2023); <https://doi.org/10.1007/s12633-023-02381-y>
42. H. A. Jawad and A. Hashim, *Nanosistemi, Nanomateriali, Nanotehnologii*, **21**, Iss. 1: 133 (2023); <https://doi.org/10.15407/nnn.21.01.133>
43. M. H. Meteab, A. Hashim, and B. H. Rabee, *Silicon*, **15**: 1609 (2023); <https://doi.org/10.1007/s12633-022-02114-7>
44. A. Hashim, I. R. Agool, and K. J. Kadhim, *Journal of Bionanoscience*, **12**, No. 5: 608 (2018); doi:10.1166/jbns.2018.1580
45. A. Hazim, A. Hashim, and H. M. Abduljalil, *International Journal of Emerging Trends in Engineering Research*, **7**, No. 8: 68 (2019); <https://doi.org/10.30534/ijeter/2019/01782019>
46. A. Hazim, H. M. Abduljalil, and A. Hashim, *International Journal of Emerging Trends in Engineering Research*, **7**, No. 8: 104 (2019); <https://doi.org/10.30534/ijeter/2019/04782019>
47. O. B. Fadil and A. Hashim, *Nanosistemi, Nanomateriali, Nanotehnologii*, **20**, Iss. 4: 1029 (2022); <https://doi.org/10.15407/nnn.20.04.1029>
48. W. O. Obaid and A. Hashim, *Nanosistemi, Nanomateriali, Nanotehnologii*, **20**, Iss. 4: 1009 (2022); <https://doi.org/10.15407/nnn.20.04.1009>
49. M. H. Meteab, A. Hashim, and B. H. Rabee, *Nanosistemi, Nanomateriali, Nanotehnologii*, **21**, Iss. 1: 199 (2023);

- <https://doi.org/10.15407/nnn.21.01.199>
50. M. H. Meteab, A. Hashim, and B. H. Rabee, *Nanosistemi, Nanomateriali, Nanotehnologii*, **21**, Iss. 2: 451 (2023); <https://doi.org/10.15407/nnn.21.02.451>
 51. H. Ahmed and A. Hashim, *International Journal of Scientific & Technology Research*, **8**, Iss. 11: 1014 (2019).
 52. B. Mohammed, H. Ahmed, and A. Hashim, *Nanosistemi, Nanomateriali, Nanotehnologii*, **20**, Iss. 1: 187 (2022); <https://doi.org/10.15407/nnn.20.01.187>
 53. M. O. Farea, A. M. Abdelghany, and A. H. Oraby, *RSC Adv.*, **10**: 1 (2020); doi:10.1039/d0ra07601e
 54. A. M. A. Henaish and A. S. Abouhaswa, *Bull. Mater. Sci.*, **43**: 1 (2020); <https://doi.org/10.1007/s12034-020-2109-5>
 55. A. Hashim, A. Hadi, N. A.-H. Al-Aaraji, and F. L. Rashid, *Silicon*, **15**: 5725 (2023); <https://doi.org/10.1007/s12633-023-02471-x>
 56. P. Rejani and B. Beena, *Indian Journal of Advances in Chemical Science*, **2**, No. 3: 244 (2013).
 57. A. Hashim, M. H. Abbas, N. A.-H. Al-Aaraji, and A. Hadi, *J. Inorg. Organomet. Polym.*, **33**: 1 (2023); <https://doi.org/10.1007/s10904-022-02485-9>
 58. A. Hashim, M. H. Abbas, N. A.-H. Al-Aaraji, and A. Hadi, *Silicon*, **15**: 1283 (2023); <https://doi.org/10.1007/s12633-022-02104-9>
 59. S. Hadi, A. Hashim, and A. Jewad, *Australian Journal of Basic and Applied Sciences*, **5**, No. 9: 2192 (2011).
 60. F. A. Jasim, A. Hashim, A. G. Hadi, F. Lafta, S. R. Salman, and H. Ahmed, *Research Journal of Applied Sciences*, **8**, Iss. 9: 439 (2013).
 61. F. A. Jasim, F. Lafta, A. Hashim, M. Ali, and A. G. Hadi, *Journal of Engineering and Applied Sciences*, **8**, No. 5: 140 (2013).
 62. A. Hashim, M. A. Habeeb, A. Khalaf, and A. Hadi, *Sensor Letters*, **15**, No. 7: 89 (2017); <https://doi.org/10.1166/sl.2017.3856>
 63. I. R. Agool, F. S. Mohammed, and A. Hashim, *Advances in Environmental Biology*, **9**, No. 11: 1 (2015).
 64. B. H. Rabee and A. Hashim, *European Journal of Scientific Research*, **60**, No. 2: 247 (2011).
 65. A. Hashim and A. Hadi, *Sensor Letters*, **15**, No. 10: 858 (2017); <https://doi.org/10.1166/sl.2017.3900>
 66. A. Hashim, A. Hadi, and M. H. Abbas, *Opt. Quant. Electron.*, **55**: 642 (2023); <https://doi.org/10.1007/s11082-023-04929-z>
 67. A. Hashim, A. Hadi, and M. H. Abbas, *Silicon*, **15**: 6431 (2023); <https://doi.org/10.1007/s12633-023-02529-w>
 68. A. Hashim and A. Jassim, *Sensor Letters*, **15**, No. 12: 1003 (2017); doi:10.1166/sl.2018.3915
 69. H. A. J. Hussien and A. Hashim, *J. Inorg. Organomet. Polym.*, **33**: 2331 (2023); <https://doi.org/10.1007/s10904-023-02688-8>
 70. A. Hashim and A. Jassim, *Journal of Bionanoscience*, **12**: 170 (2018); doi:10.1166/jbns.2018.1518

PACS numbers: 73.61.-r, 77.22.Ch, 77.22.Gm, 78.66.Li, 78.67.Sc, 81.15.Cd, 81.40.Tv

Study of the Effect of Li Doping on ZnO Films Using RF-Magnetron Sputtering Method at Low Temperature

Israa Akram Abbas, Ameera J. Kadhm, and Raheem Lafta Ali

*College of Education for Pure Science,
Department of Physics,
Al-Mustansiriyah University,
Baghdad, Iraq*

In this study, we investigate the effect of Li-doping concentrations (3, 6, and 9%) on the optical and electrical properties of Li-doped ZnO-containing films. Li-doped ZnO films are fabricated by the RF-magnetron sputtering process. The optical and electrical properties of thin-film deposition at different sputtering RF powers in the plasma chamber are investigated. The electrical and optical properties of the thin layer are studied. The results for the optical properties of thin films (ZnO/Li) show that the absorbance, absorption coefficient, and optical conductivity increase with increasing Li concentration, while the energy band gap and transmittance decrease with increasing Li concentration. For all tested temperatures, the D.C. conductivity of the ZnO film increases after Li doping. The D.C. test shows that all films have the same activation energy, and the value of this energy increases as the Li-doping ratio increases. The electrical properties of alternating current demonstrate that, as the frequency of the electric field increases, the dielectric constant and dielectric loss of all films decrease.

У цьому дослідженні ми вивчаємо вплив концентрацій легувального Літію (3, 6 і 9%) на оптичні й електричні властивості плівок, що містять ZnO, легованих Літієм. Плівки ZnO, леговані Літієм, було виготовлено методом радіочастотного (РЧ) магнетронного розпорощення. Досліджено оптичні й електричні властивості осадження тонких плівок за різних потужностей РЧ-розпорощення у плазмовій камері. Досліджено електричні й оптичні властивості тонкого шару. Результати стосовно оптичних властивостей тонких плівок (ZnO/Li) показують, що поглинання, коефіцієнт поглинання й оптична провідність зростають зі збільшенням концентрації Li, тоді як ширина забороненої зони та коефіцієнт пропускання зменшуються зі збільшенням концентрації Li. Для всіх протестованих температур провідність на постійному струмі плівки ZnO збільшується після легування Li. Тест стосовно постійного струму

показує, що всі плівки мають однакову енергію активації, а значення цієї енергії зростає зі збільшенням рівня легування Літієм. Електричні властивості стосовно змінного струму показують, що зі збільшенням частоти електричного поля діелектрична проникність і діелектричні втрати всіх плівок зменшуються.

Key words: ZnO films, RF-magnetron sputtering method, Li doping, nano-composite, optical and electrical properties.

Ключові слова: плівки ZnO, метод радіочастотного магнетронного розпорошення, легування Літієм, наноккомпозит, оптичні й електричні властивості.

(Received 4 September, 2023; in revised form, 5 January, 2024)

1. INTRODUCTION

The numerous commercial applications of ZnO nanostructures in medication, colorants, catalysts, ceramics, and elastic-added substances have made it one of the most promising oxide materials. ZnO nanostructures have the potential to be utilized in sun-powered cells, anodes, sensors, straightforward UV defensive coatings, UV outflow, surface acoustic waves, and magneto-optical frameworks [1–8]. In any case, to create ZnO-based optoelectronic gadgets, the fabric must be doped to get *n*-type and *p*-type. Common ZnO shows *n*-type conductivity due to rotating zinc or oxygen openings, as is broadly known.

Nevertheless, it is troublesome to get steady *p*-type ZnO, primarily since the acceptor can compensate for characteristic absconds [9, 10]. Another issue that limits *p*-type conduction in ZnO is the nearness of remaining pollutants at noteworthy donor-like concentrations [11].

To date, a number of reports [12–19] have been distributed on *p*-type Li-doped ZnO lean movies manufactured by different strategies and explored the impact of arrangement conditions such as temperature and post-incubation concentrations lean layer motion picture resource. In any case, to our knowledge, some papers on Li-doped ZnO sol-gel lean movies with *p*-type nanostructures have been distributed [18, 19]. It has been specified that *p*-type conduction can happen when the Li concentration is greater than or breaks even at 10%.

In this study, we examine the manufacture of Li-doped ZnO lean movies by the RF-magnetron sputtering process. How the degree of Li doping influences the optical and electrical properties of ZnO will be talked about. We particularly examined the impact of lithium concentration on the properties of ZnO.

2. EXPERIMENTAL WORK

RF-magnetron sputtering strategy was utilized to create zinc oxide coating on glass substrate.

After being treated in acetone and corrosive arrangement (1/3HCl/2/3HNO₃), the substrates (18 mm×26 mm×1 mm glass slides) were cleaned with an ultrasonic cleaner. A base radiator is mounted on the water-cooled anode. On the water-cooled anode, a foundation radiator was introduced. In expansion, the substrates were put 65 mm from the target surface and turned 15 times per miniature.

The substrate temperature was measured using a thermocouple and controlled using a feed-back-controlled radiator, which changed from room temperature to 400°C.

To avoid defilement from other gases within the chamber, the chamber was purged to an extreme background weight of 1 Pa earlier in testimony. The restricted amounts of other extra gases were at that point flushed out of the chamber, and the substrate surface was cleaned for 15 minutes with unadulterated argon gas.

After almost five minutes of pre-sputtering to evacuate the surface oxide layer from the target, testimony was started on the ZnO target.

Sputtering was carried out for 120 minutes at a weight of 0.6 Dad in high-quality argon gas (99.999%).

Optical interferon is utilized to determine the thickness of the film. The Shimadzu UV 3100 S spectrometer with double beam and coordinate circle is utilized to assess optical reflectivity and transmittance within the 300–1800 nm wavelength range. Utilizing Swanepoel's method, the refractive file was assessed from the optical information.

The test is warmed in a broiler set to a temperature of 50°C to 80°C, amid which the D.C. resistance and conductivity are recorded.

The A.C. electrical conductivity was tested using an LCR meter (HIOKI 3532-50 LCR Hi TESTER (Japan)).

3. RESULTS AND DISCUSSION

3.1. Optical Properties

The objective of this study was to determine the impact of Li-doping concentrations 3, 6, and 9 at.% on the optical properties of Li-doped ZnO movies.

Inquire about examining the ghostly absorbance of movies at moo temperatures, understanding sorts of electronic moves, and calculating vitality contrasts and optical constants.

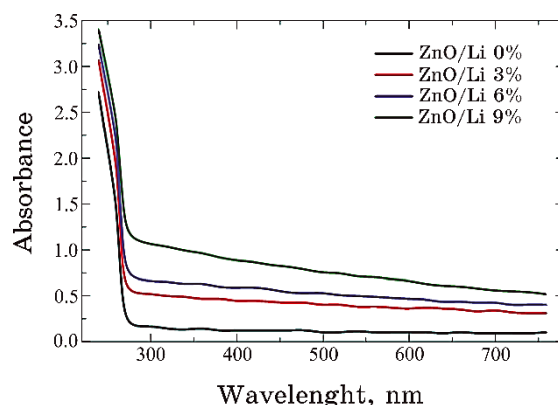


Fig. 1. Absorbance spectra of ZnO/Li thin films *versus* the wavelength.

3.1.1. Absorbance

Figure 1 shows the change in absorbance with wavelength of Li-doping concentration 3, 6 and 9 at.% at low temperature. We note that the absorbance of ZnO in the UV region is very high with different Li doping. They are almost equal because the energy of the incident photon of lengths of 400 nm and above is small and not sufficient for electronic transmission. While the energy of ultraviolet waves is high, greater than 3 eV, it is enough to shift one electron from the valence band to the conduction band. This disintegration occurs at a slower rate in the visible and near-infrared ranges, due to the absorption of the ZnO in the ultraviolet region, and the absorption of the composites increases too with the increase in the Li concentration.

3.1.2. Transmittance

Figure 2 presented the spectrum of optical transmittance as a function of the wavelength of the light incident on ZnO by adding different concentration of Li doping. The transmittance decreases as the doping ratios increase. All thin films, including Li, have a high transmittance, greater than 88%, according to the spectra. This is because scattering effects have been reduced, structural homogeneity has improved, and the crystalline state has improved.

3.1.3. Absorption Coefficient (A)

Figure 3 demonstrates that the absorption coefficient (α) of elaborated thin films increases as the Li-doping ratios increase, which is

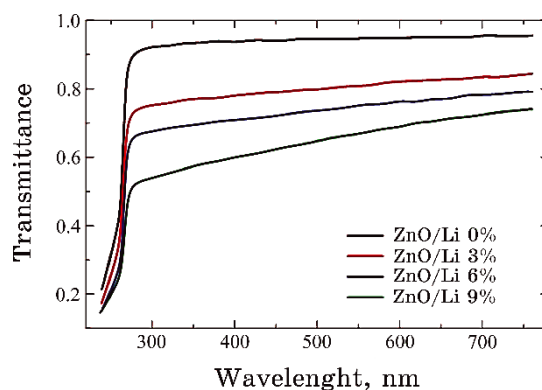


Fig. 2. Optical transmittance of the Li-ZnO films *versus* the wavelength.

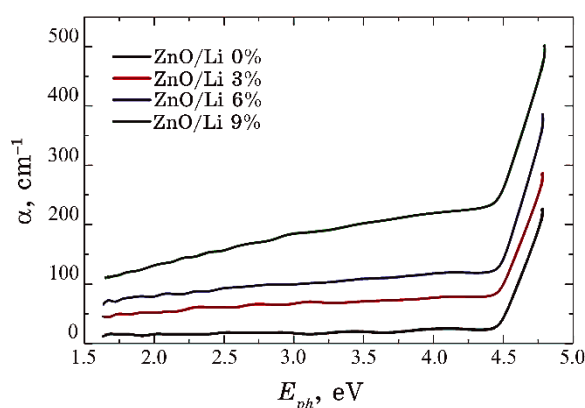


Fig. 3. Absorption coefficient as a function of the incident photon energy of the Li-doped ZnO films with various doping ratios.

due to an increase in the number of charge carriers in the films. The result of absorption coefficient (α) for all prepared nanocomposites presented smallest at low energies that could relate to the little possibility of electron transition. Whereas it increases with increasing energy of the incident photon, this indicates that the electron transition has a high probability. The energy of the incident photon is sufficient to interact with atoms. Indirect electronic transitions are extremely likely to occur in accordance with the absorption coefficient (α) values of the prepared films (less than 10^4 cm^{-1}).

3.1.4. Optical Energy Gaps Allowed

The plot of $(h\nu)^{1/r}$ at $r = 2$ *versus* the energy of the photon ($h\nu$) may

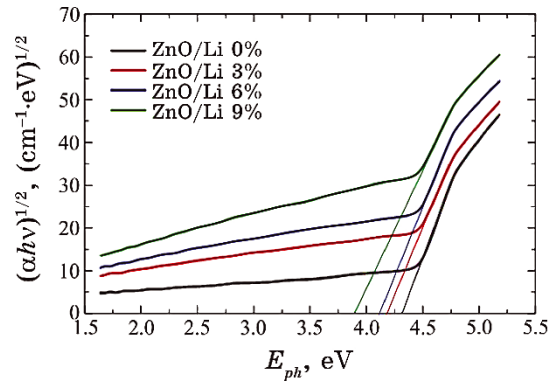


Fig. 4. Permissible direct electronic transitions of the Li-doped ZnO films with various doping ratios.

TABLE 1. Optical energy gap values allowed for the Li-doped ZnO films.

| Li doping, % | Allowed |
|--------------|---------|
| 0 | 4.25 |
| 3 | 4.1 |
| 6 | 3.29 |
| 9 | 3.7 |

be used to calculate the optical-band energy gap as shown in Fig. 4 based on the absorbance coefficient of Li-doped ZnO thin sheets.

The values, which we obtained, are shown in Table 1, where we notice that the values of the energy gap decrease with the increase in the weight percentages of Li doping. The equivalence package to the local levels and the second transition from the local levels to the delivery package is a result of increasing the proportion of the doping.

3.1.5 Refractive Index

Figure 5 represents the difference in the refractive index (n) of the Li-doped ZnO thin films with the emitted photon energy.

The values are increased with the increase in the photon energy, and this indicates that the electromagnetic radiation passes through the Li-doped ZnO films slower in the ultraviolet and visible regions; nevertheless the speed is higher in the visible and near-infrared spectrums.

The refractive index is also increased with the Li doping [in the weight percentages] in relation to the density of the composites.

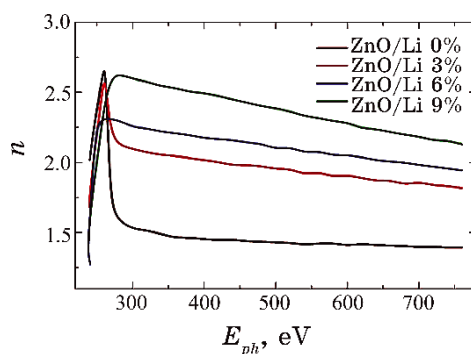


Fig. 5. Refractive index of the Li-doped ZnO films with various doping ratios.

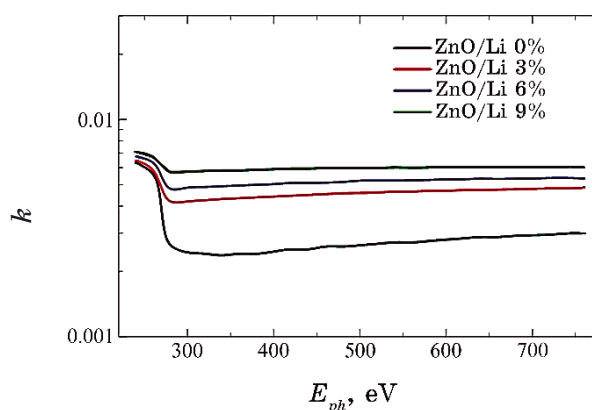


Fig. 6. Extinction coefficient of the Li-doped ZnO films with various doping ratios.

3.1.6. Extinction Coefficient

Figure 6 depicts the difference in the coefficient of extinction (k) as a function of photon energy for Li-doped ZnO thin film compounds. The coefficient of extinction increases as the concentration of Li doping increases. With an increase in the concentration of Li doping, the deviation increases, so, extinction coefficient (k) will increase as a result of the centres of diffusion in the compounds.

3.1.7. Dielectric Constant (Real and Imaginary Parts of (ϵ_r , ϵ_i))

Figures 7 and 8 present the variation of the real (ϵ_r) and imaginary (ϵ_i) components of the dielectric constant for pure ZnO and Li-doped

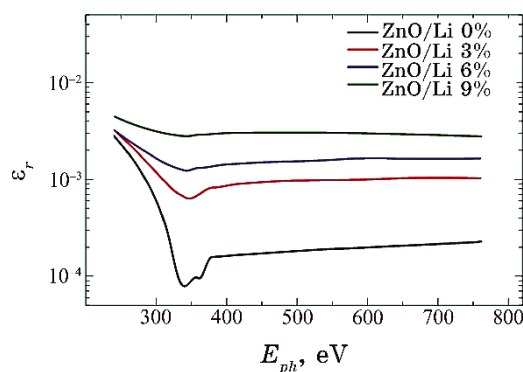


Fig. 7. Real dielectric constant of Li-doped ZnO films with various doping ratios.

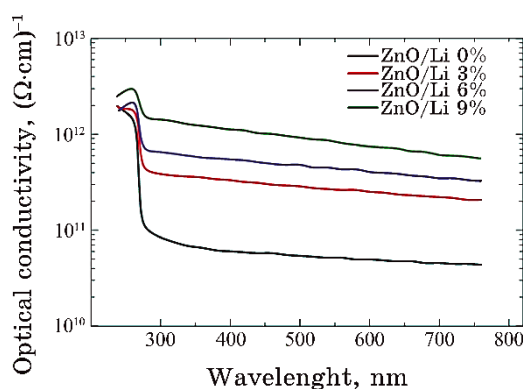


Fig. 8. Imaginary dielectric constant of Li-doped ZnO films with various doping ratios.

ZnO films as functions of photon energy (ϵ_r) presented how much the speed of light was slow down in the material, which is considered a measure of the polarity of a material, whereas (ϵ_i) demonstrated the dielectric absorb energy by the electric field through the dipole motion. It can be observed that there is an increase in the values of (ϵ_r) at low photonic energies followed by a clear decrease in the higher energies for all nanocomposite films. A rise in the dielectric constant of Li-doped ZnO films represents a little rise in ZnO internal charges.

3.1.8. The Optical Conductivity

Figure 9 shows how optical conductivity changes as a function of

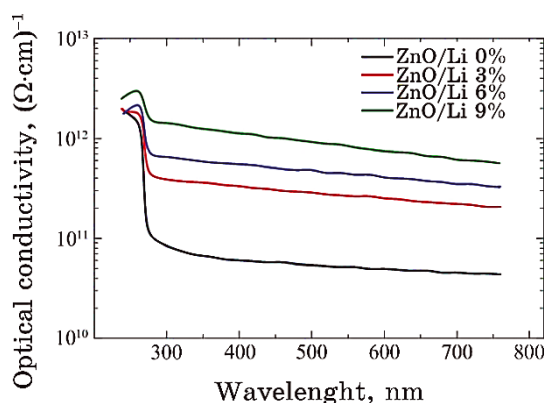


Fig. 9. The optical conductivity values *versus* wavelength of Li-doped ZnO films with various doping ratios.

wavelength. The graph demonstrates that, as the wavelength increases, the optical conductivity of all Li-doped ZnO films diminishes. This conductivity-related behaviour is strongly influenced by the radiation wavelength when it hits the nanocomposite samples.

The higher absorption of all Li-doped ZnO films in this region, and thus increased charge transfer excitations, causes an increase in optical conductivity at a low photon wavelength. The samples transmit light in the visible and near-infrared spectrum, according to the optical conductivity spectra.

3.2. The Direct Current Electrical Properties of the Li–ZnO Films

3.2.1. The Electrical Conductivity of the Li–ZnO Films

The D.C. electrical conductivity (σ) is affected by several factors, along with the preparation method and the measurement circumstances.

Figure 10 depicts the temperature (T) and Li-doping dependences of σ in ZnO films.

The increase in σ with Li-doping content could be attributed to the formation of connected networks in the matrix of the thin film. However, since ZnO is a semiconductor, doping it with Li may result in the development of energy levels inside the energy band gap that act as traps for charge carriers that bounce between these levels, boosting DC.

Figure 10 also demonstrates that the DC rises with T . This indicates that these films have undergone thermal activation and exhibit semiconductor behaviour.

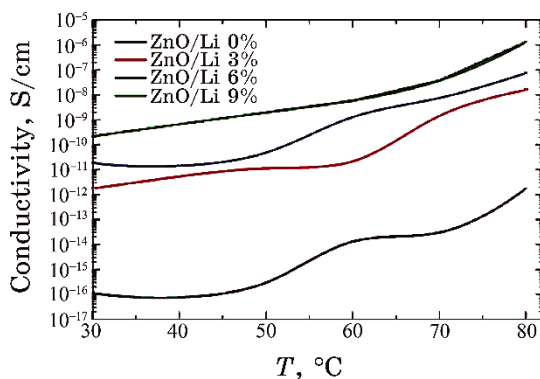


Fig. 10. The relationship between D.C. conductivity (σ) and Li-doped ZnO films with various doping ratios.

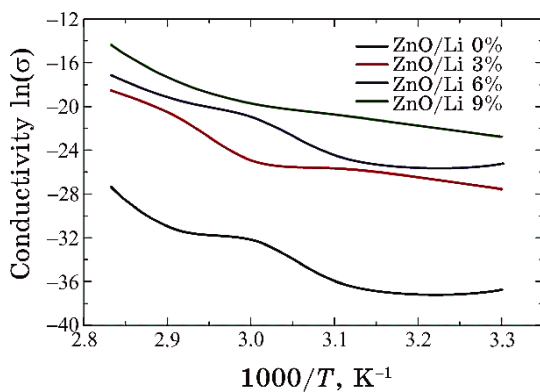


Fig. 11. $\ln\sigma$ versus ($10^3/T$) of Li-doped ZnO films with various doping ratios.

3.2.2. Activation of the Li-Doped ZnO Films

Figure 11 displays the variation of the absolute temperature $10^3/T$ measured at a temperature range 285–330 K for Li-doped ZnO films as a function of \ln .

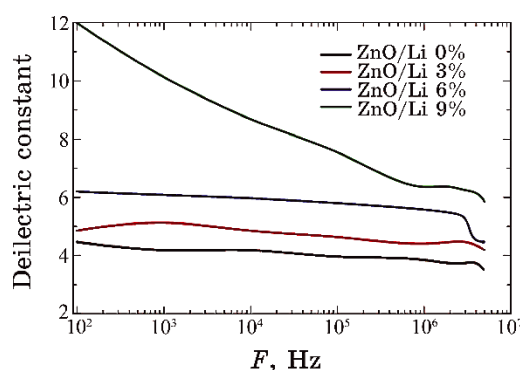
Electrical activation energy (E_{ac}) calculations showed values between 1.576 eV and 1.912 eV, as shown in Table 2.

The presence of free ions in the films is that caused the high electrical activation energy for pure ZnO.

The drop in activation energies with increasing Li doping is related to an increase the energy gap between the local and global levels, which trap charge carriers and are crucial for the transport of charges.

TABLE 2. The electrical activation-energy values' experimental results.

| Samples | Activation energy, eV |
|-----------|-----------------------|
| ZnO/Li 0% | 1.912 |
| ZnO/Li 3% | 1.743 |
| ZnO/Li 6% | 1.613 |
| ZnO/Li 9% | 1.576 |

**Fig. 12.** The dependence of dielectric constant of Li-doped ZnO films with various doping ratios and frequency at room temperature.

3.3. The Li–ZnO Films' A.C. Electrical Properties

3.3.1. The Dielectric Constant

The value of the dielectric constant indicates a materials' capacity to absorb electricity produced by an applied electric field. Figure 12 illustrates how the dielectric constant varies with the electric field frequency range of 10^2 to 10^6 Hz at room temperature. The ratio of 3% Li doping demonstrates the decrease in dielectric constant with rising electric field frequency. This could be as a result of dipole samples' propensity space charges' polarization is reducing as they try to align themselves with the directions of applied electrical fields and with respect to total polarization. The most significant form of polarization is space charge polarization at low frequencies, and as frequency rises, it loses significance.

3.3.2. The Dielectric Loss

The dielectric loss is a measurement of the amount of electrical energy lost in the sample as a result of the applied-field conversion to

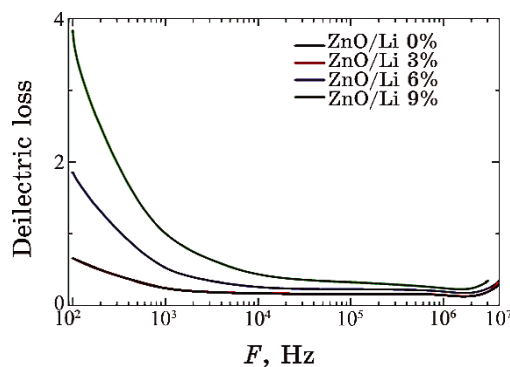


Fig. 13. Li-doped ZnO films' dependence on dielectric loss with various doping ratios and frequency at RT.

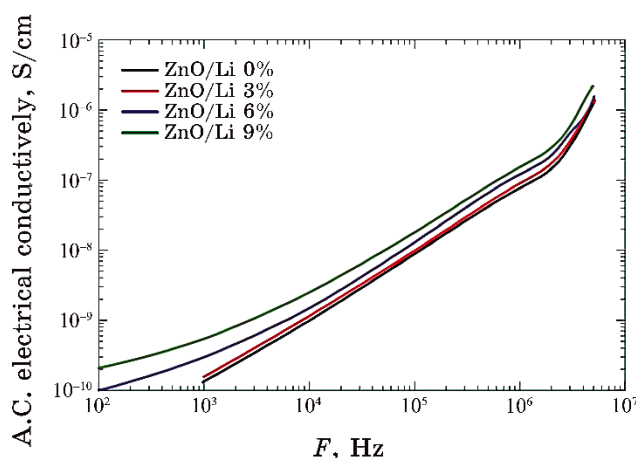


Fig. 14. Variation of A.C. electrical conductivity of Li-doped ZnO films with various doping ratios and frequency at room temperature.

thermal energy. The relationship between dielectric loss and the electric field frequency range of 10^2 – 10^6 Hz. Figure 13 shows thin Li–ZnO films at ambient temperature that thin out as the applied electric-field frequency increases. Reduced space charge polarization's contribution is what causes this.

3.3.3. The Electrical Conductivity of A.C.

As the electric-field frequency increases, the A.C. conductivity increases noticeably. This relationship between the A.C. electrical conductivity and the electric-field frequency range of 10^2 – 10^6 Hz

and both the ZnO and Li doping at room temperature is shown in Fig. 14 for all Li–ZnO thin film samples. This is caused by the hopping motion of charge carriers and space charge polarization, both of which occur at low frequencies. Moreover, as the percentage of Li doping rises, conductivity rises as well. Due to the regular distribution of charge carriers in the Li–ZnO thin films, the increase in space charge as a result of this behaviour is caused by the increase in carriers of charge.

4. CONCLUSION

In this work, we examine the impacts of Li doping concentration on the electrical and optical characteristics of Li-doped ZnO films with concentrations 3, 6, and 9 at.%. RF magnetron sputtering was used to create Li-doped ZnO films. The optical characteristics for thin films of (ZnO/Li) revealed that the absorbance, absorption coefficient, and optical conductivity increase as Li concentrations increase, whereas the transmittance and energy band gap decreased as Li concentrations increase. The Li-doped ZnO films' D.C. conductivity at low temperatures was compared to their A.C. electrical characteristics. It is shown that, for all various weight percentages of Li, the dielectric constant and dielectric loss decrease as the electric field frequency rises. All films have single activation energy, according to the electrical characteristics for D.C. measurements, and its value rises with an increase in the percentage of addition.

REFERENCES

1. J. Wang, H. Pan, X. Xu, H. Jin, W. Ma, S. Xiong, Q. Bao, Z. Tang, and Z. Ma, *ACS Appl. Mater. Interface*, **14**, No. 10: 12450 (2022); <https://doi.org/10.1021/acsami.1c22093>
2. E. Cheng, S. Huang, D. Chen, R. Huang, Q. Wang, Z. Hu, Y. Jiang, Z. Li, B. Zhao, and Z. Chen, *Acta Crystallogr. C: Struct. Chem.*, **75**, No. 7: 969 (2019); <https://doi.org/10.1107/S2053229619008222>
3. P. Bhat and S. K. Naveen Kumar, *J. Mater. Sci.: Mater. in Elect.*, **33**, No. 3: 1529 (2022); <https://doi.org/10.1007/s10854-021-07664-x>
4. K. Singh, H. Kaur, P.K. Sharma, G. Singh, and J. Singh, *Chemosphere*, **313**: 137322 (2023); <https://doi.org/10.1016/j.chemosphere.2022.137322>
5. G. Voicu, D. Miu, C. D. Ghitulica, S. I. Jinga, A. I. Nicoara, C. Busuioc, and A. M. Holban, *Ceram. Int.*, **46**, No. 3: 3904 (2020); <https://doi.org/10.1016/j.ceramint.2019.10.118>
6. X. Zhao, K. Nagashima, G. Zhang, T. Hosomi, H. Yoshida, Y. Akihiro, M. Kanai, W. Mizukami, Z. Zhu, T. Takahashi, and M. Suzuki, *Nano Lett.*, **20**, No. 1: 599 (2019); <https://doi.org/10.1021/acs.nanolett.9b04367>
7. L. Tang, Y. Jia, Z. Zhu, Y. Hua, J. Wu, Z. Zou, and Y. Zhou, *Molecules*, **27**, No. 3: 833 (2022); <https://doi.org/10.3390%2Fmolecules27030833>

8. M. Kwoka, E. Comini, D. Zappa, and J. Szuber, *Nanomaterials*, **12**, No. 15: 2666 (2022); <https://doi.org/10.3390%2Fnano12152666>
9. X. Zhan, F. Gao, Q. Zhuang, Y. Zhang, and J. Dang, *ACS Omega*, **7**, No. 10: 8960 (2022); <https://doi.org/10.1021%2Facsomega.1c07370>
10. S. Nandi, S. Kumar, and A. Misra, *Mater. Adv.*, **2**, No. 21: 6768 (2021); <https://doi.org/10.1039/D1MA00670C>
11. L. Fan, T. Xiao, C. Zhong, J. Wang, J. Chen, X. Wang, L. Peng, and W. Wu, *Cryst. Eng. Comm.*, **21**, No. 8: 1288 (2019); <https://doi.org/10.1039/c8ce01886c>
12. S. Y. Tsai, M. H. Hon, and Y. M. Lu, *J. Cryst. Growth*, **326**, No. 1: 85 (2011); <https://doi.org/10.1016/j.jcrysgro.2011.01.058>
13. S. Ghosh, G. G. Khan, A. Ghosh, S. Varma, and K. Mandal, *Cryst. Eng. Comm.*, **15**, No. 38: 7748 (2013); <https://doi.org/10.1039/c3ce40717a>
14. Z. Zhang, K. E. Knutsen, T. Merz, A. Y. Kuznetsov, B. G. Svensson, and L. J. Brillson, *J. Phys. D: Appl. Phys.*, **45**, No. 37: 375301 (2012); <https://doi.org/10.1088/0022-3727/45/37/375301>
15. S. Yu, L. Ding, H. Zheng, C. Xue, L. Chen, and W. Zhang, *Thin Solid Films*, **540**: 146 (2013); <https://doi.org/10.1016/j.tsf.2013.05.125>
16. M. Rahman, M. Kamruzzaman, J. A. Zapien, R. Afrose, T. K. Anam, M. N. Liton, M. A. Helal, and M. K. Khan, *Mater. Today Commun.*, **33**: 104278 (2022); <https://doi.org/10.1016/j.mtcomm.2022.104278>
17. K.-H. Wu, L.-Y. Peng, M. Januar, K.-C. Chiu, and K.-C. Liu, *Thin Solid Films*, **570**: 417 (2014); <https://doi.org/10.1016/j.tsf.2014.03.062>
18. D. Wang, J. Zhou, and G. Liu, *J. Alloys Compd.*, **481**, Nos. 1–2: 802 (2009); <https://doi.org/10.1016/j.jallcom.2009.03.111>
19. T. T. Wang, M. M. Dai, Y. J. Yan, H. Zhang, and Y. M. Yu, *Appl. Mech. Mater.*, **734**: 796 (2015); <https://doi.org/10.4028/www.scientific.net/AMM.734.796>

PACS numbers: 65.80.Ck, 66.70.Lm, 72.80.Tm, 81.05.ue, 81.07.Wx, 84.32.Tt

Electrophysical Properties and Thermal Conductivity of Composite Based on Zinc Oxide and Reduced Graphene Oxide (1 vol.%)

B. Turko¹, V. Vasil'ev¹, B. Sadovyi^{1,2}, R. Bihun¹, I. Pylypiv³,
V. Kapustianyk¹, and D. Leonov⁴

¹*Ivan Franko National University of Lviv,
50, Drahomanov Str.,
UA-79005 Lviv, Ukraine*

²*Institute of High Pressure Physics P.A.S.,
29/37, Sokolowska Str.,
01-142 Warsaw, Poland*

³*Systems Engineer II, SiTime,
10^a B. Khmelnytsky Str.,
UA-81100 Pustomyty, Lviv Region, Ukraine*

⁴*Technical Centre, N.A.S. of Ukraine,
13, Pokrovs'ka Str.,
UA-04070 Kyiv, Ukraine*

The thermal conductivity of the composite materials based on the commercial ZnO micropowder with reduced graphene oxide (1 vol.%) powder dispersed in the polymethylsiloxane (silicone oil) is measured using the radial heat-flow method. The thermal conductivity of the composite material based on the commercial ZnO micropowder with an average particle size of 50 μm and reduced graphene oxide is found to be 9.4 W/(m·K). At room temperature, the values of the dielectric permittivity at the measuring electric-field frequencies of 50 Hz and 1 MHz and the specific volume electrical resistance for the composite are obtained. An increase in the values of both the coefficient of thermal conductivity and the dielectric constant as well as a decrease in the specific volume electrical resistance due to a change in the volume fraction of reduced graphene oxide in the composite from 0.5 vol.% up to 1 vol.% are recorded.

Методом радіального теплового потоку вимірювали теплопровідність композиційних матеріалів на основі комерційного мікропорошку ZnO з відновленим порошком оксиду графену (1 об.%), диспергованого у поліметилсилоксані (силіконова олія). Встановлено, що теплопровідність композиційного матеріалу на основі комерційного мікропорошку ZnO

із середнім розміром частинок у 50 мкм і відновленого оксиду графену становить 9,4 Вт/(м·К). За кімнатної температури одержано значення діелектричної проникності на частотах вимірювального електричного поля у 50 Гц та 1 МГц і питомого об'ємного електричного опору для композиту. Було зафіксовано збільшення значень коефіцієнта теплопровідності й діелектричної проникності та зменшення питомого об'ємного електроопору за рахунок зміни об'ємної частки відновленого оксиду графену в композиті від 0,5 об.% до 1 об.%.

Key words: reduced graphene oxide, zinc oxide, composites, thermal conductivity, dielectric constant, specific volume electrical resistance.

Ключові слова: відновлений оксид графену, оксид Цинку, композити, теплопровідність, діелектрична проникність, питомий об'ємний електричний опір.

(Received 25 April, 2024)

1. INTRODUCTION

There is a problem with effective heat removal from heat-generating working elements of electronic devices, in particular processors, chipsets, computer video accelerators, high-power LEDs and lasers. If heat is not removed, this can lead not only to a significant deterioration in the performance of devices, but also to their failure [1]. To remove heat from the heat-generating working elements of electronic devices, thermal greases are widely used, which consist of a substance in a liquid state (for example, silicone oil, polyol, *etc.*) and a wide variety of fillers-thickeners (for example, Ag, SiO₂, ZnO, BN, AlN, Al₂O₃, graphite, graphene, carbon nanotubes, diamonds, *etc.*) [2].

Graphene has a record value of the coefficient of thermal conductivity among all known materials [3]; that is why it has attracted considerable scientific interest for its application in thermal management [1–7]. Graphene-containing commercial thermal greases are already available. For example, 'Baircool', 'Scythe Thermal Elixer G' and 'Hi-G Thermal Grease'. The thermal conductivity coefficients of the above thermal greases are in the range from 4 to 11 W/(m·K), and their composition is a trade secret. On the other hand, reduced graphene oxide (rGO) is more stable than graphene [8]. The thermal conductivity of the rGO can reach 2600 W/(m·K) and depends on the concentration of oxygen atoms in rGO [9]. In addition, according to [10], silicone thermal greases with rGO and hBN (hexagonal boron nitride) are promising.

In this work, in the continuation of our previous studies [3], we investigated the effect of increasing the volume fraction of reduced

graphene oxide from 0.5 vol.% to 1 vol.% on the specific volume resistance, dielectric permittivity, and thermal conductivity of the composite material based on ZnO, *r*GO, and polymethylsiloxane.

2. EXPERIMENT

The composite materials were produced by dispersing of ZnO micropowder with an average particle size of 50 μm (99.7%, UKRZINC, Kyiv, Ukraine) with *r*GO powder (0.5 vol.% or 1 vol.%, purchased from Sigma-Aldrich, Saint Louis, USA) in the polymethylsiloxane PMS 1000 (silicone oil, purchased from Sfera Sim, Lviv, Ukraine). The silicone oil and the fillers were taken in a volume ratio of 3:7. According to the certificate of analysis obtained from Sigma-Aldrich, the *r*GO contained 83% of carbon and 4% of nitrogen by mass.

Determination of the thermal conductivity of the composites was carried out by radial heat flow method [3, 11].

The values of dielectric permittivity and specific volume electrical resistance at room temperature and different frequencies of measuring electric field were obtained by LCR Meter IM3536-01 (HIOKI E. E. Corporation, Nagano, Japan).

The free software 'RealTemp' and 'CPU Burn-in v1.0' were used for testing of the thermally conductive composites. 'RealTemp' is a program for monitoring the temperature of computer processor cores. It was designed for Intel Single Core, Dual Core, Quad Core, and Core i7 processors. Each core in these processors has a digital thermal sensor. 'CPU Burn-in v1.0' is a program that 'heats' any processor with 'x86' architecture to the maximum possible operating temperature, accessible using a conventional software.

3. RESULT AND DISCUSSION

Figure 1 and Figure 2 presents the time dependences of the processor operating temperature. They were measured starting from the moment of turning on (Fig. 1)/off (Fig. 2) the stable load of the computer, using different layers of composite material between the surfaces of the processor and the copper heatsink used for heat dissipation. It has been found that heat was removed much better when using a composite with higher *r*GO concentration.

At room temperature, the obtained values of the dielectric permittivity ε at the frequencies of electric measuring field $\nu = 50$ Hz or $\nu = 1$ MHz and specific volume electrical resistance ρ ($\nu = 50$ Hz) for the two composites are given in Table.

The thermal-conductivity coefficient α [W/(m·K)] of the compo-

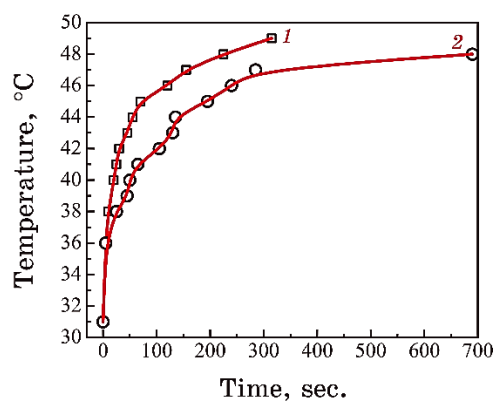


Fig. 1. The time dependences of the processor operating temperature, measured starting from the moment of turning on the stable load of the computer, using different layers of composite material between the surfaces of the processor and the copper heatsink used for heat dissipation: 1— composite based on ZnO, rGO (0.5 vol.%) and polymethylsiloxane; 2— composite based on ZnO, rGO (1 vol.%) and polymethylsiloxane.

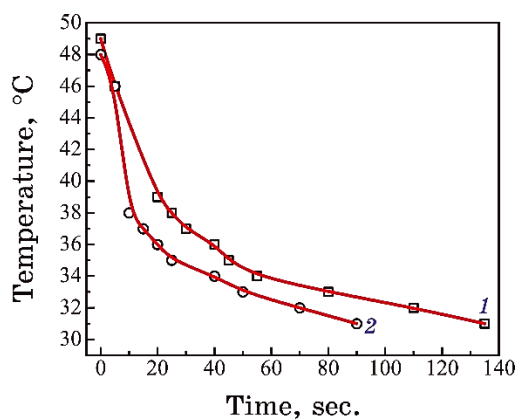


Fig. 2. The time dependences of the processor operating temperature, measured starting from the moment of turning off the stable load of the computer, using different layers of composite material between the surfaces of the processor and the copper heatsink used for heat dissipation: 1— composite based on ZnO, rGO (0.5 vol.%) and polymethylsiloxane; 2— composite based on ZnO, rGO (1 vol.%) and polymethylsiloxane.

sites is calculated on the basis of the following relation [3, 11]:

$$\alpha = K \frac{\ln(r_1 / r_2)}{2\pi l (T_1 - T_2)} UI, \quad (1)$$

TABLE. Room-temperature electrophysical parameters of the studied materials.

| Parameter | Composite based on ZnO and rGO (0.5 vol.%) powders [3] | Composite based on ZnO and rGO (1 vol.%) powders |
|---|--|--|
| Specific volume electrical resistance at frequency of 50 Hz, Ohm·cm | $8 \cdot 10^9$ | $2.5 \cdot 10^9$ |
| Dielectric constant at frequency of: | | |
| 50 Hz | 60 | 71 |
| 1 MHz | 43 | 54 |

where K is the factor of the axial heat loss through the plugs of the measuring cell (depends on the plug material and is calculated by reference to a sample with known thermal conductivity); r_1 and r_2 —the inner and outer radii of the cylindrical composite layer; T_1 and T_2 —the temperatures of the internal and external surfaces of the composite layers; l —the length of the cylindrical composite layer; U —the voltage on the heater; I —the current in a heater.

The value of the thermal conductivity of the composite materials based on ZnO powders with a grain size of 50 μm with rGO (1 vol.%), calculated according to Eq. (1), was found to be equal to 9.4 W/(m·K). The relative measurement error did not exceed 10%.

An increase in the values of the coefficient of thermal conductivity and dielectric constant and a decrease in the specific volume resistance due to a change in the volume fraction of reduced graphene oxide in the composite from 0.5 vol.% up to 1 vol.% are associated with the physical properties of rGO ($\alpha = 2600$ W/(m·K), $\varepsilon = 1130$ ($\nu = 50$ Hz), $\rho = 1.4 \cdot 10^{-2}$ Ohm·cm), the Maxwell–Wagnare–Sillars interfacial polarization and more formation of the microcapacitor structures [3].

4. CONCLUSIONS

In summary, the coefficients of thermal conductivity of the composite material based on the ZnO with rGO (1 vol.%) powders dispersed in the polymethylsiloxane were determined by radial heat flow method. It was found to be equal to 9.4 W/(m·K). The differences in the electrophysical properties of rGO (0.5 vol.%)–ZnO–polymethylsiloxane and rGO (1 vol.%)–ZnO–polymethylsiloxane composites are explained by an increase in the Maxwell–Wagnare–Sillars interfacial polarization, the concentration of microcapacitor

structures and reduced graphene oxide. The high performance of rGO–ZnO composite synthesized by a simple and facile process in this work shows promising potential in thermal control of the electronic devices.

ACKNOWLEDGMENTS

This work was done due to the supports of the Ministry of Education and Science of Ukraine (Project No. 0123U101880) and Long-Term Funding by the Polish Academy of Sciences and U.S. National Academy of Sciences (Project No. PAN.BFB.S.BWZ.369.022.2023).

REFERENCES

1. J. Khan, S. A. Momin, and M. Mariatti, *Carbon*, **168**: 65 (2020); <https://doi.org/10.1016/j.carbon.2020.06.012>
2. W. Xing, Y. Xu, C. Song, and T. Deng, *Nanomaterials*, **12**: 3365 (2022); <https://doi.org/10.3390/nano12193365>
3. B. Turko, V. Vasil'ev, and V. Kapustianyk, *Nanosistemi, Nanomateriali, Nanotehnologii*, **21**: 569 (2023); <https://doi.org/10.15407/nnn.21.03.569>
4. S. Ali, F. Ahmad, P. S. M. Yusoff, N. Muhamad, E. Onate, M. R. Raza, and K. Malik, *Composites Part A: Applied Science and Manufacturing*, **144**: 106357 (2021); <https://doi.org/10.1016/j.compositesa.2021.106357>
5. P. Huang, Y. Li, G. Yang, Z.-X. Li, Y.-Q. Li, N. Hu, S.-Y. Fu, and K. S. Novoselov, *Nano Materials Science*, **3**: 1 (2021); <https://doi.org/10.1016/j.nanoms.2020.09.001>
6. Q. Ge, J. Chu, W. Cao, F. Yi, Z. Ran, Z. Jin, B. Mao, Z. Li, and K. S. Novoselov, *Advanced Functional Materials*, **32**: 2205934 (2022); <https://doi.org/10.1002/adfm.202205934>
7. D. D. L. Chung, *Materials Chemistry and Physics*, **309**: 128432 (2023); <https://doi.org/10.1016/j.matchemphys.2023.128432>
8. R. Kamatchi and K. G. Kannan, *International Journal of Renewable Energy Research*, **8**: 313 (2018); <https://doi.org/10.20508/ijrer.v8i1.6766.g7305>
9. Y. Zeng, T. Li, Y. Yao, T. Li, L. Hu, and A. Marconnet, *Adv. Funct. Mater.*, **29**: 1901388 (2019); <https://doi.org/10.1016/j.jallcom.2010.03.076>
10. W. Liang, X. Ge, J. Ge, T. Li, T. Zhao, X. Chen, M. Zhang, J. Ji, X. Pang, and R. Liu, *Nanomaterials*, **9**: 938 (2019); <https://doi.org/10.3390/nano9070938>
11. B. I. Turko, V. B. Kapustianyk, V. P. Rudyk, and Y. V. Rudyk, *J. Nano-Electron. Phys.*, **8**: 02004 (2016); [https://doi.org/10.21272/jnep.8\(2\).02004](https://doi.org/10.21272/jnep.8(2).02004)

PACS numbers: 61.46.Bc, 71.20.-b, 73.22.-f, 81.05.Zx, 81.07.Pr, 82.35.Np

Design, Optimization, Structural and Electronic Properties of PVA/ZnO/SnO₂ Nanostructures for Nanoelectronics Fields

Ali S. Hasan¹ and Ahmed Hashim²

¹*College of materials Engineering,
Department of Physics,
University of Babylon,
Hillah, Iraq*

²*College of Education for Pure Sciences,
Department of Physics,
University of Babylon,
Hillah, Iraq*

This work aims to design the new polyvinyl alcohol (PVA)/zinc oxide (ZnO)/tin oxide (SnO₂) nanostructures as potential nanomaterials to utilize in numerous nanoelectronics devices. The optimization, structural and electronic properties of designed nanostructures are investigated. The results show that the electronic properties of PVA are enhanced by adding ZnO/SnO₂ nanostructures. The energy gap is reduced from 5.147 eV for PVA to 2.893 eV with adding ZnO/SnO₂ nanostructures. Finally, obtained results on electronic properties show that the PVA/ZnO/SnO₂ nanocomposites manifest excellent electronic properties, which made them as promising nanomaterials for nanoelectronics applications.

Цю роботу спрямовано на розробку нових наноструктур полівінілового спирту (ПВС)/оксиду Цинку (ZnO)/оксиду Стануму (SnO₂) як потенційних наноматеріалів для використання у багатьох пристроях наноелектроніки. Досліджено оптимізаційні, структурні й електронні властивості розроблених наноструктур. Результати показали, що електронні властивості ПВС поліпшуються завдяки додаванню наноструктур ZnO/SnO₂. Енергетична щільність зменшується від 5,147 eV для ПВС до 2,893 eV з додаванням наноструктур ZnO/SnO₂. Нарешті, одержані результати стосовно електронних властивостей показали, що нанокompозити ПВС/ZnO/SnO₂ мають чудові електронні властивості, що робить їх перспективними наноматеріалами для застосування в наноелектроніці.

Key words: PVA, SnO₂, ZnO, nanocomposite, energy gap, nanoelectronics.

Ключові слова: полівініловий спирт, SnO₂, ZnO, нанокompозит, енерге-

тична щілина, наноелектроніка.

(Received 18 August, 2023)

1. INTRODUCTION

Recent years have seen a rise in the use of nanocomposite materials in scientific research, with the promotion of physical properties and changes in energy storage technologies as essential components for practical applications. The current applications of nanocomposites include high-energy batteries, fuel cells, microwave absorbers, optoelectronics, gas sensors, and UV filters [1]. Polyvinyl alcohol (PVA) is an atactic, semi-crystalline polymeric material that possesses excellent biodegradability, biocompatibility, useful mechanical properties, excellent optical properties, and non-toxicity, hence its wide range of applications. Other excellent properties of polyvinyl alcohol include thermal stability, water solubility, excellent optical transmission, and non-corrosiveness. These features, especially its optical properties such as the refractive index and energy gap, promote its industrial and technological uses as an optoelectronic material, a coating material, a solar cell component, a super capacitor component, and a component of several kinds of sensors [2].

Because of its large exciton binding energy (60 meV) and direct band gap energy (3.37 eV), the applications of heterostructure based on zinc oxide attracted great interest [3]. ZnO is an interesting semiconductor for development of many advanced technologies because of its direct wide band gap and optical transparency, which lead to good optical and electronic properties. They are promising candidates in flat panel displays to see through front faced electrodes, light-emitting devices, solar cell and gas sensors [4].

Tin oxide (SnO_2) is an *n*-type semiconductor that possesses a high optical gap (3.6–4.0 eV) and has a variety of applications. Some of these applications include secondary lithium batteries, solar cells, gas sensors, and glass electrodes. It has a structure known as tetragonal rutile, and the inherent oxygen vacancies in this structure operate as an *n*-type dopant [5].

There many studies on metal oxides doped polymers to apply in various electronics and optical fields [6–10]. This work aims to design of PVA/ZnO/ SnO_2 nanocomposites as potential nanomaterials to use in many nanoelectronics fields.

2. COMPUTATIONAL DETAIL

In this work, all the geometric structures are optimized and consid-

ered by density functional theory (DFT) with B3LYP [11] functional and the 6-31G (*d*) basis set, which applied in Gaussian 09 software [12]. This chemical model has been extensively used to relax the geometry and calculate the optoelectronic properties, such as total energies (E_T), Fermi level energy (E_{Fl}), orbital distributions (HOMO, LUMO), energy gap (E_g), and electronic-transition energies. These methods are not only encouraging more profound understanding of the association between the optoelectronic properties and chemical structures of the molecule structures but also may be used to design new molecule structures. To evaluate the reactivity and the stability of the composites, DFT-based descriptors were calculated [12, 13]:

$$\mu = \left(\frac{\partial E}{\partial N} \right)_{V(\mathbf{r}), T}, \quad (1)$$

$$\eta = \frac{1}{2} \left(\frac{\partial^2 E}{\partial N^2} \right)_{V(\mathbf{r}), T}, \quad (2)$$

$$S = \frac{1}{2\eta}, \quad (3)$$

$$\omega = \frac{\mu^2}{2\eta} \quad (4)$$

with I_P , E_A , μ , η , S , and ω —the ionization potential, electron affinity, chemical hardness, chemical softness, and electrophilicity, respectively, while E , N and $V(\mathbf{r})$ are the total electron energy, number of electrons, and external potential, respectively. There are two different methods to calculate the above the global quantities. The first is a finite difference approximation, which based on the differences of total electronic energies, when an electron is removed or added in accordance with the neutral molecule.

The second is Koopmans' theorem, which based on the differences between the HOMO and LUMO energies for the neutral molecule [12]. Using a finite difference approximation, the global quantities can be given by [14–16] as follow:

$$I_P = -E_{\text{HOMO}}, \quad E_A = -E_{\text{LUMO}}, \quad \eta = \frac{(I_P - E_A)}{2}. \quad (5)$$

Then, using Koopmans' theorem, the above equations can be given as follow:

$$E_{Fl} = \frac{E_{\text{HOMO}} + E_{\text{LUMO}}}{2}, \quad \eta = \frac{E_{\text{HOMO}} - E_{\text{LUMO}}}{2}. \quad (6)$$

3. RESULTS AND DISCUSSION

The molecules studied are represented in Figs. 1, 2. Computational analyses were performed using the Gaussian 09 suite of programs [11, 15] and the density functional theory (DFT) methods.

Figures 2 and 3 display the geometrical optimization of the suggested structures investigated in this research after relaxing. These structures include polyvinyl alcohol (PVA), and PVA-ZnO-SnO₂. The studied-geometry optimization yielded results, which agree well with experimental data, particularly, in terms of the composites' structural properties. The relaxed structures under examination exhibited carbon-carbon-bond lengths within the ranges of C-C: 1.534 Å, C=C: 1.361 Å, C=C: 1.422 Å, C-H: 1.092 Å, C-O: 1.23 Å, O-H: 0.978 Å, Zn-O: 1.98 Å and Sn-O: 2.012 Å, as shown in Figs. 2 and

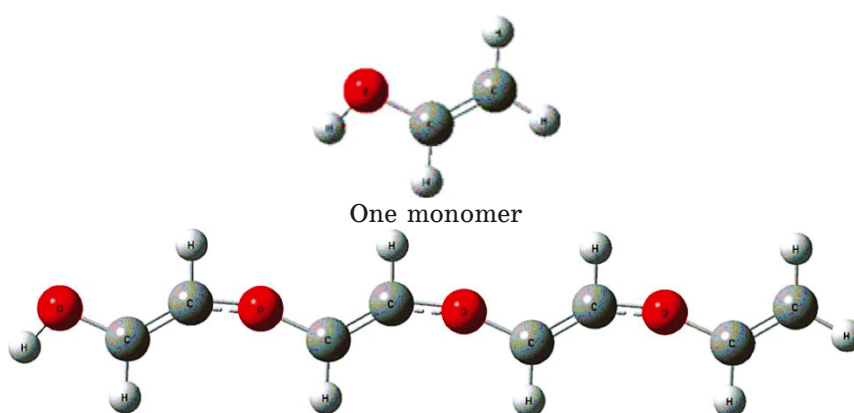


Fig. 1. Structure of PVA before relaxing.

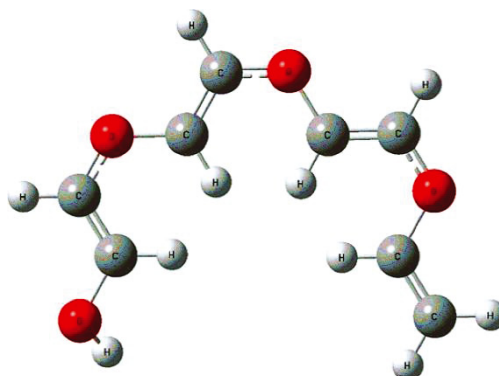


Fig. 2. Structure of PVA after relaxing.

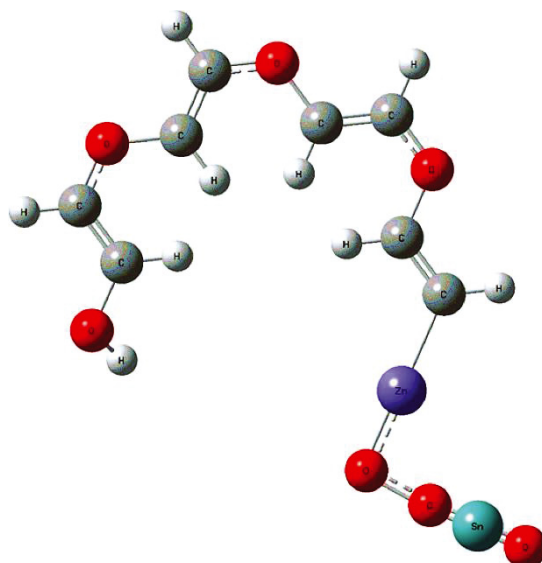


Fig. 3. Structure of PVA-ZnO-SnO₂ composites.

3. These findings are consistent with the bond lengths observed in aromatic rings [12, 13].

The atoms bonded to carbon and oxygen can vary in type, size, and electronic effects, and the presence of different atoms (Zn, Sn) adjacent to carbon and oxygen can lead to changes in the chemical environment and consequently affect the bond length. Oxidation of carbon or oxygen in the molecule can also influence the chemical environment and, consequently, the bond length. For example, the carbon in the C=O bond in ketones may have a different oxidation state compared to the carbon in the C-O bond in alcohols. Additionally, interactions between adjacent molecules and electrostatic forces between them can also affect the bond length. The presence of positive or negative electrostatic charges in neighbouring molecules can influence electron transfer, and factors such as transition-state effects, hydrogen-bonding interactions, and bond polarization can influence the bond length too. All of these factors contribute to determining the bond length between carbon and oxygen in organic molecules [13–15].

The Geometrical Optimization of Polymeric Composites, PVA and PVA-ZnO-SnO₂. It possesses structural properties, which agree well with the experimental data in terms of bond length and bond strength, and this indicates that these materials show interactions and properties that are well compatible with each other from the physical and chemical points of view as shown in Fig. 3. This means

that they are able to interact with each other effectively and form new compounds or compounds in a consistent and homogeneous manner. This compatibility indicates that the said materials may be suitable for use in joint applications or in forming composite compositions that benefit from their combined interactions [11, 12, 16].

Table shows the ground state calculations of the polymeric composites in this work at the minimum energy. These calculations are included the total energy in a.u., I_p and E_A in [eV] calculated due to Koopmans' theorem, forbidden energy gap E_g in [eV], S in [eV^{-1}], η in [eV], μ in [eV], and ω in [eV]. In addition, the calculations are included the density of states (DOS), HOMO energies (E_{HOMO}) and LUMO energies (E_{LUMO}).

The total energy E_T of polymeric composites under study is very small; this result is a reflection of the binding energy of each structure. Thus, polymeric composites with lower total energy may have limited energy storage capabilities. This is due to the specific material selection or composition of the composites that is desirable in some applications where lightweight materials are required [11, 17].

In addition, both the I_p and the E_A differ in value, where I_p and E_A for PVA-ZnO-SnO₂ are higher than for PVA. A higher value indicates that the material has a stronger tendency to retain its electrons (higher ionization potential) or to attract additional electrons (higher electron affinity). These differences in electronic properties can arise from variations in the chemical composition, structure, or bonding characteristics of the polymeric composites. Factors such as the presence of different functional groups, molecular weight, or the arrangement of atoms within the composite can influence these electronic properties [13, 18].

The above results are corresponding to S , η and ω of the structures PVA and PVA-ZnO-SnO₂; the results showed that the polymeric composites has large value of η and ω . This indicates a greater energy requirement meaning that the system is relatively more stable and less reactive towards electron transfer, while small value of S , whereas shown in Table. But, for PVA and PVA-ZnO-SnO₂, the value of chemical hardness and electrophilicity decreases, while the chemical softness increases, and this is due to the compatibility and good distribution of materials within the polymer, where you indicate higher values of chemical softness indicating a lower energy requirement for electron transfer, implying higher reactivity, and a greater tendency to undergo electronic changes [14, 19].

The results indicate a decrease in the E_g values, when adding ZnO-SnO₂ to PVA. This is an indication of the closeness of the HOMO and LUMO values to each other and, thus, the possibility of an electronic transition between the valence band and the conductivity one.

TABLE. Calculation total energies (E_T), HOMO energies (E_{HOMO}), LUMO energies (E_{LUMO}), LUMO energies (E_{LUMO}), electronic band gap (E_g), Fermi level energies (E_{FL}), ionization potential (I_p), electron affinity (E_A), chemical hardness (μ), chemical hardness (η), chemical softness (S) and electrophilicity index (ω) *via* using DFT B3LYP/6-31 (*d*) calculation in units of [eV].

| Sample | E_T | HOMO | LUMO | E_g | I_p | E_A | E_{FL} | η | S | ω |
|--------------------------|-----------|--------|--------|-------|-------|-------|-----------------|--------|-------|----------|
| PVA | -7325.547 | -7.801 | -2.654 | 5.147 | 7.801 | 2.655 | -5.22 | 2.573 | 0.194 | 5.311 |
| PVA-ZnO-SnO ₂ | -5325.278 | -5.147 | -2.254 | 2.893 | 5.148 | 2.255 | -3.70 | 1.446 | 0.346 | 4.735 |

In addition, when these materials are added to the polymer, they interact and interfere with the existing polymer structures. This reaction leads to the formation of new energy states within the polymer, and these states are less energetic than the original states that results in a decrease in the value of the energy gap [12, 14].

Through Figs. 4 and 5, one can see that the HOMO and LUMO for the PVA-ZnO-SnO₂ are more stable in comparison with PVA. There is a clear difference in the electronic distribution of shipments due to the withdrawal of shipments. HOMO (Highest Occupied Molecular Orbital) and LUMO (Lowest Unoccupied Molecular Orbital) are commonly used in the field of molecular orbital theory

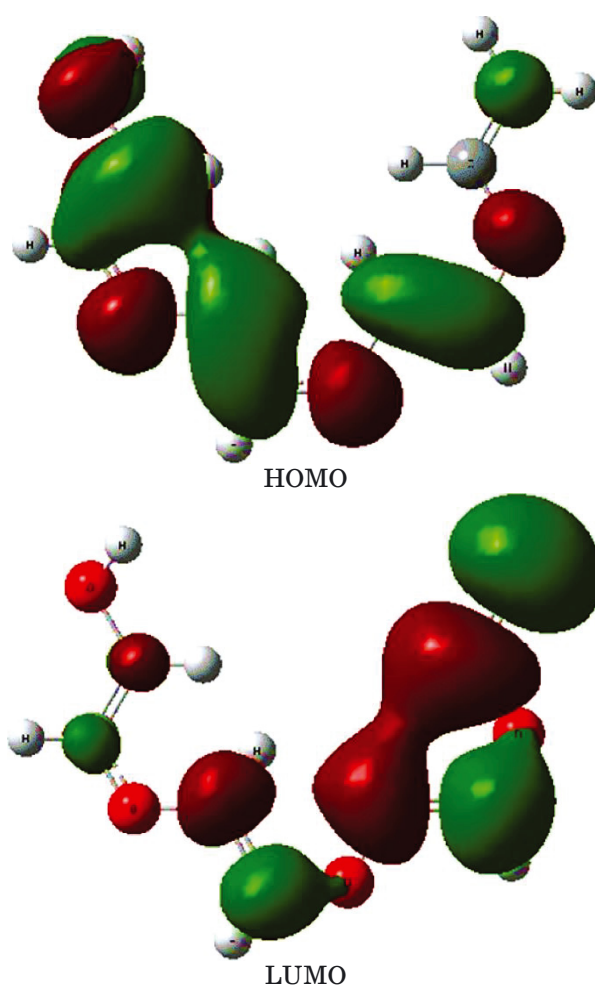


Fig. 4. The shapes of HOMO and LUMO for PVA.

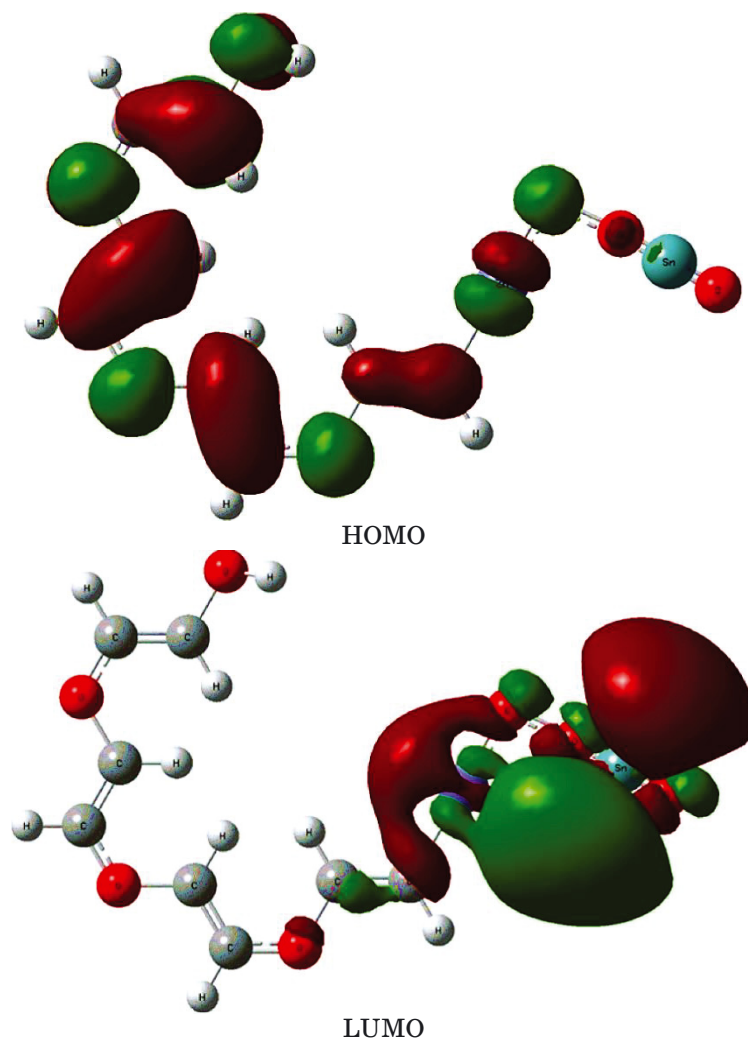


Fig. 5. The shapes of HOMO and LUMO for PVA-ZnO-SnO₂ composites.

to describe the energy levels of electrons within the molecule. These energy levels play a significant role in determining the chemical and physical properties of the molecule [14, 20, 21].

The HOMO represents the highest energy level occupied by electrons in a molecule in its ground state; it corresponds to the valence electrons, which are involved in bonding and determining the reactivity of the molecule. The energy of the HOMO is an indicator of the molecule ability to donate electrons during chemical reactions. Figures 4 and 5 show the shapes of HOMO and LUMO for these structures drawn by Gaussian View 5.0.8 using B3LYP/6-31G (*d*) method.

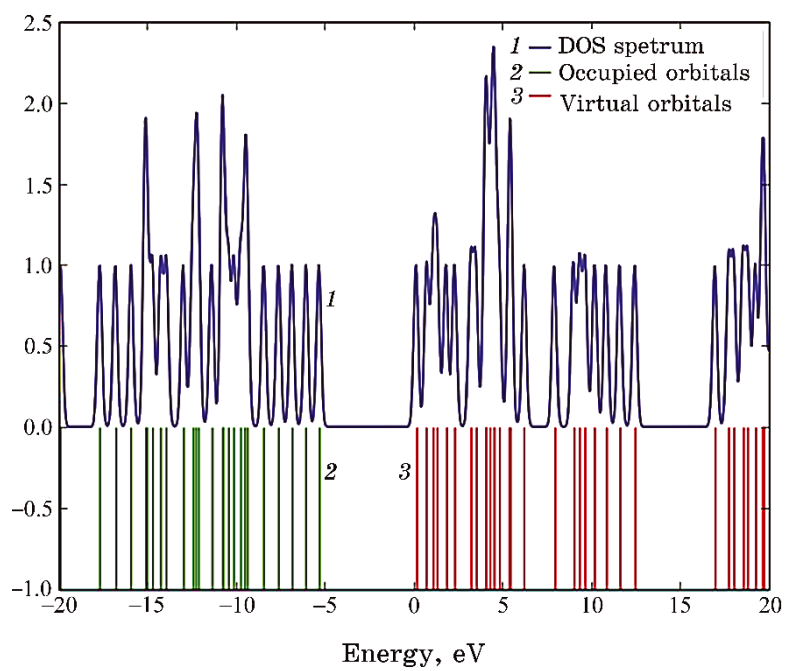


Fig. 6. Density of states (DOS) for PVA.

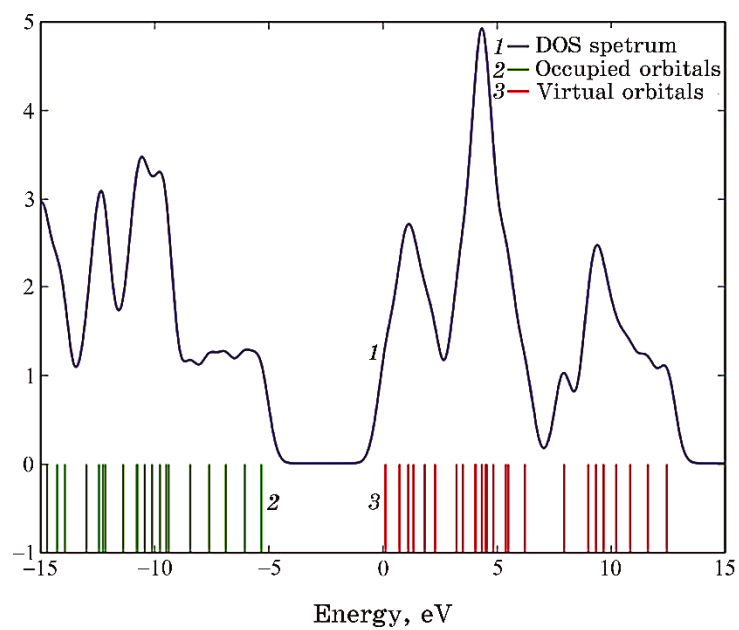


Fig. 7. Density of states (DOS) for PVA-ZnO-SnO₂ composites.

The DOS provides valuable insights into the electronic structure and properties of materials. It helps determine various properties, such as electrical conductivity, thermal conductivity, and optical properties. By analysing the DOS, one can study phenomena like band gaps, energy bands, and Fermi energy, which are essential for understanding the behaviour of electrons in solids.

The DOS is typically represented as a function of energy, denoted as $g(E)$, where E represents the energy level. It describes the number of states per unit volume per unit energy range at a particular energy level. Mathematically, the DOS can be expressed by [12, 15] as follows:

$$g(E) = (1/V)dN(E)/dE,$$

where V is the volume of the material and $dN(E)/dE$ represents the change in the number of states with respect to energy.

Through the density diagram of the polymeric compounds and, as shown in Figs. 6 and 7, there is a clear energy gap between the valence band (the highest occupied energy band) and the conduction band (the lowest unoccupied energy band). In DOS, this results in a region of zero or a very low density of states within the band gap. The DOS is relatively high in the valence and conduction bands, indicating the availability of occupied or excited electronic states.

4. CONCLUSION

The current study includes design of PVA/ZnO/SnO₂ nanocomposites as new nanomaterials to utilize in numerous nanoelectronics devices. The optimization of structural and electronic characteristics of PVA/ZnO/SnO₂ nanocomposites is studied. The results demonstrated that the electronic characteristics of PVA were enhanced with adding ZnO/SnO₂ nanostructures. The energy gap reduced from 5.147 eV for PVA to 2.893 eV with adding ZnO/SnO₂ nanostructures. The final results indicate that the PVA/ZnO/SnO₂ nanocomposites have excellent electronic characteristics, which made them as promising nanomaterials for nanoelectronics fields.

REFERENCES

1. A. N. Al-Hakimi, G. M. Asnag, F. Alminderej, I. A. Alhagri, S. M. Al-Hazmy, and T. F. Qahtan, *Crystals*, **13**: 1 (2023); <https://doi.org/10.3390/cryst13010135>
2. T. O. Owolabi and M. A. Abd Rahman, *Polymers*, **13**: 1 (2021); <https://doi.org/10.3390/polym13162697>
3. A. H. Selçuk, E. Orhan, S. Bilge Ocak, A. B. Selçuk, and U. Gökmen, *Mate-*

- rials Science–Poland*, **35**, No. 4: 885 (2017); doi:10.1515/msp-2017-0108
4. V. Sushmitha, V. Maragatham, P. D. Raj, and M. Sridharan, *IOP Conf. Series: Materials Science and Engineering*, **310**: 1 (2018); doi:10.1088/1757-899X/310/1/012022
 5. A. M. Ismail and Fawzy G. El Desouky, *Scientific Reports*, **13**: 1 (2023); <https://doi.org/10.1038/s41598-023-32090-w>
 6. A. Hashim, A. Hadi, and M. H. Abbas, *Opt. Quant. Electron.*, **55**: 642 (2023); <https://doi.org/10.1007/s11082-023-04929-z>
 7. A. Hashim, A. Hadi, and M. H. Abbas, *Silicon*, **15**: 6431 (2023); <https://doi.org/10.1007/s12633-023-02529-w>
 8. A. Hashim, M. H. Abbas, N. A.-H. Al-Aaraji, and A. Hadi, *J. Inorg. Organomet. Polym.*, **33**: 1 (2023); <https://doi.org/10.1007/s10904-022-02485-9>
 9. A. Hashim, M. H. Abbas, N. A.-H. Al-Aaraji, and A. Hadi, *Silicon*, **15**: 1283 (2023); <https://doi.org/10.1007/s12633-022-02104-9>
 10. A. Hashim, A. Hadi, N. A. H. Al-Aaraji, and F. L. Rashid, *Silicon*, **15**: 5725 (2023); <https://doi.org/10.1007/s12633-023-02471-x>
 11. M. H. Kadhim, A. S. Hasan, M. A. Akraa, and A. Y. Layla, *Journal of Ovonic Research*, **17**, No. 3: 273 (2021); doi.org/10.15251/jor.2021.173.273
 12. A. S. Hasan and H. I. Abbood, *Journal of Kufa–Physics*, **8**, No. 1: 59 (2016); <https://journal.uokufa.edu.iq/index.php/jkp/article/view/7474>
 13. F. Q. Mohammed, M. S. Edan, A. S. Hasan, and A. J. Haider, *Key Engineering Materials*, **886**, No. 1: 97 (2021); doi.org/10.4028/www.scientific.net/KEM.886.97
 14. A. S. Hasan, B. Y. Kadem, M. A. Akraa, and A. K. Hassan, *Digest Journal of Nanomaterials and Biostructures*, **15**, No. 1: 197 (2020); doi.org/10.15251/djnb.2020.151.197
 15. A. S. Hasan, F. Q. Mohammed, and M. M. Takz, *Journal of Mechanical Engineering Research and Developments*, **43**, No. 1: 11 (2020); [https://jmerd.net/Paper/Vol.43,No.1\(2020\)/11-17](https://jmerd.net/Paper/Vol.43,No.1(2020)/11-17)
 16. S. A. Habeeb, A. S. Hasan, Tālu, and A. J. Jawad, *Iranian Journal of Chemistry and Chemical Engineering*, **40**, No. 5: 1616 (2021); doi.org/10.30492/ijcce.2020.40535
 17. S. H. Abud, A. S. Hasan, M. Almaamori, and N. Bayan, *Journal of Physics: Conference Series*, **1818**, No. 1: 012235 (2021); doi.org/10.1088/1742-6596/1818/1/012235
 18. A. D. T. Thamira, A. S. H. Hasan, R. G. K. Kadhim, W. G. B. Bakheet, and H. I. Abbood, *Journal of Petroleum Research and Studies*, **8**, No. 3: 25 (2021); doi.org/10.52716/jprs.v8i3.228
 19. B. Y. Kadem, M. Al-Hashimi, A. S. Hasan, R. G. Kadhim, Y. Rahaq, and A. K. Hassan, *Journal of Materials Science: Materials in Electronics*, **29**, No. 1: 19287 (2018); doi.org/10.1007/s10854-018-0055-4
 20. S. K. Jebur, A. J. Braihi, and A. S. Hassan, *Materials Today: Proceedings*, **49**, No. 7: 2733 (2022); doi.org/10.1016/j.matpr.2021.09.255
 21. A. A. Ati, A. H. Abdalsalam, and A. S. Hasan, *Journal of Materials Science: Materials in Electronics*, **32**, No. 3: 3019 (2021); doi.org/10.1007/s10854-020-05053-4

PACS numbers: 72.80.Tm, 77.22.Ch, 77.22.Gm, 78.20.Ci, 81.07.Pr, 81.40.Tv, 82.35.Np

Fabrication and Enhanced Dielectric Properties of PVA– Cr₂O₃–Sb₂O₃ Nanocomposites for Electrical and Electronics Applications

Ahmed Hashim and M. H. Abbas

*College of Education for Pure Sciences,
Department of Physics,
University of Babylon,
Hillah, Iraq*

In present work, nanocomposites films have been prepared from Cr₂O₃–Sb₂O₃-nanoparticles-doped PVA to exploit in different electrical and electronics applications. The dielectric properties of PVA–Cr₂O₃–Sb₂O₃ nanocomposites were tested at frequency ranged from 100 Hz to 5 MHz. The experimental results confirmed that both the dielectric constant and the dielectric loss of PVA–Cr₂O₃–Sb₂O₃ nanocomposites were reduced, whereas the electrical conductivity was increased with raising the frequency. The dielectric constant, dielectric loss, and A.C. electrical conductivity of PVA were increased with raising the Cr₂O₃–Sb₂O₃-nanoparticles' concentration. The results illustrated that the PVA–Cr₂O₃–Sb₂O₃ nanocomposites can be suitable in different electrical and electronics applications.

У цій роботі нанокompозитні плівки було виготовлено з полівінілового спирту (ПВС), легованого наночастинками Cr₂O₃–Sb₂O₃, для використання в різних електричних та електронних застосуваннях. Діелектричні властивості нанокompозитів ПВС–Cr₂O₃–Sb₂O₃ перевіряли в діапазоні частот від 100 Гц до 5 МГц. Експериментальні результати підтвердили, що діелектрична проникність і діелектричні втрати нанокompозитів ПВС–Cr₂O₃–Sb₂O₃ зменшуються, тоді як електропровідність зростає зі збільшенням частоти. Діелектрична проникність, діелектричні втрати й електропровідність змінного струму ПВС зростали зі збільшенням концентрації наночастинок Cr₂O₃–Sb₂O₃. Кінцеві результати показали, що нанокompозити ПВС–Cr₂O₃–Sb₂O₃ можуть бути придатними для різних електричних та електронних застосувань.

Key words: Cr₂O₃, Sb₂O₃, PVA, nanocomposites, dielectric properties.

Ключові слова: Cr₂O₃, Sb₂O₃, полівініловий спирт, нанокompозити, діелектричні властивості.

(Received 18 August, 2023; in revised form, 26 August, 2023)

1. INTRODUCTION

Today, intercalated polymer nanocomposites (NCs) with nanometal oxides are gaining significant interest in both academic and industrial scenarios. It involves the selection of polymers and metal oxides on the nanoscale from various numbers of polymers and nanomaterials available today for the desired properties. Metal oxides are well-known materials for sensors, photocatalytic, fuel cells, coatings, optoelectronic devices, *etc.* [1]. The substrate/matrix role of organic polymers, where the substantial dispersion of inorganic oxides results in the composite formation, finds enormous applicability. The various fields, where these heterostructures involving polymeric matrix find their applicability, include optoelectronics, automotive and aerospace industries, *etc.* Polymer composites have been found to be effective in dye degradation compared to other materials. The properties of these polymeric nanocomposites get affected by various factors like interfacial bonding, the embedding of nanoparticles (NPs), and the morphological behaviour of the dispersed nanoparticles in the polymeric substrate [2].

Organic–inorganic hybrid optical materials are extremely valuable for a technological perspective. Hybrid compositions with remarkable properties may emerge once the relationships between the properties of inorganic elements and polymer matrices are clarified. Polymeric nanocomposites, because of their interesting properties, are also a significant class in the field of applied materials science technology. Polymer composites display a variety of fascinating optical features, including a high/low refractive index, tailored absorption/emission spectra, and strong optical nonlinearities. Hybrids are eligible for potential optoelectronic applications because they possess such rare properties [3].

The new characteristics of PVA-based materials have made them appropriate for a range of applications, especially, optoelectronic technology. One might modify the behaviour of optoelectronic devices by dispersing one or more nanofiller (such as metal oxide, rare earth salt, *etc.*) inside the PVA matrix [4].

Metal-oxide materials have increasing demand in the scientific community due to their eco-friendliness, stability, natural abundance, ease of synthesis, and wider application purposes. Different types of metal oxides and their nanomaterials are being used in an extensive variety of fields like adsorbents, gas sensors, photovoltaics, photoelectronics, and electrochemical, fuel cells, ceramics and other biological applications [5]. Antimony trioxide (Sb_2O_3) is a sem-

iconducting material and possesses excellent catalytic performance in photochemistry and superior chemical stability in flame retardation. So far, much attention has been focused on the synthesis of Sb₂O₃ films, and the exploration of their novel properties [6].

Nanocomposites materials of polymer as a matrix doped with nanoparticles have huge applications of optical, electronics and optoelectronics fields [7–33]. The present work deals with preparation and dielectric properties of PVA-Cr₂O₃-Sb₂O₃-nanocomposites' films to exploit in different electrical and electronics applications.

2. MATERIALS AND METHODS

The PVA-Cr₂O₃-Sb₂O₃ nanocomposites films were prepared using casting process. The PVA film was fabricated by dissolving of 0.5 gm PVA in 30 ml of distilled water by using magnetic stirrer to mix the polymer for 1 hour to obtain more homogeneous solution. The Cr₂O₃ and Sb₂O₃ nanoparticles were added to PVA with constant ratio 1:1, and different contents are 2.2%, 4.4% and 6.6%. The dielectric properties of PVA-Cr₂O₃-Sb₂O₃-nanocomposites' films were measured at frequency range from 100 Hz to 5·10⁶ Hz using LCR-meter type (HIOKI 3532-50 LCR HI TESTER). The dielectric constant (ϵ') is calculated by [34] as follows:

$$\epsilon' = C_p/C_0, \quad (2)$$

where C_p is the capacitance of matter and C_0 is the capacitance of vacuum.

Dielectric loss (ϵ'') is determined by [35] as follows:

$$\epsilon'' = \epsilon' D, \quad (2)$$

where D is the dispersion factor.

The A.C. electrical conductivity is obtained by [36] as follows:

$$\sigma_{A.C.} = 2\pi f \epsilon' D \epsilon_0. \quad (3)$$

3. RESULTS AND DISCUSSION

The performance of dielectric constant and dielectric loss for PVA-Cr₂O₃-Sb₂O₃ nanocomposites with frequency and Cr₂O₃-Sb₂O₃-NPs' concentration are demonstrated in Figs. 1–4, respectively. Because the values of dielectric constant drop with increasing frequency, the dipole is difficult to spin accurately and easily, and its oscillation begins to occur after this field. This behaviour is because of the die-

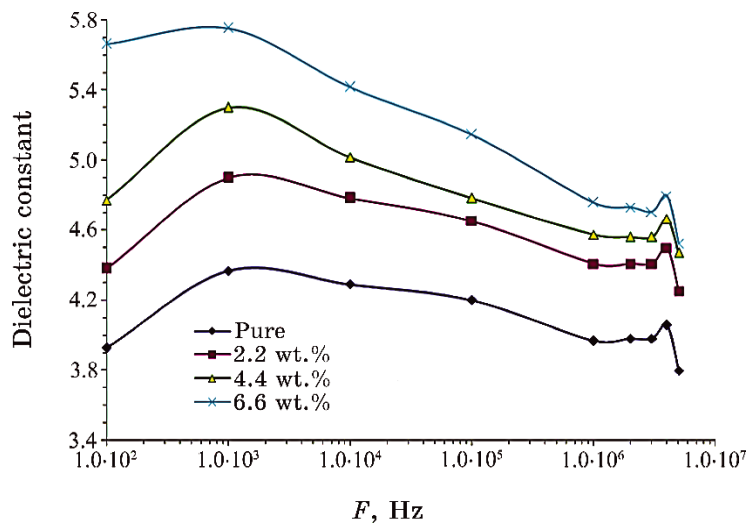


Fig. 1. Dielectric-constant variation for PVA-Cr₂O₃-Sb₂O₃ nanocomposites with frequency.

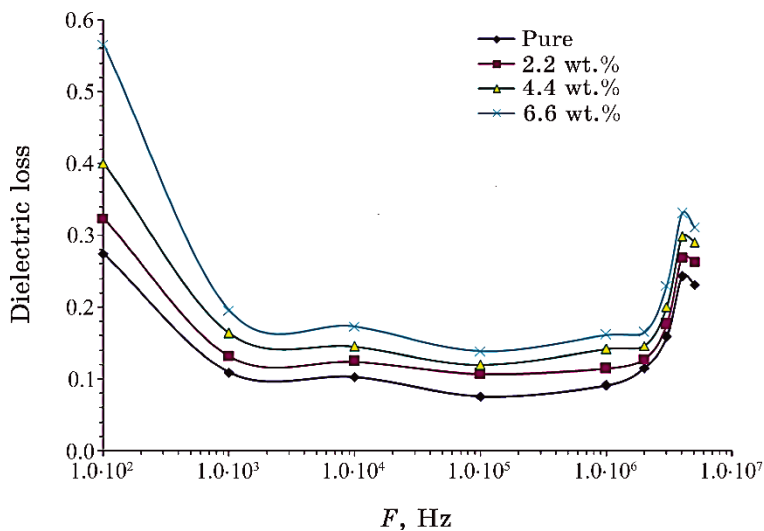


Fig. 2. Dielectric-loss behaviour for PVA-Cr₂O₃-Sb₂O₃ nanocomposites with frequency.

lectric-constant values decrease. In addition, there was no evidence of relaxation peaks, which points to a non-Debye response.

These figures show that the motion of ions is recognized as the fundamental foundation of nanocomposite dielectric loss at lower frequencies, leading to a decrease in dielectric loss as a function of

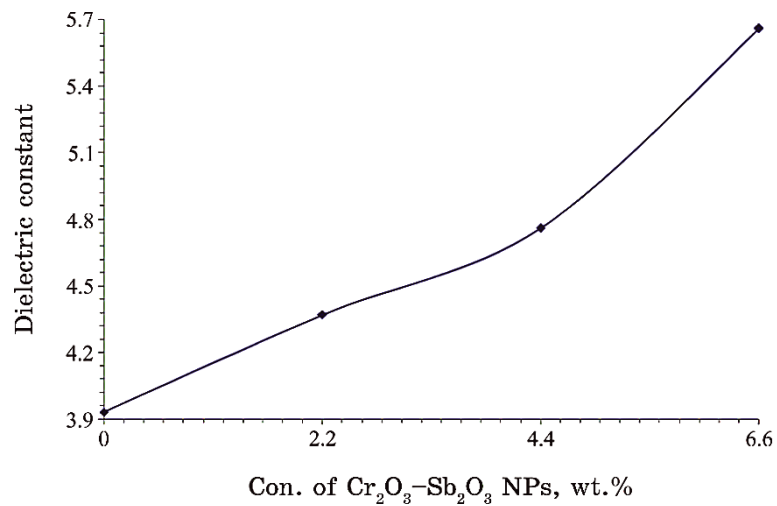


Fig. 3. Dielectric-constant performance of PVA with Cr₂O₃-Sb₂O₃-NPs' concentration.

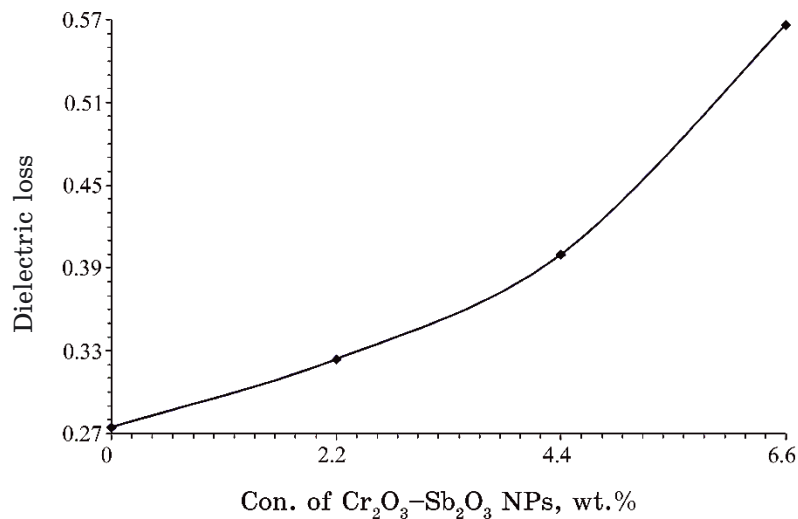


Fig. 4. Dielectric-loss behaviour of PVA with Cr₂O₃-Sb₂O₃-NPs' concentration.

raising frequency. Thus, the high value of the dielectric loss at low frequencies indicates the impact of ion jumping.

The dielectric constant and dielectric loss of PVA are increased with increasing Cr₂O₃-Sb₂O₃-NPs' concentration; this is due to increase in the charge-carriers' numbers [37-51].

Figures 5 and 6 conform the variation of electrical conductivity

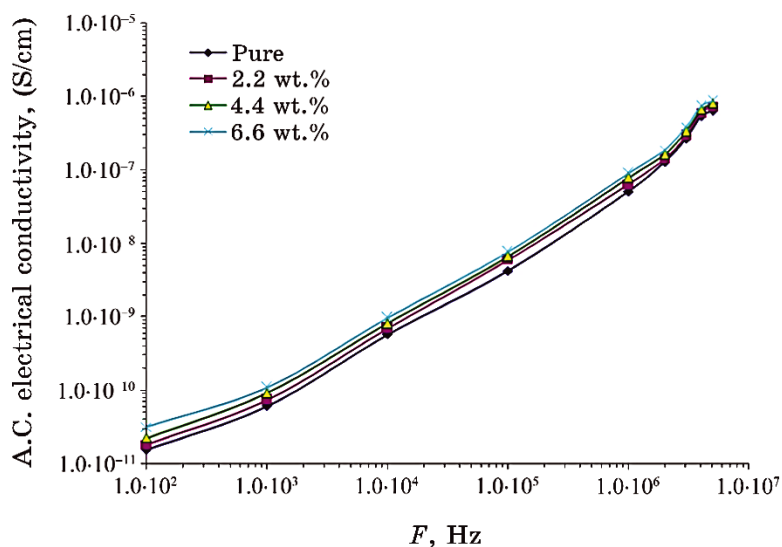


Fig. 5. Variation of electrical conductivity for PVA-Cr₂O₃-Sb₂O₃ nanocomposites with frequency.

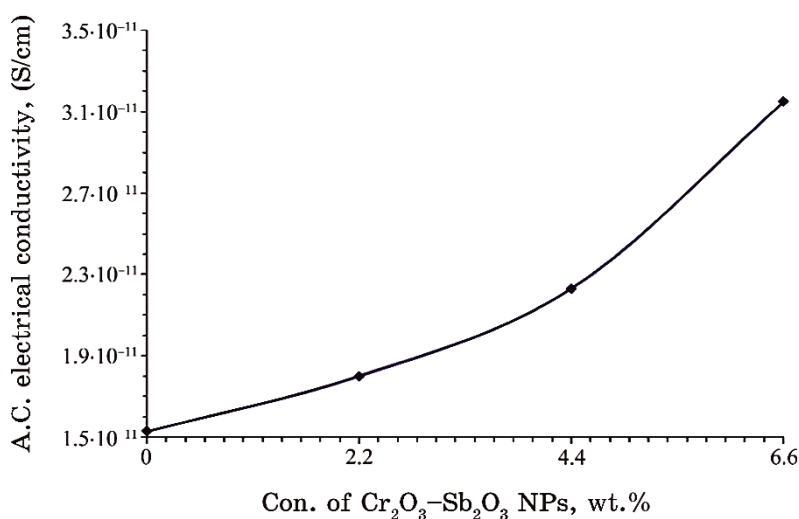


Fig. 6. Behaviour of electrical conductivity for PVA with Cr₂O₃-Sb₂O₃-NPs' concentration.

for PVA-Cr₂O₃-Sb₂O₃ nanocomposites with frequency and Cr₂O₃-Sb₂O₃-NPs' concentration, respectively.

The electrical conductivity rises with increasing concentration and frequency. The increase of electrical conductivity, as the Cr₂O₃-

Sb₂O₃-NPs' concentration increases, is attributed to raising in the charge-carriers' numbers.

The frequency-dependent conductivity is caused by the hopping of electrons in the localized states near the Fermi level and due to the excitation of charge carriers to the states in the conduction band [52–60].

4. CONCLUSIONS

This study involved preparation of nanocomposites from Cr₂O₃-Sb₂O₃-nanoparticles-doped PVA to utilize them in various electrical and electronics fields. The results showed that the dielectric constant and dielectric loss of PVA-Cr₂O₃-Sb₂O₃ nanocomposites are reduced, whereas the electrical conductivity is increased with raising frequency. The dielectric constant, dielectric loss, and A.C. electrical conductivity of PVA are increased with raising the Cr₂O₃-Sb₂O₃-NPs' content. Finally, the results demonstrated that the PVA-Cr₂O₃-Sb₂O₃ nanocomposites may be used in different electrical and electronics applications.

REFERENCES

1. M. Q. A. Al-Gunaid, G. H. Maheshwarappa, S. B. Shivanna, M. A. H. Dhaif-Allah, W. A. Ahmed, and F. H. Al-Ostoot, *European Journal of Chemistry*, **14**, No. 3: 1 (2023); <https://doi.org/10.5155/eurjchem.14.3.401-413.2439>
2. N. Rouabah, R. Nazir, Y. Djaballah, A. Mir, I. Ameer, and O. Beldjebli, *Iranian Journal of Catalysis*, **13**, No. 1: 23 (2023); [doi:10.30495/IJC.2023.1970800.1968](https://doi.org/10.30495/IJC.2023.1970800.1968)
3. A. M. El-Naggar, Z. K. Heiba, A. M. Kamal, O. H. Abd-Elkader, and M. B. Mohamed, *Polymers*, **15**: 1 (2023); <https://doi.org/10.3390/polym15092091>
4. A. M. Abd-Elnaiem, M. Rashad, T. A. Hanafy, and N. M. Shaalan, *Journal of Inorganic and Organometallic Polymers and Materials*, **1** (2023); <https://doi.org/10.1007/s10904-023-02616-w>
5. S. S. Kanakillam, B. Krishnan, D. A. Avellaned, and S. Shajia, *Mater Today Proc.*, **33**: 1444 (2020); <https://doi.org/10.1016/j.matpr.2020.08.533>
6. C. Ye, G. Wang, M. Kong, and L. Zhang, *Journal of Nanomaterials*, **2006**: 1 (2006); [doi:10.1155/JNM/2006/95670](https://doi.org/10.1155/JNM/2006/95670)
7. H. Ahmed and A. Hashim, *Silicon*, **14**: 6637 (2022); <https://doi.org/10.1007/s12633-021-01449-x>
8. H. Ahmed and A. Hashim, *Silicon*, **13**: 4331 (2020); <https://doi.org/10.1007/s12633-020-00723-8>
9. H. Ahmed and A. Hashim, *Transactions on Electrical and Electronic Materials*, **22**: 335 (2021); <https://doi.org/10.1007/s42341-020-00244-6>
10. H. B. Hassan, H. M. Abduljalil, and A. Hashim, *Nanosistemi, Nanomateriali, Nanotehnologii*, **20**, Iss. 4: 941 (2022);

- <https://doi.org/10.15407/nnn.20.04.941>
11. H. A. Jawad and A. Hashim, *Nanosistemi, Nanomateriali, Nanotehnologii*, **20**, Iss. 4: 963 (2022); <https://doi.org/10.15407/nnn.20.04.963>
 12. N. AH. Al-Aaraji, A. Hashim, A. Hadi, and H. M. Abduljalil, *Silicon*, **14**: 10037 (2022); <https://doi.org/10.1007/s12633-022-01730-7>
 13. H. Ahmed and A. Hashim, *Opt. Quant. Electron.*, **55**: 1 (2023); <https://doi.org/10.1007/s11082-022-04273-8>
 14. W. O. Obaid and A. Hashim, *Silicon*, **14**: 11199 (2022); <https://doi.org/10.1007/s12633-022-01854-w>
 15. O. B. Fadil and A. Hashim, *Silicon*, **14**: 9845 (2022); <https://doi.org/10.1007/s12633-022-01728-1>
 16. H. Ahmed and A. Hashim, *Silicon*, **15**: 2339 (2023); <https://doi.org/10.1007/s12633-022-02173-w>
 17. A. Hazim, A. Hashim, and H. M. Abduljalil, *Nanosistemi, Nanomateriali, Nanotehnologii*, **18**, Iss. 4: 983 (2020); <https://doi.org/10.15407/nnn.18.04.983>
 18. A. Hashim and Z. S. Hamad, *Nanosistemi, Nanomateriali, Nanotehnologii*, **18**, Iss. 4: 969 (2020); <https://doi.org/10.15407/nnn.18.04.969>
 19. A. Hazim, A. Hashim, and H. M. Abduljalil, *Egypt. J. Chem.*, **64**, No. 1: 359 (2021); doi:10.21608/EJCHEM.2019.18513.2144
 20. H. Ahmed and A. Hashim, *Journal of Molecular Modeling*, **26**: 1 (2020); doi:10.1007/s00894-020-04479-1
 21. H. Ahmed and A. Hashim, *Opt. Quant. Electron.*, **55**: 280 (2023); <https://doi.org/10.1007/s11082-022-04528-4>
 22. G. Ahmed and A. Hashim, *Silicon*, **15**: 3977 (2023); <https://doi.org/10.1007/s12633-023-02322-9>
 23. M. H. Meteab, A. Hashim, and B. H. Rabee, *Opt. Quant. Electron.*, **55**: 187 (2023); <https://doi.org/10.1007/s11082-022-04447-4>
 24. B. Mohammed, H. Ahmed, and A. Hashim, *Nanosistemi, Nanomateriali, Nanotehnologii*, **21**, Iss. 1: 113 (2023); <https://doi.org/10.15407/nnn.21.01.113>
 25. B. Mohammed, H. Ahmed, and A. Hashim, *Nanosistemi, Nanomateriali, Nanotehnologii*, **20**, Iss. 1: 187 (2022); <https://doi.org/10.15407/nnn.20.01.187>
 26. A. Hashim, *Nanosistemi, Nanomateriali, Nanotehnologii*, **19**, Iss. 3: 647 (2021); <https://doi.org/10.15407/nnn.19.03.647>
 27. H. Ahmed and A. Hashim, *Silicon*, **14**: 4907 (2022); <https://doi.org/10.1007/s12633-021-01258-2>
 28. A. Hashim, *Opt. Quant. Electron.*, **53**: 1 (2021); <https://doi.org/10.1007/s11082-021-03100-w>
 29. H. Ahmed and A. Hashim, *International Journal of Scientific & Technology Research*, **8**, Iss. 11: 1014 (2019).
 30. H. Ahmed and A. Hashim, *Trans. Electr. Electron. Mater.*, **23**: 237 (2022); <https://doi.org/10.1007/s42341-021-00340-1>
 31. H. Ahmed and A. Hashim, *Silicon*, **14**: 7025 (2021); <https://doi.org/10.1007/s12633-021-01465-x>
 32. A. Hazim, A. Hashim, and H. M. Abduljalil, *Trans. Electr. Electron. Mater.*, **21**: 48 (2019); <https://doi.org/10.1007/s42341-019-00148-0>
 33. A. F. Kadhim and A. Hashim, *Opt. Quant. Electron.*, **55**: 432 (2023);

- <https://doi.org/10.1007/s11082-023-04699-8>
34. S. Ishaq, F. Kanwal, S. Atiq, M. Moussa, U. Azhar, and D. Losic, *Materials*, **13**: 1 (2020); doi:10.3390/ma13010205
 35. H. Shivashankar, K. A. Mathias, P. R. Sondar, M. H. Shrishail, and S. M. Kulkarni, *J. Mater. Sci.: Mater. Electron.*, **32**: 28674 (2021); <https://doi.org/10.1007/s10854-021-07242-1>
 36. H. Bouaamlat, N. Hadi, N. Belghiti, H. Sadki, M. N. Bennani, F. Abdi, T.-D. Lamcharfi, M. Bouachrine, and M. Abarkan, *Advances in Materials Science and Engineering*, **2020**: 1 (2020); <https://doi.org/10.1155/2020/8689150>
 37. A. B. G. Trabelsi, A. M. Mostafa, F. H. Alkallas, W. B. Elsharkawy, A. N. Al-Ahmadi, H. A. Ahmed, S. S. Nafee, R. A. Pashameah, and E. A. Mwafy, *Micromachines*, **14**: 1 (2023); <https://doi.org/10.3390/mi14061195>
 38. I. R. Agool, F. S. Mohammed, and A. Hashim, *Advances in Environmental Biology*, **9**, No. 11: 1 (2015).
 39. B. H. Rabee and A. Hashim, *European Journal of Scientific Research*, **60**, No. 2: 247 (2011).
 40. A. Hashim, A. Hadi, and M. H. Abbas, *Opt. Quant. Electron.*, **55**: 642 (2023); <https://doi.org/10.1007/s11082-023-04929-z>
 41. A. Hashim, A. Hadi, and M. H. Abbas, *Silicon*, **15**: 6431 (2023); <https://doi.org/10.1007/s12633-023-02529-w>
 42. H. A. J. Hussien and A. Hashim, *J. Inorg. Organomet. Polym.*, **33**: 2331 (2023); <https://doi.org/10.1007/s10904-023-02688-8>
 43. A. Hashim, A. Hadi, N. A. H. Al-Aaraji, and F. L. Rashid, *Silicon*, **15**: 5725 (2023); <https://doi.org/10.1007/s12633-023-02471-x>
 44. A. F. Kadhim and A. Hashim, *Silicon*, **15**: 4613 (2023); <https://doi.org/10.1007/s12633-023-02381-y>
 45. H. A. Jawad and A. Hashim, *Nanosistemi, Nanomateriali, Nanotehnologii*, **21**, Iss. 1: 133 (2023); <https://doi.org/10.15407/nnn.21.01.133>
 46. B. Hussien, A. K. Algidsawi, and A. Hashim, *Australian Journal of Basic and Applied Sciences*, **5**, No. 7: 933 (2011).
 47. A. Hashim, M. H. Abbas, N. A.-H. Al-Aaraji, and A. Hadi, *J. Inorg. Organomet Polym.*, **33**: 1 (2023); <https://doi.org/10.1007/s10904-022-02485-9>
 48. A. Hashim, M. H. Abbas, N. A.-H. Al-Aaraji, and A. Hadi, *Silicon*, **15**: 1283 (2023); <https://doi.org/10.1007/s12633-022-02104-9>
 49. M. H. Meteab, A. Hashim, and B. H. Rabee, *Silicon*, **15**: 1609 (2023); <https://doi.org/10.1007/s12633-022-02114-7>
 50. N. Al-Huda Al-Aaraji, A. Hashim, A. Hadi, and H. M. Abduljalil, *Silicon*, **14**: 4699 (2022); <https://doi.org/10.1007/s12633-021-01265-3>
 51. M. H. Meteab, A. Hashim, and B. H. Rabee, *Silicon*, **15**: 251 (2023); <https://doi.org/10.1007/s12633-022-02020-y>
 52. Z. S. Hamad and A. Hashim, *Nanosistemi, Nanomateriali, Nanotehnologii*, **20**, Iss. 1: 159 (2022); <https://doi.org/10.15407/nnn.20.01.159>
 53. D. Hassan and A. Hashim, *Bulletin of Electrical Engineering and Informatics*, **7**, Iss. 4: 547 (2018); doi:10.11591/eei.v7i4.969
 54. A. Hashim and Z. S. Hamad, *Nanosistemi, Nanomateriali, Nanotehnologii*, **20**, Iss. 1: 165 (2022); <https://doi.org/10.15407/nnn.20.01.165>
 55. A. Hashim and A. Jassim, *Nanosistemi, Nanomateriali, Nanotehnologii*, **20**,

- Iss. 1: 177 (2022); <https://doi.org/10.15407/nnn.20.01.177>
56. A. Hashim and Z. S. Hamad, *Nanosistemi, Nanomateriali, Nanotehnologii*, **20**, Iss. 2: 507 (2022); <https://doi.org/10.15407/nnn.20.02.507>
57. B. Mohammed, H. Ahmed, and A. Hashim, *Journal of Physics: Conference Series*, **1879**: 1 (2021); [doi:10.1088/1742-6596/1879/3/032110](https://doi.org/10.1088/1742-6596/1879/3/032110)
58. D. Hassan and A. H. Ah-Yasari, *Bulletin of Electrical Engineering and Informatics*, **8**, Iss. 1: 52 (2019); [doi:10.11591/eei.v8i1.1019](https://doi.org/10.11591/eei.v8i1.1019)
59. M. A. Habbeb, A. Hashim, and Abdul-Raheem K. AbidAli, *European Journal of Scientific Research*, **61**, No. 3: 367 (2011).
60. A. M. K. Aippunny, S. M. Shamsudeen, P. Valparambil, S. Mathew, and U. N. Vishwambharan, *J. Appl. Polym. Sci.*, **133**, No. 25: 43568 (2016); [doi:10.1002/APP.43568](https://doi.org/10.1002/APP.43568)

PACS numbers: 78.20.Ci, 78.67.Sc, 81.07.Pr, 81.40.Tv, 82.35.Np, 85.35.-p

Exploring the Optical Properties of PVA–ZrO₂–Sb₂O₃ Nanostructures for Low-Cost Nanoelectronics Fields

Ahmed Hashim¹ and Aseel Hadi²

¹*College of Education for Pure Sciences,
Department of Physics,
University of Babylon,
Hillah, Iraq*

²*College of Materials Engineering,
Department of Ceramic and Building Materials,
University of Babylon,
Hillah, Iraq*

The present work goals are to fabricate the PVA–ZrO₂–Sb₂O₃ nanostructures to use in low-cost nanoelectronics applications. The optical properties of PVA–ZrO₂–Sb₂O₃ nanostructures are examined at wavelength ranged from 200 nm to 800 nm. The results confirm that the absorbance and absorption coefficient of PVA are increased with rising in the ZrO₂–Sb₂O₃-nanoparticles' content. The transmittance and energy gap are decreased with increasing in the ZrO₂–Sb₂O₃-nanoparticles' content. The results indicate that the PVA–ZrO₂–Sb₂O₃ nanostructures can be considered as a key for various nanoelectronics fields.

Метою даної роботи є виготовлення наноструктур полівінілового спирту (ПВС)–ZrO₂–Sb₂O₃ для використання в недорогих застосуваннях наноелектроніки. Досліджено оптичні властивості наноструктур ПВС–ZrO₂–Sb₂O₃ в діапазоні довжин хвиль від 200 нм до 800 нм. Результати підтверджують, що абсорбція та коефіцієнт поглинання ПВС зростають зі збільшенням вмісту наночастинок (НЧ) ZrO₂–Sb₂O₃. Зі збільшенням вмісту НЧ ZrO₂–Sb₂O₃ коефіцієнт пропускання й енергетична щільність зменшуються. Результати вказують на те, що наноструктури ПВС–ZrO₂–Sb₂O₃ можна вважати ключовими для різних галузей наноелектроніки.

Key words: PVA, ZrO₂–Sb₂O₃, nanocomposites, energy gap, optical properties.

Ключові слова: полівініловий спирт, ZrO₂–Sb₂O₃, наноккомпозити, енергетична щільність, оптичні властивості.

(Received 18 August, 2023)

1. INTRODUCTION

Electronics has been undergoing a disruptive evolution, investing in lightweight, soft and flexible devices instead of heavy, bulky, and rigid devices. Thus, flexible electronics is a fast-growing field that promises to develop new commercial products such as displays, solar cells, and biomedical sensors. These devices can be incorporated into clothing and other everyday items that ensure they revolutionize our daily lives. In this way, the electronic industry opens up new opportunities, and endless manufacturing advances in thin-film materials and devices will make flexible electronics ubiquitous [1]. Semiconductor materials have yielded valuable information beyond the most advanced knowledge in the technological field in recent years. These materials have essential widespread applications, including–VI semiconductor materials, such as solar cells, light emitting devices [2].

The surface of metal oxides is a key factor for effective interaction with target molecules, however, reducing the size of metal oxide particles to the nanoscale, increases the active surface area and induces a new effect due to quantum confinement such as band gap widening, UV-absorption, room temperature, and photoluminescence [3].

Polyvinyl alcohol (PVA) is a semicrystalline polymer having a high dielectric strength, good thermostability, high mechanical strength, chemical resistance, excellent film forming properties and optical transparency. The existence of the hydroxyl group, ($-OH$), gives PVA special properties due to the strong $-OH$ interaction between intra and intermolecular polymer chains [4].

Antimony trioxide nanoparticles (NPs; nano- Sb_2O_3) have been widely concerned because of good synergistic fire-retardant effect between nano- Sb_2O_3 and halogen flame-retardants [5].

Nanosize zirconia has attracted much attention due to its specific optical and electrical properties as well as other potential applications in transparent optical devices, electrochemical capacitor electrodes, oxygen sensors, fuel cells, catalysts and advanced ceramics [6].

The nanocomposites compose of two or more materials have huge applications in various fields like electronics and optoelectronics [7–21], optical fields [22–31], radiation shielding and bioenvironmental [32–37], sensors [38–40], energy storage [41–43] and antibacterial [44–50]. This work deals with fabrication and optical properties of PVA- ZrO_2 - Sb_2O_3 nanostructures to use in nanoelectronics fields.

2. MATERIALS AND METHODS

Films of PVA-ZrO₂-Sb₂O₃ nanostructures were fabricated by using casting technique. The 0.5 gm of PVA was dissolved in 30 ml of distilled water by using magnetic stirrer to mix the polymer for 1 hour to obtain more homogeneous solution. Then, ZrO₂ and Sb₂O₃ nanoparticles were added to PVA solution with constant ratio 1:1 and contents of 2.2%, 4.4% and 6.6%. The optical properties of PVA-ZrO₂-Sb₂O₃-nanostructures' films were examined using the double beam spectrophotometer (Shimadzu, UV-1800Å) at wavelength ranged from 200 nm to 800 nm.

The absorption coefficient (α) is given by [51] as follows:

$$\alpha = 2.303(A/t), \quad (1)$$

where A is the absorbance and t is the thickness of films.

The energy gap is determined by means of equation [52]

$$\alpha h\nu = C(h\nu - E_g)^r, \quad (2)$$

where C is the constant; $h\nu$ is the energy of photon; E_g is the energy gap, and $r=2$ and 3 for allowed and forbidden indirect transitions.

3. RESULTS AND DISCUSSION

Figures 1 and 2 show the performances of absorbance and transmittance of PVA-ZrO₂-Sb₂O₃ nanostructures with wavelength respectively. As shown in these figures, the absorbance is high at low wavelength (UV-region) due to the high energy at this region. The absorbance reduces and transmittance increases with increasing wavelength. The absorption of PVA rises, while the transmittance reduces, when the ZrO₂-Sb₂O₃ NPs content rises, which may be due to increase in the number of charge carriers. This enhancement in the absorption of PVA by doping with ZrO₂-Sb₂O₃ NPs can due to improve of other intermolecular bonds between cations and anions creating defects over the entire polymer medium. The reduced transmittance is due to the rise in scattering processes of the incident photons by denser NPs' filling the polymer matrix [53-65].

Figure 3 demonstrates the variation of absorption coefficient for PVA-ZrO₂-Sb₂O₃ nanostructures with photon energy. From this figure, the values of absorption coefficient are less than 10^4 cm^{-1} that indicates to the indirect transition.

Figures 4 and 5 illustrate the energy gap values for the allowed and forbidden transitions of PVA-ZrO₂-Sb₂O₃ nanostructures. The

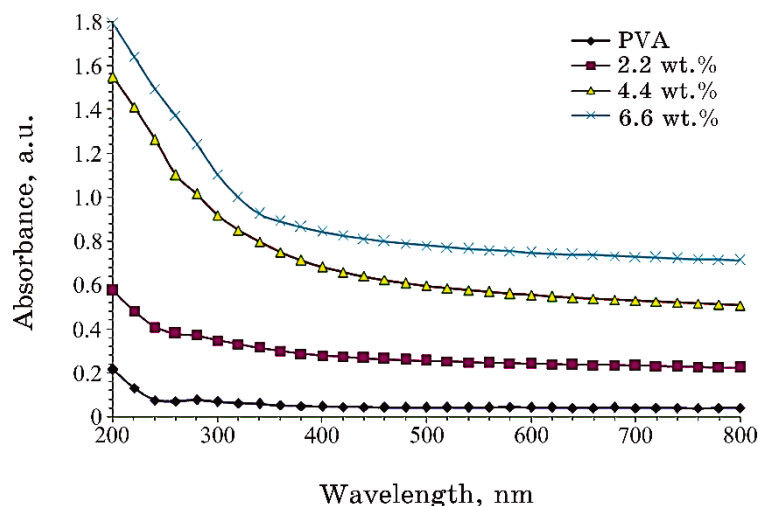


Fig. 1. Performance of absorbance for PVA-ZrO₂-Sb₂O₃ nanostructures with wavelength.

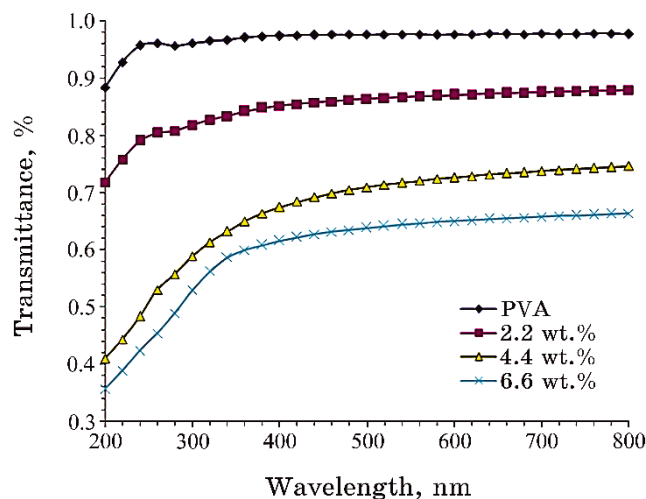


Fig. 2. Transmittance variation of PVA-ZrO₂-Sb₂O₃ nanostructures with wavelength.

energy gap of PVA is reduced with rising ZrO₂-Sb₂O₃ content; this behaviour can be due to the creation of new energy levels, which create the energy band gap. The reduced energy gap selects that the charge transfer complexes presence relate the form of defects in the polymer matrix. These defects create the localized levels in the energy gap [66–72].

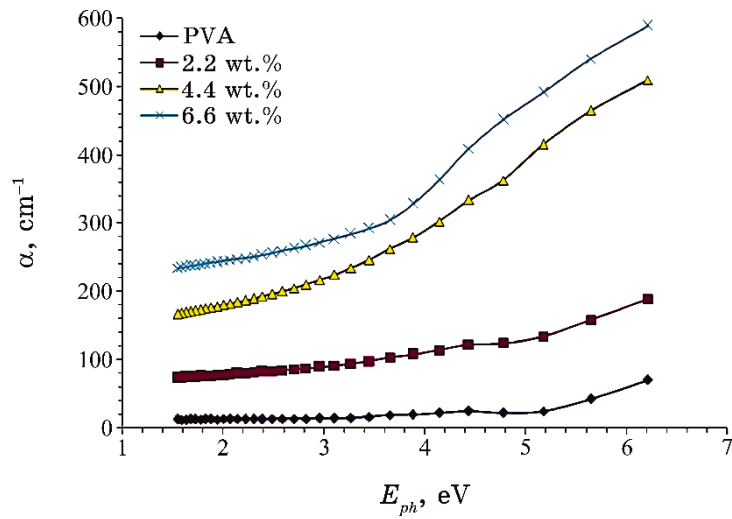


Fig. 3. Variation of absorption coefficient for PVA-ZrO₂-Sb₂O₃ nanostructures with photon energy.

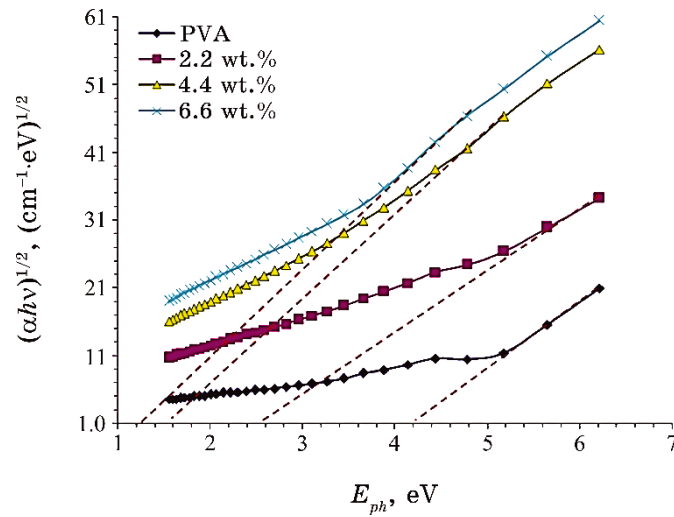


Fig. 4. Energy gap values for allowed transition for PVA-ZrO₂-Sb₂O₃ nanostructures.

4. CONCLUSION

This paper includes synthesis of PVA-ZrO₂-Sb₂O₃ nanostructures to use in low-cost nanoelectronics fields. The experimental results showed that the absorbance and absorption coefficient of PVA are

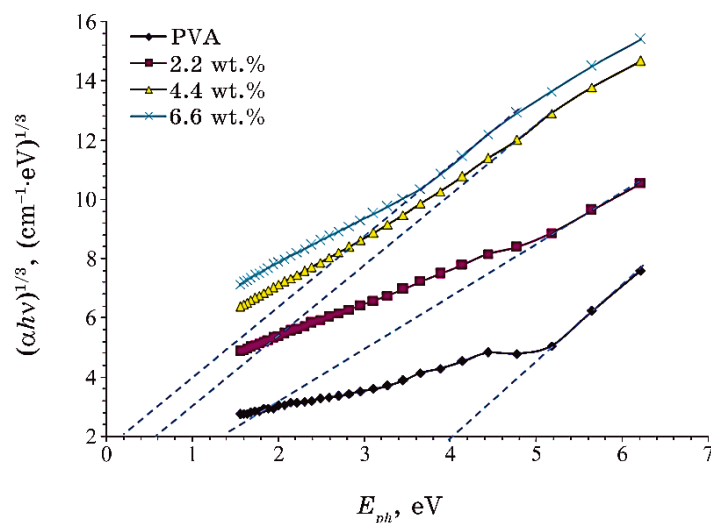


Fig. 5. Energy gap values for forbidden transition for PVA-ZrO₂-Sb₂O₃ nanostructures

increased with increasing of ZrO₂-Sb₂O₃-NPs' content. The transmittance and energy gap are decreased with increasing of the ZrO₂-Sb₂O₃-NPs' content. Finally, the results demonstrated that the PVA-ZrO₂-Sb₂O₃ nanostructures can be considered as promising materials for nanoelectronics fields.

REFERENCES

1. N. E. Guimarães, É. R. B. Ximenes, L. A. D. Silva, R. F. D. S. Santos, E. S. Araújo, and K. A. D. S. Aquino, *Materials Research*, **26**: 1 (2023); <https://doi.org/10.1590/1980-5373-MR-2022-0308>
2. S. H. Zyoud, T. H. Alabdulaal, A. Almoadi, M. S. Alqahtani, F. A. Harraz, M. S. Al-Assiri, I. S. Yahia, H. Y. Zahran, M. I. Mohammed, and M. S. Abdel-wahab, *Crystals*, **13**: 1(2023); <https://doi.org/10.3390/cryst13040608>
3. M. Q. A. Al-Gunaid, G. H. Maheshwarappa, S. B. Shivanna, M. A. H. Dhaif-Allah, W. A. Ahmed, and F. H. Al-Ostoot, *European Journal of Chemistry*, **14**, No. 3: 1 (2023); <https://doi.org/10.5155/eurjchem.14.3.401-413.2439>
4. A. Abou Elfadl, *Arab. J. Nucl. Sci. Appl.*, **52**, No. 4: 145 (2019); [doi:10.21608/ajnsa.2019.8081.1177](https://doi.org/10.21608/ajnsa.2019.8081.1177)
5. J.-L. Xu, Y.-G. Lin, W.-L. Yang, C.-H. Kang, and L. Niu, *Materials Research*, **23**: 1 (2020); <https://doi.org/10.1590/1980-5373-MR-2020-0316>
6. D. Hirani, K. Shah, and B. S. Chakrabarty, *International Journal of Scientific & Technology Research*, **8**, Iss. 12: 4001 (2019).
7. B. Mohammed, H. Ahmed, and A. Hashim, *Nanosistemi, Nanomateriali, Nanotehnologii*, **21**, Iss. 1: 113 (2023);

- <https://doi.org/10.15407/nnn.21.01.133>
8. A. Hashim, *Nanosistemi, Nanomateriali, Nanotehnologii*, **19**, Iss. 3: 647 (2021); <https://doi.org/10.15407/nnn.19.03.647>
 9. A. Hazim, A. Hashim, and H. M. Abduljalil, *Nanosistemi, Nanomateriali, Nanotehnologii*, **18**, No. 4: 983 (2020); <https://doi.org/10.15407/nnn.18.04.983>
 10. A. Hashim and Z. S. Hamad, *Nanosistemi, Nanomateriali, Nanotehnologii*, **18**, No. 4: 969 (2020); <https://doi.org/10.15407/nnn.18.04.969>
 11. A. Hazim, A. Hashim, and H. M. Abduljalil, *Egypt. J. Chem.*, **64**, No. 1: 359 (2021); doi:10.21608/EJCHEM.2019.18513.2144
 12. H. Ahmed and A. Hashim, *Journal of Molecular Modeling*, **26**: 1 (2020); doi:10.1007/s00894-020-04479-1
 14. H. Ahmed and A. Hashim, *Silicon*, **14**: 4907 (2022); <https://doi.org/10.1007/s12633-021-01258-2>
 15. A. Hashim, *Opt. Quant. Electron.*, **53**: 1 (2021); <https://doi.org/10.1007/s11082-021-03100-w>
 16. H. Ahmed and A. Hashim, *Trans. Electr. Electron. Mater.*, **23**: 237 (2022); <https://doi.org/10.1007/s42341-021-00340-1>
 17. H. Ahmed and A. Hashim, *Silicon*, **14**: 7025 (2021); <https://doi.org/10.1007/s12633-021-01465-x>
 18. A. Hazim, A. Hashim, and H. M. Abduljalil, *Trans. Electr. Electron. Mater.*, **21**: 48 (2019); <https://doi.org/10.1007/s42341-019-00148-0>
 19. A. F. Kadhim and A. Hashim, *Opt. Quant. Electron.*, **55**: 432 (2023); <https://doi.org/10.1007/s11082-023-04699-8>
 20. H. Ahmed and A. Hashim, *Opt. Quant. Electron.*, **55**: 280 (2023); <https://doi.org/10.1007/s11082-022-04528-4>
 21. G. Ahmed and A. Hashim, *Silicon*, **15**: 3977 (2023); <https://doi.org/10.1007/s12633-023-02322-9>
 22. M. H. Meteab, A. Hashim, and B. H. Rabee, *Opt. Quant. Electron.*, **55**: 187 (2023); <https://doi.org/10.1007/s11082-022-04447-4>
 23. H. Ahmed and A. Hashim, *Silicon*, **14**: 6637 (2022); <https://doi.org/10.1007/s12633-021-01449-x>
 24. H. Ahmed and A. Hashim, *Silicon*, **13**: 4331 (2020); <https://doi.org/10.1007/s12633-020-00723-8>
 25. O. B. Fadil and A. Hashim, *Silicon*, **14**: 9845 (2022); <https://doi.org/10.1007/s12633-022-01728-1>
 26. H. Ahmed and A. Hashim, *Silicon*, **15**: 2339 (2023); <https://doi.org/10.1007/s12633-022-02173-w>
 27. H. B. Hassan, H. M. Abduljalil, and A. Hashim, *Nanosistemi, Nanomateriali, Nanotehnologii*, **20**, Iss. 4: 941(2022); <https://doi.org/10.15407/nnn.20.04.941>
 28. H. A. Jawad and A. Hashim, *Nanosistemi, Nanomateriali, Nanotehnologii*, **20**, Iss. 4: 963 (2022); <https://doi.org/10.15407/nnn.20.04.963>
 29. H. Ahmed and A. Hashim, *Transactions on Electrical and Electronic Materials*, **22**: 335 (2021); <https://doi.org/10.1007/s42341-020-00244-6>
 30. N. AH. Al-Aaraji, A. Hashim, A. Hadi, and H. M. Abduljalil, *Silicon*, **14**: 10037 (2022); <https://doi.org/10.1007/s12633-022-01730-7>
 31. H. Ahmed and A. Hashim, *Opt. Quant. Electron.*, **55**: 1 (2023); <https://doi.org/10.1007/s11082-022-04273-8>

32. W. O. Obaid and A. Hashim, *Silicon*, **14**: 11199 (2022); <https://doi.org/10.1007/s12633-022-01854-w>
33. A. Hashim and N. Hamid, *Journal of Bionanoscience*, **12**, No. 6: 788 (2018); [doi:10.1166/jbns.2018.1591](https://doi.org/10.1166/jbns.2018.1591)
34. B. Abbas and A. Hashim, *International Journal of Emerging Trends in Engineering Research*, **7**, No. 8: 131 (2019); <https://doi.org/10.30534/ijeter/2019/06782019>
35. K. H. H. Al-Attiyah, A. Hashim, and S. F. Obaid, *Journal of Bionanoscience*, **12**: 200 (2018); [doi:10.1166/jbns.2018.1526](https://doi.org/10.1166/jbns.2018.1526)
36. H. A. J. Hussien, A. Hadi, and A. Hashim, *Nanosistemi, Nanomateriali, Nanotehnologii*, **20**, Iss. 4: 1001 (2022); <https://doi.org/10.15407/nnn.20.04.1001>
37. A. Hashim and Z. S. Hamad, *Journal of Bionanoscience*, **12**, No. 4: 488 (2018); [doi:10.1166/jbns.2018.1551](https://doi.org/10.1166/jbns.2018.1551)
38. A. Hashim and Z. S. Hamad, *Journal of Bionanoscience*, **12**, No. 4: 504 (2018); [doi:10.1166/jbns.2018.1561](https://doi.org/10.1166/jbns.2018.1561)
39. H. Ahmed and A. Hashim, *International Journal of Scientific & Technology Research*, **8**, Iss. 11: 1014 (2019).
40. B. Mohammed, H. Ahmed, and A. Hashim, *Nanosistemi, Nanomateriali, Nanotehnologii*, **20**, Iss. 1: 187 (2022); <https://doi.org/10.15407/nnn.20.01.187>
41. A. Hashim and A. Hadi, *Sensor Letters*, **15**, No. 10: 858 (2017); <https://doi.org/10.1166/sl.2017.3900>
42. H. Ahmed and A. Hashim, *Nanosistemi, Nanomateriali, Nanotehnologii*, **20**, Iss. 4: 951 (2022); <https://doi.org/10.15407/nnn.20.04.951>
43. A. S. Shareef, F. Lafta R., A. Hadi, and A. Hashim, *International Journal of Scientific & Technology Research*, **8**, Iss. 11: 1041 (2019).
44. A. Hadi, A. Hashim, and D. Hassan, *Bulletin of Electrical Engineering and Informatics*, **9**, No. 1: 83 (2020); [doi:10.11591/eei.v9i1.1323](https://doi.org/10.11591/eei.v9i1.1323)
45. A. Hashim, I. R. Agool, and K. J. Kadhim, *Journal of Bionanoscience*, **12**, No. 5: 608 (2018); [doi:10.1166/jbns.2018.1580](https://doi.org/10.1166/jbns.2018.1580)
46. O. B. Fadil and A. Hashim, *Nanosistemi, Nanomateriali, Nanotehnologii*, **20**, Iss. 4: 1029 (2022); <https://doi.org/10.15407/nnn.20.04.1029>
47. W. O. Obaid and A. Hashim, *Nanosistemi, Nanomateriali, Nanotehnologii*, **20**, Iss. 4: 1009 (2022); <https://doi.org/10.15407/nnn.20.04.1009>
48. M. H. Meteab, A. Hashim, and B. H. Rabee, *Nanosistemi, Nanomateriali, Nanotehnologii*, **21**, Iss. 1: 199 (2023); <https://doi.org/10.15407/nnn.21.01.199>
49. M. H. Meteab, A. Hashim, and B. H. Rabee, *Nanosistemi, Nanomateriali, Nanotehnologii*, **21**, Iss. 2: 451 (2023); <https://doi.org/10.15407/nnn.21.02.451>
50. A. Hazim, A. Hashim, and H. M. Abduljalil, *International Journal of Emerging Trends in Engineering Research*, **7**, No. 8: 68 (2019); <https://doi.org/10.30534/ijeter/2019/01782019>
51. A. Hazim, H. M. Abduljalil, and A. Hashim, *International Journal of Emerging Trends in Engineering Research*, **7**, No. 8: 104 (2019); <https://doi.org/10.30534/ijeter/2019/04782019>
52. A. A. A. Ahmed, A. M. Al-Hussam, A. M. Abdulwahab, and A. N. A. A. Ahmed, *AIMS Mater. Sci.*, **5**, Iss. 3: 1 (2018);

- doi:10.3934/matersci.2018.3.533
53. T. A. Baset, M. Elzayat, and S. Mahrous, *Int. J. of Polym. Sci.*, **2016**: 1 (2016); <http://dx.doi.org/10.1155/2016/1707018>
 54. Z. K. Heiba, M. B. Mohamed, and S. I. Ahmed, *Alexandria Engineering Journal*, **61**, Iss. 5: 3375 (2022); <https://doi.org/10.1016/j.aej.2021.08.051>
 55. P. O. Amin, K. A. Ketuly, S. R. Saeed, F. F. Muhammadsharif, M. D. Symes, A. Paul, and K. Sulaiman, *BMC Chemistry*, **15**: 1 (2021); <https://doi.org/10.1186/s13065-021-00751-4>
 56. A. Hashim, M. H. Abbas, N. A.-H. Al-Aaraji, and A. Hadi, *J. Inorg. Organomet. Polym.*, **33**: 1 (2023); <https://doi.org/10.1007/s10904-022-02485-9>
 57. A. Hashim, M. H. Abbas, N. A.-H. Al-Aaraji, and A. Hadi, *Silicon*, **15**: 1283 (2023); <https://doi.org/10.1007/s12633-022-02104-9>
 58. M. H. Meteab, A. Hashim, and B. H. Rabee, *Silicon*, **15**: 1609 (2023); <https://doi.org/10.1007/s12633-022-02114-7>
 59. N. Al-Huda Al-Aaraji, A. Hashim, A. Hadi, and H. M. Abduljalil, *Silicon*, **14**: 4699 (2022); <https://doi.org/10.1007/s12633-021-01265-3>
 60. S. Hadi, A. Hashim, and A. Jewad, *Australian Journal of Basic and Applied Sciences*, **5**, No. 9: 2192 (2011).
 61. F. A. Jasim, A. Hashim, A. G. Hadi, F. Lafta, S. R. Salman, and H. Ahmed, *Research Journal of Applied Sciences*, **8**, Iss. 9: 439 (2013).
 62. F. A. Jasim, F. Lafta, A. Hashim, M. Ali, and A. G. Hadi, *Journal of Engineering and Applied Sciences*, **8**, No. 5: 140 (2013).
 63. A. Hashim and A. Hadi, *Sensor Letters*, **15**, No. 10: 858 (2017); <https://doi.org/10.1166/sl.2017.3900>
 64. A. Hashim, M. A. Habeeb, A. Khalaf, and A. Hadi, *Sensor Letters*, **15**, No. 7: 589 (2017); <https://doi.org/10.1166/sl.2017.3856>
 65. I. R. Agool, F. S. Mohammed, and A. Hashim, *Advances in Environmental Biology*, **9**, No. 11: 1 (2015).
 66. B. H. Rabee and A. Hashim, *European Journal of Scientific Research*, **60**, No. 2: 247 (2011).
 67. A. Hashim, A. Hadi, and M. H. Abbas, *Opt. Quant. Electron.*, **55**: 642 (2023); <https://doi.org/10.1007/s11082-023-04929-z>
 68. A. Hashim, A. Hadi, and M. H. Abbas, *Silicon*, **15**: 6431 (2023); <https://doi.org/10.1007/s12633-023-02529-w>
 69. H. A. J. Hussien and A. Hashim, *J. Inorg. Organomet. Polym.*, **33**: 2331 (2023); <https://doi.org/10.1007/s10904-023-02688-8>
 70. A. Hashim, A. Hadi, N. A. H. Al-Aaraji, and F. L. Rashid, *Silicon*, **15**: 5725 (2023); <https://doi.org/10.1007/s12633-023-02471-x>
 71. G. Ahmed and A. Hashim, *Silicon*, **15**: 7085 (2023); <https://doi.org/10.1007/s12633-023-02572-7>
 72. A. Hashim, A. Hadi, and N. A.-H. Al-Aaraji, *Opt. Quant. Electron.*, **55**: 1 (2023); <https://doi.org/10.1007/s11082-023-04994-4>
 73. N. A.-H. Al-Aaraji, A. Hashim, H. M. Abduljalil, and A. Hadi, *Opt. Quant. Electron.*, **55**: 1 (2023); <https://doi.org/10.1007/s11082-023-05048-5>

PACS numbers: 72.80.Tm, 77.22.Ch, 77.22.Gm, 78.30.-j, 78.67.Sc, 81.07.Pr, 82.35.Np

Structural and A.C. Electrical Properties of Polyvinyl Alcohol/Iron Oxide Nanocomposites for Electronic and Electrical Applications

Zainab Sabri Jaber¹ and Majeed Ali Habeeb²

¹*Directorate of Education Babylon,
Ministry of Education,
Babylon, Iraq*

²*College of Education for Pure Sciences,
Department of Physics,
University of Babylon,
Hillah, Iraq*

The PVA–Fe₂O₃-nanocomposites' films were made using the casting method with various weight percentages 0, 2, 4, 6 of nanoparticles. When compared to pure PVA–Fe₂O₃ film, Fourier transform-based infrared (FTIR) spectroscopy spectra demonstrate a change in a peak location and, moreover, changes in terms of shape and intensity that suggests decoupling between the corresponding vibrations of iron-oxide nanoparticles (NPs). Images taken with optical microscopy reveal a distinct difference between the samples without and with iron-oxide NPs. When concentration reaches 6% weight, the iron-oxide nanoparticles create a continuous network inside the polymer. The dielectric characteristics of nanocomposites demonstrate that, as Fe₂O₃-NPs' concentrations rise, the dielectric constant, dielectric loss, and alternating-current electrical conductivity of PVA–Fe₂O₃ nanocomposites are increased. Additionally, when the frequency increases, the electrical conductivity of PVA–Fe₂O₃ nanocomposites increases, while their dielectric constant and dielectric loss fall. Based on these findings, nanostructures formed of PVA doped with Fe₂O₃ show themselves as promising materials for optoelectronic nanodevices due to improvements in structural and A.C. electrical properties.

Плівки нанокompозитів полівініловий спирт (ПВС)–Fe₂O₃ виготовляли методом лиття з різним ваговим вмістом наночастинок: 0, 2, 4, 6. У порівнянні з чистою плівкою ПВС–Fe₂O₃ спектри інфрачервоної спектроскопії на основі Фур'є-перетвору демонструють зміну розташування піку та, крім того, зміни форми та інтенсивності, що свідчить про розчеплення між відповідними коливаннями наночастинок оксиду Феруму. Зображення, одержані за допомогою оптичної мікроскопії, показують чітку різницю між зразками без і з наночастинками оксиду Фе-

руму. Коли концентрація сягає 6% ваги, наночастинки оксиду Феруму створюють безперервну мережу всередині полімеру. Діелектричні характеристики нанокомпозитів продемонстрували, що зі збільшенням концентрації наночастинок Fe_2O_3 зростають діелектрична проникність, діелектричні втрати й електропровідність змінного струму нанокомпозитів ПВС– Fe_2O_3 . Крім того, зі збільшенням частоти збільшується електропровідність нанокомпозитів ПВС– Fe_2O_3 , а їхні діелектрична проникність і діелектричні втрати падають. Виходячи з цих висновків, наноструктури, сформовані з ПВС, легованого Fe_2O_3 , є перспективними матеріалами для оптоелектронних нанопристроїв завдяки поліпшенню структурних та електричних (для змінного струму) властивостей.

Key words: nanocomposites, structural properties, electrical properties, electronic applications.

Ключові слова: нанокомпозити, структурні властивості, електричні властивості, електронні застосування.

(Received 11 August, 2023; in revised form, 13 August, 2023)

1. INTRODUCTION

Investigation of polyvinyl alcohol (PVA) nanomaterials with iron oxide as well as of dispersing polymers with inorganic nanoparticles (NPs) has recently increased interest to improve various functional qualities; this includes electrical, magnetic, optical, thermal, and mechanical skills [1, 2]. Under preparation conditions, the composites' characteristics were impacted. Numerous studies have demonstrated the complexity of the creation and characterization of polymer composites, as well as the relationships between their processing, structural, morphological, and functional features [3, 4]. Due to its easy processing, high transmittance, and ease of solubilization in water, PVA is useful for a variety of polymer engineering technology, pharmaceutical, and biological applications [5, 6]. Because iron oxide nanoparticles are easily made in aqueous medium and are water soluble, the preparation is non-toxic. PVA has good qualities including thermal stability and chemical resistance, which have been thoroughly demonstrated by several investigations [7]. Iron-oxide nanoparticles have been discovered and become effective magnetic, magneto-optical, and electromagnetism platforms for medicinal applications [8, 9].

Researchers were interested in PVA/iron oxide polymer nanocomposites because of their improved properties and inexpensive production costs, making them the most attractive candidate among the competition after distributing Fe_2O_3 nanoparticles of PVA band gap [10–13]. The experimental findings that are currently accessible significantly improve our comprehension of their underlying ideas,

ensuring that this class of materials can be used in a wide range of applications. The optical characteristics of PVA nanocomposites, however, are receiving less attention despite recent advancements and developments [14, 15].

The optical properties can be used to provide detailed information because they are crucial and closely related to several other qualities. The quantity of iron oxide nanoparticles and the processes used to prepare the materials can have an impact on a number of significant Iron oxide nanocomposites without PVA optical characteristics, including band gap, reflection index, dielectric value, and optical absorption. For instance, varied magnetic properties for the same substance [16, 17]. Additionally, distinct magnetic, thermal, and electrical properties were discovered as a result of the dispersion particle concentration shift [18]. This result also reveals that the optical characteristics may be greatly affected by the effect of iron oxide concentration. Thus, it should come as no surprise that this topic is now undergoing extensive research and is still nascent. Therefore, the prospective application these nanocomposites can be controlled successfully by evaluating various synthesizing processes and analysing the connection between the qualities and the approach [19, 20]. In this study, nanocomposite films of PVA-Fe₂O₃ have not been thoroughly studied, and their properties have been investigated to improve their performance in various applications.

2. EXPERIMENTAL PART

The PVA-Fe₂O₃ blend with various Fe₂O₃ nanoparticle concentrations was used to create the nanocomposites. PVA was dissolved in 40 ml of distilled water at temperature 70°C, using a magnetic stirrer, to achieve more homogeneous solution. Fe₂O₃ nanoparticles were added with concentrations of 0, 2, 4, 6 wt.% by using casting method. An optical microscope of the Olympus type Nikon-73346 with a magnification of ×10 and a tiny photographic camera was used to test the materials at various concentrations. FTIR spectra have been investigated by FTIR. The range of wave numbers 500–4000 cm⁻¹ (Bruker, of Vertex-70 is of German origin. kind). Dielectric properties comprising dielectric constant, dielectric loss, and conductivity of an alternating current for the nanocomposites were tested employing the LCR-meter type (HIOKI 3532-50 LCR HI TESTER) for a range of frequencies between 100 Hz and 5 MHz.

The dielectric constant (ϵ') is given by [21] as follows:

$$\epsilon' = C_p/C_0, \quad (1)$$

where C_p is capacitance and C_0 is a vacuum capacitance.

The dielectric loss (ϵ'') is given by the following equation [22]:

$$\epsilon'' = \epsilon' D, \quad (2)$$

where D is the displacement.

A.C. electrical conductivity is determined by [23] as follows:

$$\sigma_{\text{A.C.}} = \omega \epsilon' \epsilon_0, \quad (3)$$

where ω is angular frequency.

3. RESULTS AND DISCUSSION

In order to study interactions between atoms or ions in nanocomposites of PVA- Fe_2O_3 , changes in the vibrational modes of these interactions can include the nanocomposites. The transmittance spectra of FTIR for PVA- Fe_2O_3 nanocomposites are shown in Fig. 1, *a*, *b*, *c*, and *d*, reported in the range of $600\text{--}4500\text{ cm}^{-1}$ at standard room temperature. It is obvious from the infrared spectra that vari-

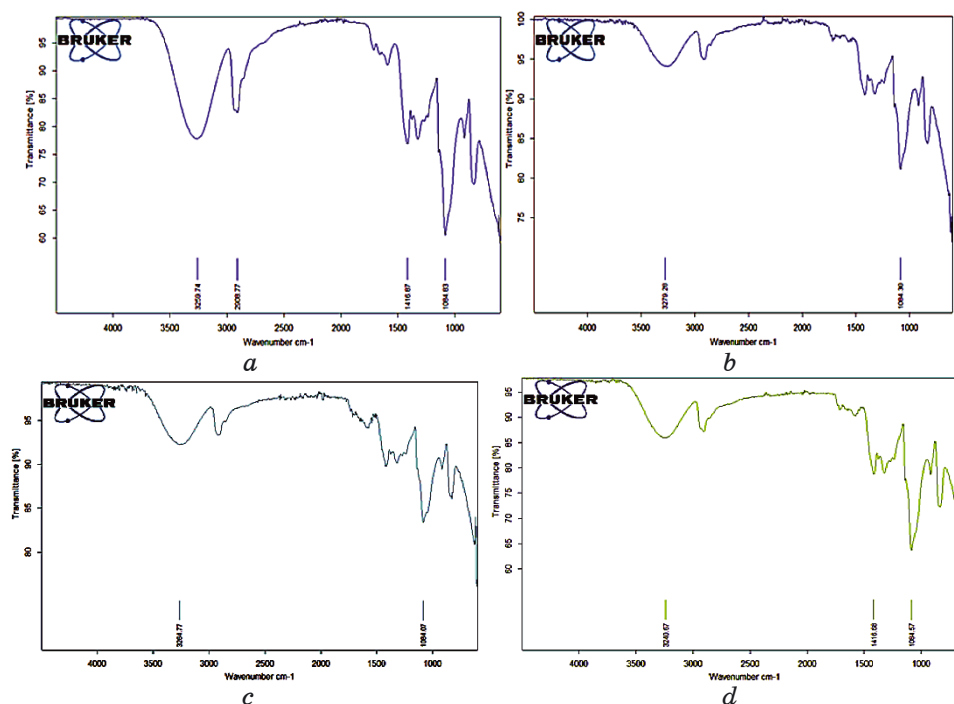


Fig. 1. FTIR spectra for PVA- Fe_2O_3 with nanocomposites: (a) PVA; (b) 2 wt.% Fe_2O_3 NPs; (c) 4 wt.% Fe_2O_3 NPs; (d) 6 wt.% Fe_2O_3 NPs.

ations in the ratio of Fe₂O₃ nanoparticles result in some discernible the spectrum of PVA changes. It causes certain new zones of absorption to form as well as small adjustments to the intensities of some existing bands. Similar to flaws caused *via* means of charge-transfer interaction in the space between the dopant species and a polymer chain, the new absorption bands may be connected. The PVA films' FTIR spectra showed broad and powerful frequencies at 3750 cm⁻¹, which is attributable to the O-H groups of hydroxyl vibrating during the stretch, and at 2921 cm⁻¹, which is attributed to the O-H vibration breaking of the hydroxyl molecules, which is attributed to the C-H shaking and stretching. The C=O, C=C elongating modes are thought to be responsible for peaks at 1558 cm⁻¹ and 1457 cm⁻¹. FTIR spectra show decrease in the transmittance with increasing ratio of nanoparticles [24, 25].

Figure 2 shows images of films made of PVA-Fe₂O₃ nanocomposites, which were captured at ×10 magnification for samples with different concentrations. This figure manifests clear differences between image *a* and images (*b*, *c*, *d*). When the concentration of iron-

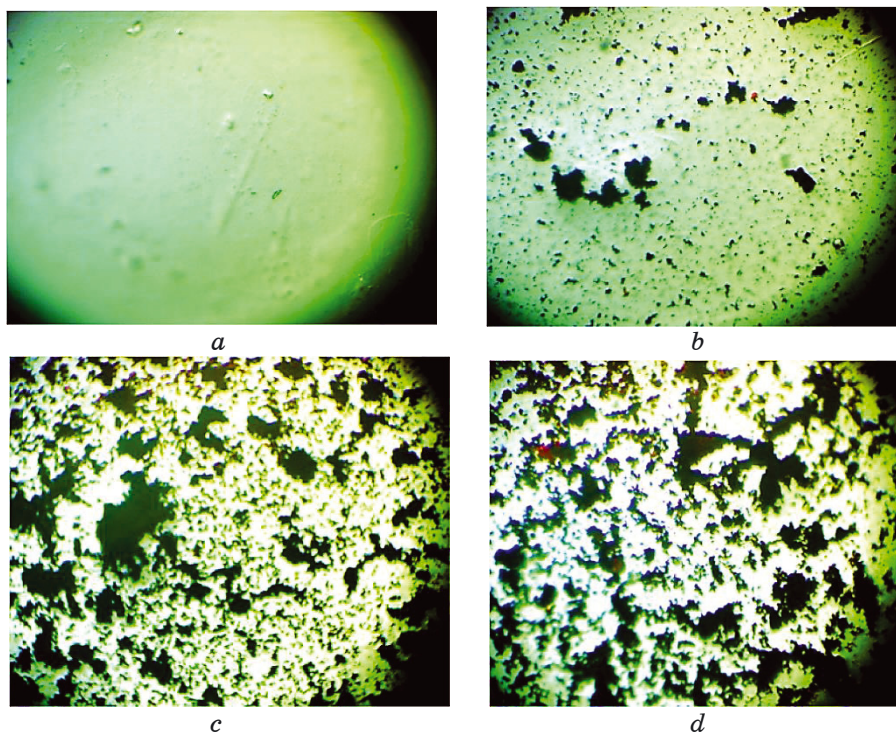


Fig. 2. Photomicrographs (×10) for nanocomposites of PVA-Fe₂O₃: (a) PVA; (b) 2 wt.% Fe₂O₃ NPs; (c) 4 wt.% Fe₂O₃ NPs; (d) 6 wt.% Fe₂O₃ NPs.

oxide nanoparticles reaches 6 wt.%, the nanoparticles form a continuous network inside the polymer. Charge carriers are allowed to move along certain channels in this network, which reduces the resistance of the polymeric material (PVA) [26, 27].

Figure 3 depicts the dielectric constant with frequency for PVA–

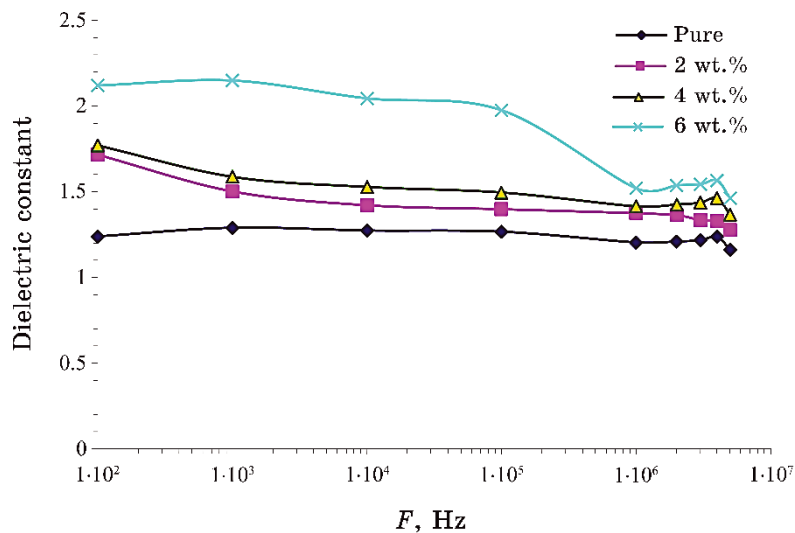


Fig. 3. Variation of the dielectric constant with frequency for PVA–Fe₂O₃ nanocomposites.

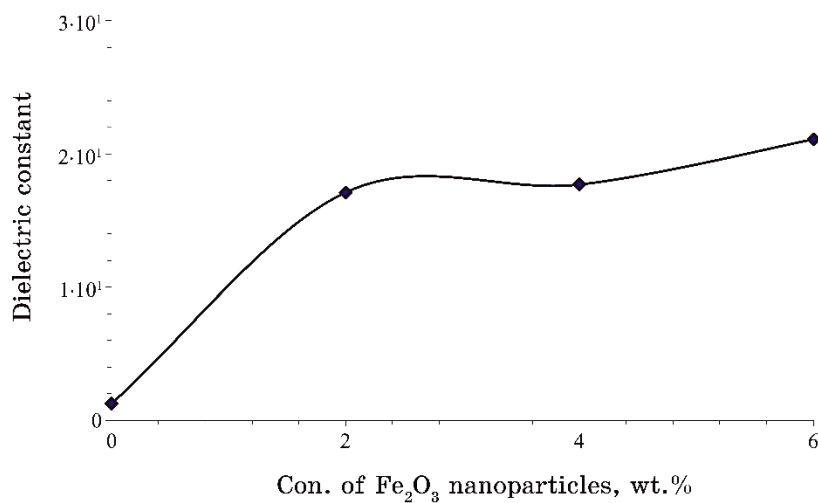


Fig. 4. Change of the dielectric constant for PVA–Fe₂O₃ nanocomposites with iron-oxide content at 100 Hz.

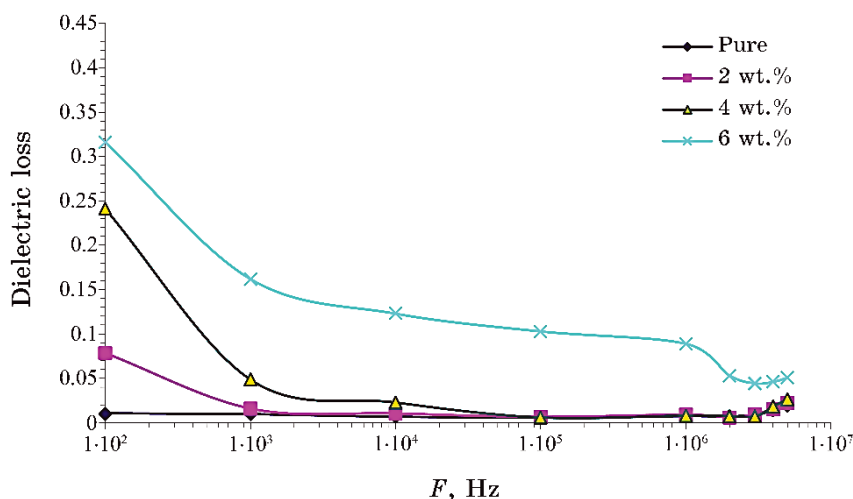


Fig. 5. The dielectric loss as a function of frequency for PVA–Fe₂O₃ nanocomposites.

Fe₂O₃ nanocomposites. The figure demonstrates that, as frequency increases, the dielectric constant falls that is due to a reduction in space charge polarization [28–30]. Additionally, as shown in Fig. 4, we can see that the dielectric constant rises as the concentration of iron-oxide nanoparticles raises that is because of an increase in the charge carried by the nanoparticles [31–34].

Figure 5 depicts the influence of frequency on the dielectric loss of PVA–Fe₂O₃ nanocomposites at various iron-oxide-nanoparticles' concentrations (see Fig. 6 too). Because there are fewer dipoles in nanocomposites, the dielectric loss lowers as frequency rises [35–38].

As shown in Fig. 7, the polymer-matrix electrical conductivity increases with an increase in weight percentage of iron-oxide nanoparticles. This is a result of an increase in the quantity of electrons in nanocomposites [39, 40]. A.C. electrical conductivity of PVA–Fe₂O₃ nanocomposites is increasing with frequency too (Fig. 8). Due to electronic polarization and transporters of charges, which move by hopping, the conductivity of alternating current (A.C.) increases as frequency rises [41–43]. According to Fig. 8, a rise in iron-oxide nanoparticles' concentration leads to an increase in electrical conductivity of nanocomposites, which is attributable to an increase in charge carriers [44, 45].

4. CONCLUSIONS

1. The FTIR spectrum shows a difference in peak position and in-

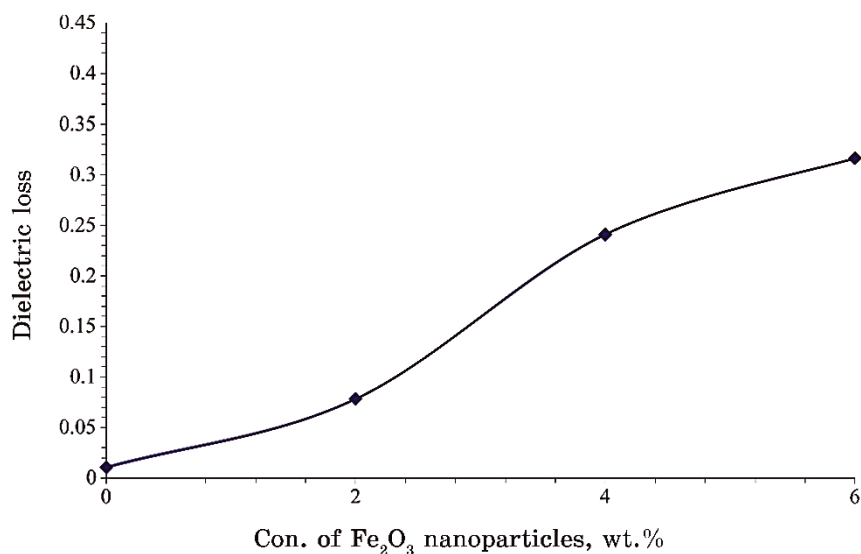


Fig. 6. The dielectric loss for PVA- Fe_2O_3 nanocomposites varying with iron-oxide nanoparticles' content at 100 Hz.

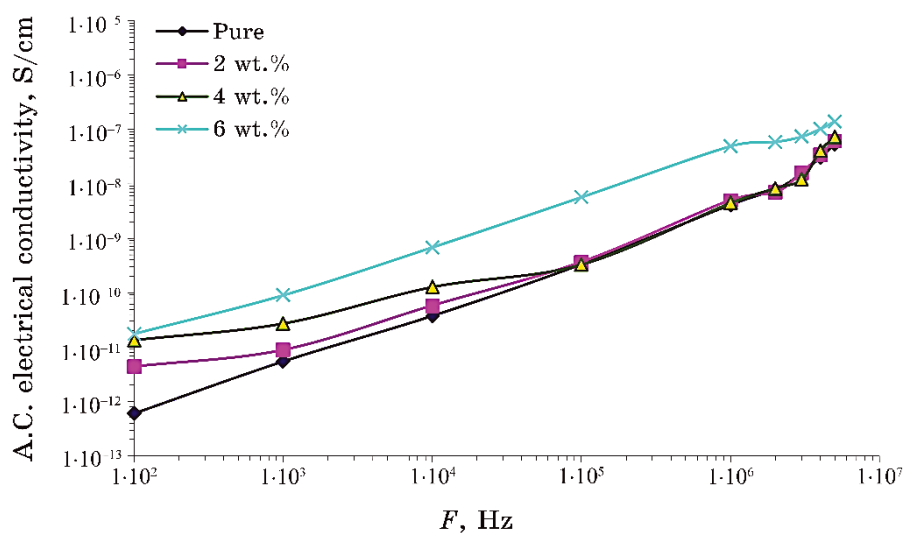


Fig. 7. The A.C. electric conductivity of PVA- Fe_2O_3 nanocomposites varying with frequency.

tensity of PVA- Fe_2O_3 nanostructures. This suggests the disassociation between the vibrations in the polymer and the iron-oxide nanoparticles.

2. From optical-microscopy images, the iron-oxide nanoparticles

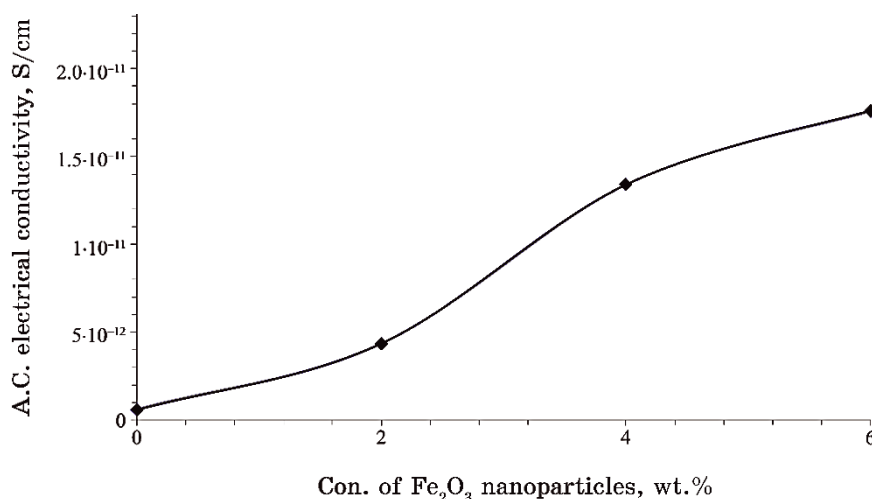


Fig. 8. A.C. electrical conductivity of PVA–Fe₂O₃ nanocomposites versus iron-oxide nanoparticles at 100 Hz.

form a continuous network within the polymer (at concentration 6 wt.%).

3. As the frequency rises, the dielectric constant and dielectric loss decrease, while A.C. electrical conductivity increases for all PVA–Fe₂O₃ nanocomposites.

4. The dielectric constant, dielectric loss and electrical conductivity are increasing with increasing of Fe₂O₃ nanoparticles.

REFERENCES

1. T. A. Taha, *Polym. Bull.*, **76**, No. 2: 903 (2019); <https://doi.org/10.1007/s00289-018-2417-8>
2. A. H. Hadi and M. A. Habeeb, *Journal of Mechanical Engineering Research and Developments*, **44**, No. 3: 265 (2021); <https://jmerd.net/03-2021-265-274>
3. R. Bouzerara, S. Achour, N. Tabet, and S. Zerkout, *Int. J. Nanoparticles*, **4**, No. 1: 10 (2011); doi:10.1504/IJNP.2011.038247
4. M. A. Habeeb and Z. S. Jaber, *East European Journal of Physics*, **4**: 176 (2022); doi:10.26565/2312-4334-2022-4-18
5. M. A. Habeeb, *European Journal of Scientific Research*, **57**, No. 3: 478 (2011).
6. Q. M. Jebur, A. Hashim, and M. A. Habeeb, *Egyptian Journal of Chemistry*, **63**: 719 (2020); <https://dx.doi.org/10.21608/ejchem.2019.14847.1900>
7. G. S. Kim and S. H. Hyun, *J. Mater. Sci.*, **38**: 1961 (2003); <https://doi.org/10.1023/A:1023560601911>
8. S. M. Mahdi and M. A. Habeeb, *Optical and Quantum Electronics*, **54**, Iss. 12: 854 (2022); <https://doi.org/10.1007/s11082-022-04267-6>

9. N. Hayder, M. A. Habeeb, and A. Hashim, *Egyptian Journal of Chemistry*, **63**: 577 (2020); doi:10.21608/ejchem.2019.14646.1887
10. D. Dibbern-Brunelli, T. D. Z. Atvars, I. Joekes, and V. C. Barbosa, *J. Appl. Polym. Sci.*, **69**, No. 4: 645 (1998); doi:10.1002/(SICI)1097-4628(19980725)69:4<645::AID-APP3>3.0.CO;2-J
11. M. A. Habeeb, A. Hashim, and N. Hayder, *Egyptian Journal of Chemistry*, **63**: 709 (2020); <https://dx.doi.org/10.21608/ejchem.2019.13333.1832>
12. A. Hashim, M. A. Habeeb, and Q. M. Jebur, *Egyptian Journal of Chemistry*, **63**: 735 (2020); <https://dx.doi.org/10.21608/ejchem.2019.14849.1901>
13. S. M. Mahdi and M. A. Habeeb, *Physics and Chemistry of Solid State*, **23**, No. 4: 785 (2022); doi:10.15330/pcss.23.4.785-792
14. N. H. El Fewaty, A. El Sayed, and R. Hafez, *Polymer Science Series A*, **58**: 1004 (2016); <https://doi.org/10.1134/S0965545X16060055>
15. M. A. Habeeb and W. S. Mahdi, *International Journal of Emerging Trends in Engineering Research*, **7**, No. 9: 247 (2019); doi:10.30534/ijeter/2019/06792019
16. M. A. Habeeb and R. S. Abdul Hamza, *Journal of Bionanoscience*, **12**, No. 3: 328 (2018); <https://doi.org/10.1166/jbns.2018.1535>
17. S. Nambiar and J. T. Yeow, *ACS Applied Materials & Interfaces*, **4**, No. 11: 5717 (2012); doi:10.1021/am300783d
18. M. A. Habeeb, A. Hashim, and N. Hayder, *Egyptian Journal of Chemistry*, **63**: 697 (2020); <https://dx.doi.org/10.21608/ejchem.2019.12439.1774>
19. M. A. Habeeb and W. K. Kadhim, *Journal of Engineering and Applied Sciences*, **9**, No. 4: 109 (2014); doi:10.36478/jeasci.2014.109.113
20. M. Hdidar, S. Chouikhi, A. Fattoum, M. Arous, and A. Kallel, *Journal of Alloys and Compounds*, **750**: 375 (2018); <https://doi.org/10.1016/j.jallcom.2018.03.272>
21. M. A. Habeeb, *Journal of Engineering and Applied Sciences*, **9**, No. 4: 102 (2014); doi:10.36478/jeasci.2014.102.108
22. H. J. Park, A. Badakhsh, I. T. Im, M.-S. Kim, and C. W. Park, *Applied Thermal Engineering*, **107**: 907 (2016); doi:10.1016/j.applthermaleng.2016.07.053
23. S. M. Mahdi and M. A. Habeeb, *Digest Journal of Nanomaterials and Biostructures*, **17**, No. 3: 941(2022); <https://doi.org/10.15251/DJNB.2022.173.941>
24. G. A. Eid, A. Kany, M. El-Toony, I. Bashter, and F. Gaber, *Arab. J. Nucl. Sci. Appl.*, **46**, No. 2: 226 (2013).
25. A. H. Hadi and M. A. Habeeb, *Journal of Physics: Conference Series*, **1973**: No. 1: 012063 (2021); doi:10.1088/1742-6596/1973/1/012063
26. Q. M. Jebur, A. Hashim, and M. A. Habeeb, *Egyptian Journal of Chemistry*, **63**, No. 2: 611 (2020); <https://dx.doi.org/10.21608/ejchem.2019.10197.1669>
27. G. Aras, E. L. Orhan, I. F. Selçuk, S. B. Ocağ and M. Ertuğrul, *Procedia-Social and Behavioral Sciences*, **95**: 1740 (2015).
28. M. A. Habeeb and A. H. Mohammed, *Optical and Quantum Electronics*, **55**, Iss. 9: 791 (2023); <https://doi.org/10.1007/s11082-023-05061-8>
29. M. H. Dwech, M. A. Habeeb, and A. H. Mohammed, *Ukr. J. Phys.*, **67**, No. 10: 757 (2022); <https://doi.org/10.15407/ujpe67.10.757>
30. C. U. Devi, A. K. Sharma, and V. Rao, *Materials Letters*, **56**, No. 3: 167

- (2002).
31. M. Martin, N. Prasad, M. M. Siva Lingam, D. Sastikumar, and B. Karthikeyan, *Journal of Material Science: Material in Electronics*, **29**: 365 (2018).
 32. M. A. Habeeb and W. H. Rahdi, *Optical and Quantum Electronics*, **55**, Iss. 4: 334 (2023); <https://doi.org/10.1007/s11082-023-04639-6>
 33. W. Yingkang, Y. Yang, and R. Ruicheng, *Chin. J. Polym. Sci.*, **3**: 289 (2009); <https://doi.org/10.1002/pola.23288>
 34. R. Dalven and R. Gill, *J. Appl. Phys.*, **38**, No. 2: 753 (1967); [doi:10.1063/1.1709406](https://doi.org/10.1063/1.1709406)
 35. V. M. Mohan, P. B. Bhargav, V. Raja, A. K. Sharma, and N. Rao, *Soft Matter*, **5**, No. 1: 33 (2007); <https://doi.org/10.1080/15394450701405291>
 36. R. N. Bhagat and V. S. Sangawar, *Int. J. Sci. Res. (IJSR)*, **6**: 361 (2017).
 37. R. S. Abdul Hamza and M. A. Habeeb, *Optical and Quantum Electronics*, **55**, Iss. 8: 705 (2023); <https://doi.org/10.1007/s11082-023-04995-3>
 38. A. Goswami, A. K. Bajpai, and B. K. Sinha, *Polym. Bull.*, **75**, No. 2: 781 (2018).
 39. S. M. Mahdi and M. A. Habeeb, *AIMS Materials Science*, **10**, No. 2: 288 (2023); [doi:10.3934/matersci.2023015](https://doi.org/10.3934/matersci.2023015)
 40. O. E. Gouda, S. F. Mahmoud, A. A. El-Gendy, and A. S. Haiba, *Indonesian Journal of Electrical Engineering*, **12**, No. 12: 7987 (2014).
 41. M. A. Habeeb and R. S. A. Hamza, *Indonesian Journal of Electrical Engineering and Informatics*, **6**, No. 4: 428 (2018); [doi:10.11591/ijeel.v6i1.511](https://doi.org/10.11591/ijeel.v6i1.511)
 42. Z. S. Jaber, M. A. Habeeb, and W. H. Radi, *East European Journal of Physics*, **2**: 228 (2023); [doi:10.26565/2312-4334-2023-2-25](https://doi.org/10.26565/2312-4334-2023-2-25)
 43. Z. Guo, *J. Nanoparticle Res.*, **12**: 2415 (2010).
 44. A. A. Mohammed and M. A. Habeeb, *East European Journal of Physics*, **2**: 157 (2023); [doi:10.26565/2312-4334-2023-2-15](https://doi.org/10.26565/2312-4334-2023-2-15)
 45. N. K. Al-Sharifi and M. A. Habeeb, *East European Journal of Physics*, **2**: 341 (2023); [doi:10.26565/2312-4334-2023-2-40](https://doi.org/10.26565/2312-4334-2023-2-40)

PACS numbers: 78.20.Ci, 78.66.Sq, 78.67.Sc, 81.07.Pr, 81.40.Tv, 82.35.Np, 85.60.-q

Exploring the Optical Properties of BaTiO₃/CuO-Nanoparticles-Doped PVA Polymer for Optoelectronic Applications

Majeed Ali Habeeb¹ and Araa Hassan Hadi²

¹College of Education for Pure Sciences,
Department of Physics,
University of Babylon,
Hillah, Iraq

²College of Biotechnology,
University Al-Qasim Green University,
Al-Qasim District, 51013 Babylon, Iraq

This study aims to prepare of barium titanate (BaTiO₃)/copper oxide (CuO)-nanoparticles-doped polyvinyl alcohol (PVA) as new optical material, which can be used in variety optoelectronics applications with a few cost, light-weight, excellent optical properties, and high efficiency. We investigate the impact of the barium titanate and copper oxide nanoparticles with different concentrations 0, 2, 4, and 6 wt.% on polyvinyl alcohol. The solution casting process is used to fabricate the samples. The optical properties findings show that the optical conductivity, complex dielectric constant (with real and imaginary parts), extinction coefficient, absorption, absorption coefficient, and refractive index increase with increasing of BaTiO₃-CuO-nanoparticles' concentration, while the optical energy gap and transmittance decrease. This behaviour makes it suitable for several optical nanodevices. In the end, it is clear that the PVA-BaTiO₃-CuO nanostructures have useful optical characteristics for applications related to optics and electronics.

Це дослідження спрямоване на одержання легованого наночастинками титанату Барію (BaTiO₃)/оксиду Купруму (CuO) полівінілового спирту (ПВС), оскільки новий оптичний матеріал може бути використаний у різноманітних оптоелектронних застосуваннях із невеликою ціною, малою вагою, чудовими оптичними властивостями та високою ефективністю. Досліджено вплив наночастинок титанату Барію й оксиду Купруму різної концентрації у 0, 2, 4 та 6 мас.% на полівініловий спирт. Для виготовлення зразків використовувався процес лиття розчину. Результати стосовно оптичних властивостей показали, що оптична провідність, діелектрична проникність (як реальна, так і уявна), коефіцієнт екстинкції, поглинання, коефіцієнт поглинання та показник заломлення — все це підвищується зі збільшенням концентрації наночастинок

BaTiO₃-CuO, тоді як оптична енергетична щільність та пропускна здатність зменшуються. Така поведінка робить це придатним для ряду оптичних нанопристроїв. Зрештою, було зрозуміло, що наноструктури ПВС-BaTiO₃-CuO мають корисні оптичні характеристики для застосування в оптиці й електроніці.

Key words: PVA, barium titanate, copper oxide, nanocomposites, optical properties.

Ключові слова: полівініловий спирт, титанат Барію, оксид Купруму, наноккомпозити, оптичні властивості.

(Received 3 September, 2023)

1. INTRODUCTION

Recent years have seen a surge in interest in nanocomposites. Significant attempts are being made to regulate anion the structures using cutting-edge synthetic methods [1]. Nanocomposites' properties are influenced not only by those methods, not just by the morphology and interfacial properties of their component parents, but also by the composite itself. Unlike the qualities of matter at the level of individual particles or molecules, anion. materials have unique physical, chemical, and biological characteristics. Nanotechnology has made it feasible to modify the melting point, magnetic characteristics, charge capacity, and even colour of materials without altering their chemical makeup [2, 3].

Nanotechnology typically involves the creation of materials or devices with dimensions between 1 nm and 100 nm in at least one dimension. It is possible to approach nanotechnology from either the top down, in which case large structures are broken down into smaller ones (as in the case of photonic applications in nanoelectronics and nan engineering) or the bottom up, in which case atoms and molecules are transformed into nanostructures that are more akin to biological systems [4, 5]. Research in nanotechnology is massive because of how important it will be to society in the 21st century. It is possible that brand-new software will soon be accessible [6, 7].

Many potential nanotechnology's uses stem from the fact that macroscopic and submicroscopic applications of nanoscale structural characteristics exhibit strikingly diverse physical, chemical, and biological properties [8].

The polyvinyl alcohol (PVA) is one of the first and most extensively distributed polymers, and it finds extensive usage in semiconductor applications today. PVA dissolves quickly in water and in organic compounds, which contain hydroxyl groups [9, 10]. PVA is

often considered a superior host medium for a variety of nanoparticles. The need to create films with superior transparency and optical properties is the driving force. Their dielectric characteristics, particularly, their flexibility and robustness, have garnered a lot of interest. The flexible ceramic powder barium titanate (BaTiO₃) is a ferroelectric that has attracted a lot of interest as a transducer in polymer nanocomposite films due to its high dielectric properties [11, 12]. Copper oxide has an important place among the metal oxides. Despite being the most basic copper molecule, CuO has many desirable features, including high-temperature superconductivity, electronic correlation, and non-toxicity. Crystal structure with a tiny band gap gives it promising photovoltaic and photoconductive capabilities [13, 14]. This paper deals with the preparation and optical characteristics of PVA–BaTiO₃–CuO nanostructures for use in different optoelectronic fields.

2. EXPERIMENTAL WORK

PVA–BaTiO₃–CuO nanocomposites were made of PVA, barium titanate (BaTiO₃) and copper oxide (CuO) by using the solution casting method. Polyvinyl alcohol (PVA) was dissolved in 40 ml of distilled water, to get a more homogenous solution by swirling with a magnetic stirrer at 75°C for 45 minutes. Barium titanate (BaTiO₃) and copper oxide (CuO) nanoparticles have been added to the PVA at concentrations of 2, 4, and 6 wt.%. The optical features of PVA–CuO–BaTiO₃ nanostructures were investigated by using a Shimadzu-UV-1800-spectrophotometer in the wavelength range 200–800 nm.

The absorbance A is calculated from equation by [15] as follows:

$$A = \frac{I_a}{I_0},$$

where I_0 is the intensity of incident light, I_a denotes the intensity of light that is absorbed by the medium.

Transmittance T is calculated using the equation by [16]:

$$T = 10^{-A}.$$

The absorbance coefficient α is calculated using the equation by [17]:

$$\alpha = \frac{2.303A}{t},$$

where t is thickness of sample.

Optical energy gap is determined by [18] as follows:

$$B(h\nu - E_g^{opt.})^r = \alpha h\nu,$$

where B is constant; $h\nu$ indicates the photon energy, and $E_g^{opt.}$ is the optical energy gap when $r = 3$ (for the forbidden indirect transition) and $r = 2$ (for the allowed indirect transition).

The extinction coefficient k is obtained by [19] with equation:

$$k = \frac{\alpha \lambda}{4\pi},$$

where the wavelength is λ .

Refractive index n is given by [20] as follows:

$$n = \sqrt{4R - \frac{k^2}{(R-1)^2} - \frac{(R+1)}{(R-1)}},$$

where R is reflection.

The dielectric constant has real and imaginary parts (ϵ_1, ϵ_2). Each of these parts may be determined by [21, 22] using the formulae:

$$\epsilon_1 = n^2 - k^2, \quad \epsilon_2 = 2nk.$$

The optical conductivity σ is calculated by [23] using the equation:

$$\sigma = \frac{\alpha n c}{4\pi}.$$

3. RESULTS AND DISCUSSION

Figure 1 shows how PVA–BaTiO₃–CuO nanocomposites absorb light at various wavelengths. As can be seen in this figure, the absorbance is decreased with increasing wavelength and is increased with increasing of concentration of nanoparticles. This behaviour can be attributed to the interaction of composite materials with atoms, which ultimately leads to the transmission of photons. At shorter wavelengths, particularly, in proximity to the fundamental absorption edge, a phenomenon arises, wherein the incident photon and material interact, leading to the absorption of the photon. The positive correlation between the weight percentages of BaTiO₃–CuO nanoparticles and the absorbance values can be attributed to the absorption of incident light by free electrons [24, 25].

Figure 2 shows how PVA–BaTiO₃–CuO nanocomposites' transmittance varies with wavelength. This graph shows that the transmittance decreases with increasing of BaTiO₃–CuO-nanoparticles' concentration. This is because the BaTiO₃–CuO nanoparticles add elec-

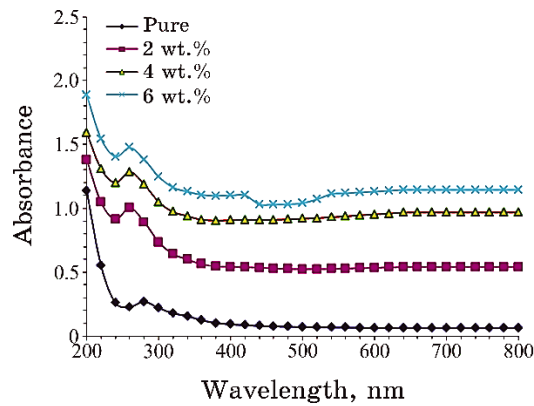


Fig. 1. Connection between absorption and wavelength for PVA-BaTiO₃-CuO nanocomposites.

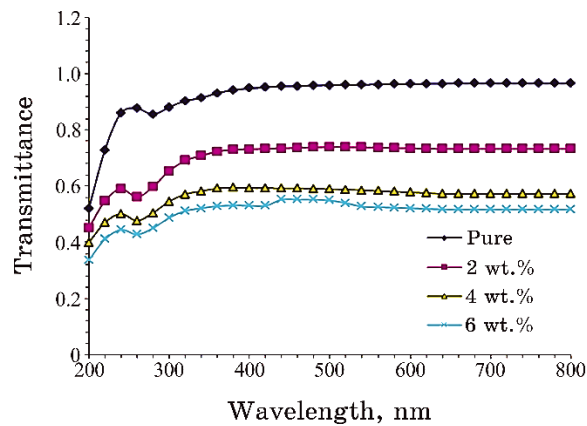


Fig. 2. Connection between transmittance and wavelength for PVA-BaTiO₃-CuO nanocomposites.

tron, which has occupied unoccupied energy band positions after being transported to a higher energy level; so, the process does not lead to outer-orbital electron emission, where the electrons are vulnerable to electromagnetic forces radiation [26]. Pure PVA, on the other hand, has a low permeability and a high transmittance, allowing docents to pass through it, while absorbing part of the incident light. This is because an electron bond must be broken in order for it to transition to the conduction band, requiring a high-energy photon [27].

Figure 3 shows variation of absorbance coefficient with photon energy for PVA-BaTiO₃-CuO nanocomposites. We can observe that, since the incoming photon lacks the necessary energy to move the

electron from the valence band (V.B) to the conduction band (C.B), hence, the absorption coefficient is the smallest at high wavelength and low energy. Larger absorption at higher energies is indicative of an abundance of possible electron transitions. In order to move the electron from the V.B to the C.B, the incoming photon must have energy greater than this prohibited energy difference [28, 29]. Since a direct transition of an electron is predicted, the nature of an electron transmission is affected by the absorption coefficient, which is substantial ($> 10^4 \text{ cm}^{-1}$) at high energies, when the energy and moment are maintained by the (electrons and photons). In a phonon-mediated indirect transition, the electronic momentum of an electron is likely to be retained [30, 31], since absorption coefficients are (of 10^4 cm^{-1}) at low energies.

Absorbance data for PVA–BaTiO₃–CuO nanocomposites reveal

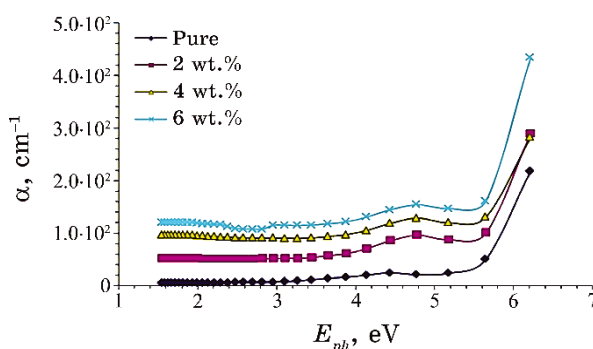


Fig. 3. Connection between absorption coefficient and photon energy for PVA–BaTiO₃–CuO nanocomposites.

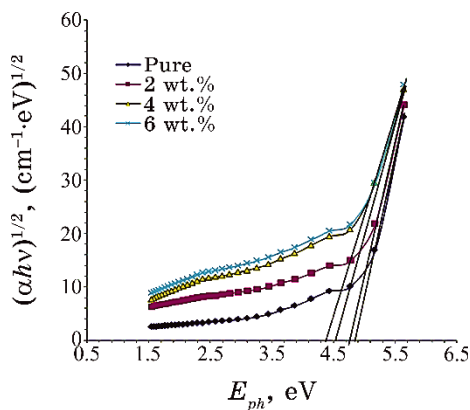


Fig. 4. Connection between absorption edge $(\alpha h\nu)^{1/2}$ and photon energy for PVA–BaTiO₃–CuO nanocomposites.

that the electron transition occurs at wavelengths of less than 10^4 cm^{-1} .

Figure 4 shows the relationship between $(\alpha h\nu)^{1/2}$ and photon energy for PVA–BaTiO₃–CuO nanocomposites. Drawing a straight line from the curve highest point to the axis (x) at the position, when $(\alpha h\nu)^{1/2} = 0$ (allowable), we get an indirect energy-gap transition. From this figure, the optical energy gap decreases by increasing of BaTiO₃–CuO-nanoparticles' concentration. This is can be attributed to the density of localized state increased with increasing concentration of BaTiO₃–CuO nanoparticles due to the heterogeneous nature of nanocomposites (*i.e.*, electronic conduction depends on the added concentration) [32, 33].

Figure 5 depicts the relation between $(\alpha h\nu)^{1/3}$ and photon energy for PVA–BaTiO₃–CuO nanocomposites. A similar approach takes into account the prohibited transition for the indirect energy gap.

Figure 6 shows the relationship between refractive index of PVA–BaTiO₃–CuO nanocomposites and wavelength. From this figure, we can see that the refractive index of PVA–BaTiO₃–CuO nanocomposites increases with increasing concentration of BaTiO₃–CuO nanoparticles. Upon exposure to incident light, a sample exhibiting high refractivity in the UV region will demonstrate a proportional elevation in its refractive-index values [34, 35].

Figure 7 shows the connection between extinction coefficient and wavelength for PVA–BaTiO₃–CuO nanocomposites. The extinction coefficient increases with increasing BaTiO₃–CuO-nanoparticles' concentration, as seen in this figure. It is because of the higher absorption coefficient. This occurs because the absorption coefficient increases with increasing concentrations of the barium titanate and copper oxide nanoparticles. This result suggests that the structure

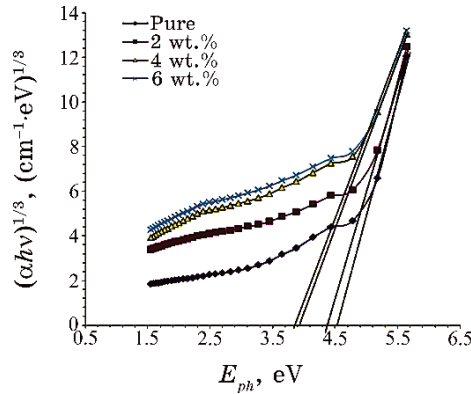


Fig. 5. Connection between $(\alpha h\nu)^{1/3} (\text{cm}^{-1}.\text{eV})^{1/3}$ and photon energy for PVA–BaTiO₃–CuO.

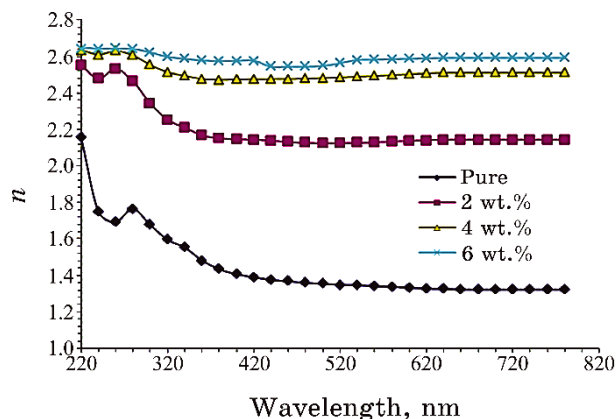


Fig. 6. Connection between refractive index with wavelength for PVA-BaTiO₃-CuO nanocomposites.

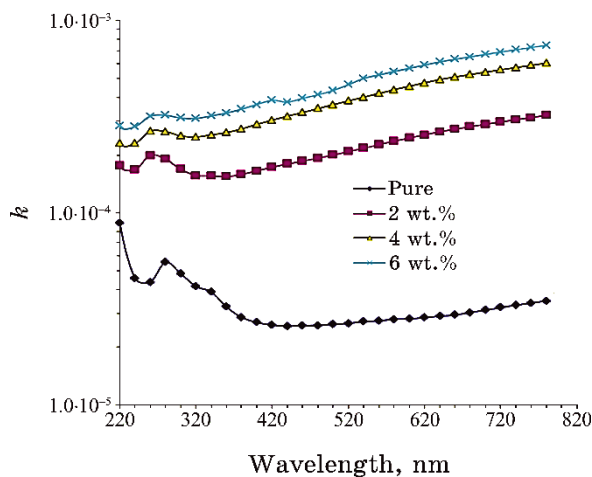


Fig. 7. Connection between extinction coefficient and wavelength for PVA-BaTiO₃-CuO nanocomposites.

of the polymer will be affected by the presence of BaTiO₃-CuO nanoparticles [36, 37].

Figure 8 presents variation of the real part of dielectric constant with wavelength for PVA/BaTiO₃/CuO nanocomposites. This figure manifests the real dielectric constant increased with increasing concentrations of BaTiO₃-CuO nanoparticles. Because of the smaller value of n^2 , this figure demonstrates that ϵ_1 is highly dependent on k^2 [38, 39].

The relation between wavelength and imaginary part of dielectric constant for PVA/BaTiO₃/CuO nanocomposites is displayed in Fig.

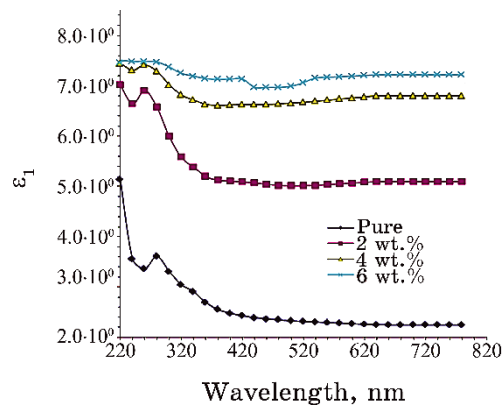


Fig. 8. Connection between real part of the dielectric constant and wavelength for PVA–BaTiO₃–CuO nanocomposites.

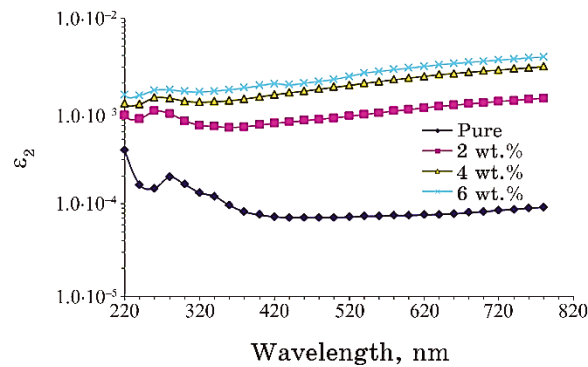


Fig. 9. Connection between imaginary part of dielectric constant and wavelength for PVA–BaTiO₃–CuO nanocomposites.

9. We can see the imaginary part values, which vary due to the absorption coefficient dependent on k because of their relationship between ϵ_2 and k . On the other hand, imaginary part of dielectric constant increases with increasing concentration of nanoparticles. Because of the heightened electric polarization induced by the nanoparticles, the rise in electric polarization results in a higher density of dipoles, which, in turn, leads to an increase in the dielectric constant [40, 41].

Figure 10 shows the dependence of optical conductivity of PVA–BaTiO₃–CuO nanocomposites on wavelength. Increasing the BaTiO₃–CuO proportion in the PVA was shown to increase the optical conductivity. Because the introduction of additional band gap levels facilitates electron transport from the valence band to the conduc-

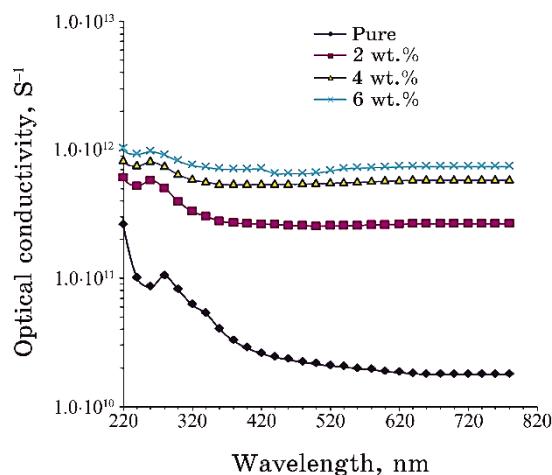


Fig. 10. Connection between optical conductivity and wavelength for PVA–BaTiO₃–CuO nanocomposites.

tion band through localized levels, the band gap closes and the conductivity increases as a consequence of this one [42, 43].

4. CONCLUSION

In this paper, the solution casting technique was used to fabricate PVA–BaTiO₃–CuO-nanocomposites' films. The optical properties of PVA–BaTiO₃–CuO nanostructures have been studied. The optical characteristics showed that the absorption, absorption coefficient, extinction coefficient, refractive index, real and imaginary dielectric-constant parts, and optical conductivity increase with increasing concentration of BaTiO₃–CuO nanoparticles. On the other hand, transmittance and optical energy gap decrease as the concentration of BaTiO₃–CuO nanoparticles increases. According to how light interacts with them, nanostructures made of PVA–BaTiO₃–CuO are attractive candidates for use in optical and photonic nanodevices.

REFERENCES

1. J. Su and J. Zhang, *Journal of Materials Science: Materials in Electronics*, **30**, No. 3: 1957 (2019); <https://doi.org/10.1007/s10854-018-0494-y>
2. M. A. Habeeb and Z. S. Jaber, *East European Journal of Physics*, **4**: 176 (2022); doi:10.26565/2312-4334-2022-4-18
3. M. Vinyas and S. C. Kattimani, *Mater. Today Proc.*, **5**: 7410 (2018); <https://doi.org/10.1016/j.matpr.2017.11.412>
4. A. H. Hadi and M. A. Habeeb, *Journal of Mechanical Engineering Research*

- and Developments*, **44**, No. 3: 265 (2021); <https://jmerd.net/03-2021-265-274>
5. Q. M. Jebur, A. Hashim, and M. A. Habeeb, *Egyptian Journal of Chemistry*, **63**: 719 (2020); <https://dx.doi.org/10.21608/ejchem.2019.14847.1900>
 6. M. A. Habeeb, *European Journal of Scientific Research*, **57**, No. 3: 478 (2011).
 7. S. Shankar, O. P. Thakur, and M. Jayasimhadri, *Mater. Chem. Phys.*, **234**: 110 (2019); <https://doi.org/10.1016/j.matchemphys.2019.05.095>
 8. S. M. Mahdi and M. A. Habeeb, *Optical and Quantum Electronics*, **54**, Iss. 12: 854 (2022); <https://doi.org/10.1007/s11082-022-04267-6>
 9. N. Hayder, M. A. Habeeb, and A. Hashim, *Egyptian Journal of Chemistry*, **63**: 577 (2020); [doi:10.21608/ejchem.2019.14646.1887](https://doi.org/10.21608/ejchem.2019.14646.1887)
 10. N. Kumar, V. Crasta, and B. Praveen, *Physics Research International*, **2014**: Article ID 742378-1–9 (2014); <https://doi.org/10.1155/2014/742378>
 11. M. A. Habeeb, A. Hashim, and N. Hayder, *Egyptian Journal of Chemistry*, **63**: 709 (2020); <https://dx.doi.org/10.21608/ejchem.2019.13333.1832>
 12. A. Hashim, M. A. Habeeb, and Q. M. Jebur, *Egyptian Journal of Chemistry*, **63**: 735 (2020); <https://dx.doi.org/10.21608/ejchem.2019.14849.1901>
 13. S. M. Mahdi and M. A. Habeeb, *Physics and Chemistry of Solid State*, **23**, No. 4: 785 (2022); [doi:10.15330/pcss.23.4.785-792](https://doi.org/10.15330/pcss.23.4.785-792)
 14. S. Muntaz Begum, M. Rao, and R. Ravikumar, *Journal of Inorganic and Organometallic Polymers and Materials*, **23**: 350 (2013); <https://doi.org/10.1007/s10904-012-9783-8>
 15. M. A. Habeeb and W. S. Mahdi, *International Journal of Emerging Trends in Engineering Research*, **7**, No. 9 : 247 (2019); [doi:10.30534/ijeter/2019/06792019](https://doi.org/10.30534/ijeter/2019/06792019)
 16. M. A. Habeeb and R. S. Abdul Hamza, *Journal of Bionanoscience*, **12**, No. 3: 328 (2018); <https://doi.org/10.1166/jbns.2018.1535>
 17. Q. Zhang, K. Zhang, D. Xu, G. Yang, H. Huang, F. Nie, C. Liu, and S. Yang, *Progress in Materials Science*, **60**: 208 (2014); <https://doi.org/10.1016/j.pmatsci.2013.09.003>
 18. M. A. Habeeb, A. Hashim, and N. Hayder, *Egyptian Journal of Chemistry*, **63**: 697 (2020); <https://dx.doi.org/10.21608/ejchem.2019.12439.1774>
 19. M. A. Habeeb and W. K. Kadhim, *Journal of Engineering and Applied Sciences*, **9**, No. 4: 109 (2014); [doi:10.36478/jeasci.2014.109.113](https://doi.org/10.36478/jeasci.2014.109.113)
 20. M. Hdidar, S. Chouikhi, A. Fattoum, M. Arous, and A. Kallel, *Journal of Alloys and Compounds*, **750**: 375 (2018); <https://doi.org/10.1016/j.jallcom.2018.03.272>
 21. M. A. Habeeb, *Journal of Engineering and Applied Sciences*, **9**, No. 4: 102 (2014); [doi:10.36478/jeasci.2014.102.108](https://doi.org/10.36478/jeasci.2014.102.108)
 22. H. J. Park, A. Badakhsh, I. T. Im, M.-S. Kim, and C. W. Park, *Applied Thermal Engineering*, **107**: 907 (2016); <https://doi.org/10.1016/j.applthermaleng.2016.07.053>
 23. S. M. Mahdi and M. A. Habeeb, *Digest Journal of Nanomaterials and Biostructures*, **17**, No. 3: 941 (2022); <https://doi.org/10.15251/DJNB.2022.173.941>
 24. G. A. Eid, A. Kany, M. El-Toony, I. Bashter, and F. Gaber, *Arab. J. Nucl. Sci. Appl.*, **46**, No. 2: 226 (2013).
 25. A. H. Hadi and M. A. Habeeb, *Journal of Physics: Conference Series*, **1973**:

- No. 1: 012063 (2021); doi:10.1088/1742-6596/1973/1/012063
26. Q. M. Jebur, A. Hashim, and M. A. Habeeb, *Egyptian Journal of Chemistry*, **63**, No. 2: 611 (2020); <https://dx.doi.org/10.21608/ejchem.2019.10197.1669>
 27. R. Grigalaitis, M. M. Vijatović Petrović, J. D. Bobić, A. Dzunuzovic, R. Sobiestianskas, A. Brilingas, and B. D. Stojanović, *J. Banys Int.*, **40**: 6165 (2014); <https://doi.org/10.1016/j.ceramint.2013.11.069>
 28. M. A. Habeeb and A. H. Mohammed, *Optical and Quantum Electronics*, **55**, Iss. 9: 791 (2023); <https://doi.org/10.1007/s11082-023-05061-8>
 29. M. H. Dwech, M. A. Habeeb, and A. H. Mohammed, *Ukr. J. Phys.*, **67**, No. 10: 757 (2022); <https://doi.org/10.15407/ujpe67.10.757>
 30. R. N. Bhagat and V. S. Sangawar, *Int. J. Sci. Res. (IJSR)*, **6**: 361 (2017).
 31. Z. S. Jaber, M. A. Habeeb, and W. H. Radi, *East European Journal of Physics*, **2**: 228 (2023); doi:10.26565/2312-4334-2023-2-25
 32. R. Dalven and R. Gill, *J. Appl. Phys.*, **38**, No. 2: 753 (1967); doi:10.1063/1.1709406
 33. V. Suryawanshi, A. S. Varpe, and M. D. Deshpande, *Thin Solid Films*, **645**: 87 (2018); <https://doi.org/10.1016/j.tsf.2017.10.016>
 34. R. S. Abdul Hamza and M. A. Habeeb, *Optical and Quantum Electronics*, **55**, Iss. 8: 705 (2023); <https://doi.org/10.1007/s11082-023-04995-3>
 35. A. Goswami, A. K. Bajpai, and B. K. Sinha, *Polym. Bull.*, **75**, No. 2: 781 (2018); <https://doi.org/10.1007/s00289-017-2067-2>
 36. A. A. Mohammed and M. A. Habeeb, *East European Journal of Physics*, **2**: 157 (2023); doi:10.26565/2312-4334-2023-2-15
 37. I. Oreibi and J. M. Al-Issawe, *Turkish Computational and Theoretical Chemistry*, **7**, No. 2: 12 (2023); <https://doi.org/10.33435/tcandtc.1161253>
 38. M. A. Habeeb and R. S. A. Hamza, *Indonesian Journal of Electrical Engineering and Informatics*, **6**, No. 4: 428 (2018); doi:10.11591/ijeei.v6i1.511
 39. N. K. Al-Sharifi and M. A. Habeeb, *East European Journal of Physics*, **2**: 341 (2023); doi:10.26565/2312-4334-2023-2-40
 40. S. Lather, A. Gupta, J. Dalal, V. Verma, R. Tripathi, and A. Ohlan, *Ceram. Int.*, **43**: 3246 (2017); <https://doi.org/10.1016/j.ceramint.2016.11.152>
 41. M. A. Habeeb and W. H. Rahdi, *Optical and Quantum Electronics*, **55**, Iss. 4: 334 (2023); <https://doi.org/10.1007/s11082-023-04639-6>
 42. S. M. Mahdi and M. A. Habeeb, *AIMS Materials Science*, **10**, No. 2: 288 (2023); doi:10.3934/matserci.2023015
 43. C. V. Reddy, B. Babu, I. N. Reddy, and J. Shim, *Ceramics International*, **44**, No. 6: 6940 (2018); <https://doi.org/10.1016/j.ceramint.2018.01.123>

PACS numbers: 31.15.es, 76.60.Pc, 77.22.Ej, 78.30.-j, 78.40.-q, 81.05.Zx, 82.35.Np

Exploring the Structure, Optical and Electronic Properties of New PVA–PEO–Ba–Si₃N₄ Structures for Electronics Applications

Hind Ahmed and Ahmed Hashim

*College of Education for Pure Sciences,
Department of Physics,
University of Babylon,
Hillah, Iraq*

The present work aims to design the new PVA–PEO–Ba–Si₃N₄ structures to use them in various optoelectronics nanodevices. The structural, thermal, optical and electronic characteristics of PVA–PEO–Ba–Si₃N₄ structures are studied. The structure of PVA–PEO–Ba–Si₃N₄ is analysed by GaussView 5.0.8 and relaxed using the Gaussian 09 package of programs employing the density functional theory (DFT) with the B3LYP/LanL2DZ level. The studied characteristics of PVA–PEO–Ba–Si₃N₄ structures include the energy, ionization potentials, energy gap, and electron affinity. The PVA–PEO–Ba–Si₃N₄ structures are optimized successfully with the Gaussian 09 package. The results show that the PVA–PEO–Ba–Si₃N₄ structures have good optical and electronic properties. In addition, the PVA–PEO–Ba–Si₃N₄ nanostructures have wide absorption spectrum that makes the PVA–PEO–Ba–Si₃N₄ structures suitable in various electronics devices like transistors, photovoltaic cell, sensors and other devices.

Цю роботу спрямовано на розробку нових структур полівініловий спирт (ПВС)–поліоксиетилен (ПОЕ)–Ba–Si₃N₄ для використання в різних нанопристроях оптоелектроніки. Досліджено структуру, теплові, оптичні й електронні характеристики структур ПВС–ПОЕ–Ba–Si₃N₄. Структуру ПВС–ПОЕ–Ba–Si₃N₄ було проаналізовано за допомогою GaussView 5.0.8 і зрелаксовано за допомогою пакета програм Gaussian 09, що використовує теорію функціоналу густини (DFT) на рівні B3LYP/LanL2DZ. Досліджувані характеристики структур ПВС–ПОЕ–Ba–Si₃N₄ включали енергію, потенціали йонізації, енергетичну щільність та спорідненість до електрона. Структури ПВС–ПОЕ–Ba–Si₃N₄ були успішно оптимізовані за допомогою пакета Gaussian 09. Результати показали, що структури ПВС–ПОЕ–Ba–Si₃N₄ мають хороші оптичні й електронні властивості. Крім того, наноструктури ПВС–ПОЕ–Ba–Si₃N₄ мають широкий спектр поглинання, що робить структури ПВС–ПОЕ–Ba–Si₃N₄ придатними для різних електронних пристроїв, таких як транзистори, фотоелектричні

елементи, давачі й інші пристрої.

Key words: polymer blend, Si_3N_4 , optical properties, Gaussian 09, electronics devices.

Ключові слова: полімерна суміш, Si_3N_4 , оптичні властивості, Gaussian 09, електронні пристрої.

(Received 3 September, 2023; in revised form, 4 September, 2023)

1. INTRODUCTION

Polymers are considered as organic materials, which have conjugated chains and show high electrical conduction; this one relates to their characteristics such charges' carriers as p -electrons, which cause the mobility of charge alongside the polymers' chain backbone as well, inorganic materials like metal oxides and metals. Polymers' characteristics are as good as with inorganic materials although polymers have some pros and cons, like flexibility, low cost, processability, lightweight, and resistance to corrosion. The inorganic materials as well have important characteristics like good mechanical strength and high thermal stability. Thus, polymer/inorganic systems have different applications in various fields [1]. The improvement of practical organic materials is a quickly increasing of science area, which possibly may replace the conventionally employed materials with low cost and improved performing novel ones in the future and carry out several novel applications [2, 3]. The Si_3N_4 material has large chemical stability, resistance to heat and mechanical characteristics [4]. Gaussian 03 program (computer software is to make the calculation, which is capable of predicting various characteristics of reactions and molecules, including the structures and molecular energy [5]. There are numerous studies on composites and nanocomposites to utilize in a variety of fields like antibacterial defence [6–12], electronics and optoelectronics [13, 30], energy storage [31–33], radiation shielding and bioenvironmental technology [34–39], optical fields [40–51] and sensors [52, 53]. The present work aims to design of novel PVA–PEO–Ba– Si_3N_4 structures for flexible optoelectronics devices. The PVA/PEO blend doped with barium and Si_3N_4 have promising materials in the flexible and low-cost applications for different modern industrial fields.

2. THEORETICAL PART

Energy gap (E_g) is the difference between the energies of (HOMO) and (LUMO) [5]:

$$E_{gap} = E_{LUMO} - E_{HOMO}. \quad (1)$$

The ionization energy is expressed (in [eV]) by [54] as follows:

$$I_E = -E_{HOMO}. \quad (2)$$

Electron affinity can be defined by [5] as follows:

$$E_A = -E_{LUMO}. \quad (3)$$

The chemical potential (μ) is determined by [55] as follows:

$$\mu \approx \frac{1}{2}(E_{HOMO} + E_{LUMO}) \approx -\frac{1}{2}(I_E + E_A). \quad (4)$$

Chemical hardness (H) is given by [56] as follows:

$$H = \frac{I_E - E_A}{2}, \quad (5)$$

Chemical softness (S) is the inverse of hardness by [57] as below:

$$S = \frac{1}{2H}, \quad (6)$$

Electrophilicity (ω) can be defined by [58] as follows:

$$\omega = \frac{\mu^2}{2H}. \quad (7)$$

The electronegativity (E_N) is given by [59] as follows:

$$E_N = \frac{1}{2}(I_E + E_A). \quad (8)$$

The electric dipole polarizability represents a second order variation in energy [60]. The polarizability is given by [61] as follows:

$$\langle \alpha \rangle = \frac{1}{3}(\alpha_{xx} + \alpha_{yy} + \alpha_{zz}). \quad (9)$$

4. RESULTS AND DISCUSSION

The structure of PVA-PEO-Ba-Si₃N₄ was designed by GaussView 5.0.8 and relaxed using the Gaussian 09 package of programs by employing the DFT with the B3LYP/LanL2DZ level. Figure 1 shows the optimized relaxed PVA-PEO-Ba-Si₃N₄ structure. Table 1 represents the standard orientation of all atoms in the molecule. The

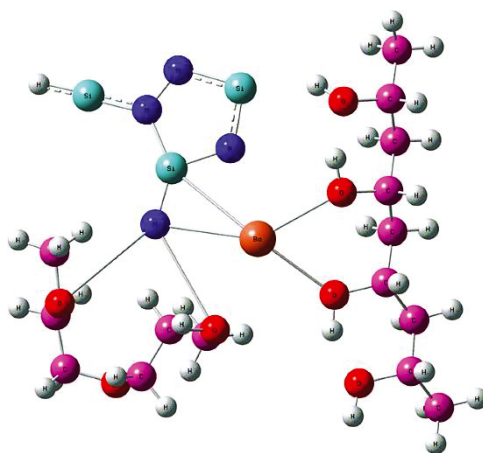


Fig. 1. Optimization of PVA-PEO-Ba-Si₃N₄ structure.

TABLE 1. Average lengths of bond in [Å] and the angles in [degrees].

| Measurements | The optimization parameters | Values |
|--------------|-----------------------------|---------|
| Bonds, Å | C-C | 1.532 |
| | C-O | 1.481 |
| | C-H | 1.099 |
| | O-H | 0.993 |
| | Si=N | 1.755 |
| | N-N | 1.411 |
| | Ba-Si | 3.271 |
| Angles, deg. | C-C-C | 113.201 |
| | C-O-H | 106.959 |
| | N-Si-N | 121.899 |
| | Ba-N-Si | 152.830 |

bonds' values in present work are agreed with Refs. [4, 62, 63].

Figure 2 shows the IR spectrum of PVA-PEO-Ba-Si₃N₄ structure calculated using DFT. As found, the strong peak observed at 3300 cm⁻¹ is attributed to the O-H groups.

In the Raman spectra, a variation is observed in the molecules' polarization; that is, the ultraviolet or visible photons interact with the vibrating bonds of molecules losing or gaining parts of their energy, thereby, creating the spectra [64]. Figure 3 represents the Raman spectra of PVA-PEO-Ba-Si₃N₄ structure. Intensities of Raman spectra depend on the probability that photon with particular wavelength will be absorbed. As seen in figure, the active IR

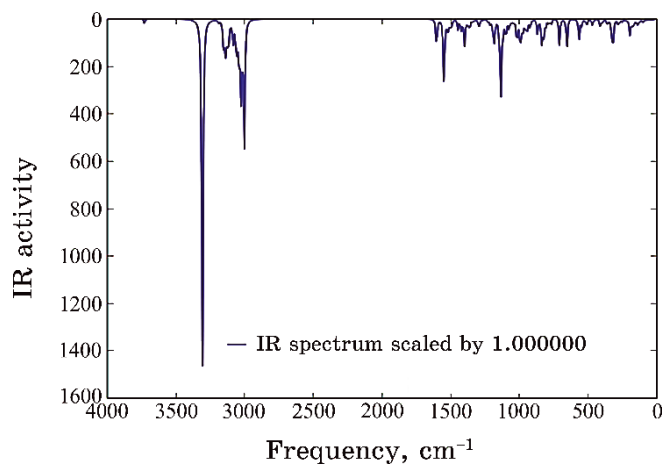


Fig. 2. IR spectra of PVA-PEO-Ba-Si₃N₄ structure.

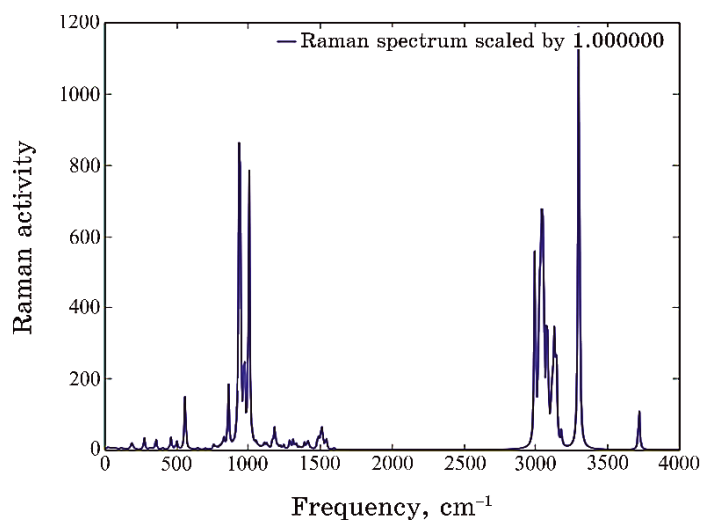


Fig. 3. Raman intensities of PVA-PEO-Ba-Si₃N₄ structure with vibration frequency.

region is similar with less activity in Raman intensities. The peak intensities in Raman spectrum depend on the probability that a particular wavelength photon will be absorbed. These probabilities can be computed from the wave function by computing the transition dipole moments. This gives relative peak intensities, since the calculation does not include the density of the substance.

The time dependence of electron absorption spectra of PVA-PEO-Ba-Si₃N₄ was performed using TD-SCF at B3LYP/DFT level of

calculations.

Figure 4 show the visible and ultraviolet spectra. The UV-Vis-calculations of PVA-PEO-Ba-Si₃N₄ composites carried out by means of the B3LYP-TD/6-31G method included the excitation energy, wavelength, oscillator strength and electronic transition. The spectrum lies within the UV-Vis limits, because the spectrum in theoretical study taking into account concentrations will be calculated at the highest concentration, where the sample will be completely opaque only seen in the visible area of the spectrum, and, at the lower concentration, it will be seen in the ultraviolet area of the spectrum.

The NMR data of PVA-PEO-Ba-Si₃N₄ composites are given in

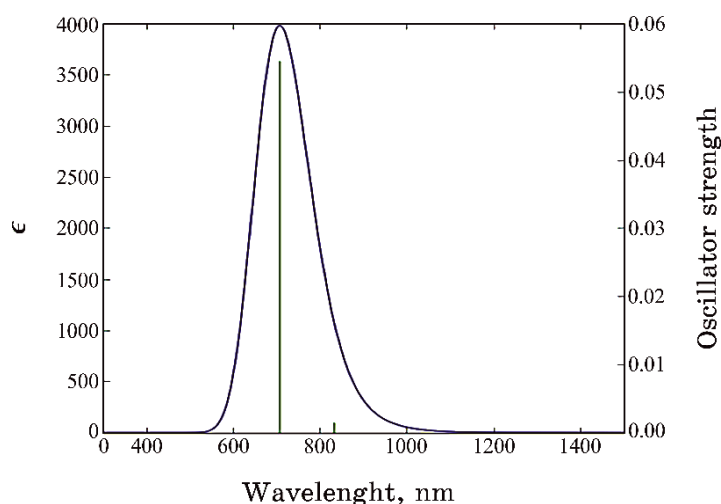


Fig. 4. UV-Vis spectrum for PVA-PEO-Ba-Si₃N₄ structures.

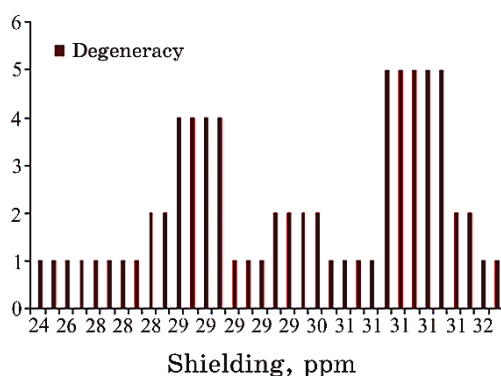


Fig. 5. Nuclear magnetic resonance of PVA-PEO-Ba-Si₃N₄ structures.

Fig. 5. $^1\text{H-NMR}$ reveals several types of protons in high shielding. The high shielding of H may be resonated to the H-bond formation with N and O atoms in ammine and hydroxyl ligands.

Table 2 gives the values of E_{HOMO} , E_{LUMO} and E_g in [eV] for PVA-PEO-Ba-Si₃N₄ structure. The E_{LUMO} is larger than the E_{HOMO} with big separation between the two molecular orbitals ($E_g = 5.75$ eV). This behaviour is in a good agreement with Refs. [4, 65] and refers that PVA-PEO-Ba-Si₃N₄ structure requests high energy to accepting or donating an electron. Concerning DOS spectra, the charge density is small in occupied orbital and elevated in virtual orbital for pure, O- and H-substituted Si₃N₄ structures. This mentions the localization of charges along the virtual orbitals rather than in occupied orbitals.

Figure 6 shows the LUMO and HOMO distributions for PVA-PEO-Ba-Si₃N₄ structures.

Figure 7 represents the electrostatic potential (ESP) distribution

TABLE 2. Energy gap values in [eV] for structures.

| PVA-PEO-Ba-Si ₃ N ₄ structures | | |
|--|-----------------|------------|
| E_{HOMO} , eV | E_{LUMO} , eV | E_g , eV |
| -9.01 | -3.26 | 5.75 |

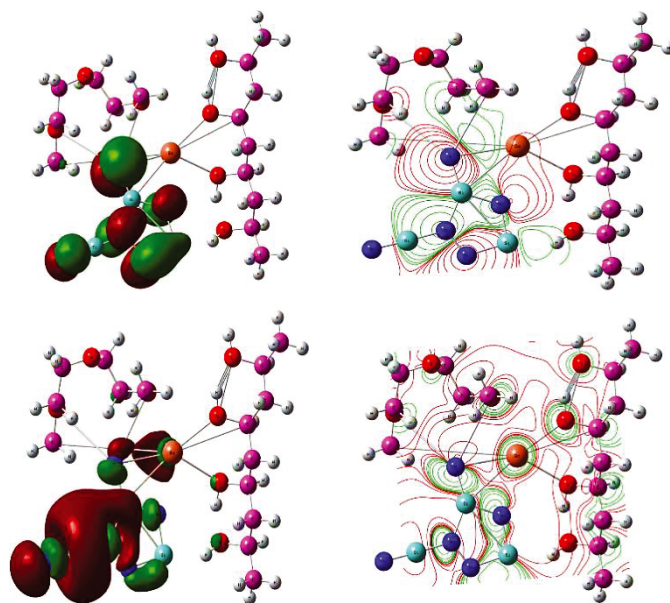


Fig. 6. The distribution of HOMO(up) and LUMO(down) for PVA-PEO-Ba-Si₃N₄ structures.

for PVA-PEO-Ba-Si₃N₄ structures from the total self-consistent field (SCF) approximation. ESP distributions for PVA-PEO-Ba-Si₃N₄ structures are created by repulsive forces or attracting regions around each structure. In commonly, the ESP surfaces for PVA-PEO-Ba-Si₃N₄ structures are dragged toward the positions of negative charges in each molecule based on the high electronegativity oxygen atoms (3.5 eV).

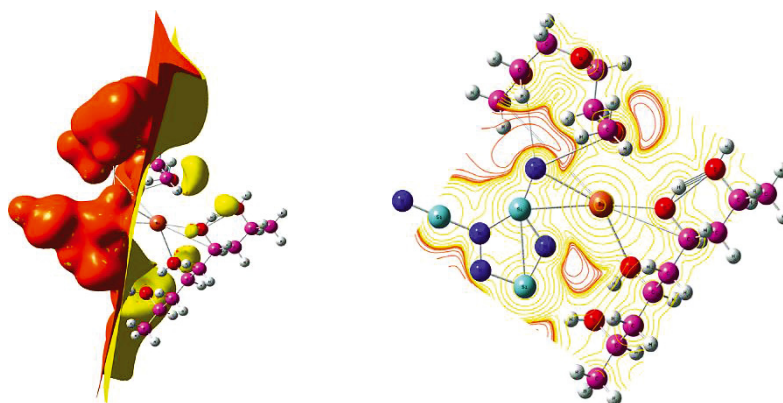


Fig. 7. Electrostatic-potential distribution surface for PVA-PEO-Ba-Si₃N₄.

TABLE 3. Electronic-characteristics values in [eV] for the structures.

| Property | PVA-PEO-Ba-Si ₃ N ₄ composites |
|-----------------------|--|
| Total energy | -1428.997 (a.u.) |
| Ionization potential | 9.01 |
| Electron affinity | 3.26 |
| Electronegativity | 6.135 |
| Chemical hardness | 2.875 |
| Chemical softness | 0.173 |
| Chemical potential | -6.135 |
| Electrophilicity | 6.545 |
| Dipole moment [Debye] | 27.149 |

TABLE 4. The calculated average $\langle\alpha\rangle$ and its components for PVA-PEO-Ba-Si₃N₄ composites.

| Polarizability, a.u. | | | |
|----------------------|----------------------|----------------------|-------------------------------|
| α_{xx} , a.u. | α_{yy} , a.u. | α_{zz} , a.u. | $\langle\alpha\rangle$, a.u. |
| 409.985 | 402.077 | 234.338 | 348.8 |

Table 3 represents the ground state energy (E_T) results in [a.u.]. These characteristics include I_E , E_A , E_N , H and ω [66].

Table 4 shows the average polarizability $\langle\alpha\rangle$ and its components in [a.u.] for PVA-PEO-Ba-Si₃N₄ structures.

The density of states (DOS) for PVA-PEO-Ba-Si₃N₄ structures as a function of energy levels was calculated by the DFT-B3LYP/LanL2DZ level of theory. Figure 8 shows the degenerated states as a function of energy levels for the structure; this degeneracy is caused by the existence of the new types of atoms that leads to varying the bond lengths and angles or changing the geometry of the structure.

Table 5 represents the E_{th} , C_v and S_{th} values of thermal characteristics for PVA-PEO-Ba-Si₃N₄ structures. These characteristics include all the electronic, translational, rotational, vibrational and total thermal degrees of freedom.

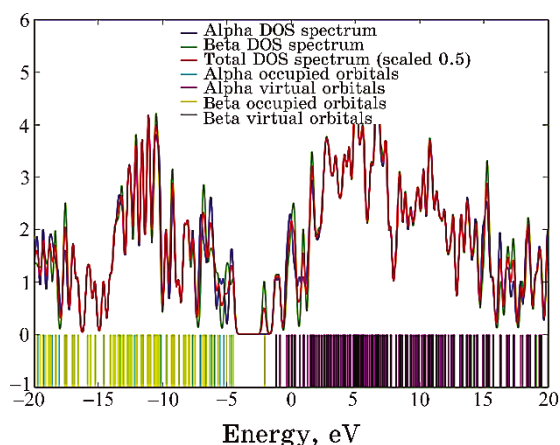


Fig. 8. DOS for PVA-PEO-Ba-Si₃N₄ structure.

TABLE 5. E_{th} , C_v and S_{th} of PVA-PEO-Ba-Si₃N₄ structure.

| Thermal corrections, Hartree/partical scheme | | | |
|--|---------------------|---------------------|------------------------|
| | E_{th} , kcal/mol | C_v , cal/(mol·K) | S_{th} , cal/(mol·K) |
| Electronic | 0.000 | 0.000 | 1.377 |
| Translational | 0.889 | 2.981 | 45.147 |
| Rotational | 0.889 | 2.981 | 38.177 |
| Vibrational | 351.958 | 135.902 | 176.463 |
| Total | 353.736 | 141.864 | 261.165 |

5. CONCLUSIONS

This work included exploring the structure, thermal, optical and electronic characteristics for electronics and optics devices. By using the DFT method, a good relaxation of the PVA-PEO-Ba-Si₃N₄ structures was determined. The ionization potential is greater than the electron affinity; so, the studied structure needs high energy to become cation. According to the high of the electrophilicity, the PVA-PEO-Ba-Si₃N₄ structures are more reactive. The results showed that the PVA-PEO-Ba-Si₃N₄ structures have good optical and electronic properties. In addition, the designed nanostructures have wide absorption spectrum that makes the PVA-PEO-Ba-Si₃N₄ structures as suitable in various electronics devices like transistors, photovoltaic cell, sensors and other devices.

REFERENCES

1. H. Ahmed and A. Hashim, *Silicon*, **14**: 4907 (2022); <https://doi.org/10.1007/s12633-021-01258-2>
2. J. H. Burroughes, D. D. Bradley, A. R. Brown, R. N. Marks, K. Mackay, R. H. Friend, P. L. Buns, and A. B. Holmes, *Nature*, **347**: 539 (1990); <https://doi.org/10.1038/347539a0>
3. G. Gustafsson, Y. Cao, G. M. Treacy, F. Klavetter, N. Colaneri, and A. J. Heeger, *Nature*, **357**: 477 (1992); <https://doi.org/10.1038/357477a0>
4. J. Zhang, Z. Huang, Z. Yin, M. Li, F. Chen, and Q. Shen, *J. of Wuhan University of Technology-Mater. Sci. Ed.*, **35**: 863 (2020); <https://doi.org/10.1007/s11595-020-2331-4>
5. M. J. Frisch, F. R. Clemente, M. J. Frisch, G. W. Trucks, H. B. Schlegel, G. E. Scuseria, M. A. Robb, J. R. Cheeseman, G. Scalmani, V. Barone, B. Mennucci, G. A. Petersson, H. Nakatsuji, M. Caricato, X. Li, H. P. Hratchian, A. F. Izmaylov, J. Bloino, and G. Zhe, *Gaussian 09, Revision A. 01*.
6. A. Hashim, I. R. Agool, and K. J. Kadhim, *Journal of Bionanoscience*, **12**, No. 5: 608 (2018); doi:10.1166/jbns.2018.1580
7. A. Hazim, A. Hashim, and H. M. Abduljalil, *International Journal of Emerging Trends in Engineering Research*, **7**, No. 8: 68 (2019); <https://doi.org/10.30534/ijeter/2019/01782019>
8. A. Hazim, H. M. Abduljalil, and A. Hashim, *International Journal of Emerging Trends in Engineering Research*, **7**, No. 8: 104 (2019); <https://doi.org/10.30534/ijeter/2019/04782019>
9. O. B. Fadil and A. Hashim, *Nanosistemi, Nanomateriali, Nanotehnologii*, **20**, Iss. 4: 1029 (2022); <https://doi.org/10.15407/nnn.20.04.1029>
10. W. O. Obaid and A. Hashim, *Nanosistemi, Nanomateriali, Nanotehnologii*, **20**, Iss. 4: 1009 (2022); <https://doi.org/10.15407/nnn.20.04.1009>
11. M. H. Meteab, A. Hashim, and B. H. Rabee, *Nanosistemi, Nanomateriali, Nanotehnologii*, **21**, Iss. 1: 199 (2023); <https://doi.org/10.15407/nnn.21.01.199>

12. M. H. Meteab, A. Hashim, and B. H. Rabee, *Nanosistemi, Nanomateriali, Nanotehnologii*, **21**, Iss. 2: 451 (2023); <https://doi.org/10.15407/nnn.21.02.451>
13. A. Hazim, A. Hashim, and H. M. Abduljalil, *Nanosistemi, Nanomateriali, Nanotehnologii*, **18**, Iss. 4: 983 (2020); <https://doi.org/10.15407/nnn.18.04.983>
14. A. Hashim and Z. S. Hamad, *Nanosistemi, Nanomateriali, Nanotehnologii*, **18**, Iss. 4: 969 (2020); <https://doi.org/10.15407/nnn.18.04.969>
15. A. Hazim, A. Hashim, and H. M. Abduljalil, *Egypt. J. Chem.*, **64**, No. 1: 359 (2021); doi:10.21608/EJCHEM.2019.18513.2144
16. H. Ahmed and A. Hashim, *Journal of Molecular Modeling*, **26**: 1 (2020); doi:10.1007/s00894-020-04479-1
17. H. Ahmed and A. Hashim, *Silicon*, **14**: 4907 (2022); <https://doi.org/10.1007/s12633-021-01258-2>
18. A. Hashim, *Opt. Quant. Electron.*, **53**: 1 (2021); <https://doi.org/10.1007/s11082-021-03100-w>
19. H. Ahmed and A. Hashim, *Trans. Electr. Electron. Mater.*, **23**: 237 (2022); <https://doi.org/10.1007/s42341-021-00340-1>
20. H. Ahmed and A. Hashim, *Silicon*, **14**: 7025 (2021); <https://doi.org/10.1007/s12633-021-01465-x>
21. A. Hazim, A. Hashim, and H. M. Abduljalil, *Trans. Electr. Electron. Mater.*, **21**: 48 (2019); <https://doi.org/10.1007/s42341-019-00148-0>
22. A. F. Kadhim and A. Hashim, *Opt. Quant. Electron.*, **55**: 432 (2023); <https://doi.org/10.1007/s11082-023-04699-8>
23. H. Ahmed and A. Hashim, *Opt. Quant. Electron.*, **55**: 280 (2023); <https://doi.org/10.1007/s11082-022-04528-4>
24. G. Ahmed and A. Hashim, *Silicon*, **15**: 3977 (2023); <https://doi.org/10.1007/s12633-023-02322-9>
25. M. H. Meteab, A. Hashim, and B. H. Rabee, *Opt. Quant. Electron.*, **55**: 187 (2023); <https://doi.org/10.1007/s11082-022-04447-4>
26. B. Mohammed, H. Ahmed, and A. Hashim, *Nanosistemi, Nanomateriali, Nanotehnologii*, **21**, Iss. 1: 113 (2023); <https://doi.org/10.15407/nnn.21.01.113>
27. A. Hashim, *Nanosistemi, Nanomateriali, Nanotehnologii*, **19**, Iss. 3: 647 (2021); <https://doi.org/10.15407/nnn.19.03.647>
28. A. F. Kadhim and A. Hashim, *Silicon*, **15**: 4613 (2023); <https://doi.org/10.1007/s12633-023-02381-y>
29. H. A. Jawad and A. Hashim, *Nanosistemi, Nanomateriali, Nanotehnologii*, **21**, Iss. 1: 133 (2023); <https://doi.org/10.15407/nnn.21.01.133>
30. M. H. Meteab, A. Hashim, and B. H. Rabee, *Silicon*, **15**: 1609 (2023); <https://doi.org/10.1007/s12633-022-02114-7>
31. A. S. Shareef, F. Lafta Rashid, A. Hadi, and A. Hashim, *International Journal of Scientific & Technology Research*, **8**, Iss. 11: 1041 (2019).
32. A. Hadi, A. Hashim, and D. Hassan, *Bulletin of Electrical Engineering and Informatics*, **9**, No. 1: 83 (2020); doi:10.11591/eei.v9i1.1323
33. H. Ahmed and A. Hashim, *Nanosistemi, Nanomateriali, Nanotehnologii*, **20**, Iss. 4: 951 (2022); <https://doi.org/10.15407/nnn.20.04.951>
34. A. Hashim and N. Hamid, *Journal of Bionanoscience*, **12**, No. 6: 788 (2018); doi:10.1166/jbns.2018.1591

35. A. Hashim and Z. S. Hamad, *Journal of Bionanoscience*, **12**, No. 4: 488 (2018); doi:10.1166/jbns.2018.1551
36. A. Hashim and Z. S. Hamad, *Journal of Bionanoscience*, **12**, No. 4: 504 (2018); doi:10.1166/jbns.2018.1561
37. B. Abbas and A. Hashim, *International Journal of Emerging Trends in Engineering Research*, **7**, No. 8: 131 (2019); <https://doi.org/10.30534/ijeter/2019/06782019>
38. K. H. H. Al-Attiyah, A. Hashim, and S. F. Obaid, *Journal of Bionanoscience*, **12**: 200 (2018); doi:10.1166/jbns.2018.1526
39. H. A. J. Hussien, A. Hadi, and A. Hashim, *Nanosistemi, Nanomateriali, Nanotehnologii*, **20**, Iss. 4: 1001 (2022); <https://doi.org/10.15407/nnn.20.04.1001>
40. H. Ahmed and A. Hashim, *Silicon*, **14**: 6637 (2022); <https://doi.org/10.1007/s12633-021-01449-x>
41. H. Ahmed and A. Hashim, *Silicon*, **13**: 4331 (2020); <https://doi.org/10.1007/s12633-020-00723-8>
42. O. B. Fadil and A. Hashim, *Silicon*, **14**: 9845 (2022); <https://doi.org/10.1007/s12633-022-01728-1>
43. H. Ahmed and A. Hashim, *Silicon*, **15**: 2339 (2023); <https://doi.org/10.1007/s12633-022-02173-w>
44. H. B. Hassan, H. M. Abduljalil, and A. Hashim, *Nanosistemi, Nanomateriali, Nanotehnologii*, **20**, Iss. 4: 941 (2022); <https://doi.org/10.15407/nnn.20.04.941>
45. H. A. Jawad and A. Hashim, *Nanosistemi, Nanomateriali, Nanotehnologii*, **20**, Iss. 4: 963 (2022); <https://doi.org/10.15407/nnn.20.04.963>
46. A. S. Shareef, F. Lafta Rashid, A. Hadi, and A. Hashim, *International Journal of Scientific & Technology Research*, **8**, Iss. 11: 1041 (2019).
47. A. Hadi, A. Hashim, and D. Hassan, *Bulletin of Electrical Engineering and Informatics*, **9**, No. 1: 83 (2020); doi:10.11591/eei.v9i1.1323
48. H. Ahmed and A. Hashim, *Transactions on Electrical and Electronic Materials*, **22**: 335 (2021); <https://doi.org/10.1007/s42341-020-00244-6>
49. N. A.-H. Al-Aaraji, A. Hashim, A. Hadi, and H. M. Abduljalil, *Silicon*, **14**: 10037 (2022); <https://doi.org/10.1007/s12633-022-01730-7>
50. H. Ahmed and A. Hashim, *Opt. Quant. Electron.*, **55**: 1 (2023); <https://doi.org/10.1007/s11082-022-04273-8>
51. W. O. Obaid and A. Hashim, *Silicon*, **14**: 11199 (2022); <https://doi.org/10.1007/s12633-022-01854-w>
52. H. Ahmed and A. Hashim, *International Journal of Scientific & Technology Research*, **8**, Iss. 11: 1014 (2019).
53. B. Mohammed, H. Ahmed, and A. Hashim, *Nanosistemi, Nanomateriali, Nanotehnologii*, **20**, Iss. 1: 187 (2022); <https://doi.org/10.15407/nnn.20.01.187>
54. H. M. Kampen, H. Méndez, and D. R. T. Zahn, *University of Chemnitz, Institut für Physik, Germany*, **28**: 1 (1999); https://www.tu-chemnitz.de/physik/HLP/ublications/p_src/438.pdf
55. K. Sadasivam and R. Kumaresan, *Computational and Theoretical Chemistry*, **963**: 1 (2011); <https://doi.org/10.1016/j.comptc.2010.10.025>
56. O. A. Kolawole and S. Banjo, *Anal. Bioanal. Electrochem.*, **10**: 136 (2018).
57. P. W. Atkins and R. S. Friedman, *Molecular Quantum Mechanics* (Oxford

- University Press: 2011); http://sutlib2.sut.ac.th/sut_contents/H96900.pdf
58. V. Subramanian, *Cen. Leather Res. Inst. Chem. Laboratory*, **1** (2005); https://scholar.google.com/scholar?hl=ar&as_sdt=0%2C5&q=Subramanian%2C+V.+%282005%29.+Quantum+Chemical+Descriptors+in+Computation+Medicinal+Chemistry+for+Chemoinformatics.+Central+Leather+Research+Institute%2C+Chemical+Laboratory%2C+0-0000&btnG=
59. L. Shenghua, Y. He, and J. Yuansheng, *Int. J. of Mole. Sci.*, **5**: 13 (2004).
60. A. J. Camargo, K. M. Honorio, R. Mercadante, F. A. Molfetta, C. N. Alves, and A. B. da Silva, *Journal of the Brazilian Chemical Society*, **14**: 809 (2003); <https://doi.org/10.1590/S0103-50532003000500017>
61. P. Udhayakala and T. V. Rajendiran, *Journal of Chemical, Biological and Physical Sciences*, **2**: 172 (2011).
62. F. L. Riley, *Journal of the American Ceramic Society*, **83**: 245 (2000); <https://doi.org/10.1111/j.1151-2916.2000.tb01182.x>
63. V. M. Bermudez, *Surface Sci.*, **691**: 1 (2020); <https://doi.org/10.1016/j.susc.2019.121511>
64. Peter J. Larkin, *Infrared and Raman Spectroscopy: Principles and Spectral Interpretation* (USA: Elsevier Inc.: 2013).
65. H. Zhu, L. Shi, S. Li, S. Zhang, T. Tang, and W. Xia, *physica status solidi (b)*, **255**: 1 (2018); <https://doi.org/10.1002/pssb.201700676>
66. V. Nagarajan, S. Venkatesan, and R. Chandiramouli, *Int. J. of Chem. Tech. Res.*, **6**: 5466 (2014).

PACS numbers: 31.15.es, 61.46.Bc, 71.20.-b, 73.22.-f, 81.05.Zx, 81.07.Pr, 82.35.Np

Design and Exploring the Structure and Electronic Characteristics of PS/MnO₂/NiO Nanosystem for Optics and Electronics Nanodevices

Ali S. Hasan¹, Ahmed Hashim², and Zinah S. Hasan³

¹*College of Materials Engineering,
Department of Polymer and Petrochemical Industries,
University of Babylon,
Hillah, Iraq*

²*College of Education for Pure Sciences,
Department of Physics,
University of Babylon,
Hillah, Iraq*

³*Babylon Technical Institute,
Al-Furat Al-Awsat Technical University,
Najaf, Iraq*

The present work comprises design of new polystyrene (PS)/MnO₂/NiO nanosystem to exploit it in many optics and electronics nanodevices. The optimization, structural and electronic characteristics of PS/MnO₂/NiO nanosystem are studied. The results indicate that the electronics characteristics of PS are improved, when the MnO₂/NiO nanostructures are added. The energy gap of PS is decreased from 5.773 eV to 3.814 eV with adding of MnO₂/NiO nanostructures. The results show that the PS/MnO₂/NiO nanosystem has excellent electronic characteristics, which make the PS/MnO₂/NiO nanosystem suitable for different optics and electronics fields.

Ця робота включає проектування нової наносистеми полістирол (ПС)/MnO₂/NiO для використання в багатьох оптичних і електронних нанопристроях. Досліджено оптимізацію, структуру й електронні характеристики наносистеми ПС/MnO₂/NiO. Результати показали, що електронні характеристики полістиролу було поліпшено із додаванням наноструктур MnO₂/NiO. Енергетична заборонена зона ПС зменшилася від 5,773 еВ до 3,814 еВ через додавання наноструктур MnO₂/NiO. Остаточні результати показали, що наносистема ПС/MnO₂/NiO має відмінні електронні характеристики, які роблять наносистему ПС/MnO₂/NiO придатною для різних областей оптики й електроніки.

Key words: polystyrene, MnO₂/NiO, nanosystem, electronic characteris-

tics, energy gap.

Ключові слова: полістирол, MnO_2/NiO , наносистема, електронні характеристики, енергетична заборонена зона.

(Received 3 September, 2023)

1. INTRODUCTION

Composite materials have a wide variety of applications in electrical devices, mobile communication systems, *etc.* Therefore, composite tailoring was initiated to suit the specific needs for different usage. In the past decade, there have been several researches carried out with different metal oxides due to their application in various electronic devices such as smart window, optical detector, cathode coating in high-capacity lithium batteries, high performance capacitor, thermistor and others. Transition elements have mixed valence ions; hence, those compounds have unique properties and are very useful in various fields [1]. Nanostructured manganese dioxide (MnO_2) is a promising transition metal oxide for its admirable chemical stability, transparency, low toxicity, low cost, functional biocompatibility, excellent adsorption capacity, catalytic properties, and widespread availability [2].

Nickel oxide (NiO) is the most investigated metal oxide and it has attracted considerable attention because of its low cost material, and also for its application in several fields such as a catalyst, transparent conducting oxide, photodetectors, electrochromic, gas sensors, photovoltaic devices, electrochemical supercapacitors, heat reflectors, photoelectrochemical cell, solar cells and many optoelectronic devices. NiO is an IV group and it can be used as a transparent *p*-type semiconductor layers, it has a band gap energy ranging from 3.45 eV to 3.85 eV. Band gap energy is significant to adjust the energy level state of NiO [3]. Polystyrene (PS) is a commercial thermoplastic polymer. It is rather brittle, clear and has good mechanical properties and a low cost price. Thus, PS has a wide range of applications as construction materials, packaging, disposable cups, consumer electronics, cassette boxes, compact disks and medical uses [4]. There are several studies on the electronic, optical and electrical properties of polystyrene nanocomposites [5–11]. The current study includes design of $\text{PS}/\text{MnO}_2/\text{NiO}$ nanostructures and investigating the electronic properties to employ in various optoelectronics nanodevices.

2. COMPUTATIONAL DETAIL

In this work, all the geometric structures are optimized and considered by time-dependent density-functional theory (TDDFT) with

B3LYP [12, 13] functional and the 6-31G (*d, p*) basis set, which applied in Gaussian 09 software [14]. TDDFT methods provide a powerful approach for studying the electronic structure and properties of molecules. They offer several advantages that contribute to enhancing the accuracy and reliability of computational results in comparison to other methods. TDDFT allows for the investigation of excited electronic states, which are crucial for understanding phenomena such as absorption spectra, fluorescence, and photochemical reactions. By including the description of excited states, TDDFT can provide a more comprehensive understanding of molecular behaviour. In addition, TDDFT is computationally more efficient compared to methods based on wave function theory, such as traditional *ab initio* methods. TDDFT calculations scale linearly with system size, making it feasible to study larger systems and perform more extensive sampling of potential energy surfaces. One of the most important reasons for choosing a method TDDFT is applicable to a wide range of molecular systems, including organic molecules, inorganic complexes, and materials, especially polymers. It can be used to investigate various properties, such as electronic spectra, response properties, and excited-state dynamics. This chemical model has been extensively used to relax the geometry and calculate the optoelectronic properties, such as total energies (E_T), Fermi energy (E_F), HOMO (Highest Occupied Molecular Orbital) and LUMO (Lowest Unoccupied Molecular Orbital), energy gap (E_g) and electronic transition energies. These methods are not only encouraging more profound understanding of the association between the optoelectronic properties and chemical structures of the molecule structures but also may be used to design new molecule structures. To evaluate the reactivity and the stability of the composites, TDDFT-based descriptors were calculated [15, 16]:

$$\mu = \left(\frac{\partial E}{\partial N} \right)_{V(\mathbf{r}), T}, \quad \eta = \frac{1}{2} \left(\frac{\partial^2 E}{\partial N^2} \right)_{V(\mathbf{r}), T}, \quad S = \frac{1}{2\eta}, \quad \omega = \frac{\mu^2}{2\eta},$$

where I_p , E_A , μ , η , S , and ω are the ionization potential, electron affinity, chemical potential, chemical hardness, chemical softness, and electrophilicity, respectively, while E , N and $V(\mathbf{r})$ are the total electron energy, number of electrons, and external potential, respectively. There are two different methods to calculate the above the global quantities, the first is a finite difference approximation which based on the differences of total electronic energies when an electron is removed or added in accordance with the neutral molecule [17]. The second is Koopmans' theorem, which based on the differences between the HOMO and LUMO energies for the neutral molecule [13]. Using a finite difference approximation, the global

quantities can be given by [18–20] as follow:

$$I_P = -E_{HOMO}, E_A = -E_{LUMO}, \eta = \frac{(I_P - E_A)}{2}.$$

Then, using Koopmans' theorem, the above equations can be given as follow:

$$E_F = \frac{(E_{HOMO} + E_{LUMO})}{2}, \eta = \frac{(E_{HOMO} - E_{LUMO})}{2}.$$

3. RESULTS AND DISCUSSION

In this research study, computational analyses were conducted using the Gaussian 09 suite of programs and the TDDFT methods to investigate certain molecules, as shown in Fig. 1. The focus was on the geometrical optimization of polystyrene (PS) and PS-MnO₂-NiO structures. The relaxation process aimed to find the most stable configurations for these structures based on the computational analyses. In the research study, computational analyses were conducted using Gaussian 09, a widely recognized software package for computational chemistry [17, 21, 22]. To improve the accuracy and reliability of the results, the study employed Time-Dependent Density Functional Theory (TDDFT) methods.

Specifically, the carbon-carbon bond lengths fell within the ranges for C-C: 1.511 Å, C=C: 1.401 Å, and C-H: 1.057 Å. Additionally, the bond lengths for Mn-O and Ni-O were determined to be 1.83 Å and 1.748 Å, respectively. These values are consistent with the typical bond lengths observed in aromatic rings [18, 23, 24]. The

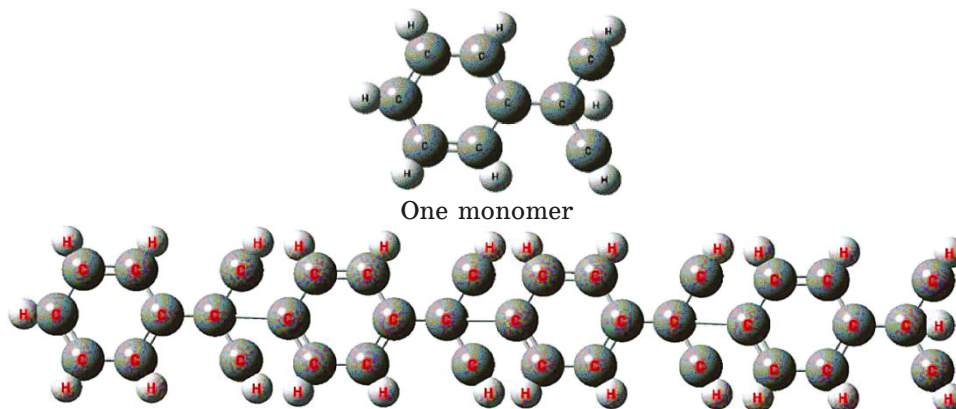


Fig. 1. Structural of PS before relaxing.

bond length between carbon and hydrogen in organic molecules can be influenced by electrostatic forces between molecules, influenced by positive or negative charges, can influence electron transfer and impact the bond length. In addition, hydrogen bonding interactions and other intermolecular forces can also influence the bond length between carbon and hydrogen. Hydrogen bonding can lead to elongation or contraction of the bond length, depending on the strength and directionality of the hydrogen bond. As well, molecules can go through transition states where bond lengths may deviate from their equilibrium values. Factors such as reaction pathways, activation energies, and intermediate states can temporarily affect the bond length between carbon and hydrogen [24–26].

The research focused on the geometrical optimization of polymeric composites, specifically PS and PS-MnO₂-NiO. The obtained structural properties were found to be in good agreement with experimental data, both in terms of bond length and bond strength. This agreement suggests that these materials exhibit interactions and properties that are highly compatible with each other from both physical and chemical perspectives, as illustrated in Figs. 2 and 3.

The compatibility observed between PS and the MnO₂-NiO composite implies that they can effectively interact with each other,

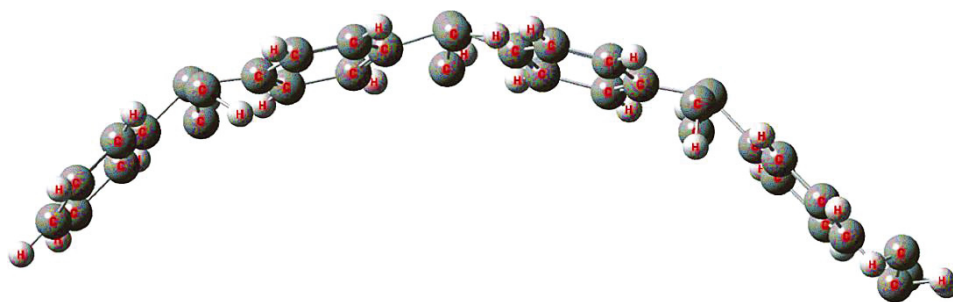


Fig. 2. Structure of PS after relaxing.

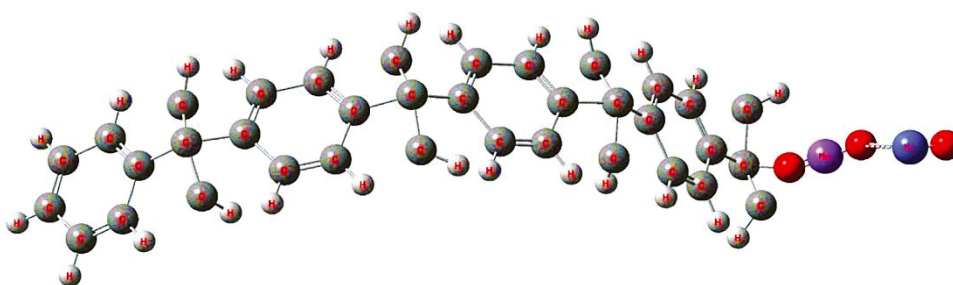


Fig. 3. Structure of PS-MnO₂-NiO composites.

leading to the formation of new compounds or compounds in a consistent and homogeneous manner. The presence of MnO_2 and NiO in the composite can create a favourable environment for chemical reactions with PS. These metal oxides can act as catalysts or initiators, facilitating chemical reactions with the polymer. This compatibility opens up possibilities for joint applications or the creation of composite compositions that can benefit from the combined interactions of these materials.

With the observation of Fig. 3 after relaxation, we notice the significant change in the shape of the polymer chain, so that PS and the MnO_2 - NiO compound participate in intermolecular interactions, such as hydrogen bonding, van der Waals forces, or stacking interactions. Thus, these interactions promote the alignment and aggregation of the polymer chains with the composite, leading to the formation of new structures or phases within the composite material [17, 27].

Table presents the ground state calculations of polymeric composites in this study, specifically focusing on the minimum energy configurations. The calculations include the following parameters: total energy (in atomic units, [a.u.]), I_p and E_A (measured in [eV]) calculated using Koopmans' theorem, E_g in [eV], S in [(eV)⁻¹], η in [eV], ω in [eV], density of states (DOS) and the energies of the HOMO and LUMO. E_T of the polymeric composites in this study is observed to be very small. This indicates that the binding energy within each structure is also low. Consequently, polymeric composites with lower total energy tend to have limited energy storage capabilities. However, this characteristic can be advantageous in certain applications that prioritize lightweight materials. The specific selection or composition of the composites plays a crucial role in achieving these properties [18, 22, 27].

Where lightweight materials play a crucial role in renewable energy technologies? For instance, in wind energy, lightweight composite materials are used for turbine blades to enable efficient energy conversion. Similarly, in solar energy, lightweight materials are utilized for constructing solar panels and supporting structures. In addition, lightweight materials are integral to portable electronic devices such as smartphones, laptops, and tablets. Materials like aluminium, magnesium alloys, and polymers are used to reduce weight and enhance portability without compromising durability [18, 19, 28].

Indeed, the I_p and E_A values can vary between different materials or composite systems. In the case of PS- MnO_2 - NiO , both the I_p and E_A values are higher compared to PS. A higher I_p indicates that the material has a stronger tendency to retain its electrons, while a higher E_A suggests a greater ability to attract additional electrons.

TABLE. Calculation total energies (E_T), HOMO energies (E_{HOMO}), LUMO energies (E_{LUMO}), electronic band gap (E_g), Fermi energies (E_F), ionization potentials (I_p), electron affinities (E_A), chemical potentials (μ), chemical hardnesses (η), chemical softnesses (S) and electrophilicity indexes (ω) (in [eV]) *via* using TDDFT B3LYP/6-31 (d, p) scheme.

| Sample | E_T | HOMO | LUMO | E_g | I_p | E_A | E_F | η | S | ω |
|--------------------------|-----------|---------|---------|-------|-------|-------|--------|--------|-------|----------|
| PS | -9541.325 | -5.9874 | -0.2147 | 5.773 | 5.987 | 0.215 | -3.101 | 2.886 | 0.173 | 1.666 |
| PS-MnO ₂ -NiO | -6378.325 | -4.0124 | -0.1987 | 3.814 | 4.012 | 0.199 | -2.106 | 1.907 | 0.262 | 1.163 |

These differences in electronic properties between composites can be attributed to several factors, including variations in chemical composition, structure, or bonding characteristics, where the incorporation of MnO_2 and NiO into the PS matrix can introduce additional electron-donating or electron-accepting groups, altering the overall electronic behaviour of the composite. Changes in the composite's chemical environment, such as the presence of transition metal ions or different bonding configurations, can also influence the I_p and E_A values. Understanding these electronic property differences is crucial for tailoring the behaviour and functionality of polymeric composites for specific applications, such as energy storage, catalysis, or electronic devices [14, 16, 29].

The results obtained for the parameters S , η , and ω in the structures PS and PS- MnO_2 - NiO indicate important characteristics of the polymeric composites. A large value of η and ω suggests a higher energy requirement, indicating that the system is relatively more stable and less reactive towards electron transfer, whereas shown in Table. This one indicates that the polymeric composites have a greater energy threshold for electron transfer processes, making them less prone to electronic changes or reactivity. On the other hand, a small value of S suggests a lower energy requirement for electron transfer, implying higher reactivity and a greater tendency to undergo electronic changes. This can be attributed to the compatibility and good distribution of materials within the polymer matrix, which facilitates electron transfer processes and enhances reactivity [19]. Additionally, it is observed that the chemical hardness decreases and the chemical softness increases in both PS and PS- MnO_2 - NiO structures. Higher values of chemical softness indicate a lower energy requirement for electron transfer, implying greater reactivity and a higher propensity for electronic changes. The compatibility and good distribution of the materials within the polymer matrix contribute to these changes in chemical hardness, softness, and electrophilicity. The specific arrangement and distribution of the MnO_2 and NiO components within the polymer matrix enhance the reactivity and electronic changes in the composite [30, 31].

The concepts of chemical hardness, softness, and electrophilicity are relevant in understanding the reactivity and stability of polymeric composites. A decrease in chemical hardness and an increase in chemical softness indicate a lower energy requirement for electron transfer, implying higher reactivity and a greater tendency to undergo electronic changes. This is attributed to the compatibility and good distribution of materials within the polymer matrix. Changes in these properties can have implications for the design and application of polymeric composites in areas such as catalysis, energy storage, and electronic devices [14].

Through the Table, the information suggests that the addition of $\text{MnO}_2\text{-NiO}$ to the polymer PS leads to a decrease in the E_g values, indicating a decrease in the energy gap between the HOMO and LUMO levels. This suggests the possibility of an electronic transition between the valence band and conductivity. When $\text{MnO}_2\text{-NiO}$ is added to the polymer, it interacts with the existing polymer structures through various mechanisms, such as chemical bonding, electrostatic interactions, and intermolecular forces. These interactions can result in changes in the electronic structure of the polymer and the formation of new energy states within the polymer. One possible mechanism is the formation of chemical bonds between the $\text{MnO}_2\text{-NiO}$ particles and the polymer chains. This can occur through covalent bonding or coordination bonding, depending on the nature of the materials and the specific conditions. The formation of chemical bonds introduces new energy levels within the polymer electronic structure. Additionally, the presence of $\text{MnO}_2\text{-NiO}$ particles can induce changes in the local electric field and electronic environment around the polymer chains. This can lead to polarization effects and redistribution of electron density within the polymer. As a result, new energy states may emerge within the polymer's electronic band structure [15, 21, 31].

Figures 4 and 5 depict the HOMO and LUMO energy levels for

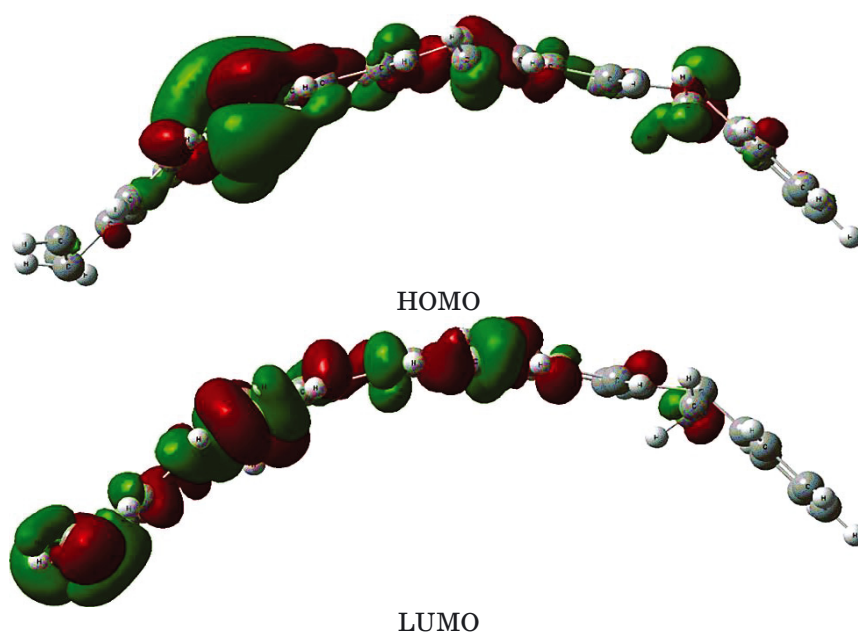


Fig. 4. The shapes of HOMO and LUMO for PS.

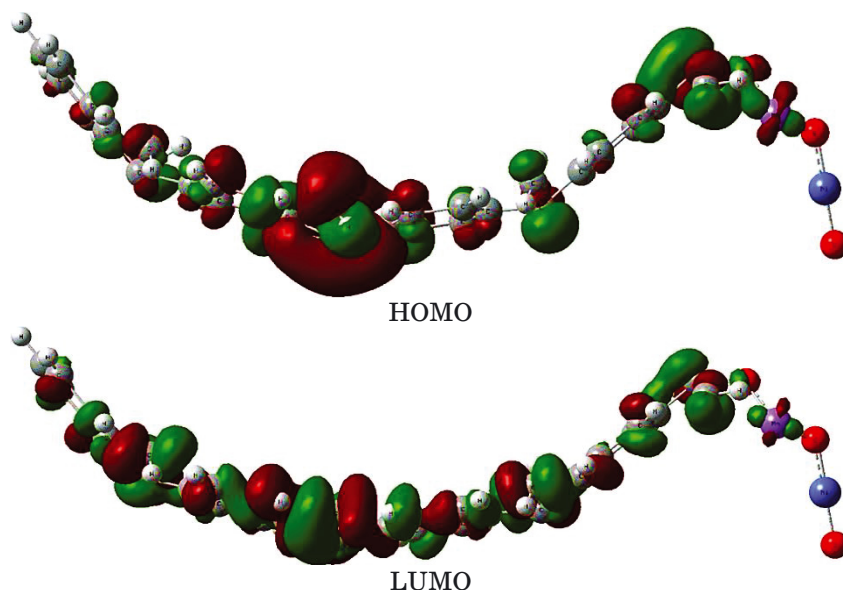


Fig. 5. The shapes of HOMO and LUMO for PS-MnO₂-NiO composites.

the PS-MnO₂-NiO structure, showing a more stable electronic distribution compared to PS alone. This stability is likely due to the withdrawal of electrons by the MnO₂-NiO materials. This enhanced stability can be attributed to the withdrawal of electrons by the MnO₂-NiO materials. MnO₂-NiO, being transition metal oxide materials, can have a higher electron affinity compared to the polymer PS. This means that they have a stronger tendency to attract and accept electrons. When MnO₂-NiO is incorporated into the PS matrix, it can act as an electron acceptor, causing a redistribution of electron density within the system. As MnO₂-NiO withdraws electrons from the surrounding PS molecules, it can induce a more balanced distribution of electron density throughout the structure. This redistribution of electrons helps stabilize the electronic system by reducing any localized charge imbalances or electron-rich regions within the polymer [14, 29, 30].

The provided information highlights the significance of the density of states (DOS) in understanding the electronic structure and properties of materials. The DOS provides valuable insights into various material properties, including electrical conductivity, thermal conductivity, and optical properties. The DOS is a function of energy, denoted as $g(E)$, where E represents the energy level. It describes the number of states per unit volume per unit energy range at a specific energy level. Mathematically, the DOS can be expressed as follows:

$$g(E) = V^{-1}dN(E)/dE,$$

where V represents the volume of the material, and $dN(E)/dE$ represents the change in the number of states with respect to energy.

In the context of polymeric compounds, the density diagram or DOS plot (as shown in Figs. 6 and 7) reveals the presence of an en-

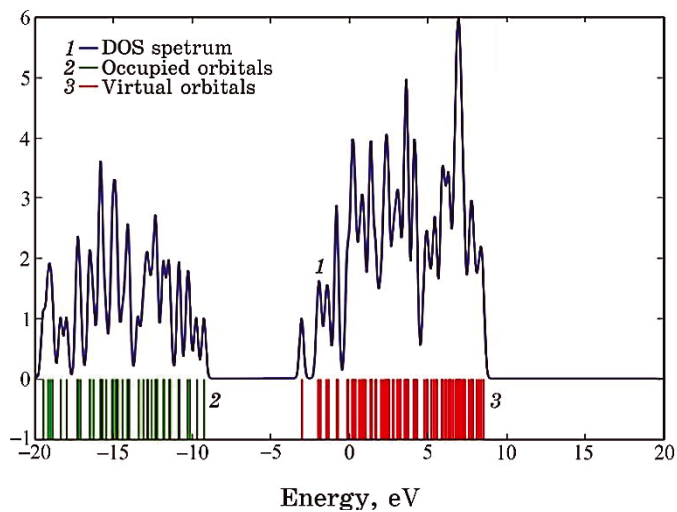


Fig. 6. Density of states (DOS) for PS.

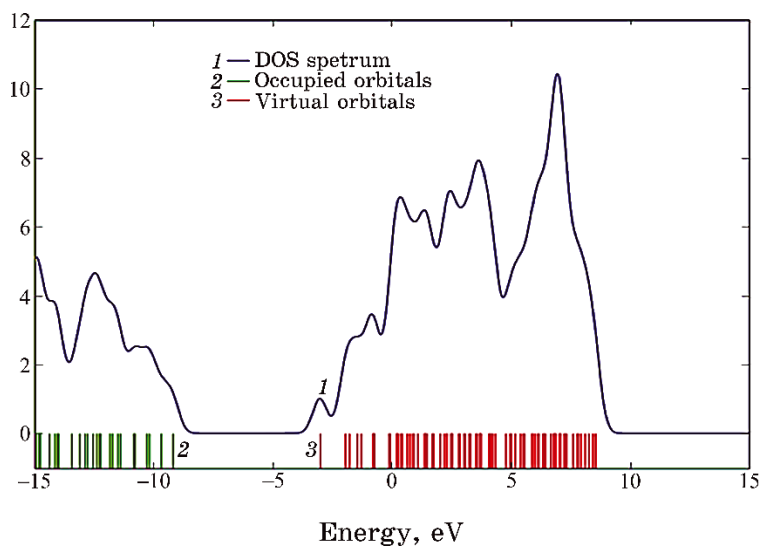


Fig. 7. Density of states (DOS) for PS-MnO₂-NiO composites.

ergy gap between the valence band (the highest occupied energy band) and the conduction band (the lowest unoccupied energy band) [17, 28].

Within the band gap, the DOS exhibits a region of either zero or very low density of states. This indicates a lack of available electronic states in that energy range. On the other hand, the DOS is relatively high in the valence and conduction bands, indicating the presence of occupied or excited electronic states. The presence of a distinct energy gap between the valence and conduction bands is a characteristic feature of semiconductors and insulators as in polymers. By analysing the DOS, researchers can study phenomena such as energy bands, and the E_F energy, which is a key concept in solid-state physics and is related to DOS. It represents the highest energy level that electrons occupy at a temperature of absolute zero. Moreover, as shown in Table, while the E_F increases when $\text{MnO}_2\text{-NiO}$ is added, this confirms that the E_F exists within the band gap in the polymers, which is the energy band where no electronic states are allowed. The DOS near the E_F in this region is low, reflecting the lack of available occupancy electronic states. This energy gap prevents large electron mobility and leads to poor electrical conductivity. However, in $\text{PS-MnO}_2\text{-NiO}$ composites, the band gap is relatively small compared to insulators, which allows some thermal excitation of electrons across the gap, leading to their partial conduction [25, 31].

4. CONCLUSIONS

This work involved design and investigating the optimization, structure and electronic characteristics of $\text{PS/MnO}_2\text{/NiO}$ nanosystem as a new nanostructure to utilize in a lot of optics and electronics applications. The obtained results illustrated that the electronics characteristics of polystyrene were improved, when the $\text{MnO}_2\text{/NiO}$ nanostructures added. The energy gap of PS decreased from 5.773 eV to 3.814 eV among adding of $\text{MnO}_2\text{/NiO}$ nanostructures. The final results indicated to the $\text{PS/MnO}_2\text{/NiO}$ nanosystem have excellent electronic characteristics, which make the $\text{PS/MnO}_2\text{/NiO}$ nanosystem appropriate for different optics and electronics applications.

REFERENCES

1. T. F. Khoon, J. Hassan, Z. A. Wahab, and R. S. Azis, *Results in Physics*, **6**: 420 (2016); <https://doi.org/10.1016/j.rinp.2016.07.011>
2. M. Zahan and J. Podder, *SN Applied Sciences*, **2**: 1 (2020); <https://doi.org/10.1007/s42452-020-2191-8>

3. M. Ghougali, O. Belahssen, and A. Chala, *Journal of Nano- and Electronic Physics*, **8**, No. 2: 1 (2016); doi:10.21272/jnep.8(4(2)).04059
4. G. M. Nasr, T. A. Mohamed, and R. M. Ahmed, *IOP Conf. Series: Materials Science and Engineering*, **956**: 1 (2020); doi:10.1088/1757-899X/956/1/012002
5. H. Ahmed and A. Hashim, *Silicon*, **15**: 2339 (2023); <https://doi.org/10.1007/s12633-022-02173-w>
6. H. Ahmed and A. Hashim, *Opt. Quant. Electron.*, **55**: 1 (2023); <https://doi.org/10.1007/s11082-022-04273-8>
7. M. H. Meteab, A. Hashim, and B. H. Rabee, *Silicon*, **15**: 1609 (2023); <https://doi.org/10.1007/s12633-022-02114-7>
8. A. Hashim, M. H. Abbas, N. A.-H. Al-Aaraji, and A. Hadi, *J. Inorg. Organomet. Polym.*, **33**: 1 (2023); <https://doi.org/10.1007/s10904-022-02485-9>
9. M. H. Meteab, A. Hashim, and B. H. Rabee, *Opt. Quant. Electron.*, **55**: 187 (2023); <https://doi.org/10.1007/s11082-022-04447-4>
10. H. Ahmed and A. Hashim, *Silicon*, **14**: 7025 (2021); <https://doi.org/10.1007/s12633-021-01465-x>
11. M. H. Meteab, A. Hashim, and B. H. Rabee, *Silicon*, **15**: 251 (2023); <https://doi.org/10.1007/s12633-022-02020-y>
12. M. H. Kadhim, A. S. Hasan, M. A. Akraa, and A. Y. Layla, *Journal of Ovonic Research*, **17**: 3 (2021); doi.org/10.15251/jor.2021.173.273
13. Y. Son, M. Cohen, and S. Louie, *Nature*, **444**: 7117 (2006); <https://doi.org/10.1038/nature05180>
14. A. S. Hasan and H. I. Abbood, *Journal of Kufa-Physics*, **8**: 59 (2016); <https://journal.uokufa.edu.iq/index.php/jkp/article/view/7474>
15. S. Hu, L. Collins, V. Goncharov, J. Kress, R. McCrory, and S. Skupsky, *Physics of Plasmas*, **23**: 4 (2016); <https://doi.org/10.1063/1.4945753>
16. F. Q. Mohammed, M. S. Edan, A. S. Hasan, and A. J. Haider, *Key Engineering Materials*, **886**, No. 1: 97 (2021); doi.org/10.4028/www.scientific.net/KEM.886.97
17. Z. Huang, M. Shanmugam, Z. Liu, A. Brookfield, E. Bennett, R. Guan, D. Vega Herrera, J. Lopez-Sanchez, A. Slater, E. McInnes, X. Qi, and J. Xiao, *Journal of the American Chemical Society*, **144**: 14 (2022); <https://doi.org/10.1021/jacs.2c01410>
18. A. S. Hasan, B. Y. Kadem, M. A. Akraa, and A. K. Hassan, *Digest Journal of Nanomaterials and Biostructures*, **15**: 1 (2020); doi.org/10.15251/djnb.2020.151.197
19. A. S. Hasan, F. Q. Mohammed, and M. M. Takz, *Journal of Mechanical Engineering Research and Developments*, **43**: 11 (2020); [https://jmerd.net/Paper/Vol.43,No.1\(2020\)/11-17](https://jmerd.net/Paper/Vol.43,No.1(2020)/11-17)
20. X. Zhang, Z. Chen, Z. Wan, C. Liu, R. He, X. Xie, and Z. Huang, *International Journal of Molecular Sciences*, **23**: 20 (2022); <https://doi.org/10.3390/ijms232012158>
21. S. A. Habeeb, A. S. Hasan, Țălu, and A. J. Jawad, *Iranian Journal of Chemistry and Chemical Engineering*, **40**: 5 (2021); doi.org/10.30492/ijcce.2020.40535
22. T. Chantawansri, T. Sirk, E. Byrd, J. Andzelm, and B. Rice, *Journal of Chemical Physics*, **137**: 20 (2012); <https://doi.org/10.1063/1.4767394>
23. S. H. Abud, A. S. Hasan, M. Almaamori, and N. Bayan, *Journal of Physics*:

- Conference Series*, **1818**: 1 (2021); doi.org/10.1088/1742-6596/1818/1/012235
24. K. Johnston and V. Harmandaris, *Soft Matter*, **8**: 23 (2012); <https://doi.org/10.1039/c2sm25567g>
 25. A. D. T. Thamira, A. S. H. Hasan, R. G. K. Kadhim, W. G. B. Bakheet, and H. I. Abbood, *Journal of Petroleum Research and Studies*, **8**: 3 (2021); doi.org/10.52716/jprs.v8i3.228
 26. Y. Kong, M. Tao, X. Cao, Z. Wang, and B. Xing, *Journal of Hazardous Materials*, **459**: 1 (2023); <https://doi.org/10.1016/j.jhazmat.2023.132071>
 27. B. Y. Kadem, M. Al-Hashimi, A. S. Hasan, R. G. Kadhim, Y. Rahaq, and A. K. Hassan, *Journal of Materials Science: Materials in Electronics*, **29**: 1 (2018); doi.org/10.1007/s10854-018-0055-4
 28. S. K. Jebur, A. J. Braihi, and A. S. Hassan, *Materials Today: Proceedings*, **49**: 7 (2022); doi.org/10.1016/j.matpr.2021.09.255
 29. R. Akbarzadeh, O. Ayeler, Q. Ibrahim, P. Olubambi, and P. Ndungu, *Heliyon*, **8**: 2 (2022); <https://doi.org/10.1016/j.heliyon.2022.e08903>
 30. A. A. Ati, A. H. Abdalsalam, and A. S. Hasan, *Journal of Materials Science: Materials in Electronics*, **32**: 3 (2021); doi.org/10.1007/s10854-020-05053-4
 31. J. Soler, F. Artacho, J. Gale, A. Garcia, J. Junquera, P. Ordejón, and D. Sánchez-Portal, *Journal of Physics: Condensed Matter*, **14**: 11 (2002); <https://doi.org/10.1088/0953-8984/14/11/302>

PACS numbers: 78.20.Ci, 78.66.Sq, 78.67.Sc, 81.07.Pr, 81.40.Tv, 82.35.Np, 85.60.-q

Effect of ZrO₂–CuO Nanofiller on the Optical Constants and Optical Conductivity of Biopolymer

Majeed Ali Habeeb¹, Idrees Oreibi², and Rehab Shather Abdul Hamza¹

¹*College of Education for Pure Sciences,
Department of Physics,
University of Babylon,
Hillah, Iraq*

²*Directorate of Education Babylon,
Ministry of Education,
Babylon, Iraq*

Creating polymer nanocomposite specimens is carried out using the solution-casting technique. The specimens are comprised of a host matrix of polyvinyl alcohol (PVA), in which varying concentrations of zirconium oxide (ZrO₂) and copper oxide (CuO) nanoparticles are incorporated, spanning a range from 0 to 6 wt.%. The nanostructures composed of PVA–ZrO₂–CuO exhibit notable attributes, such as low expenses, enhanced resistance to corrosion, favourable optical properties, and a relatively lightweight nature compared to alternative nanosystems. The optical properties are measured within the wavelength range (λ) from 200 nm to 840 nm. Optical properties show that the absorption coefficient, refractive index, and dielectric-constant real and imaginary parts for PVA–ZrO₂–CuO nanocomposite increase with increasing concentrations of the ZrO₂–CuO nanoparticles; so, the optical parameters at wavelength $\lambda = 400$ nm: absorption coefficient (α), refractive index (n), extinction coefficient (k), real (ϵ_1) and imaginary (ϵ_2) parts of dielectric constants, and optical conductivity (σ_{op}) for PVA are enhanced by about 1540%, 100%, 2216%, 302%, 1116%, and 3025%, respectively, with adding of 6 wt.% ZrO₂–CuO nanoparticles. The performance of the PVA–ZrO₂–CuO nanocomposites suggests that they possess favourable characteristics as optical nanomaterials in the domains of electronics and optics.

Створення зразків полімерних нанокompatитів проводили методом лиття з розчину. Зразки включали головну матрицю з полівінілового спирту (ПВС), в яку було втілено різні концентрації наночастинки оксиду Цирконію (ZrO₂) й оксиду Купруму (CuO), що охоплювали діяпазон від 0 до 6 масових відсотків. Наноструктури, що складаються з ПВС–ZrO₂–CuO, демонструють помітні характеристики, такі як низьку

вартість, підвищену стійкість до корозії, сприятливі оптичні властивості та відносно легку природу порівняно з альтернативними наносистемами. Оптичні властивості міряли в діапазоні довжин хвиль λ від 200 нм до 840 нм. Оптичні властивості показали, що коефіцієнт поглинання, показник заломлення та дійсна й уявна частини діелектричної проникності для нанокompозиту ПБС–ZrO₂–CuO зростають зі збільшенням концентрації наночастинок ZrO₂–CuO; так, оптичні параметри на довжині хвилі $\lambda = 400$ нм: коефіцієнт поглинання (α), показник заломлення (n), коефіцієнт екстинкції (k), дійсна (ϵ_1) й уявна (ϵ_2) частини діелектричної проникності та оптична провідність (σ_{op}) для ПБС збільшуються приблизно на 1540%, 100%, 2216%, 302%, 1116% і 3025% відповідно з додаванням наночастинок ZrO₂–CuO (6 мас.%). Експлуатаційні показники нанокompозитів ПБС–ZrO₂–CuO наводять на думку, що вони мають сприятливі характеристики як оптичні наноматеріали в областях електроніки й оптики.

Key words: PVA, ZrO₂, CuO, nanocomposites, optical properties.

Ключові слова: полівініловий спирт, ZrO₂, CuO, нанокompозити, оптичні властивості.

(Received 21 August, 2023)

1. INTRODUCTION

Since immemorial, polymers have been integral to the fabric of existence, constituting all life forms' fundamental constituents. Before the mid-twentieth century, humans had an incomplete understanding regarding polymers' fundamental characteristics and properties. Polymers have permeated various facets of human existence. Contemplating contemporary society devoid of synthetic polymeric materials and their myriad opulent and convenient attributes proves challenging. In recent years, realizing a fully customized polymer has been made possible due to advancements in comprehending the interrelationships between polymer structure and properties, emerging ground-breaking polymerization techniques, and the accessibility of innovative and cost-effective monomers [1, 2]. Polymers with corrosion resistance, low weight, and strong hardness make various products, including homemade plastics, automobile internal and external components, biomedical equipment, and satellite applications [3, 4].

A polymer blend refers to the amalgamation of two or more polymers, forming a novel material exhibiting distinct physical characteristics. Polymer mixtures, known as heat mixes, are a specific category within the broader classification of polymer mixtures. The phenomenon of heat mixing and the characteristics of thermoplastic heat mixtures have been extensively investigated in previous re-

search [5, 6]. In contemporary times, polymers are commonly employed in electrical and electronic applications. The utilization of polymers as insulators has been attributed to their remarkable resistivity and dielectric properties. Electrical equipment utilizes polymer-based insulators to isolate electrical conductors, thereby inhibiting electric current flow efficiently. Polymer insulators are utilized in diverse fields, encompassing the manufacturing of printed circuit boards, cable sheathing materials, corrosion-resistant electronics, and wire encapsulation. Polymers offer many advantages, such as their inherent processability, exceptional flexibility, notable strength and mechanical properties, and cost-effectiveness [7, 8].

Polyvinyl alcohol (PVA) is a water-soluble synthetic polymer. The substance exhibits a notable lack of toxicity and possesses notable attributes in terms of its application as a wound dressing and as a material for bioreactors. The semi-crystalline nature of polyvinyl alcohol is a notable attribute, as the presence of both amorphous and crystalline regions characterizes it. This structural arrangement gives rise to interfacial effects that enhance the physical properties of the material [9, 10]. Polyvinyl alcohol exhibits distinct characteristics, including biodegradability, favourable chemical stability, environmental friendliness, notable charge storage capacity, high resistance to abrasion, thermal stability, tensile strength, flexibility, elongation, ease of film processing, and cost-effectiveness in manufacturing [11, 12]. The rapid decomposition of the substance occurs at elevated temperatures. Various additives, including polymers, salts, nanocomposites, and ions, are commonly incorporated into polyvinyl alcohol (PVA) to enhance and alter its properties [13, 14]. PVA exhibits sub-optimal electrical insulation properties, yet it transforms conductivity, when doped with specific inorganic fillers [15].

Zirconium oxide (ZrO_2), commonly called zirconia, is widely recognized for its exceptional chemical and physical characteristics. Consequently, it finds extensive utility in various fields, including fuel cells, gas sensors, optoelectronics, catalysts, and corrosion-resistant materials. Zirconium dioxide (ZrO_2) has a band gap exceeding 5 eV, making it a significant luminescent material characterized by favourable optical transparency. Moreover, its considerable surface area and abundance of oxygen vacancies establish it as a promising contender for applications in photocatalysis [16, 17]. Zirconium dioxide (ZrO_2) nanoparticles exhibit notably low thermal conductivity and a high thermal expansion coefficient. Additionally, the materials above possess numerous engineering applications due to their exceptional strength, durability, thermal shock resistance, rigidity, and enhanced wear resistance [18, 19].

Copper oxide is a type of material that exhibits semiconductor

behaviour and possesses distinctive optical, electrical, and magnetic characteristics. It has found diverse applications in supercapacitor development, near-infrared filtering, magnetic storage media, sensor technology, catalysis, and semiconductor devices [20, 21]. Copper oxide nanoparticles (CuO NPs) have been employed to enhance polymer films derived from petrochemical-based or bio-based polymers. The characteristics mentioned above are attributable to the remarkable surface-to-volume ratio, thermal stability, comparatively diminished toxicity, and capacity to enhance the mechanical properties of polymers [22].

This work used ZrO_2 -CuO nanoparticles to improve the nanocomposite's optical properties PVA- ZrO_2 -CuO. The results of this study showed a significant improvement in these characteristics.

2. MATERIALS AND METHODS

Nanocomposite films were fabricated using the casting technique, incorporating polyvinyl alcohol (PVA), zirconium oxide (ZrO_2), and copper oxide (CuO) nanoparticles. The experimental procedure involved dissolving pure polyvinyl alcohol (PVA) in 35 ml of distilled water for 35 minutes. The solution was stirred using a magnetic stirrer at a temperature of 50°C to attain a higher level of homogeneity. The polymer underwent the introduction of zirconium oxide (ZrO_2) and copper oxide (CuO) nanoparticles at different weight percentages 0%, 2%, 4%, and 6%. Following three days of air-drying the solution at room temperature, the observed outcome entailed the development of polymer nanocomposites. The nanocomposites consisting of PVA- ZrO_2 -CuO were retrieved from the Petri dish and employed for measurement purposes. The optical properties of nanocomposites comprising PVA, ZrO_2 , and CuO were examined using a Shimadzu U.V./1800 spectrophotometer over a wavelength range of 200–800 nm.

The evaluation of the absorption coefficient (α) of the current materials is heavily reliant on the optical transmission, reflection, and thickness of the film, as determined by the following equation [23]: $\alpha = 2.303A/d$, where d is the sample thickness, and A is the absorption of the material.

The extinction coefficient (k) was calculated using the following equation [24, 25]:

$$k = \frac{\alpha\lambda}{4\pi},$$

where λ is the wavelength. The refractive index (n) is calculated by [26] from equation:

$$n = \sqrt{4R - \frac{k^2}{(R-1)^2} - \frac{(R+1)}{(R-1)}},$$

where R is the reflectance. The dielectric constant real and imaginary parts are calculated by [27, 28] as follow: $\varepsilon_1 = n^2 - k^2$, $\varepsilon_2 = 2nk$. The optical conductivity (σ_{op}) is obtained by using the relation [29]: $\sigma_{op} = \alpha nc/4\pi$, where c is the velocity of light.

3. RESULTS AND DISCUSSION

3.1. The Optical Properties of PVA-ZrO₂-CuO Nanocomposites

Figure 1 illustrates the correlation between the absorption coefficient of nanocomposites composed of polyvinyl alcohol (PVA), zirconium dioxide (ZrO₂), and copper oxide (CuO) and the varying proportions of ZrO₂-CuO nanoparticles (NPs). The absorption coefficient increases as the ratios of ZrO₂-CuO NPs increase. This phenomenon can be attributed to the augmentation of charge carriers within the nanocomposite films. The absorption coefficient (α) for all the prepared nanocomposites exhibited the lowest values at lower energies, which can be attributed to the limited likelihood of electron transitions.

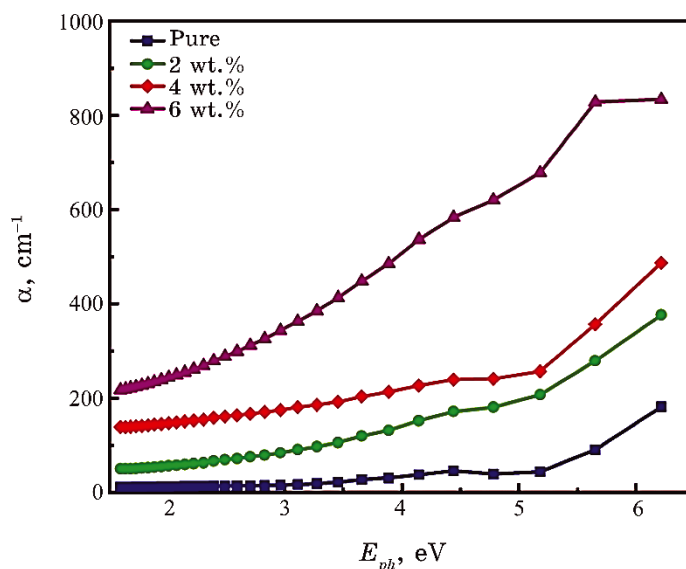


Fig. 1. Absorption coefficient for PVA-ZrO₂-CuO nanocomposites as a function of photon energy.

The probability of electron transition is high, when the energy of the incident photon increases, indicating that the energy of the photon is adequate for atom interaction. Based on the observed α

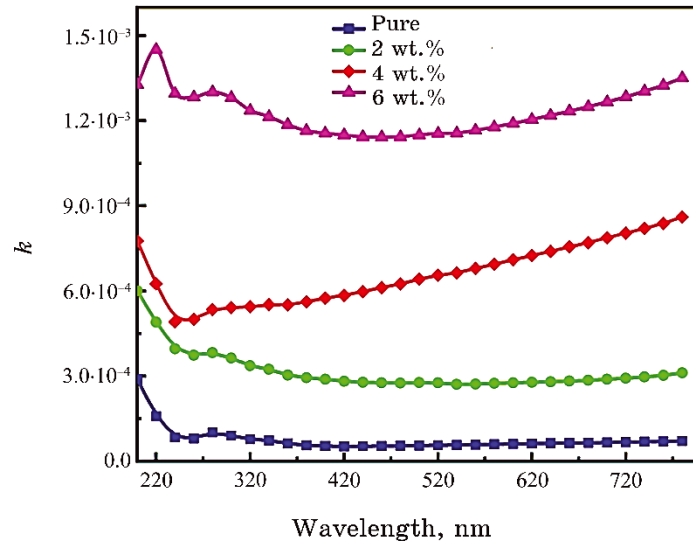


Fig. 2. Difference of extinction coefficient for PVA-ZrO₂-CuO nanocomposites with wavelength.

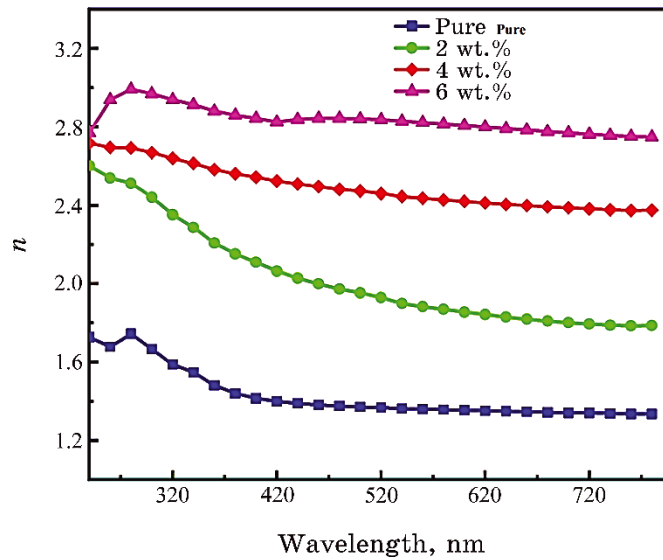


Fig. 3. The refractive index for PVA-ZrO₂-CuO nanocomposites as a function of wavelength.

values for the prepared films, which are less than 104 cm⁻¹, it can be inferred that indirect electron transitions are highly probable [30, 31].

Figure 2 illustrates the variation in the extinction coefficient concerning the wavelength. The figure observations suggest a positive correlation between the concentration of ZrO₂-CuO nanoparticles and the extinction coefficient. This relationship can be attributed to the amplified optical absorption and enhanced dispersion of photons within the polymer matrix. The extinction coefficient is contingent upon the absorption coefficient, with the former exhibiting elevated values within the UV region. Moreover, the extinction coefficient demonstrates an upward trend as the wavelength increases within the visible spectrum, extending into the near-infrared spectrum [32, 33].

The refractive index for nanocomposites consisting of PVA-ZrO₂-CuO is depicted in Fig. 3, illustrating its variation for wavelength. The figure demonstrates a positive correlation between the weight percentages of ZrO₂-CuO nanoparticles in the PVA and the corresponding refractive index; this can be attributed to the increased density of the nanocomposites. High refractive index values are observed in the ultraviolet region due to the restricted transmittance within this specific spectral range. On the other hand, the visible region exhibits low refractive index values due to increased transmittance within this specific range of wavelengths. The findings obtained by the researcher align with these results [34, 35].

The real dielectric constant (ϵ_1) indicates the extent to which the speed of light is reduced within a material, indicating the material's polarity. On the other hand, the imaginary dielectric constant (ϵ_2) signifies the ability of the dielectric to absorb energy from the electric field through dipole motion. Figures 4 and 5 depict the fluctuations in the real component (ϵ_1) and the imaginary component (ϵ_2) of the dielectric constant for both pure polymer films and nanocomposite films, as influenced by varying ratios of ZrO₂-CuO nanoparticles. These variations are observed across different photon energy levels. There is a rise in the values of ϵ_1 at lower photonic energies, which is subsequently followed by a distinct decline at higher energies across all nanocomposite films [36]. The dielectric constant of polymers demonstrates an increase corresponding to a fractional amplification of charges within the polymer materials.

The relationship between the real component of the dielectric constant and the refractive index can be attributed to the minimal value of the extinction coefficient. The empirical evidence indicates a positive correlation between the concentrations of ZrO₂-CuO nanoparticles and the observed increase in the real dielectric constant. The behaviour of the hypothetical dielectric constant before and af-

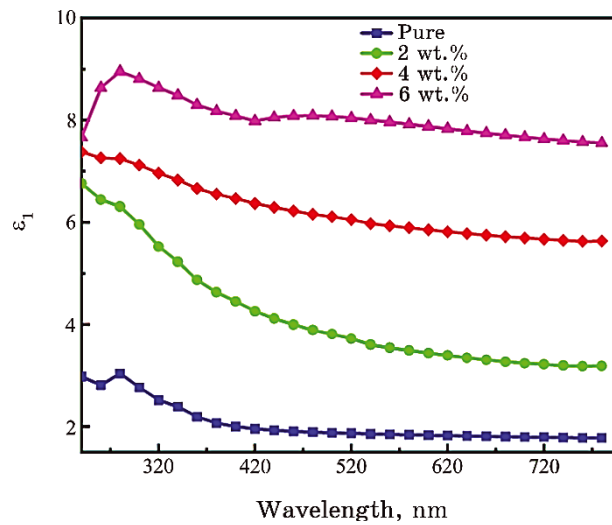


Fig. 4. The real dielectric constant (ϵ_1) as a function of incident wavelength for PVA-ZrO₂-CuO nanocomposites.

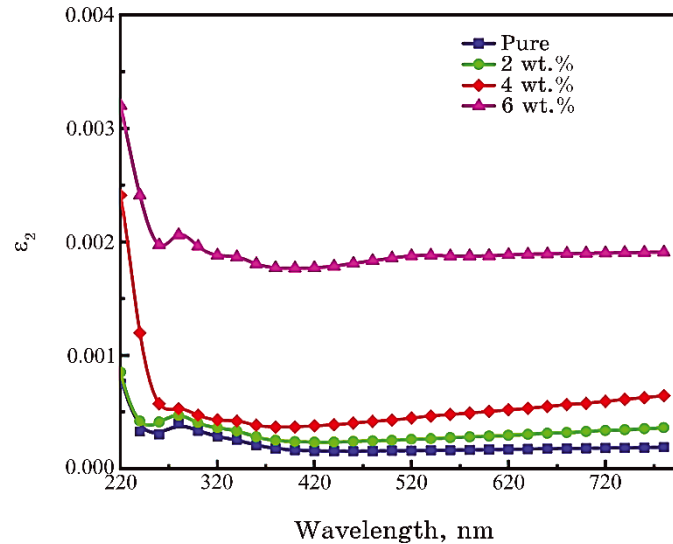


Fig. 5. The imaginary dielectric constant (ϵ_2) as a function of wavelength for PVA-ZrO₂-CuO nanocomposites.

ter inclusion of nanoparticles demonstrates resemblances to that of the actual dielectric constant [37, 38].

However, it is important to note that the value of the imaginary dielectric constant is lower, as depicted in Fig. 5. The correlation

between the imaginary component of the dielectric constant and the extinction coefficient is of significant significance, particularly within the visible and near-infrared spectra. In the context of this specific regime, it is evident that the refractive index exhibits a consistent and unchanging value. On the contrary, the extinction coefficient exhibits an increasing trend with the rise in wavelength [39, 40].

Figure 6 demonstrates a decrease in the optical conductivity of the composite samples as the wavelength increases. The observed phenomenon exhibits a significant reliance on the wavelength of the incoming radiation on the composite samples and can be clarified by considering the concept of optical conductivity. The observed rise in optical conductivity at shorter photon wavelengths can be ascribed to the heightened absorbance exhibited by all composite samples within this particular range of the electromagnetic spectrum. Consequently, this phenomenon leads to an augmentation in charge transfer excitations [41, 42]. The optical conductivity spectra indicate that the examined samples possess the ability to propagate light within the visible and near-infrared regions.

Furthermore, incorporating $\text{ZrO}_2\text{-CuO}$ nanoparticles leads to an observed enhancement in the optical conductivity of composites. The observed phenomenon can be ascribed to the formation of localized states within the energy gap. More precisely, an increased concentration of $\text{ZrO}_2\text{-CuO}$ nanoparticles results in a higher density of these localized states within the band structure. Consequently, the

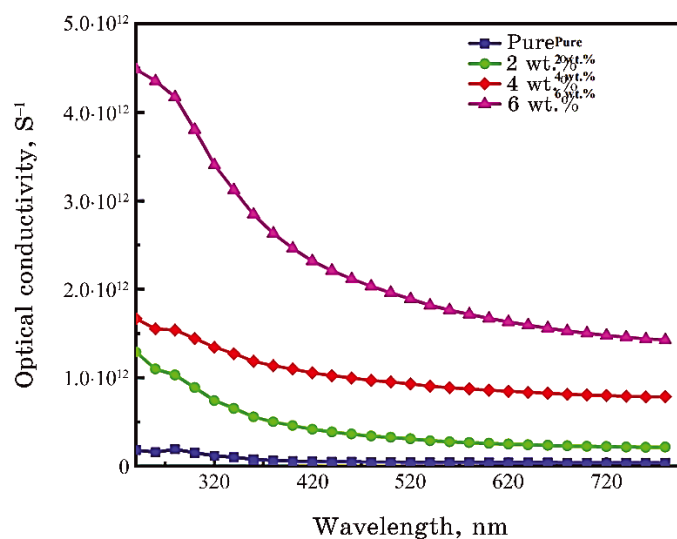


Fig. 6. Difference of optical conductivity of PVA- $\text{ZrO}_2\text{-CuO}$ nanocomposites with wavelength.

augmentation of the absorption coefficient results in a subsequent elevation in the optical conductivity of nanocomposites comprising polyvinyl alcohol–zirconium oxide–copper oxide (PVA–ZrO₂–CuO) [43].

4. CONCLUSION

The current study involves the production of nanostructured films composed of a combination of polyvinyl alcohol (PVA), zirconium dioxide (ZrO₂), and copper oxide (CuO) through the solution casting method. A comprehensive investigation has been conducted on the optical characteristics of nanostructures composed of polyvinyl alcohol (PVA), zirconium dioxide (ZrO₂), and copper oxide (CuO). The analysis of optical properties revealed that the absorption coefficient, refractive index, and dielectric constant (both real and imaginary components) of the PVA–ZrO₂–CuO nanocomposite exhibit a positive correlation with the concentrations of ZrO₂–CuO nanoparticles. These findings indicate significant improvements in the optical properties of the nanocomposite. The extinction coefficient exhibits elevated values within the UV-range, demonstrating a positive correlation with increasing wavelength within the visible spectrum, extending into the near-infrared spectrum. Moreover, composites' optical conductivity increases, when ZrO₂–CuO nanoparticles are incorporated. The findings of this study indicate that the material exhibits potential suitability for various optoelectronic applications.

REFERENCES

1. D. R. Paul and L. M. Robeson, *Polymer*, **49**, No. 15: 3187 (2008); <https://doi.org/10.1016/j.polymer.2008.04.017>
2. A. H. Hadi and M. A. Habeeb, *Journal of Mechanical Engineering Research and Developments*, **44**, No. 3: 265 (2021); <https://jmerd.net/03-2021-265-274/>
3. N. Othman, N. A. Azahari, and H. Ismail, *Malaysian Polymer Journal*, **6**, No. 6: 147 (2011).
4. M. A. Habeeb and Z. S. Jaber, *East European Journal of Physics*, **4**: 176 (2022); doi:10.26565/2312-4334-2022-4-18
5. M. A. Habeeb, *European Journal of Scientific Research*, **57**, No. 3: 478 (2011).
6. Q. M. Jebur, A. Hashim, and M. A. Habeeb, *Egyptian Journal of Chemistry*, **63**: 719 (2020); <https://dx.doi.org/10.21608/ejchem.2019.14847.1900>
7. S. Muntaz Begum, M. Rao, and R. Ravikumar, *Journal of Inorganic and Organometallic Polymers and Materials*, **23**: 350 (2013); <https://doi.org/10.1007/s10904-012-9783-8>
8. S. M. Mahdi and M. A. Habeeb, *Optical and Quantum Electronics*, **54**, Iss. 12: 854 (2022); <https://doi.org/10.1007/s11082-022-04267-6>

9. N. Hayder, M. A. Habeeb, and A. Hashim, *Egyptian Journal of Chemistry*, **63**: 577 (2020); doi:10.21608/ejchem.2019.14646.1887
10. N. Kumar, V. Crasta, and B. Praveen, *Physics Research International*, **2014**: Article ID 742378-1 (2014); <https://doi.org/10.1155/2014/742378>
11. M. A. Habeeb, A. Hashim, and N. Hayder, *Egyptian Journal of Chemistry*, **63**: 709 (2020); <https://dx.doi.org/10.21608/ejchem.2019.13333.1832>
12. A. Hashim, M. A. Habeeb, and Q. M. Jebur, *Egyptian Journal of Chemistry*, **63**: 735 (2020); <https://dx.doi.org/10.21608/ejchem.2019.14849.1901>
13. S. M. Mahdi and M. A. Habeeb, *Physics and Chemistry of Solid State*, **23**, No. 4: 785 (2022); doi:10.15330/pcss.23.4.785-792
14. C. V. Reddy, B. Babu, I. N. Reddy, and J. Shim, *Ceramics International*, **44**, No. 6: 6940 (2018); <https://doi.org/10.1016/j.ceramint.2018.01.123>
15. M. A. Habeeb and W. S. Mahdi, *International Journal of Emerging Trends in Engineering Research*, **7**, No. 9: 247 (2019); doi:10.30534/ijeter/2019/06792019
16. M. A. Habeeb and R. S. Abdul Hamza, *Journal of Bionanoscience*, **12**, No. 3: 328 (2018); <https://doi.org/10.1166/jbns.2018.1535>
17. Q. Zhang, K. Zhang, D. Xu, G. Yang, H. Huang, F. Nie, C. Liu, and S. Yang, *Progress in Materials Science*, **60**: 208 (2014); <https://doi.org/10.1016/j.pmatsci.2013.09.003>
18. M. A. Habeeb, A. Hashim, and N. Hayder, *Egyptian Journal of Chemistry*, **63**: 697 (2020); <https://dx.doi.org/10.21608/ejchem.2019.12439.1774>
19. M. A. Habeeb and W. K. Kadhim, *Journal of Engineering and Applied Sciences*, **9**, No. 4: 109 (2014); doi:10.36478/jeasci.2014.109.113
20. M. Hdidar, S. Chouikhi, A. Fattoum, M. Arous, and A. Kallel, *Journal of Alloys and Compounds*, **750**: 375 (2018); <https://doi.org/10.1016/j.jallcom.2018.03.272>
21. M. A. Habeeb, *Journal of Engineering and Applied Sciences*, **9**, No. 4: 102 (2014); doi:10.36478/jeasci.2014.102.108
22. H. J. Park, A. Badakhsh, I. T. Im, M.-S. Kim, and C. W. Park, *Applied Thermal Engineering*, **107**: 907 (2016); <https://doi.org/10.1016/j.applthermaleng.2016.07.053>
23. S. M. Mahdi and M. A. Habeeb, *Digest Journal of Nanomaterials and Biostructures*, **17**, No. 3: 941 (2022); <https://doi.org/10.15251/DJNB.2022.173.941>
24. G. A. Eid, A. Kany, M. El-Toony, I. Bashter, and F. Gaber, *Arab. J. Nucl. Sci. Appl*, **46**, No. 2: 226 (2013).
25. A. H. Hadi and M. A. Habeeb, *Journal of Physics: Conference Series*, **1973**, No. 1: 012063 (2021); doi:10.1088/1742-6596/1973/1/012063
26. Q. M. Jebur, A. Hashim, and M. A. Habeeb, *Egyptian Journal of Chemistry*, **63**, No. 2: 611 (2020); <https://dx.doi.org/10.21608/ejchem.2019.10197.1669>
27. G. Aras, E. L. Orhan, I. F. Selçuk, S. B. Ocak and M. Ertuğrul, *Procedia-Social and Behavioral Sciences*, **95**: 1740 (2015); <https://doi.org/10.1016/j.sbspro.2015.06.295>
28. M. A. Habeeb and A. H. Mohammed, *Optical and Quantum Electronics*, **55**, Iss. 9: 791 (2023); <https://doi.org/10.1007/s11082-023-05061-8>
29. M. H. Dwech, M. A. Habeeb, and A. H. Mohammed, *Ukr. J. Phys.*, **67**, No. 10: 757 (2022); <https://doi.org/10.15407/ujpe67.10.757>

30. M. Martin, N. Prasad, M. M. Siva lingam, D. Sastikumar, and B. Karthikeyan, *Journal of Material Science: Material in Electronics*, **29**: 365 (2018); <https://doi.org/10.1007/s10854-017-7925-z>
31. M. A. Habeeb and W. H. Rahdi, *Optical and Quantum Electronics*, **55**, Iss. 4: 334 (2023); <https://doi.org/10.1007/s11082-023-04639-6>
32. R. Dalven and R. Gill, *J. Appl. Phys.*, **38**, No. 2: 753 (1967); [doi:10.1063/1.1709406](https://doi.org/10.1063/1.1709406)
33. R. N. Bhagat and V. S. Sangawar, *Int. J. Sci. Res. (IJSR)*, **6**: 361 (2017).
34. R. S. Abdul Hamza and M. A. Habeeb, *Optical and Quantum Electronics*, **55**, Iss. 8: 705 (2023); <https://doi.org/10.1007/s11082-023-04995-3>
35. A. Goswami, A. K. Bajpai, and B. K. Sinha, *Polym. Bull.*, **75**, No. 2: 781 (2018); <https://doi.org/10.1007/s00289-017-2067-2>
36. S. M. Mahdi and M. A. Habeeb, *AIMS Materials Science*, **10**, No. 2: 288 (2023); [doi:10.3934/mat.2023015](https://doi.org/10.3934/mat.2023015)
37. I. Oreibi and J. M. Al-issawe, *Turkish Computational and Theoretical Chemistry*, **7**, No. 2: 12 (2023); <https://doi.org/10.33435/tcandtc.1161253>
38. M. A. Habeeb and R. S. A. Hamza, *Indonesian Journal of Electrical Engineering and Informatics*, **6**, No. 4: 428 (2018); [doi:10.11591/ijeel.v6i1.511](https://doi.org/10.11591/ijeel.v6i1.511)
39. N. K. Al-Sharifi and M. A. Habeeb, *East European Journal of Physics*, **2**: 341 (2023); [doi:10.26565/2312-4334-2023-2-40](https://doi.org/10.26565/2312-4334-2023-2-40)
40. V. Suryawanshi, A. S. Varpe, and M. D. Deshpande, *Thin Solid Films*, **645**: 87 (2018); <https://doi.org/10.1016/j.tsf.2017.10.016>
41. Z. S. Jaber, M. A. Habeeb, and W. H. Radi, *East European Journal of Physics*, **2**: 228 (2023); [doi:10.26565/2312-4334-2023-2-25](https://doi.org/10.26565/2312-4334-2023-2-25)
42. A. A. Mohammed and M. A. Habeeb, *East European Journal of Physics*, **2**: 157 (2023); [doi:10.26565/2312-4334-2023-2-15](https://doi.org/10.26565/2312-4334-2023-2-15)
43. M. I. Baker, S. P. Walsh, Z. Schwartz, and B. D. Boyan, *Journal of Biomedical Materials Research Part B: Applied Biomaterials*, **100**, No. 5: 1451 (2012); <https://doi.org/10.1002/jbm.b.32694>

PACS numbers: 68.37.Hk, 68.37.Ps, 68.37.Vj, 73.50.Pz, 78.30.Na, 81.07.-b, 88.40.hj

Low-Cost $\text{TiO}_2/\text{MWCNT}/\text{Ag}$ Dye-Sensitized Solar Cell Based on Polypyrrole/SDS Counter Electrode

Nuhad Saad and Oraas Adnan

*College of Science,
Department of Chemistry,
University of Al-Qadisiyah
Al Diwaniyah, Al-Qadisiyah, Iraq*

In this study, titanium dioxide/multiwall carbon nanotube and silver nanoparticles ($\text{TiO}_2/\text{MWCNTs}/\text{Ag}$) nanocomposite is employed as photoanode incorporated with polypyrrole/sodium dodecyl sulphate (PPy + SDS) counter electrode 1 (C_1) and polypyrrole/sodium dodecyl sulphate/multiwall carbon nanotube (PPy + SDS + MWCNT) counter electrode 2 (C_2) as low-cost counter electrodes compared with a platinum counter electrode to construct dye-sensitized solar cells (DSSCs) using Ru-based dyes Z907, pomegranate dye, arugula dye, and hibiscus dye as a photosensitized one. The working electrode composite is deposited on a transparent-conducting $\text{F}:\text{SnO}_2$ (FTO) glass substrate by a thermal chemical spraying technique and, then, anchored with dyes, while the counter electrodes are prepared by the electropolymerization method. The structural and optical properties and interconnectivity of the materials within the composite are investigated thoroughly through various characterization techniques x-ray diffraction (XRD), Raman scattering, field-emission scanning electron microscopy (FESEM), and atomic force microscopy (AFM). Finally, the photovoltaic performances of the assembled DSSCs are tested under photoirradiation ($100 \text{ mW}/\text{cm}^2$). The measured current–voltage (I – V) curve shows that the efficiency of DSSCs in the case of Z907 dye with C_1 and C_2 is of 2.537% and 2.453%, respectively, compared with the reference cell based on the Pt counter electrode, which has an efficiency of 3.57%, that indicates a good efficiency of the low-cost prepared DSSCs. The natural dyes exhibit a moderate efficiency ranging from 1.44–0.53%.

У цьому дослідженні наноконкомпозит діоксид Титану/багатошарові вуглецеві нанотрубки та наночастинки срібла ($\text{TiO}_2/\text{MWCNTs}/\text{Ag}$) використовували як фотоаноду, об'єднану з протиелектродою 1 (C_1) поліпірол/додецилсульфат натрію (PPy + SDS) та протиелектродою 2 (C_2) поліпірол/додецилсульфат натрію/багатостінні вуглецеві нанотрубки (PPy + SDS + MWCNT) як недорогими протиелектродами порівняно з

платиноюю протиелектродою для створення сенсiбiлiзованих до барвника сонячних елементiв (DSSCs) з використанням барвника Z907 на основi Ru, гранатового барвника, барвника-руколи, барвника-гiбiскусу як фотосенсiбiлiзаторiв. Робочий електродний композит був нанесений на прозору провiдну скляну пiдкладинку з F:SnO₂ (FTO) методом термiчного хемiчного напорошення, а потiм закрiплений барвниками, тодi як протиелектроди були пiдготовленi методом електрополiмеризацiї. Структурнi й оптичнi властивостi та взаємозв'язок матерiялiв у складi композиту ретельно дослiджено за допомогою рiзних методiв визначення характеристик рентгенiвської дифракцiї (XRD), комбiнацiйного розсiяння, польової емiсiйної сканувальної електронної мiкроскопiї (FESEM) та атомно-силової мiкроскопiї (AFM). Нарештi, фотоелектричнi характеристики зiбраних DSSCs було перевiрено пiд дiєю фотоопромiнення (100 мВт/см²). Вимiряна вольт-амперна крива ($I-V$) показує, що ефективнiсть DSSCs у випадку барвника Z907 з C₁ i C₂ становила 2,537% i 2,453% вiдповiдно порiвняно з еталонною комiркою на основi Pt-протиелектроди, яка має ефективнiсть у 3,57%, а це свiдчить про хорошу ефективнiсть недорогих виготовлених DSSCs. Натуральнi барвники показали помiрну ефективнiсть у межах 1,44–0,53%.

Key words: TiO₂, silver nanoparticles, MWCNT, Z907, SDS, PPy, dye-sensitized solar cell.

Ключовi слова: TiO₂, наночастинки сiбла, MWCNT, Z907, SDS, PPy, сенсiбiлiзований до барвника сонячний елемент.

(Received 20 July, 2023; in revised form, 26 July, 2023)

1. INTRODUCTION

Due to its low cost, simple manufacturing process, and greener design, dye-sensitized solar cells (DSSCs) have undergone extensive research as a substitute energy source. A DSSC is made up of a glass substrate covered with a transparent conducting oxide layer, an electron-transporting mesoporous metal oxide layer, dye, electrolyte, and a counter electrode. Generally, the spectral sensitization of wide bandgap semiconductors like TiO₂ is used in DSSCs to convert visible light into electricity, TiO₂ continues to be the most promising semiconductor discovered so far for DSSCs [1]. Natural dyes employed in DSSC as sensitizers are less expensive than synthetic dyes, although their stated efficiencies are fairly poor [2]. Tennakone *et al.* first proposed the idea of a dye-sensitized solid-state solar cell in 1988, and later O'Regan and Grätzel reported an efficiency of 7.1% and a current density greater than 12 mA·cm⁻² for DSSC in which I⁻³/I⁻ redox couple and TiO₂ were used as liquid electrolytes, respectively.

Nazeeruddin *et al.* later reported the maximum efficiency of

11.1% [3].

The performance of DSSCs is nonetheless hampered by the relaxation of oxidized dye and recombination processes linked to the charge carriers. Utilizing a doped TiO₂ electrode is one of the alternate methods to lessen the aforementioned issue in DSSCs. It is obvious that dopant materials affect features such as conduction band energy, charge transit, recombination, and collection of charge carriers by narrowing the bandgap and increasing the charge traps of TiO₂. While many different dopants, including transition metals, alkali earth metals, non-metals, and rare earth elements, have been used, the incorporation of transition metals into TiO₂ results in the formation of a wide variety of new energy levels because the partially filled *d*-orbitals of transition metals close to the conduction band (CB) are responsible transition metal Ag have been used as dopant in TiO₂ [4].

H. Hwang *et al.* [5] developed the efficiency of TiO₂ Photoanode using the surface plasmonic effect of silver nanoparticles (NPs) and the high electron mobility of CNTs with Pt counter electrode. The TiO₂/CNT composite working electrode with 0.5 wt.% CNTs had increased efficiency over that of the conventional pure TiO₂ working electrode. Finally, a two-fold higher efficiency than the conventional working electrode was achieved by using a TiO₂/Ag/CNT composite working electrode. This greater efficiency may be caused by the synergism between the surface plasmonic effect of the silver nanoparticles and the high electron mobility of the MWCNT network. This cell was use as reference cell in the current study.

As alternative cost-efficient materials, various counter electrode (CE) materials including carbon-based materials, conducting polymers, sulphides, nitrides, and carbides have been integrated into DSSCs.

Polypyrrole (PPy) has attracted much research attention due to its high conductivity, low cost, large electrochemical surface area, and good electrocatalytic activity for I₃⁻ reduction enabling application in electronics, catalysis, energy storage, and sensing [6, 7]. Wu *et al.* [8] have prepared PPy nanoparticles and applied as CE catalyst in DSSC and got remarkable power conversion efficiency.

The combination of surfactant with polypyrrole tends to be improved the counter electrode properties. Sodium dodecyl sulphate (SDS) surfactant and MWCNT are expecting to achieve better catalytic activity and device performance. Introduction of SDS surfactant additive significantly enhances the photovoltaic performance [9].

At present study and as alternative cost-efficient DSSCs, we attempted to study the effect of merge both Pt/Ag/MWCNT as working electrode and PPy/SDS as counter electrode with different types of dye.

2. MATERIALS AND METHODS

2.1. Materials

All materials and solvents used were obtained from commercial sources: titanium dioxide TiO_2 (97%, PanReac), silver nanoparticles Ag ($\geq 99.9\%$, QSI, Nano), multiwall carbon nanotube MWCNT (98.9%, Sigma Aldrich), ethanol ($\geq 99.8\%$, Honeywell), pyrrole (99%, Sigma Aldrich), Perchloric acid (99.9%, THOMAS BAKER), sodium dodecyl sulphate SDS ($\geq 99\%$, Sigma Aldrich), Iodide ($\geq 94\%$, Sigma Aldrich), potassium iodide (99%, Sigma Aldrich), ethylene glycol (97%, BrcelonaEspan), ruthenium complex dye Z907 (95%, Ossila), tert-butanole (99%, Sigma Aldrich), acetonitrile (99.8%, Sigma Aldrich).

2.2. Methods

2.2.1. Preparation of TiO_2/Ag 2.0 wt.%/MWCNT 0.5 wt.%

The purified MWCNTs were dispersed in ethanol ($> 99.9\%$ purity) using a sonicator for 30 min, and the well-dispersed MWCNTs were then separated from the solution by centrifugation for 3 min. Silver nanoparticles (QSI-Nano; $> 99.9\%$ purity, 20–40 nm in diameter) and TiO_2 were added to the prepared MWCNTs solution *via* ultrasonication.

Photoanode was fabricated using the prepared $\text{TiO}_2/\text{Ag}/\text{MWCNT}$ composite solution with 140 ml ethanol. Firstly, the prepared $\text{TiO}_2/\text{Ag}/\text{CNT}$ composite solution was spray on a fluorine-doped tin oxide FTO glass substrate using the thermal chemical spraying method then thermally sintered at 500°C for 2 hours, modified [5].

2.2.2. Preparation of Counter Electrodes

Electrochemical polymerization of PPy1 onto FTO glass was carried out in a deionized (DI) water containing 4 drops of perchloric acid (HClO_4), 0.1 M pyrrole monomer, 0.1 M sodium dodecyl sulphate (SDS) as an anionic surfactant and by using the potentiostatic method by applying a potential value of 0.8 V for 30 sec.

In the case of PPy1/MWCNT CEs, we used 0.01 g of MWCNT in addition to the previous mixture. Prior to the film deposition, the solution was stirred for 3 h in an ice bath and then purged with nitrogen. A three-electrode system was used with FTO glass as working electrode, Pt sheet as counter electrode, and Ag/AgCl as reference electrode for electrochemical polymerization, modified [9].

2.2.3. Preparation of Pomegranate Dye

In this research, pomegranate extract was used as a dye. This raw material was collected from the local market and washed to reduce the dust particles. The pure juice was extracted by hand grinding method was applied on pomegranate. The extracted dye was filtered through the net and then filter paper to obtain clear dye [10].

2.2.4. Preparation of Hibiscus Leaf Extract Dye Solution

10 g of hibiscus leaves was mixed with 160 ml of deionized water and leave it for a 6hours , Then 10 ml of ethanol and 10 ml of dilute acetic acid were added to the mixture, stirred for an hour at room temperature after which it was filtered [11].

2.2.5. Preparation of the Chlorophyll Dye by Arugula Leaves (Fresh)

60 g of Arugula is crushing using mortar into small size 100 ml of ethanol is added into the Arugula and is placed into the ultrasonic for 30 minutes with the frequency of 37 Hz using Degas mode for extracting chlorophyll process. After that, enter the solvents into a centrifuge for 25 minutes with 5000 rpm [12].

2.2.6. Preparation of Z907 Dye

0.3 mM of Z907 dye was prepared in 1:1 mixture of acetonitrile tert-butanol, where the electrodes are immersed for 20 hours [13].

2.2.7. Preparation of Electrolyte

The iodide solution is prepared by dissolving 0.127 g iodine (I^2) in 10 mL of ethylene glycol to which 0.83 g potassium iodide (KI) is added, stirred and stored in a dark container [14].

2.3. Fabrication of DSSCs

The fluorine-doped tin oxide (FTO) coated conducting glass was used as the current collector. It was cleaned initially with soap water and subsequently with distilled water and ethanol using an ultrasonic bath. Then, the synthesized TiO₂ nanomaterial was made into solution by mixing with silver nanoparticles, multiwall carbon nanotube and ethanol and coated on FTO by the thermal chemical

spraying technique. Then, the coated glasses were soaked in 0.3 mM solution of Z907 dye in acetonitrile/tert-butyl alcohol for 24 h. The dye-coated Ru-doped TiO₂ electrode and Pt counter electrode were used to assemble the cell and I³/I⁻ electrolyte was used as redox electrolyte.

2.4. Characterization

The structural properties of the synthesized nanomaterials were studied by the x-ray diffraction method. A Raman spectroscopic study was carried out using a laser confocal Raman microscope. The optical absorbance spectra were recorded using DRS spectrophotometer. The elemental composition of the synthesized nanomaterials was analysed by the energy-dispersive x-ray spectroscopy technique. Current–voltage (*I*–*V*) characteristics in the illumination were measured as well as surface pours by FESEM. The effective area of the photoelectrode was 0.25 cm². Electrochemical impedance spectroscopy (EIS) measurements were carried out on the DSSCs using MetrohmAutolabpotentiostat.

3. RESULTS AND DISCUSSION

3.1. XRD of Films

X-ray diffraction spectroscopy is used to determine some structural properties such as crystalline phase and crystalline size. The crystal size can be calculated by the Debye equation:

$$D = k\lambda / \beta \cos \theta, \quad (1)$$

D is crystal size rate; *K*—the form factor, whose value is usually 0.9; λ —the wavelength of x-rays, which has a value of 0.154056; β —the total width is half of the greatest height; θ —deviation angle.

Crystal layers are also calculated by Bragg's law:

$$d = n\lambda / \beta \cos \theta, \quad (2)$$

d is the spacing between the crystal planes; *n* represents an integer (1, 2, 3, ...).

The x-ray diffraction (XRD) pattern of anode (TiO₂, MWCNT and Ag) revealed that the highest peak of MWCNT appeared at 27.33°. Based on the results, it can be concluded that surface functionalization has little effect on the average *d*-spacing [15]. The strongest diffraction peaks, located at 38.14°, corresponded to anatase TiO₂.

The anatase structure also accounted for the peak at 51.73°, while the peak at 55.44° was attributed to the rutile structure. These results indicate that the primary crystal phase of the TiO₂ nanoparticles was anatase with trace amounts of rutile phases present in the sample. The broad peaks in the XRD pattern indicated that the particles were in the nanometer size range and did not contain any contaminants. The TiO₂ NPs were found to have a tetragonal anatase structure with trigonal planar and octahedral geometry, which is consistent with previous studies in the literature survey [16, 17].

The XRD pattern also shows a prominent peak at 62.02°, indicating the presence of green-synthesized Ag NPs with a face centred

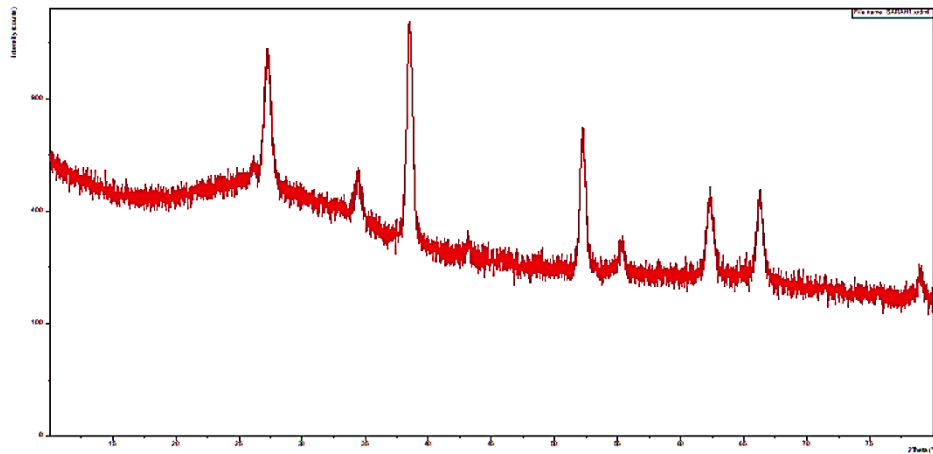


Fig. 1. XRD patterns of photoanode.

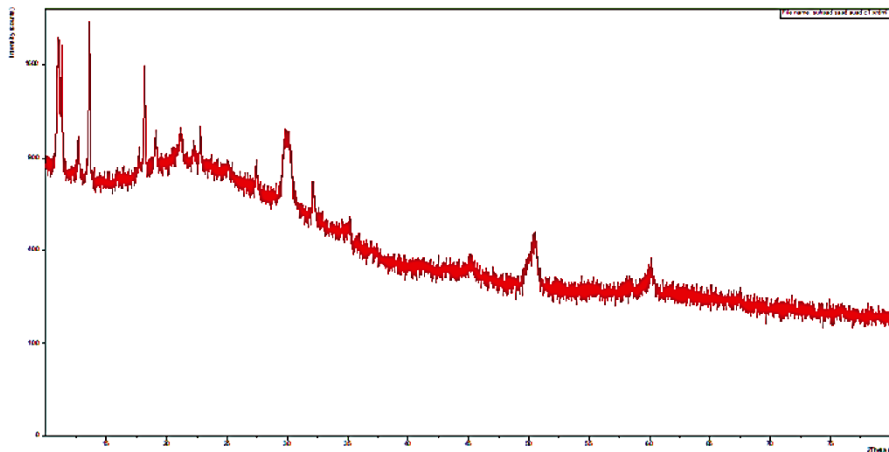


Fig. 2. XRD patterns of Cathode 1.

cubic structure (f.c.c. structure). The average crystalline size of the silver nanoparticles was estimated using the Debye equation [18].

For Cathode 1, the x-ray diffraction patterns revealed the presence of multiple distinct peaks, indicating the presence of SDS as crystalline materials. These peaks were found to have characteristic diffraction angles of 4.5° and 8.9° [19]. On the other hand, the XRD pattern of the PPy exhibited a broad peak at 29.8° , suggesting that it was amorphous in nature [20].

To determine the structural properties of Cathode 2, x-ray diffraction (XRD) analysis was conducted. The XRD pattern showed two peaks at 25° and 45° corresponding to MWCNT a broad peak centred at a characteristic angle, indicating the presence of amorphous carbon material. The most prominent diffraction peak in the

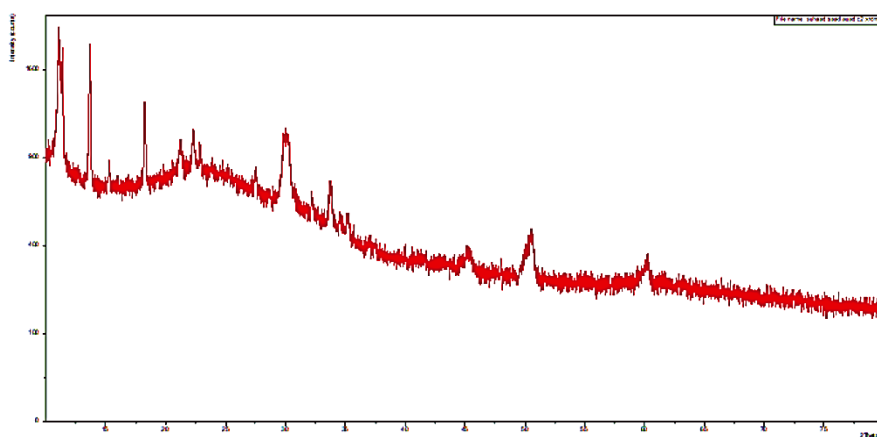


Fig. 3. XRD patterns of Cathode 2.

TABLE 1. X-ray diffraction variables for electrodes.

| Compound | 2θ , degree | d , Å | FWHM | D , nm | Intensity I/I_0 , % |
|---|--------------------|---------|--------|----------|-----------------------|
| Anode 1 (TiO ₂ , MWCNT, Ag) | 27.3397 | 3.25947 | 0.1596 | 17.9 | 36 |
| | 38.1484 | 2.35715 | 0.2112 | 44 | 76 |
| | 51.7375 | 2.16237 | 0.3168 | 26.3 | 105 |
| | 55.4402 | 2.03216 | 0.4224 | 19 | 199 |
| | 62.0249 | 1.49508 | 0.3168 | 28.9 | 52 |
| Cathode 1 (PPy, SDS) | 29.8069 | 2.99505 | 0.1732 | 57.5 | 3532 |
| Cathode 2 (PPy, SDS, MWCNT) | 35.3015 | 2.54045 | 0.2598 | 37.3 | 797 |
| | 50.6211 | 1.80177 | 0.2598 | 39.3 | 1628 |
| | 32.2251 | 2.77560 | 0.1732 | 57.9 | 778 |

XRD pattern of PPy is usually observed around $2\theta = 20^\circ$. This peak corresponds to the interplanar spacing between the polymer chains and is indicative of the degree of ordering in the material. Thus, it can be concluded that the amorphous character of carbon dominates in the MWCNTs/PPy1 nanocomposite. Moreover, the shift in the position of the XRD peaks of the fabricated nanocomposite indicates the successful formation of the MWCNTs/PPy1 nanocomposite [21]. The x-ray diffraction patterns revealed also the presence of multiple distinct peaks, indicating the presence of SDS as crystalline materials. These peaks were found to have characteristic diffraction angles of 4.5° and 8.9° [19].

3.2. Field-Emission Scanning Electron Microscopy (FESEM)

The displayed images in Fig. 4 are FESEM pictures. Raw MWCNTs tend to collect together like bundles due to the van der Waals forces between the tubes. The FESEM pictures of the MWCNTs/TiO₂ and Ag nanocomposites show that the CNTs were linked to semi-spheres of TiO₂/Ag NPs with varying diameters. Chemical oxidation using powerful oxidizing agents led to severe etching of the graphitic surface of the tubes, resulting in a significant number of disordered sites. However, the MWCNTs' structure remained intact even after being coated with TiO₂/Ag NPs, as evidenced by the aforementioned findings. The FESEM pictures at different magnifications revealed the presence of uniformly distributed, spherical nanoparticles of TiO₂/Ag NPs [22].

The typical structure of aggregates is evident on the surface facing the opposing electrode, as depicted in Fig. 5. Despite undergoing several scans, the surface has developed numerous fissures, resulting in an increase in electroactivity due to the increased surface area resulting from the fractures. The polymer surface has degrad-

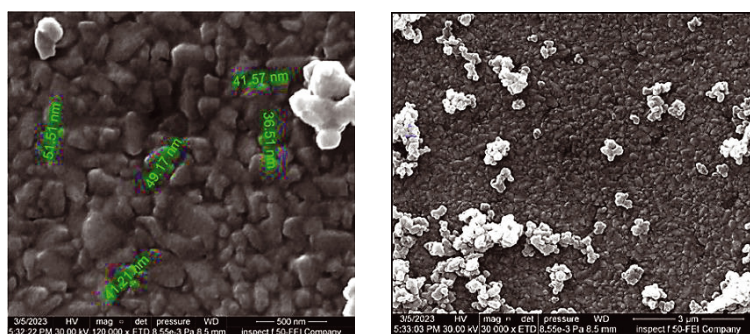


Fig. 4. FESEM images of photoanode.

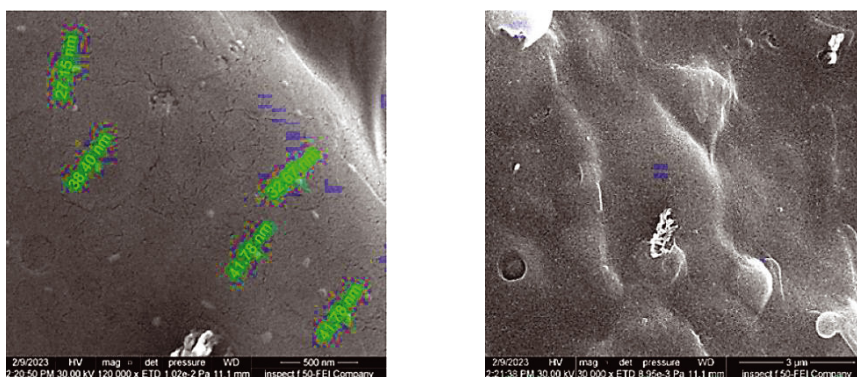


Fig. 5. FESEM images of Cathode 1.

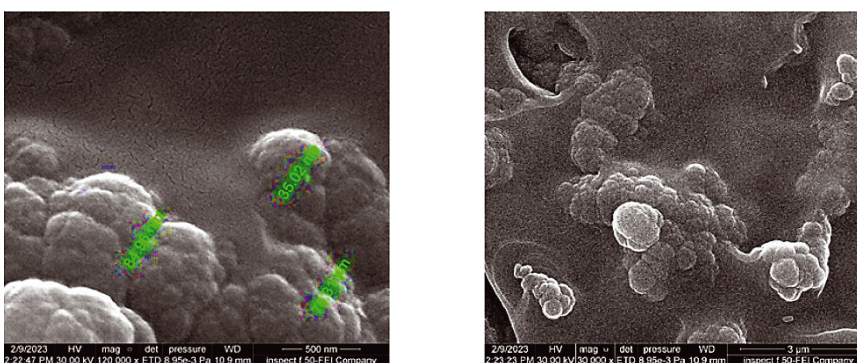


Fig. 6. FESEM images of Cathode 2.

ed, and the extended potential scan has caused the loss of multiple active spots [23].

To investigate further, the surface carbon and oxygen levels of the PPy/SDS–CNT electrodes were measured using FESEM. The cross-sectional FESEM images demonstrate a smoothed-out surface, with a reduced thickness of the PPy/SDS–CNT electrode. Rather than forming a uniform plane enclosing the SDS–CNT micelles, a cauliflower-like structure was formed [24].

3.3. Raman Spectroscopy

Figure 7 displays MWCNTs with complex spectra that can be understood by examining individual components and any potential interactions within the composite. Unmodified MWCNT samples exhibit two distinct peaks at approximately 1451 and 4023 cm^{-1} , with

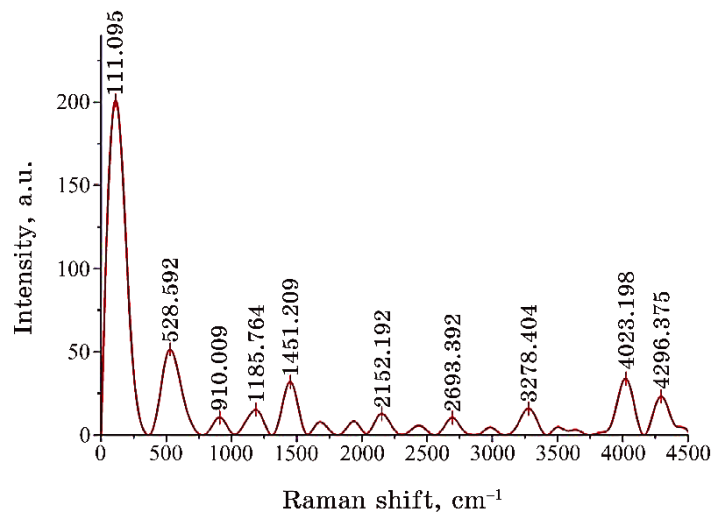


Fig. 7. Raman spectrum of photoanode.

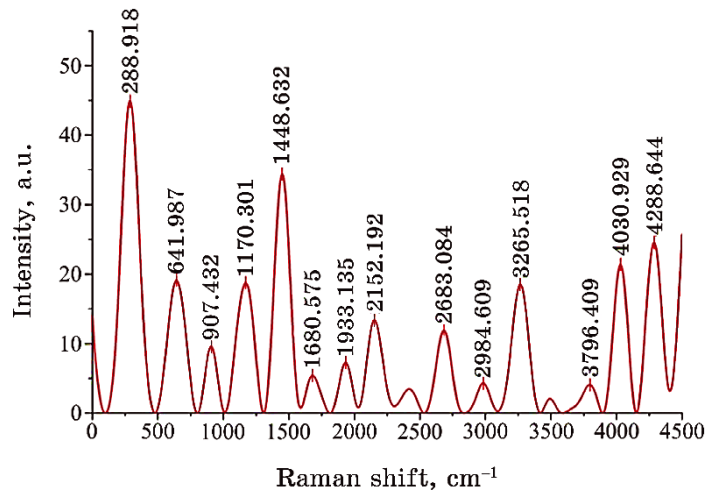


Fig. 8. Raman spectrum of Cathode 1.

additional peaks at 1185 cm⁻¹ attributed to poorly structured graphite or the *D*-band [25]. The Raman spectrum of TiO₂ is well-known, with the rutile tetragonal phase containing four Raman active modes ($A_{1g} + B_{1g} + B_{2g} + E_g$) and the anatase phase having six Raman active modes ($A_{1g} + 2B_{1g} + 3E_g$) [23].

Figure 9 demonstrates two distinct anatase phase peaks at 111 (B_{1g}) and 592 (B_{1g}) E_g in TiO₂ nanoparticle samples, with no rutile phase Raman peaks observed. Vibrational modes in nanoparticle

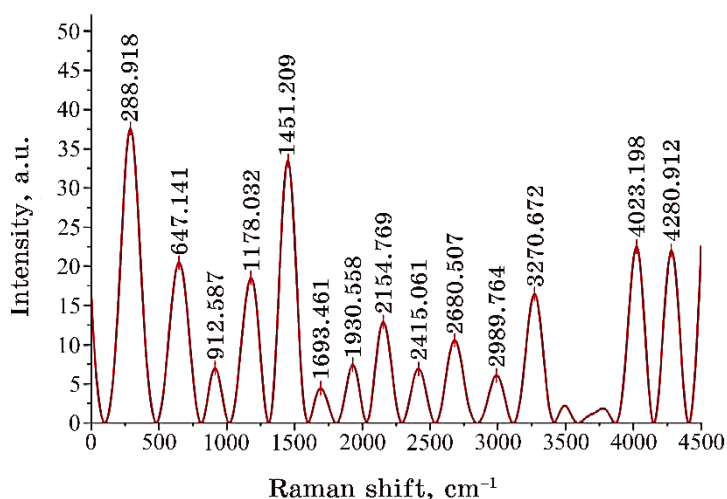


Fig. 9. Raman spectrum of Cathode 2.

composites coated with Ag nanoparticles are influenced by the connections between components resulting from chemical or physical interactions. The phonon confinement effect may explain the wave-number shift and/or widening of Raman peaks observed [26, 27]. Due to the high refraction index of TiO₂, the surface band of Ag-TiO₂ supported on CNT nanoparticles is red-shifted and widened. The *D*-band and *G*-band of AgTiO₂-CNT nanoparticle composites display blue shifts, which can be attributed to adhesion between Ag-TiO₂ nanoparticles and CNTs, as well as strain effects at the Ag-TiO₂-CNT interface [28].

The Raman spectra indicate significant dissimilarities in the chemical arrangement of PPy_SDS. Enhanced charge carrier proportion in PPy_SDS is manifested by intensified bands, which are typically linked to the dictation species at 288, 1448, 4030, and 3256 cm⁻¹ [29]. Additionally, the extent of conjugation in PPy can be estimated by the intensity ratio of vibrations within the 1680–2948 cm⁻¹ range. Based on this, the conjugation length in the PPy_SDS film is considerably extensive [30].

The Raman spectra of the PPy/SDS-MWCNT electrode were examined using a wavelength of 514 nm. A significant modification near 1000–1500 cm⁻¹ was observed, indicating that functional groups were attached to the surface [31]. In the Raman spectra of the PPy-MWCNT composite films, the characteristic peak of pure MWCNT at 1693 cm⁻¹ is associated with the *E*_{2g} mode of the graphite wall [32]. It has been theoretically predicted that a single-cylinder nanotube would exhibit an *E*_{2g} mode at 1930 cm⁻¹ [33]. The Raman spectra of the composite films displayed bands correspond-

ing to both pure PPy and MWCNT. Additionally, the intensity of the band located at 1451 cm^{-1} escalated with the increase of the MWCNT to pyrrole feeding mass ratio, indicating an increase in MWCNT content within the composite film [34].

3.4. Atomic Force Microscopy (AFM)

3.4.1. Atomic Force Microscopy (AFM) of Photoanode

TiO₂ nanoparticles influence surface roughness and height metrics including root mean square height (R_q) and total height (R_t). TiO₂ nanoparticles may provide a somewhat rough surface with large height variations. TiO₂ nanoparticles can also have an impact on spatial characteristics like autocorrelation length (R_{al}) and dominant spatial wavelength (R_{sw}). TiO₂ nanoparticle size and distribution may introduce periodic patterns and influence the overall surface structure. The TiO₂ coating could have an effect on the material ratio characteristics (R_{mr} and R_{mc}).

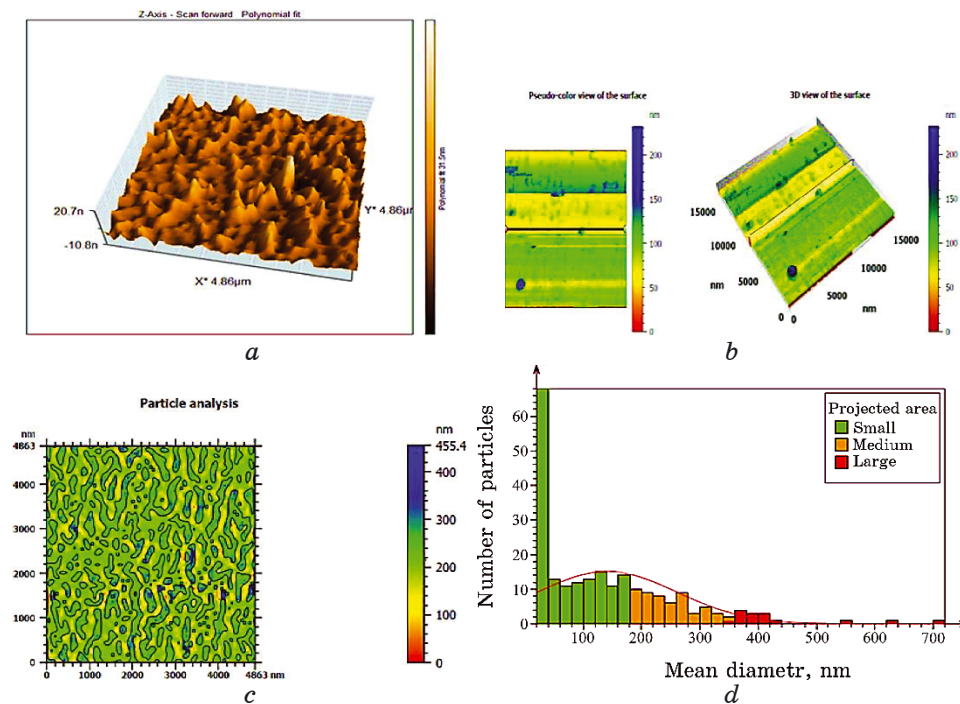


Fig. 10. AFM images of photoanode: (a) surface topography; (b) 3D view of the surface; (c) particle analysis; (d) histogram.

TABLE 2. AFM parameters of photoanode.

| Height parameter | | | |
|------------------------------|----------|--|---|
| R_q | 13.67 nm | | Root mean square height |
| R_{sk} | 2.861 | | Skewness |
| R_{ku} | 11.45 | | Kurtosis |
| R_t | 75.99 nm | | Total height |
| R_{pt} | 59.19 nm | Max of values on: All λ_c (1) | Maximum hill height |
| R_p | 59.19 nm | Average of values on: All λ_c (1) | Mean hill height |
| R_{vt} | 16.80 nm | Max of values on: All λ_c (1) | Maximum dale depth |
| R_v | 16.80 nm | Average of values on: All λ_c (1) | Mean dale depth |
| R_{zx} | 75.99 nm | Max of values on: All λ_c (1) | Maximum height |
| R_z | 75.99 nm | Average of values on: All λ_c (1) | Mean height |
| R_a | 8.312 nm | | Arithmetic mean absolute height |
| Spatial parameters | | | |
| R_{al} | 492.6 nm | $s = 0.2$ | Autocorrelation length |
| R_{sw} | 3012 nm | | Dominant spatial wavelength |
| Hybrid parameters | | | |
| R_{dq} | 3.850 | | Root mean square gradient |
| R_{da} | 1.968 | | Arithmetic mean absolute gradient |
| R_{dt} | 23.30 | | Maximum absolute gradient |
| R_{dl} | 14031 nm | | Developed length |
| R_{dr} | 0.2231 % | | Developed length ratio |
| Material ratio parameters | | | |
| R_{mr} | 100.0 % | $c = 1000$ nm below highest peak | Material ratio |
| R_{mc} | 55.09 nm | $p = 20\%$ | Inverse material ratio |
| R_{dc} | 12.53 nm | $p = 20\%, q = 80\%$ | Profile section height difference |
| Feature parameters (element) | | | |
| R_{sm} | 1410 nm | | Mean width of the profile elements |
| R_{smx} | 3174 nm | | Maximum profile element width |
| R_{smq} | 845.9 nm | | Standard deviation of profile element width |
| R_c | 21.00 nm | | Mean height of the profile elements |
| R_{cx} | 68.67 nm | | Maximum height profile elements |

A uniform and evenly distributed TiO_2 layer would result in a

greater material ratio and more even TiO₂ distribution across the surface [35].

On the other hand, MWCNTs may affect the height parameters (R_q , R_t) by introducing extra surface characteristics such as nano-tube bundles or agglomerates. These characteristics may lead to overall roughness and height differences.

MWCNTs can also have an effect on hybrid parameters like root mean square gradient (R_{dq}) and maximum absolute gradient (R_{dt}). The presence of MWCNTs with their distinctive cylindrical architecture may cause variations in surface slope and greater gradient values.

By introducing elongated and tubular structures to the surface, MWCNTs may alter the feature parameters (R_{sm} , R_{smx} , R_{smq}), resulting in wider and more diversified feature sizes [36].

Furthermore, Ag nanoparticles on the surface may contribute to the height parameters (R_q , R_t) by producing localized agglomerations or clusters. These agglomerations can cause height fluctuations and enhance roughness overall.

By incorporating Ag nanoparticles, the material ratio characteristics (R_{mr} , R_{mc}) may be influenced by introducing areas with increased Ag concentration. This can cause localized differences in material distribution and have an impact on the overall material ratio.

By introducing extra nanoscale features or clusters, Ag nanoparticles can also alter the feature parameters (R_{sm} , R_{smx} , R_{smq}). These characteristics can contribute to larger feature sizes and greater feature width variability [37].

3.4.2. Atomic Force Microscopy (AFM) of Cathode 1

The aforementioned AFM results can be related to polypyrrole ability to generate a rough and porous structure, which can lead to an enhanced roughness parameter such as R_q [34]. Polypyrrole rough surface shape provides for a higher surface area, which promotes dye adsorption and facilitates charge transfer inside the cathode [38].

Sodium dodecyl sulphate (SDS), on the other hand, is a surfactant that is frequently used to change the surface characteristics of materials. The addition of SDS surfactant to the DSSC cathode can impact surface shape and improve film formation [39].

Surfactant molecules can improve wetting qualities and assist the creation of a smoother, more uniform layer. This might result in reduced surface roughness (lower R_q) and smoother surface characteristics, as shown by smaller changes in height metrics like R_{pt} and R_p [40].

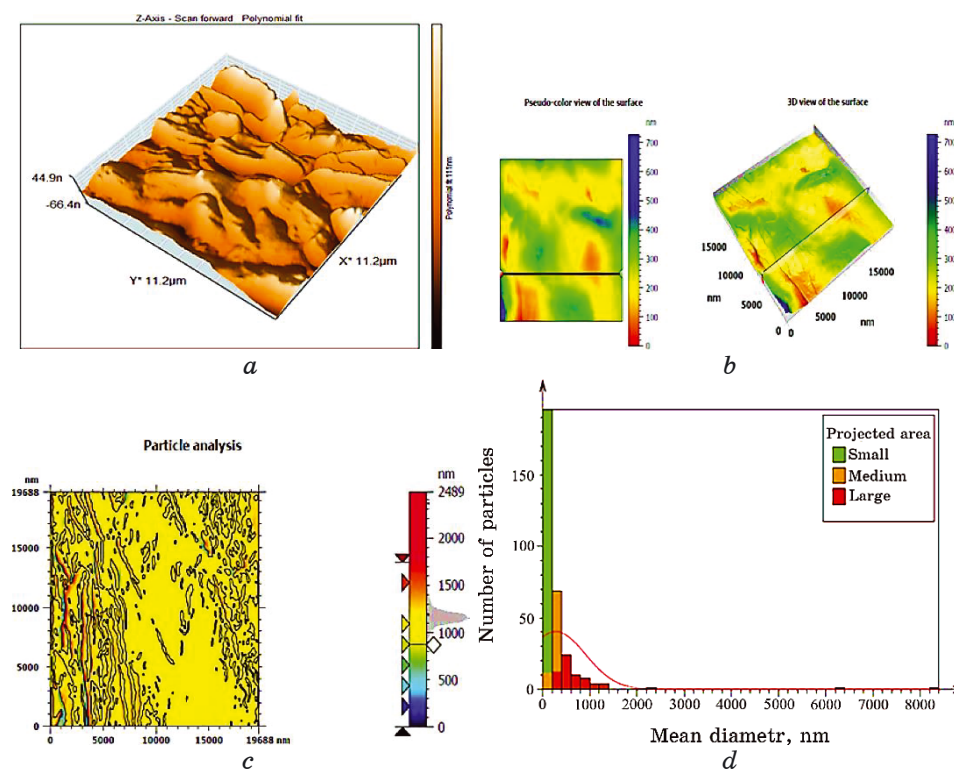


Fig. 11. AFM images of Cathode 1: (a) surface topography; (b) 3D view of the surface; (c) particle analysis; (d) histogram.

3.4.3. Atomic Force Microscopy (AFM) of Cathode 2

The root mean square height (R_q) and total height (R_t) measures show that PPy contributes to the overall roughness of the cathode surface. Because of its naturally textured and irregular structure, the presence of PPy promotes surface roughness.

The spatial parameters autocorrelation length (R_{al}) and dominant spatial wavelength (R_{sw}) are likewise influenced by PPy. These metrics show the presence of periodic structures or recurring patterns that can be caused by the arrangement and alignment of PPy chains inside the cathode [41].

The material ratio parameter (R_{mr}) indicates that PPy distributes uniformly throughout the surface features. It means that PPy helps to generate the surface roughness, elevations, and depressions seen in the AFM studies.

The profile section height difference (R_{dc}) parameter, which reflects the height difference between preset portions of the surface

profile, may also be affected by PPy.

TABLE 3. AFM parameters of Cathode 1.

| Height parameter | | | | |
|------------------------------|----------|----|--|---|
| R_q | 51.46 | nm | | Root mean square height |
| R_{sk} | 0.001505 | | | Skewness |
| R_{ku} | 2.018 | | | Kurtosis |
| R_t | 213.7 | nm | | Total height |
| R_{pt} | 116.9 | nm | Max of values on: All λ_c (1) | Maximum hill height |
| R_p | 116.9 | nm | Average of values on: All λ_c (1) | Mean hill height |
| R_{vt} | 89.70 | nm | Max of values on: All λ_c (1) | Maximum dale depth |
| R_v | 89.70 | nm | Average of values on: All λ_c (1) | Mean dale depth |
| R_{zx} | 206.6 | nm | Max of values on: All λ_c (1) | Maximum height |
| R_z | 206.6 | nm | Average of values on: All λ_c (1) | Mean height |
| R_a | 44.00 | nm | | Arithmetic mean absolute height |
| Spatial parameters | | | | |
| R_{al} | 1736 | nm | $s = 0.2$ | Autocorrelation length |
| R_{sw} | 9882 | nm | | Dominant spatial wavelength |
| Hybrid parameters | | | | |
| R_{dq} | 3.359 | | | Root mean square gradient |
| R_{da} | 2.381 | | | Arithmetic mean absolute gradient |
| R_{dt} | 13.55 | | | Maximum absolute gradient |
| R_{dl} | 19025 | nm | | Developed length |
| R_{dr} | 0.1721 | % | | Developed length ratio |
| Material ratio parameters | | | | |
| R_{mr} | 100.0 | % | $c = 1000$ nm below highest peak | Material ratio |
| R_{mc} | 77.86 | nm | $p = 20\%$ | Inverse material ratio |
| R_{dc} | 100.4 | nm | $p = 20\%, q = 80\%$ | Profile section height difference |
| Feature parameters (element) | | | | |
| R_{sm} | 11506 | nm | | Mean width of the profile elements |
| R_{smx} | 11891 | nm | | Maximum profile element width |
| R_{smq} | 11519 | nm | | Standard deviation of profile element width |
| R_c | 145.7 | nm | | Mean height of the profile elements |
| R_{cx} | 152.6 | nm | | Maximum height profile elements |

Because of its organization and distribution inside the cathode, PPy presence may cause changes in height across various portions [42].

Moreover MWCNTs contribute significantly to the roughness and texture of the cathode surface. They contribute to the parameters of root mean square height (R_q), total height (R_t), and maximum height (R_{zx}), resulting in a rough surface morphology.

MWCNTs have an effect on slope variations, as evidenced by the root mean square gradient (R_{dq}) and arithmetic mean absolute gradient (R_{da}) parameters. MWCNTs create linked networks or clusters on the surface, introducing different slope angles.

MWCNTs can also have an effect on the developed length (R_{dl}) parameter, which measures the length of the surface features that have been produced. MWCNTs can cause prolonged features or structures that contribute to the total developed length [43].

The material ratio parameter (R_{mr}) demonstrates that MWCNTs are uniformly distributed across the surface characteristics, emphasizing their contribution to the roughness and elevations reported

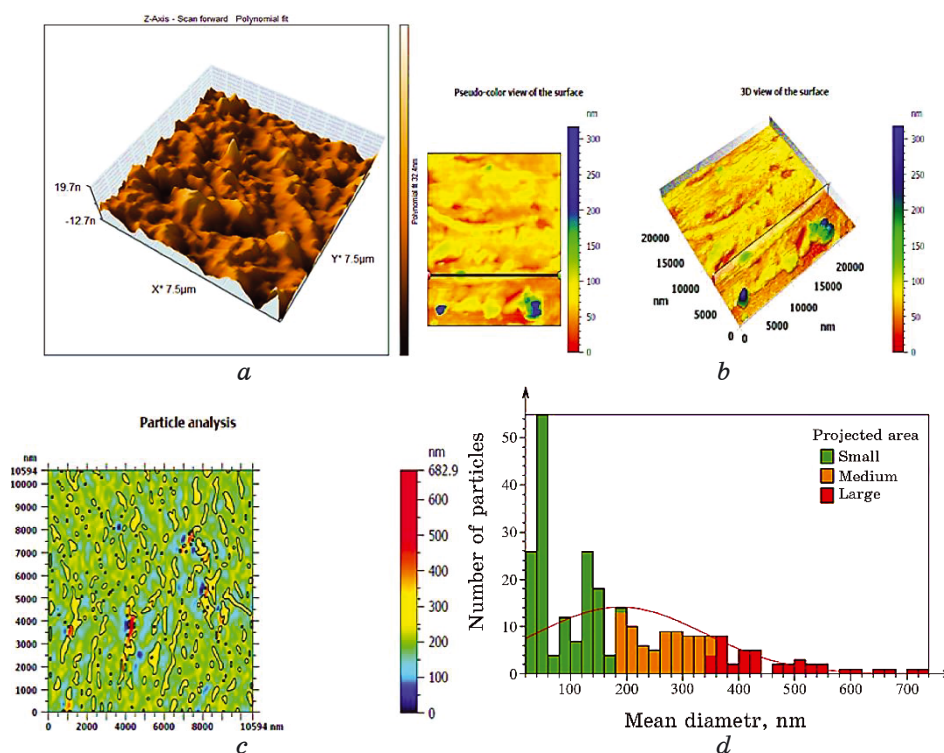


Fig. 12. AFM images of Cathode 2: (a) surface topography; (b) 3D view of the surface; (c) particle analysis; (d) histogram.

in the AFM data.

TABLE 4. AFM parameters of Cathode 2.

| Height parameter | | | |
|------------------------------|---------|----|--|
| R_q | 24.55 | nm | Root mean square height |
| R_{sk} | 1.028 | | Skewness |
| R_{ku} | 3.861 | | Kurtosis |
| R_t | 104.1 | nm | Total height |
| R_{pt} | 67.26 | nm | Max of values on: All λ_c (1) Maximum hill height |
| R_p | 67.26 | nm | Average of values on: All λ_c (1) Mean hill height |
| R_{vt} | 36.88 | nm | Max of values on: All λ_c (1) Maximum dale depth |
| R_v | 36.88 | nm | Average of values on: All λ_c (1) Mean dale depth |
| R_{zx} | 104.1 | nm | Max of values on: All λ_c (1) Maximum height |
| R_z | 104.1 | nm | Average of values on: All λ_c (1) Mean height |
| R_a | 18.76 | nm | Arithmetic mean absolute height |
| Spatial parameters | | | |
| R_{al} | 1386 | nm | $s = 0.2$ Autocorrelation length |
| R_{sw} | 12047 | nm | Dominant spatial wavelength |
| Hybrid parameters | | | |
| R_{dq} | 1.826 | | Root mean square gradient |
| R_{da} | 1.153 | | Arithmetic mean absolute gradient |
| R_{dt} | 8.645 | | Maximum absolute gradient |
| R_{dl} | 19021 | nm | Developed length |
| R_{dr} | 0.05095 | % | Developed length ratio |
| Material ratio parameters | | | |
| R_{mr} | 100.0 | % | $c = 1000$ nm below highest peak Material ratio |
| R_{mc} | 56.73 | nm | $p = 20\%$ Inverse material ratio |
| R_{dc} | 31.45 | nm | $p = 20\%, q = 80\%$ Profile section height difference |
| Feature parameters (element) | | | |
| R_{sm} | 7555 | nm | Mean width of the profile elements |
| R_{smx} | 7555 | nm | Maximum profile element width |
| R_{smq} | ***** | nm | Standard deviation of profile element width |
| R_c | 93.60 | nm | Mean height of the profile elements |
| R_{cx} | 93.60 | nm | Maximum height profile elements |

The metrics mean width of profile elements (R_{sm}) and maximum width of profile elements (R_{smx}) show the existence of broad surface features, which can be linked to the presence of MWCNTs [44].

SDS surfactant is often used to improve the dispersion and stability of carbon nanotubes in solution, such as MWCNTs. It aids in the uniform dispersion of MWCNTs and inhibits agglomeration during the production process. The presence of SDS surfactant may have an indirect effect on surface roughness and texture by influencing the dispersion and arrangement of MWCNTs within the cathode [45]. From AFM results, it is clearly observed that C_1 has a higher roughness (R_q) and total height (R_t) than C_2 , indicating a rougher surface with larger height variability. MWCNTs in C_1 may aid in the creation of higher structures and deeper troughs, resulting in greater surface roughness. Also, C_2 has a lower autocorrelation length (R_{al}) than C_1 , indicating a distinct periodicity or spatial arrangement of surface features. Furthermore, the dominating spatial wavelength (R_{sw}) in C_2 is much higher, indicating the presence of unique and larger-scale surface patterns.

The surface properties of cathodes revealed by AFM can have an impact on their performance. A rougher surface (as seen in C_1) may provide more active areas for catalytic processes while also increasing light absorption. Excessive roughness, on the other hand, can result in higher charge recombination and decreased efficiency. The smoother surface of C_2 , on the other hand, may offer superior charge transport capabilities and lower surface-related losses.

3.5. The Photovoltaic Performance of Prepared DSSCs

The anode material (PHOTOANODE), namely, TiO_2 -MWCNT-Ag nanoparticles, plays a crucial role in enhancing the efficiency of DSSCs. TiO_2 component acts as the main electron acceptor and provides a large surface area for dye adsorption and plasmonic effects. The presence of MWCNTs improves electron transport, while the incorporation of Ag nanoparticles and these factors contribute to efficient charge generation, transport, and collection, resulting in higher overall device efficiency. However, the specific impact of the anode material may vary depending on the choice of dye and cathode materials used in the configuration [46]. The efficiency of DSSCs can be influenced by various factors, including the choice of dye, cathode material, and the resulting interactions between the dye, photoanode, and cathode. The use of Z907 dye generally leads to higher efficiencies compared to plant extracts. However, the choice of cathode material can also play a significant role in enhancing the performance of DSSCs, as demonstrated by the improved efficien-

cies observed in configurations using C_2 except in the case of PHOTOANODE + C_1 + Z907 DSSCs which may be attributed to synergistic interaction where the combination of C_1 (polypyrrole and SDS surfactant) with Z907 dye may result in a more favourable and efficient interaction between the dye molecules and the photoanode (PHOTOANODE). This synergistic interaction can enhance the light absorption, charge separation, and transport processes within the DSSC, leading to improved performance and higher efficiency [47]. Moreover, the energy levels of the components in C_1 , including the poly pyrrole and SDS surfactant, may be better aligned with the energy levels of Z907 dye and the photoanode material (TiO₂-MWCNT-Ag). This alignment can facilitate efficient electron injection from the excited dye molecules into the conduction band of the photoanode, minimizing energy losses and improving overall device performance [48]. Also, composition of C_1 may provide better charge transport properties, allowing for efficient extraction and collection of photo-generated electrons from the photoanode. This improved charge transport can minimize electron recombination and ensure a high current output, resulting in higher short-circuit current (I_{sc}) and overall efficiency [49]. Eventually, the characteristics of C_1 may promote better dye adsorption and coverage on the photoanode surface, ensuring a higher dye loading and maximizing light harvesting. This optimized dye adsorption can enhance the utilization of incident photons and increase the photocurrent, contributing to higher efficiency.

In contrast, while C_2 (polypyrrole, SDS, and MWCNT) may provide certain advantages for specific dyes (Hab., Pom., Aru.) in terms of charge transport or energy level alignment, it may not be as suitable for the Z907 dye. The specific interaction between C_2 and Z907 may be less favourable, resulting in lower efficiency compared to the C_1 configuration [50].

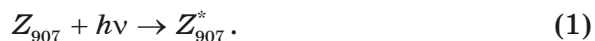
TABLE 5. Photovoltaic properties of DSSCs with different counter electrodes and different dyes.

| Compounds | V_{oc} | I_{sc} | V_{max} | I_{max} | FF | η , % |
|--------------------|----------|----------|-----------|-----------|-------|------------|
| $A_1 + C_1 + Z907$ | 0.807 | 15.1 | 0.72 | 14.1 | 0.833 | 2.537 |
| $A_1 + C_1 + Hab.$ | 0.52 | 9.8 | 0.49 | 9 | 0.865 | 1.102 |
| $A_1 + C_1 + Pom.$ | 0.252 | 17.6 | 0.24 | 17.5 | 0.946 | 1.04 |
| $A_1 + C_1 + Aru.$ | 0.326 | 7.6 | 0.3 | 6.5 | 0.86 | 0.535 |
| $A_1 + C_2 + Z907$ | 0.496 | 24.5 | 0.45 | 21.8 | 0.807 | 2.453 |
| $A_1 + C_2 + Aru.$ | 0.749 | 8.8 | 0.67 | 8.6 | 0.874 | 1.44 |
| $A_1 + C_2 + Hab.$ | 0.435 | 12.9 | 0.43 | 11.5 | 0.898 | 1.24 |
| $A_1 + C_2 + Pom.$ | 0.463 | 13.9 | 0.39 | 12.5 | 0.946 | 1.16 |

3.6. The Work Principle of DSSCs

The working principle of DSSC can be explained with the help of Figs. 13–15.

Photosensitizer absorbs electrons when light is incident on it:



After that, the excitation sensitizer Z_{907}^* introduces an electron into the semiconductor conduction band:

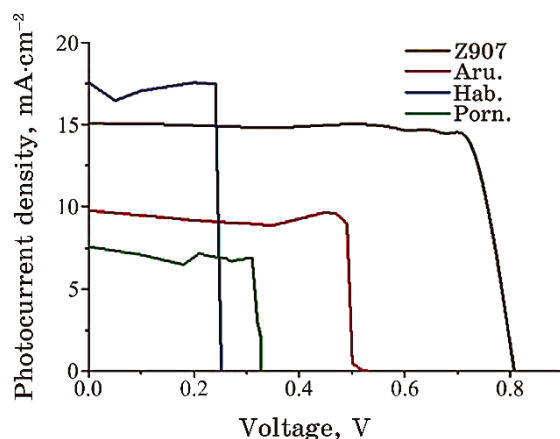


Fig. 13. Current density–voltage (I – V) curves for DSSCs for counter electrode C_1 employing different dyes.

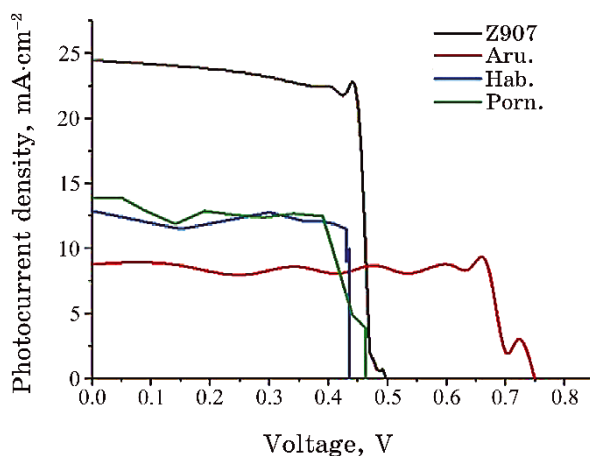
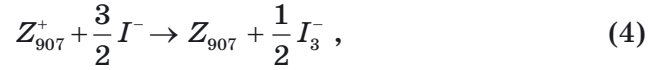
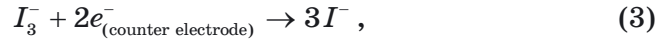


Fig. 14. Current density–voltage (I – V) curves for DSSCs for counter electrode C_2 employing different dyes.



Now, these electrons are transferred into the upper bands, called the conduction band of TiO₂. The liquid electrolyte I⁻ / I³⁻ couple helps the electrons to return to the dye through external load:



This movement of electrons creates a current [51].

In general, the composition of the photocathodes can have a significant impact on their performance and efficiency, Cathode 1 Composition: polypyrrole, SDS surfactant, and MWCNT [52].

Polypyrrole (PPy) is a polymer with strong electrical conductivity and electrocatalytic characteristics. It can improve charge transfer efficiency and provide a pathway for electron transport in the photocathode [53].

SDS (sodium dodecyl sulphate) is a surfactant that is often used to improve the dispersion and stability of nanoparticles. SDS might help in the dispersion of MWCNT (Multi-Walled Carbon Nanotubes) within the polypyrrole matrix in the context of PC1 [54].

MWCNTs are multilayered carbon nanotubes. They have high electrical conductivity and can improve the photocathode's charge transport capabilities. MWCNTs can also provide more surface area for catalytic processes, potentially increasing the efficiency of the photocathode [55].

C₂ is a simpler structure than C₁ since it lacks the incorporation

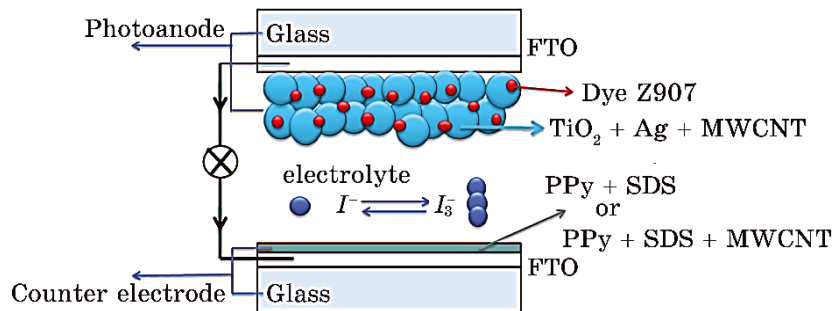


Fig. 15. Dye-sensitized solar-cells' scheme.

of MWCNTs in its composition. Polypyrrole (PPy) continues to be the most important conducting polymer in C_2 , contributing to charge transfer and electron transport mechanisms. SDS surfactant is once again present in C_2 to aid in polypyrrole dispersion and stability [56].

Because carbon nanotubes have good conductive qualities, the insertion of MWCNTs in C_1 may improve the total conductivity of the photocathode. This increased conductivity may allow for more effective charge transport and extraction, perhaps leading to higher efficiency than C_2 [57].

The presence of MWCNTs in C_1 may provide additional catalytic sites for electrochemical processes, thus, boosting the catalytic activity, and performance of the photocathode also may influence surface morphology, potentially resulting in a rougher surface with a larger surface area. This expanded surface area can improve light absorption and charge generation efficiency. MWCNTs in C_1 may affect photocathode stability due to interactions between the carbon nanotubes and the surrounding components. However, the particular implications on stability would be dependent on the fabrication method and component compatibility [58].

3.7. The Effect of Dyes

The choice of dyes in dye-sensitized solar cells (DSSCs) plays a crucial role in determining the efficiency of the solar cell. Different dyes exhibit variations in light absorption properties, energy levels, and electron injection efficiencies, which directly impact the overall performance of the DSSCs [59].

This can be explained accordingly. Z907 is a specific dye used in DSSCs. The impact of Z907 on DSSC efficiency is as follows.

a. Light Absorption: Z907 dye has a broad absorption spectrum, allowing it to capture a wide range of sunlight wavelengths. This broad absorption capability increases the overall light harvesting efficiency of the solar cell, enhancing its performance.

b. Energy Level Alignment: The energy levels of the Z907 dye are optimized to facilitate efficient electron injection from the excited dye molecule to the semiconductor electrode (*e.g.*, TiO_2). This efficient electron injection minimizes charge recombination and enhances the overall efficiency of the solar cell [60].

1. Pomegranate Juice: Pomegranate juice contains natural pigments, such as anthocyanins, which can serve as sensitizers in DSSCs. The impact of pomegranate juice as a dye in DSSCs can be as follows.

a. Light Absorption: Pomegranate juice contains anthocyanins that can absorb a broad range of visible light wavelengths. This

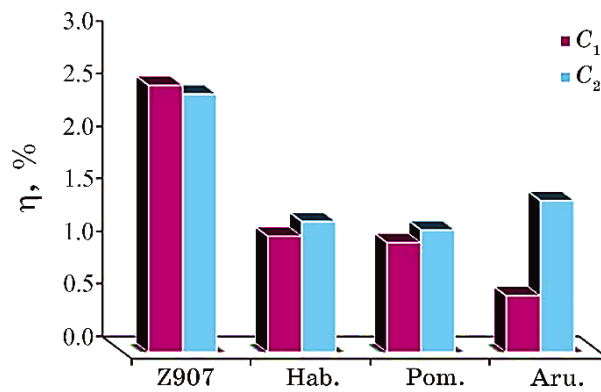


Fig. 16. Scheme for evaluating the efficiency of dyes on PHOTOANODE.

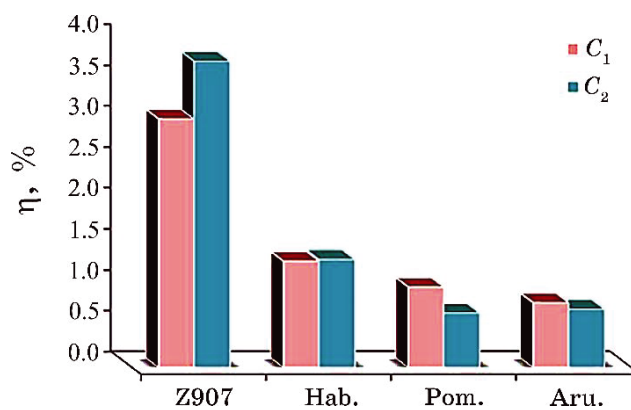


Fig. 17. Scheme for evaluating the efficiency of dyes on PA2.

broad absorption spectrum allows for efficient harvesting of solar radiation, leading to improved light absorption and higher efficiency of DSSCs.

b. Charge Injection Efficiency: Anthocyanins in pomegranate juice can effectively inject electrons into the conduction band of the semiconductor (*e.g.*, TiO₂). This efficient charge injection minimizes charge recombination, thus enhancing the overall performance and efficiency of the DSSC.

c. Stability: The stability of pomegranate juice-based dyes in DSSCs is a crucial factor. Anthocyanins can be susceptible to degradation under prolonged exposure to light and environmental conditions. Therefore, strategies to enhance the stability of pomegranate juice dyes, such as encapsulation or chemical modification, may be necessary to improve the long-term performance of DSSCs [61].

2. Spinach Leaf Extract: Spinach leaf extract contains chloro-

phyll pigments that can be utilized as sensitizers in DSSCs. The impact of spinach leaf extract as a dye in DSSCs can be as follows:

a. Light Absorption: Chlorophyll pigments in spinach leaves have strong absorption in the blue and red regions of the visible spectrum. This absorption profile allows for efficient light harvesting and enhances the overall light absorption capability of DSSCs.

b. Electron Injection Efficiency: Chlorophyll pigments possess suitable energy levels for efficient electron injection into the conduction band of the semiconductor. This efficient electron injection process reduces charge recombination, leading to improved device performance and higher DSSC efficiency.

c. Sensitizer Loading and Stability: Optimizing the loading concentration of spinach leaf extract in DSSCs is crucial to achieve an appropriate balance between light absorption and charge injection. Additionally, the stability of chlorophyll-based dyes under light exposure and environmental factors should be considered to ensure long-term device performance [62].

3. Hibiscus (Roselle) Flower Extract: Hibiscus (Roselle) flower extract contains various pigments, including anthocyanins, which can be used as sensitizers in DSSCs. The impact of hibiscus flower extract as a dye in DSSCs can be as follows:

a. Light Absorption: Anthocyanin pigments present in hibiscus flowers exhibit strong absorption in the visible light region, particularly in the blue and red wavelengths. This characteristic enables efficient light harvesting, contributing to enhanced light absorption and improved DSSC efficiency.

b. Electron Injection Efficiency: Hibiscus flower extract dyes can facilitate efficient electron injection into the semiconductor, promoting efficient charge separation and reducing recombination. This attribute positively influences the overall performance and efficiency of the DSSC.

c. pH Sensitivity: Anthocyanin pigments in hibiscus flower extract can exhibit pH-dependent properties. It is important to consider the pH conditions during the extraction process and optimize the pH of the electrolyte to maintain stable dye performance and maximize the efficiency of the DSSCs [63].

4. CONCLUSION

In conclusion, the anode material, cathode composition, and dye selection all have an impact on the efficiency of dye-sensitized solar cells (DSSCs). The anode material (TiO_2 -MWCNT-Ag nanoparticles) improves efficiency by increasing dye adsorption surface area and boosting electron transport. The dye used, such as Z907, is critical in achieving effective light absorption and energy level alignment

for electron injection. Because of increased charge transfer, extraction of photo-generated electrons, and optimal dye adsorption, the cathode composition C₁ (polypyrrole, SDS surfactant, and MWCNT) performs better with Z907 dye. Other colours, including as pomegranate juice, spinach leaf extract, and hibiscus flower extract, have an effect on DSSC efficiency due to their light absorption and electron injection efficiencies. Understanding these interactions is critical for developing high-efficiency DSSCs and moving renewable energy technologies forward.

ACKNOWLEDGEMENTS

The authors offer their appreciations for Al-Qadisiyah University, College of science Chemistry Department for its instrumental and technical support.

REFERENCES

1. B. O'regan and M. Grätzel, *Nature*, **353**, Iss. 6346: 737 (1991); doi:10.1038/353737a0
2. N. Gokilamani, N. Muthukumarasamy, M. Thambidurai, A. Ranjitha, and D. Velauthapillai, *J. Sol-Gel Sci. Technol.*, **66**, Iss. 2: 212 (2013); doi:10.1007/s10971-013-2994-9
3. N. Memarian, I. Concina, A. Braga, S. M. Rozati, A. Vomiero, and G. Sberveglieri, *Angewandte Chemie*, **123**, Iss. 51: 12529 (2011); <https://doi.org/10.1002/ange.201104605>
4. R. Bart, P. Sandeep, and S. Ullrich, *Chemical Society Reviews*, **44**, Iss. 22: 8326 (2015); <https://doi.org/10.1039/C5CS00352K>
5. H. J. Hwang and H. S. Kim, *Journal of Composite Materials*, **48**, Iss. 14: 1679 (2014); doi:10.1177/0021998313490215
6. C. Hyonkwang, K. Hyunkook, H. Sookhyun, H. Youngmoon, and J. Minhyon, *J. Mater. Chem.*, **21**, Iss. 21: 7548 (2011); <https://doi.org/10.1039/C1JM11145K>
7. G. Feng, W. Hong, X. Xin, Z. Gang, and W. Zhong-Sheng, *J. Am. Chem. Soc.*, **134**, Iss. 26: 10953 (2012); doi:10.1021/ja303034w
8. J. Wu, Q. Li, L. Fan, Z. Lan, P. Li, J. Lin, and S. Hao, *J. Power Sources*, **181**, Iss. 1: 172 (2008); <https://doi.org/10.1016/j.jpowsour.2008.03.029>
9. T. C. T. Thanh, P. J. Young, L. S. Woo, S. Thogiti, and K. J. Hong, *J. Nanosci. Nanotechnol.*, **16**, Iss. 5: 5263 (2016); <https://doi.org/10.1166/jnn.2016.12266>
10. K. B. Erande, P. Y. Hawaldar, S. R. Suryawanshi, B. M. Babar, A. A. Mohite, H. D. Shelke, S. V. Nipane, and U. T. Pawar, *Materials Today*, **43**, Iss. 4: 2716 (2021); <https://doi.org/10.1016/j.matpr.2020.06.357>
11. R. F. Mansa, G. Govindasamy, Y. Y. Farm, H. Abu Bakar, J. Dayou, and C. S. Sipaut, *Journal of Physical Science*, **25**, Iss. 2: 85 (2014);
12. S. A. Taya, T. M. El-Agez, H. S. El-Ghamri, and M. S. Abdel-Latif, *International Journal of Materials Science and Applications*, **2**, Iss. 2: 37 (2013);

- doi:10.11648/j.ijmsa.20130202.11
13. L. Chun Hung, S. Ryan, and C. B. O'Regan, *Journal of Materials Chemistry A*, **1**, Iss. 45: 14154 (2013); <https://doi.org/10.1039/C3TA13145A>
 14. Md. H. Miah and S. Miah, *Asian Journal of Applied Sciences*, **3**, Iss. 4: 806 (2015).
 15. Sung Ho Song, Ho-Kyun Jeong, Yong-Gu Kang, and Choon-Tack Cho, *Polymer (Korea)*, **34**, Iss. 2: 108 (2010); doi:10.7317/pk.2010.34.2.108
 16. K. R. Gota and S. Suresh, *Asian Journal of Chemistry*, **26**, Iss. 21: 7087 (2014); doi:10.14233/ajchem.2014.17142
 17. R. S. Dubey, K. V. Krishnamurthy, and S. Singh, *Results in Physics*, **14**: 102390 (2019); <https://doi.org/10.1016/j.rinp.2019.102390>
 18. B. Ajitha, Y. A. K. Reddy, and R. P. Sreedhara, *Molecular and Biomolecular Spectroscopy*, **121**: 164 (2014); doi:10.1016/j.saa.2013.10.077
 19. Y. D. Guang, Z. B. Y. W. Li, and Qian, *International Journal of Nanomedicine*, **6**: 3271 (2011); <https://doi.org/10.2147/IJN.S27468>
 20. H. Vijeth, K. S. P. Ashok, L. Yesappa, M. Niranjana, M. Vandana, and H. Devendrappa, *AIP Conference Proceedings*, **2142**, Iss. 1: 150029 (2019); <https://doi.org/10.1063/1.5122578>
 21. M. A. Rashed, M. Faisal, M. Alsaiari, S. A. Alsareii, and F. A. Harraz, *Electrocatalysis*, **12**: 650 (2021); <https://doi.org/10.1007/s12678-021-00675-6>
 22. R. M. Mohammad, S. A. Duha, and A. K. M. Mustafa, *Journal of Sol-Gel Science and Technology*, **90**: 498 (2019); doi:10.1007/s10971-019-04973-w
 23. H. Rhee et al., *Synthetic Metals*, **28**, Iss. 1-2: 605 (1989).
 24. S. Hiroshi, O. Kentaro, K. Daisuke, D. Bhavana, S. Usha, and N. Tsutomu, *Journal of the Electrochemical Society*, **150**, Iss. 5: H119 (2003); doi:10.1149/1.1566420
 25. Yang Zhao, Yue Hu, Yan Li, Han Zhang, Shaowen Zhang, Liangti Qu, Gaoquan Shi, and Liming Dai, *Nanotechnology*, **21**, Iss. 50: 505702 (2010); doi:10.1088/0957-4484/21/50/505702
 26. P. P. Lottici, D. Bersani, M. Braghini and A. Montenero, *Journal of Materials Science*, **28**, Iss. 1: 177 (1993); doi:10.1007/bf00349049
 27. N. K. Konstantin, O. Bulent, C. S. Hannes, K. P. Robert, A. A. Ilhan, and C. Roberto, *Nano Letters*, **8**, Iss. 1: 36 (2008); <https://doi.org/10.1021/nl071822y>
 28. H. Chang, H.T. Jung, C. Tien-Li, H. K. David, J.C. Song and C. S. Hua, *Materials Transactions*, **50**, Iss. 12: 2879 (2009); <https://doi.org/10.2320/matertrans.M2009203>
 29. Y. Furukawa, S. Tazawa, Y. Fujii, and I. Harada, *Synthetic Metals*, **24**, Iss. 4: 329 (1988); [https://doi.org/10.1016/0379-6779\(88\)90309-8](https://doi.org/10.1016/0379-6779(88)90309-8)
 30. D. C. Sophie and S. P. Yves, *Chemistry of Materials*, **11**, Iss. 3: 829 (1999); <https://doi.org/10.1021/cm9807541>
 31. C. D. Chouvy and T. T. M. Tran, *Electrochemistry Communications*, **10**, Iss. 6: 947 (2008); <https://doi.org/10.1016/j.elecom.2008.04.024>
 32. H. Hiura, T. W. Ebbesen, K. Tanigaki, and H. Takahashi, *Chemical Physics Letters*, **202**, Iss. 6: 509 (1993); [https://doi.org/10.1016/0009-2614\(93\)90040-8](https://doi.org/10.1016/0009-2614(93)90040-8)
 33. R. A. Jishi, L. Venkataraman, M. S. Dresselhaus, and G. Dresselhaus, *Chemical Physics Letters*, **209**, Iss. 1-2: 77 (1993); <https://doi.org/10.1016/0009->

- 2614(93)87205-H
34. M. F. Islam, E. Rojas, D. M. Bergey, A. T. Johnson, and A. G. Yodh, *Nano Letters*, **3**, Iss. 2: 269 (2003); <https://doi.org/10.1021/nl025924u>
 35. W. C. Oh and M. L. Chen, *Chemical Society*, **29**, Iss. 1: 159 (2008); [doi:10.5012/bkcs.2008.29.1.159](https://doi.org/10.5012/bkcs.2008.29.1.159)
 36. K. Youngmi, L. Ginaya; C. Boyce, Y. Yeoheung, N. S. Vesselin, S. Mark, P. Devdas, and S. Jagannathan, *Composites Part B: Engineering*, **57**: 105 (2014); <https://doi.org/10.1016/j.compositesb.2013.09.004>
 37. C. Ling-Yu, L. Chun-Ting, L. Yu-Yan, L. Chuan-Pei, Y. Min-Hsin, H. Kuo-Chuan, and L. Jiang-Jen, *Electrochimica Acta*, **155**: 263 (2015); <https://doi.org/10.1016/j.electacta.2014.12.127>
 38. S. V. Ahmad, M. M. Ghasem, and J. Majid, *Synthetic Metals*, **191**: 104 (2014); <https://doi.org/10.1016/j.synthmet.2014.02.021>
 39. L. Woranan, K. T. Chyuan, S. Chaochin, S. Pedaballi, K. Sasipriya, L. Ya-Fen, C. Bo-Ren, and L. Wen-Ren, *Solar Energy*, **142**: 1 (2017); <https://doi.org/10.1016/j.solener.2016.12.017>
 40. I. M. V. Ana, G. G. Emilio, J. A. María, and J. G. S. María, *Solar Energy*, **91**: 263 (2013); <https://doi.org/10.1016/j.solener.2013.02.009>
 41. C. Sadik, E. E. Sule, Ali, A. A. Khalaf, C. C. Gamze, M. Matej, O. Maria, and U. O. Aysegul, *Research on Chemical Intermediates*, **44**: 3325 (2018); [doi:10.1007/s11164-018-3309-0](https://doi.org/10.1007/s11164-018-3309-0)
 42. S. Thogiti, T. T. C. Thi, K. J. Yoon, Y. E. Joo, A. K. Soon, B. Y. Shin, L. S. Woo, and K. J. Hong, *Molecular Crystals and Liquid Crystals*, **620**, Iss. 1: 71 (2015); <https://doi.org/10.1080/15421406.2015.1094870>
 43. S. Napisah, J. Aidah, J. Mohammad, and K. Anish, *Polymers*, **12**, Iss. 11: 2522 (2020); <https://doi.org/10.3390/polym12112522>
 44. X. Zhang, J. Zhang, R. Wang, T. Zhu, and Z. Liu, *Chem. Phys. Chem.*, **5**, Iss. 7: 998 (2004); <https://doi.org/10.1002/cphc.200301217>
 45. S. Z. Yao and M. T. Lee, *Materials*, **10**, Iss. 5: 555 (2017); [doi:10.3390/ma10050555](https://doi.org/10.3390/ma10050555)
 46. S. Dandan, C. Peng, W. Tianyue, X. Bixia, J. Yongjian, L. Meicheng, L. Yaoyao, D. Sheng, H. Yue, L. Zhuohai, and M. J. Michel, *Nano Energy*, **23**: 122 (2016); <https://doi.org/10.1016/j.nanoen.2016.03.006>
 47. K. Sharma, V. Sharma, and S. S. Sharma, *Nanoscale Res. Lett.*, **13**: 381 (2018); <https://doi.org/10.1186/s11671-018-2760-6>
 48. P. Dhanasekaran and R. Marimuthu, *Frontiers in Energy Research*, **10**: 1 (2023); <https://doi.org/10.3389/fenrg.2022.998038>
 49. D. Kumar, *Engineering Research Express*, **3**, Iss. 4: 042004 (2021); [doi:10.1088/2631-8695/ac3b29](https://doi.org/10.1088/2631-8695/ac3b29)
 50. C. Yan, J. Wang, W. Kang, M. Cui, X. Wang, C. Y. Foo, and K. J. Chee, *Nanyang Technological University*, **26**, Iss. 13: 1950 (2014); <https://doi.org/10.1002/adma.201470083>
 51. M. Mujahid, M. Ahmad and O. A. Al-Hartomy, *Optoelectronics and Advanced Materials-Rapid Communications*, **16**, Iss. 9–10: 464 (2022).
 52. S. Mohanty, S. K. Nayak, B. S. Kaith, and S. Kalia, *Polymer Nanocomposites based on Inorganic and Organic Nanomaterials*, 89 (2015); <https://doi.org/10.1002/9781119179108.ch4>
 53. Q. Zhou, J. Qiu, Y. Wang, M. Yu, J. Liu, and X. Zhang, *ACS Energy Letters*, **6**, Iss. 4: 1596 (2021); <https://doi.org/10.1021/acseenergylett.1c00291>

54. H. Monalisa and M. A. Kumar, *Journal of Materials Science: Materials in Electronics*, **30**: 4792 (2019); doi:10.1007/s10854-019-00773-8
55. C. Ziyi, X. Guoxin, H. Feng, W. Weiqi, G. Dan, and W. Wei, *Advanced Materials Interfaces*, **4**, Iss. 23: 1700998 (2017); <https://doi.org/10.1002/admi.201700998>
56. L. Jianneng, C. Dachang, A. Keegan, S. Qian, H. N. Graham, Z. Yang, S. Yipeng, L. Jing, L. Ruying, Z. Li, Z. Shangqian, L. Shigang, H. Huan, Z. Xiaoxing, S. C. Veer, and S. Xueliang, *Advanced Energy Materials*, **11**, Iss. 1: 2002455 (2021); <https://doi.org/10.1002/aenm.202002455>
57. J. C. R. Morales, D. M. López, M. G. Sánchez, J. C. Vázquez, C. Savaniud, and S. N. Savvina, *Energy & Environmental Science*, **3**, Iss. 11: 1670 (2010); <https://doi.org/10.1039/C0EE00166J>
58. Yiding Song, Nan Wang, Yuanhao Wang, Renyun Zhang, Hekan Olin, and Ya Yan, *Advanced Energy Materials*, **10**, Iss. 45: 2002756 (2020); <https://doi.org/10.1002/aenm.202002756>
59. S. P. Wulan, Y. D. Kusuma, and D. A. Handrini, *AIP Conference Proceedings*, **1755**, Iss. 1: 160003 (2016); doi:10.1063/1.4958596
60. N. Gokilamani, N. Muthukumarasamy, M. Thambidurai, A. Ranjitha, V. Dhayalan, T. S. Senthil, and R. Balasundaraprabhu, *Journal of Materials Science: Materials in Electronics*, **24**, Iss. 9: 3394 (2013); doi:10.1007/s10854-013-1261-8
61. A. Arunachalam, S. Govindan, and S. Vadivel, *Subramanian and Balasubramanian, Materials in Electronics*, **28**: 18455 (2017); doi:10.1007/s10854-017-7792-7
62. A. Brüger, G. Fafilek, and M. N. Spallart, *Solar Energy*, **205**: 74 (2020); <https://doi.org/10.1016/j.solener.2020.05.035>
63. H. Masuda, Y. Ohta, and M. Kitayama, *Journal of Materials Science and Chemical Engineering*, **7**, Iss. 02: 1 (2019); doi:10.4236/msce.2019.72001

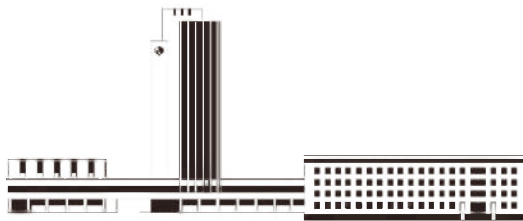
Наукове видання

НАНОСИСТЕМИ, НАНОМАТЕРІАЛИ, НАНОТЕХНОЛОГІЇ

ЗБІРНИК НАУКОВИХ ПРАЦЬ
ТОМ 22
випуск 3
(2024)

Підписано до друку 19.09.2024. Формат 70×100/16.
Папір офсетний. Друк різнографічний.
Ум. друк. арк. 21,13. Обл.-вид. арк. 19,44.
Наклад 61 прим. Зам. № 3

Поліграфічно-розмножувальна дільниця РВВ ІМФ ім. Г. В. Курдюмова НАН України
бульв. Акад. Вернадського, 36; 03142 Київ, Україна



НАЦІОНАЛЬНА АКАДЕМІЯ НАУК УКРАЇНИ



Засновник: ІНСТИТУТ МЕТАЛОФІЗИКИ ім. Г. В. КУРДЮМОВА НАН УКРАЇНИ
Видавець: ІНСТИТУТ МЕТАЛОФІЗИКИ ім. Г. В. КУРДЮМОВА НАН УКРАЇНИ

Передплатний індекс 94919

ISSN 1816-5230

Інформація про передплату на збірник наукових праць
«НАНОСИСТЕМИ, НАНОМАТЕРІАЛИ, НАНОТЕХНОЛОГІЇ»

Редакція щоквартального збірника наукових праць

«НАНОСИСТЕМИ, НАНОМАТЕРІАЛИ, НАНОТЕХНОЛОГІЇ»

(CODEN: NNNAAT; ISSN (Print): 1816-5230, ISSN (Online): 2617-3794;

у «Каталозі видань України» передплатний індекс: **94919**)

повідомляє про передплату (починаючи з поточного кварталу випуску).

Рекомендуємо оформити передплату безпосередньо перерахуванням оплати

у гривнях:

«ОТРИМУВАЧУ»: Інститут металофізики ім. Г. В. Курдюмова НАН України

на розрахунковий рахунок № UA058201720313291001201001901 в банку ГУДКСУ в м. Києві

код банку 820172

код ЗКПО: 05417331

для «ПОСТАЧАЛЬНИКА» — Інституту металофізики ім. Г. В. Курдюмова НАН України

Свідоцтво платника податку № 36283185

ПІН 054173326066

Код ПРИЗНАЧЕННЯ ПЛАТЕЖУ: 25010100

ПРИЗНАЧЕННЯ ПЛАТЕЖУ: за збірник «Наносистеми, наноматеріали, нанотехнології» для РВВ

ІМФ НАНУ

ПідСТАВА: передоплата 100%

в іноземній валюті (доларах США, євро) через відповідні банки-кореспонденти АТ «Державний експортно-імпорتنний банк України»:

«ОТРИМУВАЧУ»: Філія АТ «Державний експортно-імпорتنний банк України» в м. Києві (Україна, 04053 Київ, вул. Бульварно-Кудрявська, 11^б)

на розрахунковий рахунок № UA60322313000002530800000067

МФО 322313

для «ПОСТАЧАЛЬНИКА» — Інституту металофізики ім. Г. В. Курдюмова НАН України

ПРИЗНАЧЕННЯ ПЛАТЕЖУ: за збірник «Наносистеми, наноматеріали, нанотехнології» для РВВ

ІМФ НАНУ

ПідСТАВА: передоплата 100%

За цього способу передплати необхідно сповістити редакцію збірника за поштовою адресою:

РВВ (№ 83) ІМФ НАНУ,

бульв. Акад. Вернадського, 36,

03142 Київ, Україна

e-mail: tatar@imp.kiev.ua; факс: +380 44 4242561; телефон: +380 44 4241221, +380 44 4249042

дату сплати, назву установи або найменування передплатника, адресу для поштової доставки, а за потреби — свої реквізити для податкової накладної.

Періодичність — том з 4 випусків у рік.

Із врахуванням поштової пересилки

для передплатників в Україну передплатна ціна: одного примірника випуску — 390 грн., тому — 1560 грн.;

для іноземних передплатників передплатна ціна: одного примірника випуску — 40 US\$ (37 EUR), тому — 160 US\$ (148 EUR).

✂

Зразок для оплати річної передплати

Рахунок-фактура

«ПОСТАЧАЛЬНИК»: Інститут металофізики ім. Г. В. Курдюмова НАН України

«ОТРИМУВАЧ»: Філія АТ «Державний експортно-імпорتنний банк України» в м. Києві

(Україна, 04053 Київ, вул. Бульварно-Кудрявська, 11^б)

на розрахунковий рахунок № UA60322313000002530800000067, МФО 322313

ПРИЗНАЧЕННЯ ПЛАТЕЖУ: за збірник «Наносистеми, наноматеріали, нанотехнології» для ІМФ НАНУ

«ПЛАТНИК»:

ПідСТАВА: передоплата 100%

| № | Назва | Од. вим. | Кількість | Ціна | Сума |
|-----------------------|--|----------|-----------|---------|-----------------|
| 1 | збірник «Наносистеми, наноматеріали, нанотехнології» (включаючи доставку поштою) | прим. | 4 | 40 US\$ | 160 US\$ |
| Сума до сплати | | | | | 160 US\$ |

